A veto for the ZEPLIN-III Dark Matter Detector

Emma Jayne Barnes

School of Physics

The University of Edinburgh

Thesis submitted for the degree of
Doctor of Philosophy in the subject of *Physics*

2010

For
Mam & my brother Wayne

Abstract

Cold dark matter in the form of weakly interacting massive particles (WIMPs) is a favoured explanation to the galactic dark matter puzzle and could account for a large proportion of the missing mass of the Universe. There are currently numerous detectors around the world attempting to observe a WIMP signal. The ZEPLIN-III detector is one such device. Utilising liquid xenon as a target medium, identification is based on extraction of scintillation and electroluminescence signals from the two-phase xenon target caused when WIMPs scatter and has recently completed its first science run (FSR). With no WIMP signal observed, ZEPLIN-III has excluded a WIMP-nucleon spin-independent cross section above 8.1×10^{-8} pb (90% confidence limit) for a WIMP mass of 60 GeV/c^2 and also set a 90% confidence upper limit of a pure WIMP-neutron spin-dependent cross section of 1.9×10^{-2} pb for a 55 GeV/c^2 WIMP mass. However, the focus of this thesis is the future of the ZEPLIN-III detector with regards to the second science run (SSR).

As with all dark matter detectors, background reduction from neutrons and gamma-rays plays a significant part in obtaining competitive WIMP detection sensitivities. The author has contributed significantly to the design, development and testing of a low radioactivity veto for the ZEPLIN-III detector, to be retrofitted in time for the SSR. It will detect neutrons and gamma-rays in coincidence with the ZEPLIN-III target allowing these events to be removed as candidate WIMP events.

This thesis describes the author's contribution to the design, construction, testing and evaluation of the veto. Also discussed is the development of a comprehensive Monte Carlo simulation, utilised to aid in the design process, to determine the background rates emanating from the veto components (and therefore possible impact on the low sensitivity running of ZEPLIN-III), and to provide an accurate estimation of the overall veto efficiency to reject coincident neutrons

and gamma-rays. The veto will have a neutron rejection factor of 67%, reducing the expected neutron background in ZEPLIN-III from 0.4 neutrons/year to 0.14 neutrons/year, a significant factor in the event of a possible WIMP observation.

In addition to the work performed on the ZEPLIN-III veto, the author has also contributed to the first science run analysis program by profiling the historical evolution of the electron lifetime throughout the FSR, and implementing consideration of this to improve the data quality.

Acknowledgements

Firstly I would like to thank my supervisor, Dr Alex Murphy, for providing me with support and encouragement throughout the duration of my Ph.D. His knowledge and guidance has been invaluable.

I would also like to acknowledge EPSRC for providing the funding that has allowed me to carry out this research and the STFC for support of the ZEPLIN-III collaboration and the Boulby mine laboratory. I would also like to thank all the members of the ZEPLIN-III collaboration, past and present whose guidance and instruction has been invaluable and who have made Boulby mine a wonderful place to work. I would also like to mention to Henrique Araújo for his guidance throughout the ZEPLIN-III first science run data analysis. Chamkaur Ghag also deserves a special mention in teaching me the ways of GEANT4, going above the call of duty by proof reading my thesis and being generally supportive throughout my Ph.D.

I would also like to thank the ZEPLIN-III collaborators at the University of Coimbra, Portugal and the Institute of Theoretical and Experimental Physics, Moscow who made me feel welcome when I visited and took the time to impart their knowledge.

Furthermore I would like to acknowledge everyone in the University of Edinburgh nuclear physics group, Derek Glazier, Dan Watts, Phil Woods, Marialuisa Aliotta and Tom Davinson and all other members of the group who have each contributed in one way or another. I would like to thank my fellow dark matter colleagues, Paul Scovell, Anthony Hollingsworth and Lea Reichhart and my office mates past and present - Claire, Daria, Alexis, Gavin, Steve, Tom, Jo, Pauline, Mark and Phil who have all made my Ph.D. a positive experience.

I must also mention my wonderful family, in particular my mam and my brother Wayne (to whom this thesis is dedicated) who have always encouraged and believed in me even when I have not. Finally I would like to thank my partner Laurence who has had to endure all

of the ups and downs throughout my Ph.D. I am extremely fortunate to have both my family and Laurence in my life.

Declaration

The work presented in this thesis was carried out within the School of Physics at The University of Edinburgh and the institutions of the ZEPLIN-III collaboration. A substantial contribution of the work described from Chapter 3 onwards was made by myself, but since the ZEPLIN-III programme is a collaborative effort, some of the work must be attributed to several workers at a time within the ZEPLIN-III collaboration. My work involves the electron lifetime analysis for the ZEPLIN-III first science run. I made a significant contribution to the design, construction and testing of the veto components. All Monte Carlo simulations described in the thesis were conducted by myself, unless otherwise stated. This thesis has been composed by myself and no portion has been submitted for any other degree or professional qualification.

Emma Jayne Barnes

Contents

List of Figures

List of Tables

Chapter 1

Introduction to Dark Matter

1.1 Introduction

Over the past century great insight has been made into the evolution of the Universe and how the material existing within it has shaped its development. It was once thought that the majority of matter existed in luminous stars; however through observational evidence provided by Fritz Zwicky and Vera Rubin, it is now thought that non-luminous 'dark matter' is the main contributor. This dark matter is expected not to interact electromagnetically, but can be deduced through its gravitational effects. An exciting area of research has developed around detecting and understanding the nature of dark matter. In this chapter the origins of the Universe, the motivation and evidence for dark matter and dark matter candidates are discussed.

1.1.1 Important Cosmological Principles

Big bang cosmology attempts to describe the origin and nature of the Universe in its entirety. Central to this is the *Cosmological Principle*, that states that the Universe is isotropic and homogeneous. This thesis contributes to the quest for the discovery of dark matter, an integral part of big bang cosmology. Understanding what constitutes the universe can reveal details on its probable fate. In this chapter the author will introduce big bang cosmology and show why the existence of dark matter is important for current cosmological theories.

1.1.1.1 The Expanding Universe

Big bang cosmology epitomises the idea of an expanding universe. The notion of an expanding universe was theorised by Alexander Alexandrovich Friedmann in 1922 and also Georges Lemaître in 1927. Very strong supporting evidence was then provided by Edwin Hubble, refuting the steady state universe theories of the time. Using Doppler red-shifted spectral lines from distant galaxies, Hubble showed that galaxies were receding with a velocity $\vec{v}$, proportional to their distance $\vec{d}$. Hubble's law may be written as,

$$\vec{v} = H_0 \vec{d}. \tag{1.1}$$

The constant of proportionality, H_0 (referred to as Hubble's constant) has the value today of $H_0 = 70.5 \pm 1.3 kms^{-1}Mpc^{-1}$ [1]. It can be shown that at earlier stages of the Universe H_0 took different values.

For an isotropic and homogeneous universe the distance between two points can be described using co-moving co-ordinates. The relationship between the real distance of a particle ($\vec{r}$) and the co-moving distance ($\vec{x}$) is described as,

$$\vec{r} = a(t)\vec{x} \tag{1.2}$$

where a(t) is the cosmological expansion parameter. Hubble's law may also then be re-defined in terms of co-moving co-ordinates, thus describing the rate of change of the expansion parameter where

$$H(t) = \frac{\dot{a(t)}}{a(t)} \tag{1.3}$$

1.1.1.2 The Friedmann Equations

The expansion (or collapse) of the Universe can be described by the Friedmann equations where the Universe is assumed to be isotropic and homogeneous with a corresponding mass density and pressure. These were derived from the Friedmann-Lemaitre-Robertson-Walker (FLRW) solutions to Einstein's general relativity field equations (EFE).

By assuming the cosmological principle, the Roberson-Walker line element describes the Universe as a three-dimensional curved space (3-sphere) with 4-dimensional boundaries [2],

$$ds^2 = c^2dt^2 - a^2(t)\left(\frac{dr^2}{1-kr^2} + r^2d\theta^2 + r^2\sin^2\theta d\phi^2\right). \tag{1.4}$$

where s is the proper distance between space-time points; c is the speed of light; t is the cosmological proper time; r, ϕ and θ describe the co-moving spherical polar co-ordinates and k is the parameter that defines the spatial curvature of the Universe (for a complete derivation of Equation 1.4 see [3; 4]). k can have values of ± 1 or 0 depending on whether the constant curvature of space is positive, negative or flat.

In the early 20^{th} century Albert Einstein published his seminal work on General Relativity describing how matter effects the curvature of space. Central to this body of work is how the Universe (as thus described) obeys the Einstein field equations (EFE):

$$R_{\mu v} - \frac{1}{2}g_{\mu v}R - \Lambda g_{\mu v} = \frac{8\pi}{c^4}G_N T_{\mu v} \tag{1.5}$$

where G_N is Newton's gravitational constant, R is the scalar curvature and $R_{\mu v}$ is the Ricci tensor which describes the extent of any curvature in a system. The energy and momentum of matter within the Universe is accounted for using the energy-momentum tensor $T_{\mu v}$ and finally Λ is a cosmological constant. A positive Λ can drive the expansion of the Universe and is more commonly referred to as either *vacuum energy* or *dark energy*. The purpose of the Einstein field equations is in describing the effect of matter on space; however the Friedmann equations solve EFEs for different types of matter and their effect on space.

In deriving the Friedmann equations, the early universe is assumed to have had an energy density that was smooth. Therefore by describing the matter within the Universe as a homogeneous, isotropic, frictionless, ideal fluid, Equation 1.5 yields the following,

$$\left(\frac{\dot{a}}{a}\right)^2 + \frac{kc^2}{a^2} - \frac{\Lambda}{3} = \frac{8\pi G}{3}\rho_t \tag{1.6}$$

and the acceleration equation,

$$\frac{2\ddot{a}}{a} + \left(\frac{\dot{a}}{a}\right)^2 + \frac{kc^2}{a^2} - \Lambda = -\frac{8\pi G}{3}\rho_t. \tag{1.7}$$

ρ_t is the total energy density of the Universe where $\rho_t = \rho_m + \rho_r$ with contributions from matter and radiation respectively. The acceleration equation

is derived by differentiating Equation 1.6 and then assuming conservation of energy for a perfect fluid,

$$\frac{d}{dt}(\rho a^3) = -\frac{P}{c^2}\frac{d}{dt}a^3. \tag{1.8}$$

Equation 1.8 shows that for positive pressure the density of the Universe will decrease whilst the volume (i.e. $V = a^3$) increases. Equations of state for a matter, radiation or 'vacuum energy' dominated universe, reveal how the volume and evolving scale factor can diverge. A summary of the different scale factors for the different regimes is indicated in Table 1.1

Regime	**EOS**	**Energy Density**
Radiation	$P = \frac{\rho c^2}{3}$	$\rho \sim \frac{1}{a^4}$
Matter	$P = \frac{2}{3}\rho c^2\left(\frac{v^2}{c^2}\right)$	$\rho \sim \frac{1}{a^3}$
Vacuum	$P = -\rho c^2$	ρ =constant

Table 1.1: *The equations of state and energy densities for matter, radiation and vacuum regimes.*

1.1.1.3 The Energy Density Parameter, Ω_o

Using the Friedmann equations it is possible to predict the fate of the Universe based on its curvature (k). The evolution of curvature is linked to the density of the Universe, ρ, which can be expressed in terms of the critical density (ρ_c). ρ_c is derived from the Friedmann equations by assuming a matter dominated, flat universe (i.e $\rho_r = 0$ and $\Lambda = 0$ and $k = 0$),

$$\rho_c(t) = \frac{3H^2(t)}{8\pi G}. \tag{1.9}$$

A dimensionless density parameter (Ω) can then be deduced, which is the ratio of the density of the Universe today, to the critical density,

$$\Omega(t) \equiv \frac{\rho(t)}{\rho_c(t)} = \frac{8\pi G}{3H^2(t)}\rho. \tag{1.10}$$

The density of matter in the Universe will dictate its fate. For a flat universe where $k = 0$ and $\Omega(t) = 1$ the Universe will continue to expand forever but with a slower rate over time. For $\Omega(t) > 1$ ($k = +1$) the density is sufficient to force

the Universe to collapse inwards and for $\Omega(t) < 1$ ($k = -1$) it will continue to perpetually expand. The effect of Ω on the geometry and fate of a matter dominated universe is summarised in Table 1.2.

Ω_t	k	**Geometry**	**Scale factor**	**Fate**
< 1	-1	Negative Curvature	a(t)$\propto t$	Open
1	0	Zero Curvature	a(t)$\propto t^{2/3}$	Flat
> 1	1	Positive Curvature	a(t)$\longrightarrow 0$	Closed

Table 1.2: *Showing the relationship of the curvature of the Universe and hence its fate to the total energy density parameter*

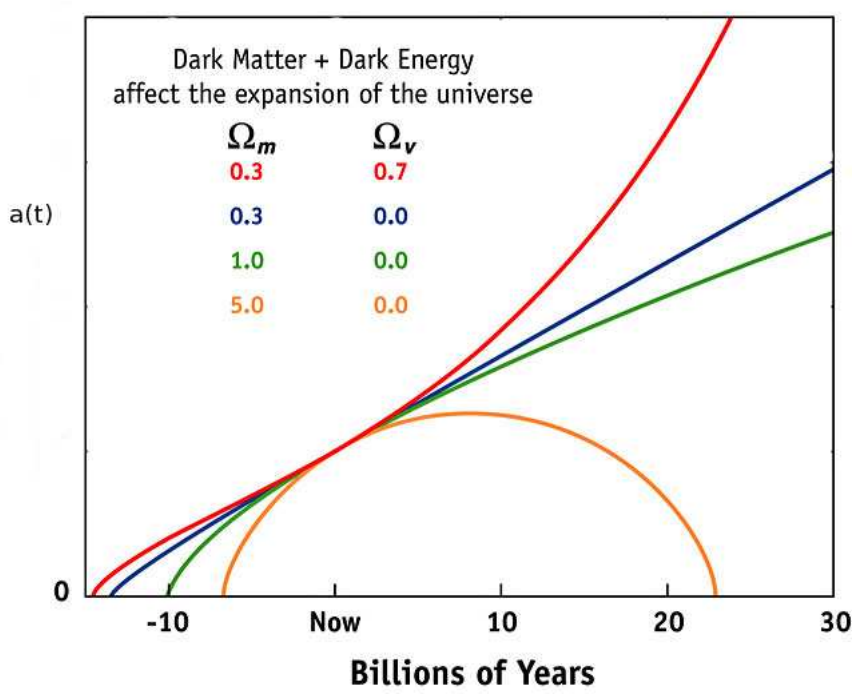

Figure 1.1: *The rate of expansion described by the scale factor a(t). The fate of the Universe is intimately linked to the matter density contained within it. Four scenarios are displayed, showing the fate of the Universe as function of the density of matter and dark energy. If $\Omega_m = 0.3$ and $\Omega_\Lambda = 0.7$ in accordance to current experimental data, the Universe should expand indefinitely with the rate of expansion increasing over time (red line). Figure adapted from [5].*

So far there has been little mention of a 'vacuum energy' contribution. Over

the past 15 years the significance of the 'vacuum energy' term (Λ) has become a topic of great debate. Current estimates suggest a contribution to the total energy density of the universe (Ω_{tot}) of $\sim 74\%$. The different contributions from matter, radiation (r) and also vacuum energy (Λ) can be also shown as a ratio of ρ_c,

$$\Omega_m = \frac{\rho_m(0)}{\rho_c}; \Omega_r = \frac{\rho_r(0)}{\rho_c}; \Omega_\Lambda = \frac{\rho_\Lambda(0)}{\rho_c} \tag{1.11}$$

where the total energy density of the Universe is the sum of all contributions, $\Omega_{tot} = \Omega_m + \Omega_r + \Omega_\Lambda$. The curvature constant k can also be redefined in terms of Ω_{tot},

$$k = \frac{H_0^2 a_0}{c^2} \left(\Omega_{tot} - 1\right), \tag{1.12}$$

again relating evolution of the Universe to the mass that resides within it. Even with the inclusion of a dark energy term, Ω and k still relate as in a matter dominated universe, as already shown in Table 1.2; however the extent of individual contributions from matter, radiation and dark energy is significantly more important. Figure 1.2 from [6] shows the cosmological constrains based on three different measurements from supernovae, galaxy clusters and WMAP. Convergence of these results indicate a dark energy content of ~ 0.75 and a matter content of ~ 0.25.

Quantitative information on the geometrical structure of the Universe can be derived by accurately measuring the different contributions to Ω_{tot}. The data indicates that today the Universe is flat and expanding; this requires $\Omega_{tot} \approx 1$. However for accurate measurements of the mass component Ω_m, knowledge of the non-baryonic matter content within the Universe, i.e. dark matter, is essential. It is currently thought that dark matter contributes $\sim 23\%$ of the total mass of the Universe.

Despite the dominance of dark matter and dark energy on the total energy density of the Universe, it is thought that at different stages of the evolution of the Universe these contributions varied. The first major epoch was radiation domination over matter and dark energy, this changed at $z \sim 3000$ when matter became dominant therefore enabling structure formation. With $\Omega_\Lambda > \Omega_m$ The current epoch is said to be dark energy dominated. The Λ cold dark matter (ΛCDM) model describes the Universe in a Λ dominated scenario.

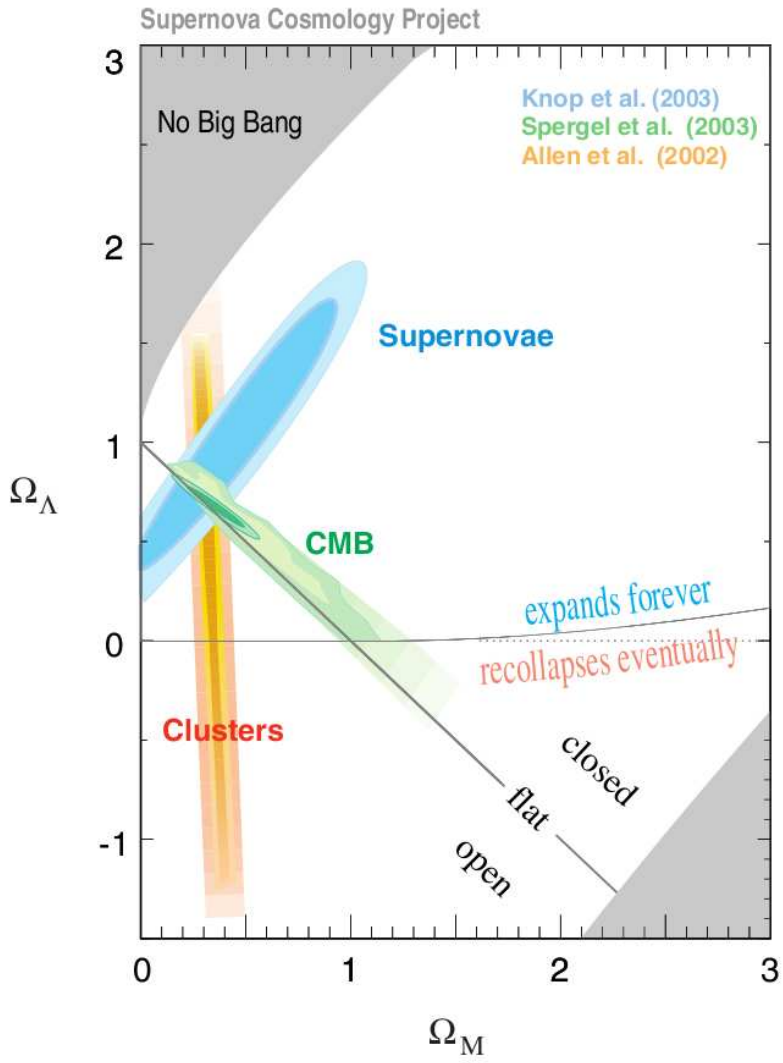

Figure 1.2: *Allowed regions for Ω_m and Ω_Λ values based on Type 1a supernova data, cosmic microwave background data and galaxy clusters. All data sets converge at around $\Omega_\Lambda \sim 0.75$ and $\Omega_m \sim 0.25$. The combined data sets also imply a flat universe where $\Omega_{tot} = 1$. [6]*

1.1.2 Evidence in Support of Big Bang Theory and Dark Matter

Without the big bang theory the possibility of a dark matter component is less obvious. In this section the author will explain the role the big-bang model and also the part dark matter plays in the evolution of the Universe.

1.1.2.1 ΛCDM

The ΛCDM cosmology model, or 'Benchmark model', builds on what has been discussed in the preceding section. Using information from the Cosmic Microwave Background (CMB, see section 1.1.2.2), supernova observations (see section 1.1.2.3), and details of large scale structure (1.2.3), a model with six basic parameters, Ω_b (baryon density), Ω_m (total matter density including the baryon density and a cold dark matter component, i.e. $\Omega_m = \Omega_b + \Omega_c$), H_0, τ, A_s (scalar fluctuation amplitude) and n_s (scalar spectral index) and five derived parameters ρ_0, Ω_Λ, z_{ion} (ionisation parameter), σ_B (galaxy fluctuation amplitude) and t_0 have been deduced. The ΛCDM model describes a flat universe where $k = 0$ and $\Omega = 1$, dominated by dark energy ($\sim 75\%$), supplemented with dark and baryonic matter (contributing $\sim 25\%$). Moreover, ΛCDM describes the various transitions of the Universe, from radiation dominated to matter dominated eras and the current Λ dominated phase. It also aims to explain observations of large-scale structure and primordial fluctuations in the early universe in an effort to model the complete evolution of the Universe from the big-bang.

1.1.2.2 The Cosmic Microwave Background (CMB)

The Cosmic Microwave Background (CMB) was discovered in 1964 by radio astronomers Arno Penzias and Robert Wilson [7] and could arguably be described as the best evidence for big bang theory. The CMB originated from an era in the Universe when the temperature had cooled sufficiently for recombination to occur. Approximately 10^{-6} s after the big bang, the Universe is thought to have been a dense plasma of electrons, photons and baryons where photons interacted with the plasma via Thomson scattering. As the Universe expanded, it also cooled, eventually enabling electrons to recombine with protons forming hydrogen ($T \sim 3000$ K). At this juncture ($\sim 380,000$ years) photons decoupled from the plasma, travelling unhindered through the expanding universe. This

radiation was then red-shifted to the microwave wavelength as the Universe continued to expand.

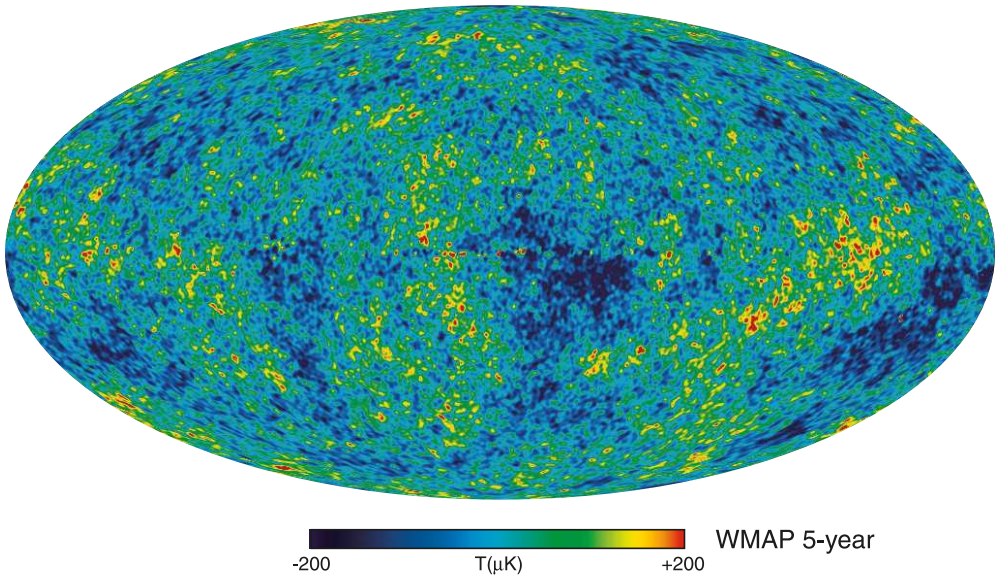

Figure 1.3: *The cosmic microwave temperature fluctuations from 5-year WMAP data as seen over the full sky [1]. The different colours indicate different temperature variations, where blue regions are cooler and red regions are warmer. The average temperature is 2.725 K. Here, the dipole asymmetry and the galactic contributions have been removed.*

The CMB has a thermal blackbody spectrum with an average temperature of 2.725 K. Experiments such as COBE ([8]) and more recently WMAP ([9]) have accurately mapped the CMB (see Figure 1.3), revealing temperature fluctuations and anisotropies (i.e. spots that can be seen on Figure 1.3). These fluctuations allow cosmologists to develop a picture of the early universe and provide information on early structure formation. There are two types of anisotropies observed in the CMB, primary and secondary. Primary anisotropies arise from the scattering of photons prior to decoupling from matter when the Universe resembled a hot ionised fluid-like plasma. Pre-recombination fluid behaviour provides information on how sound waves propagated during this time, hence revealing details on the velocity of the gas at the surface of last scatter. Other anisotropies can arise from photons undergoing gravitational interactions with matter, attributed to the development of gravity wells where matter (such as cold dark matter) began to 'clump' together. Consequently photons are red-shifted as they 'climb

out' of these gravity wells, a mechanism known as the early integrated Sachs-Wolfe effect. Secondary anisotropies can be associated with the interactions of photons with interstellar gas or gravitational wells on their journey to Earth. Secondary anisotropies can smear out the primary anisotropies.

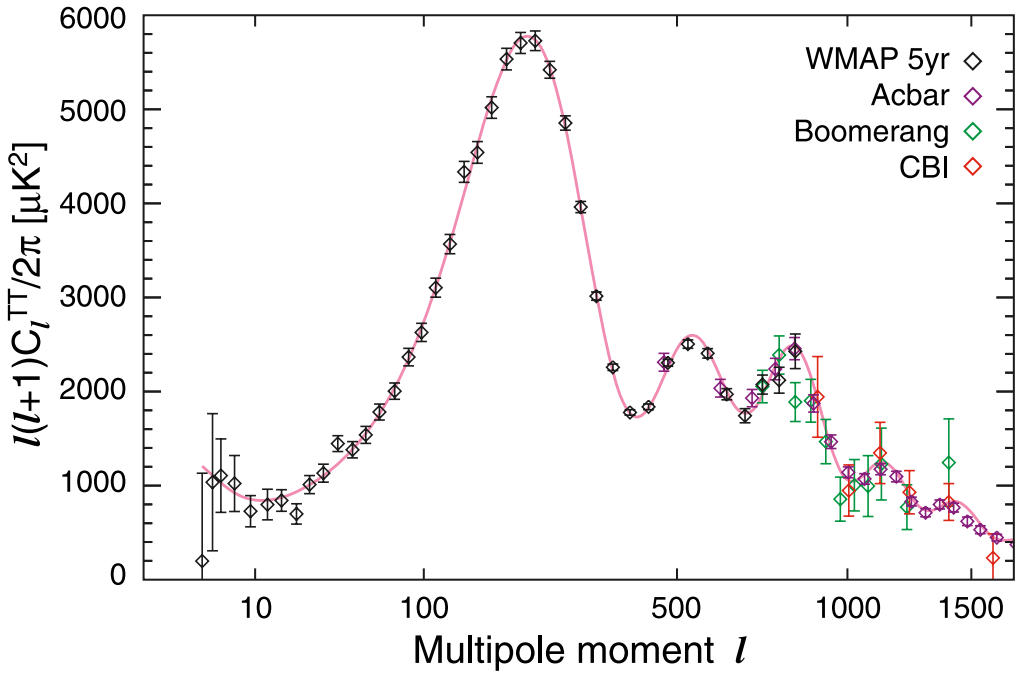

Figure 1.4: *WMAP 5-year power spectrum as a function of multipole moment (ℓ) with results from several other experiments. The red curve is the best-fit ΛCDM model which yields various cosmological parameters (see text).* [10]

Figure 1.4 shows temperature variations at different angular scales from the 5-year results from WMAP and data from several other experiments as comparison. The peak locations provide details of the energy-matter content of a pre-recombination fluid and post-recombination universe. The peak at $\ell \approx 200$ for example, gives details on the largest fluctuations due to the early integrated Sachs-Wolfe effect and therefore information on the density of dark matter in the early universe. Using details such as the heights and locations of the smaller peaks to the right of Figure 1.4, properties of the gas prior to the last scatter can be obtained. Also by determining the size of anisotropies and using H_0 to determine the distance to the fluctuation, it is possible to place constraints on the geometry of the Universe by identifying how the light propagated towards

Earth. Currently the ΛCDM model gives the best fit to the data yielding the parameters summarised in Table 1.3.

Cosmological Parameter	**Value**
Baryonic matter	$\Omega_b = 0.0456 \pm 0.0015$
Non-baryonic dark matter	$\Omega_c = 0.228 \pm 0.013$
Dark energy	$\Omega_\Lambda = 0.726 \pm 0.015$
Hubble parameter (today)	$H_0 = 70.5 \pm 1.3$ kms^{-1}
Total Density	$\Omega_{tot} = 1.0050^{+0.0060}_{-0.0061}$

Table 1.3: Current values for various cosmological parameters in the ΛCDM model for the Universe including data from supernovae and baryon acoustic oscillations (BAO). Cosmological parameters taken from 5-year WMAP data [1]

Measurements of the CMB have produced a plethora of evidence in support of the big-bang theory, and in particular the Λ dominated big bang model, relevant to this thesis. Gas during the period of recombination existed as a hot, ionised plasma, additional cold dark matter would have been imperative to allow gravitational wells to form and thus create the conditions of the early integrated Sachs-Wolfe effect.

1.1.2.3 Dark Energy

In sections 1.1.1, 1.1.2.1, 1.1.2.2 there has already been reference to a dark energy term which contributes $\sim 70\%$ of the total energy density of the Universe. Hubble's discovery of an expanding universe discredited the steady state model and thus the idea of a cosmological constant stalled. However, in recent years, the debate has reopened. Observations of type 1a supernovae have shown the Universe is accelerating faster than expected, especially at high red-shift. One theory is that there is a cosmological constant or 'dark energy' term that has negative pressure and positive energy density that is aiding this acceleration. Evidence for dark energy has also now been provided from gravitational lensing, galaxy redshift surveys, CMB observations of the late-time integrated Sachs-Wolf effect and in particular Type 1a supernovae.

Type 1a Supernovae

Type 1a Supernovae have provided the most conclusive evidence to date for dark

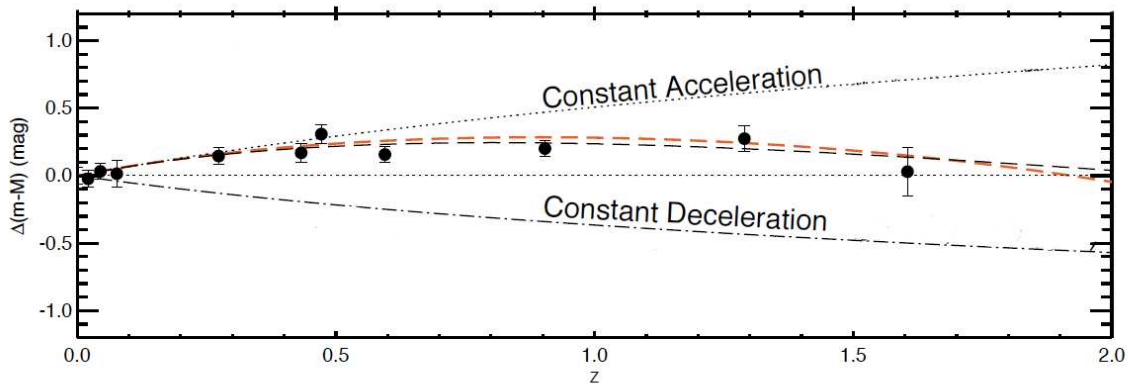

Figure 1.5: *Differential Hubble plot from Type 1a supernovae adapted from [11] showing the experimental points of averages over several supernovae. The two labelled dotted lines indicate the requirement for an accelerating or decelerating universe. The horizontal unlabelled dotted line represents an empty universe. The line of best fit to the data (red and black dashed lines) obtains parameters of* $\Omega_m = 0.27$ *and* $\Omega_\Lambda = 0.73$.

energy. This category of supernovae have highly luminous, well defined light curves and spectra. The predictable nature of these supernovae make them excellent candidates as standard candles. (For further details on the mechanisms producing supernovae, in particular Type 1a supernovae see [12; 13]). The distance to a Type 1a supernova is determined using its light-curve. The relationship between distance to the object and its red-shift reveals the recessional velocity of an object from an observer. For red-shifts$\leq$ 0.5 the distance to the object is related linearly to the brightness scale; for high red-shift supernovae the relationship between distance and luminosity is dependent on the matter and energy density of the Universe. Results published in 1998 by Reiss *et. al* [14], and independently in 1999 by Perlmutter *et. al* [15], have claimed to observe acceleration, based on such measurements. They suggest this acceleration may be attributed to dark energy.

Figure 1.5 shows the plotted averages for several experimental supernovae results. A fit to the data indicates that at $z > 0.5$ the Universe was originally decelerating, and provides information on present cosmological parame-

ters, deducing $\Omega_m = 0.27$ and $\Omega_\Lambda = 0.73$. Figure 1.6 shows the latest results using samples from the Supernova Legacy Survey and ESSENCE survey. Application of the best fit ΛCDM model constrains the cosmological constant to $\Omega_\Lambda = 0.713^{+0.027}_{-0.029}(stat)^{+0.036}_{-0.039}(sys)$ [16], which is in good agreement with results from WMAP. However, results from supernova experiments are heavily dependent on having an excellent understanding of the characteristics of Type Ia supernova. If the metalicity of high z supernova is different to low z counterparts there could be a reduction in the light output from the supernova misleading observations.

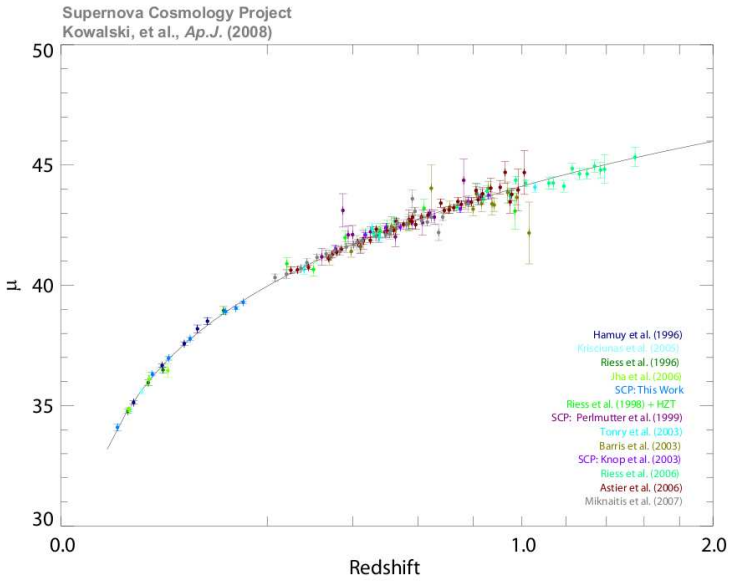

Figure 1.6: *Data complied from various type Ia supernova data as a function of redshift showing distance modulus μ as a function of redshift. Obtained from [16]*

What is dark energy?

The true nature of dark energy is still undefined. One possible solution is that dark energy is vacuum energy which permeates space isotropically. Quantum physics predicts vacuum fluctuations that enable the production of particle-antiparticle pairs that can spontaneously annihilate according to the uncertainty

principle. Calculations of the energy density of vacuum energy have revealed an unrealistic value of 10^{123} GeV m^{-3} [17] indicating that the Universe is only seconds old. This would require extreme fine tuning.

Quintessence is alternative model which manifests in the form of scalar fields and can vary in space and time. A quintessence field would track the radiation-matter density until equilibrium occurred, when dark energy would then start to dominate the Universe. Some believe the Casimir effect may reveal details of dark energy. A detailed analysis of dark energy is beyond the scope of this thesis but a good review can be found by P. J. E Peebles and B. Ratra [18].

1.1.3 Problems with Big Bang Theory

Despite the success of the big-bang theory, it is not without problems. The three most problematic issues relating to the big-bang theory are discussed along with their possible solution in the form of inflation theory. Although no deep understanding of inflation exists, its ability to resolve these issues is so compelling to make it now a central tenet of modern cosmology.

1.1.3.1 The Horizon Problem

The particle horizon describes the maximum distance that a particle can be observed through the exchange of photons travelling at speed c, within the age of the Universe. In such a scenario the observer and the particle can be considered causally connected; particles beyond the horizon are not. The speed of light, c, and the age of the Universe, t, are finite, thus in an expanding universe the horizon distance will be greater than ct. This is problematic, as the CMB appears to be extremely isotropic out to large angles [17], despite small anisotropies discovered to a level of 10^{-5}. This implies that at some point everything was causally connected. The time when matter and radiation decoupled ($z \sim 1000$) only subtends out to regions of the sky to 1°, implying that points beyond this are causally disconnected and if so, how can they have been causally connected at an earlier time?

1.1.3.2 The Monopole Moment

The second problem relates to a hypothesised particle that has an isolated north or south pole known as a monopole. Magnetic monopoles were originally pos-

tulated by Paul Dirac in the 1930s in an attempt to explain the quantisation of charge for stable particles and to enable symmetry between electric and magnetic fields in electromagnetism. In 1974 Sasha Polyakov [19] predicted the existence of monopoles in Grand Unification Theories (GUT). GUT predicts that at some point in the early universe, the strong and electroweak forces were unified as one force. As the Universe expanded and cooled it is believed that it underwent several phase transitions, including the breaking of the strong force with the weak and electromagnetic forces. GUT predicts that monopoles should be stable particles, created in abundance. However, they have yet to be observed, leaving scientists to reconsider their existence (for further reading see [20]).

1.1.3.3 Flatness

The third problem with the big-bang theory is the flatness issue. Equation 1.12 implies that the curvature of the Universe grows with time in contrast to the observation that our universe appears to be flat. Some of the initial conditions of the Universe appear to be precisely fine-tuned to have enabled the Universe to appear flat today. Safe limits of $0.01 \leq \Omega_{tot} \leq 10$ can be confidently applied, since otherwise the Universe would have lasted only seconds. Measurements from experiments such as WMAP [1] further constrain Ω_{tot} to be close to unity. Extrapolating back to the Planck time ($\sim 10^{-43}$), Ω_{tot} would have to have a value of $\Omega_{tot}(t_p) = 1 \pm 10^{-60}$ to provide consistency with data. Any earlier deviation from unity would have resulted in a rapidly exaggerated curved universe due to expansion. To enable a flat universe in the present epoch, a simple solution is found in assuming the Universe was flat and $\Omega_{tot} = 1$ in previous epochs. This however would require extreme fine-tuning and leads to the question of why cosmological parameters would yield unity as opposed to the infinity of values it could have?

1.1.3.4 The Inflationary Universe Model

A possible solution to the horizon, flatness and monopole problems of standard big bang theory was proposed in 1982 by Alan Guth [21] and Andrei Linde [22] called inflation theory. Inflation theory proposes that the early universe underwent a period of rapid expansion. This expansion is hypothesised to have started $\sim 10^{-35}$ s after the birth of space-time, and lasted $\sim 10^{-32}$ s. Conceptually, inflation theory can be understood by assuming that the cosmological constant, Λ,

was the most dominant parameter during the time of inflation from the Friedmann equations (in particular Equation 1.6). This assumption can be inferred for two reasons; firstly, the matter and radiation terms are significantly reduced during the rapid expansion, and secondly, the negative pressure induced by Λ is necessary for rapid expansion. Note that Λ is not necessarily the dark energy term observed in the Universe today. Mathematically a scalar field can be attributed to the inflation period by behaving with a negative pressure, analogous to an effective cosmological constant.

Necessarily inflation must have ceased. This is thought to be due to a cosmological phase transition controlled by a scalar field (or Λ). The phase transition corresponds to a temperature when GUT symmetry breaking occurred, releasing energy that caused the Universe to rapidly expand. Once the phase transition was complete Λ decayed away releasing energy in the form of matter and radiation as latent heat.

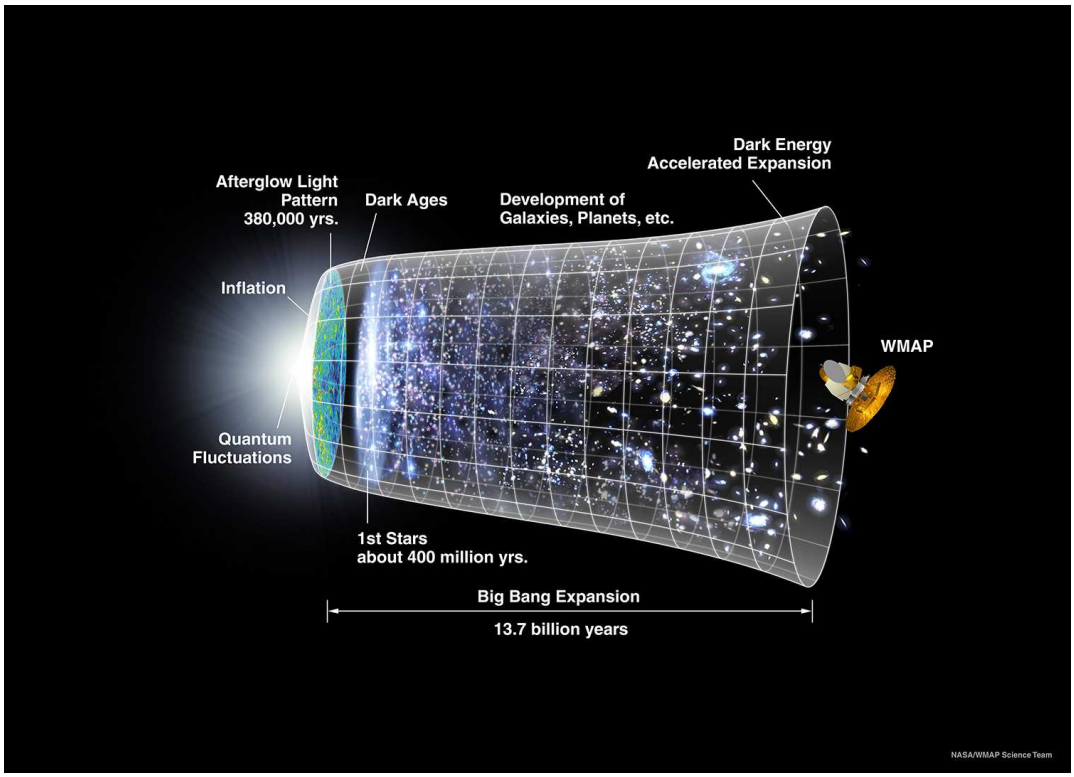

Figure 1.7: *The different epochs of the Universe from the big bang, rapid expansion (inflation) to the creation of galaxies and super structures built due to the seeds of the initial quantum fluctuations [5].*

Using inflation theory the flatness, horizon and monopole problems are resolved. The rapid, exponential expansion of the Universe resolves the flatness problem. $\Omega(t1)$ at the start of inflation will be of the order of unity as the curvature term is now reduced by a factor of $\pm 10^{52}$ [17]. Any deviation from unity after inflation will be negligible where $\Omega(t1) = 1 \pm 10^{-52}$. Also, due to rapid expansion, any indication of curvature would be rapidly flattened out. The horizon issue is also resolved. This comes about because the expansion of the Universe was faster than the speed of light. Therefore particles that started in causal contact prior to inflation can expand to distances larger than the horizon distance. Hence, causally disconnected particles would still have similar temperatures as thermal equilibrium was achieved prior to inflation. Lastly, the monopole issue is also resolved. Due to their large masses, monopoles could have only been created at high temperatures prior to inflation and therefore, as the Universe exponentially increased the monopole density exponentially decreased. The temperature after inflation would have been too low for further monopole creation.

To conclude, big-bang theory has been extremely successful (even with inflationary modifications) in explaining a range of recent astronomical observations (Figure 1.7 shows the different epochs that have occurred with the universe since the big-bang). The evolution and long term future of the Universe is found to depend on Ω_{tot} and therefore any undetected mass component must be fully understood. Dark matter is therefore an integral part of big bang theory and thus has required such an introduction. The remainder of this chapter will focus on evidence for the existence of dark matter and to its nature.

1.2 Astrophysical Evidence for the existence of Dark Matter

1.2.1 The dynamics of galaxies and galaxy clusters

1.2.1.1 Observations of galaxy clusters

The initial inspiration for the existence of dark matter originated from the scientist Fritz Zwicky. Zwicky published results in 1933 [23] having undertook observations of the velocity distribution of galaxies within the Coma cluster.

Such measurements can provide information on the mass content of the system. The viral theorem allows the mass content to be inferred from the expression:

$$< T >_{\tau} = -\frac{1}{2} \sum_{k=1}^{N} < m_k . |\mathbf{v}_k|^2 >_{\tau} \tag{1.13}$$

where T is the kinetic energy and $\mathbf{v}$ is the velocity of the mass m, τ denotes the time average values assuming stability within the system. Zwicky calculated a light-to-mass ratio (in solar units $M_{\odot}/L_{\odot}$) of the Coma cluster of ~ 400, showing that luminous matter only contributed to a small proportion of the total mass observed within the cluster. As to what provided the extra mass, that had yet to be determined, although a logical solution would be to assume that different measurements taken at different wavelengths would reveal it. However, from 1933 measurements of other galaxy clusters at different wavelengths (e.g. X-ray) had yet to observe enough mass to account for these clusters remaining intact, strongly suggesting the existence of a large dark component. Measuring the mass content of galaxy clusters has become very important for constraining values for Ω_m and Ω_{Λ} as they are the largest structures in the Universe currently under observation.

X-ray emission spectra

It has been observed, using X-ray observations, that at the centre of galaxy clusters lies superheated ($10^7 - 10^8$ K) X-ray emitting gas, also known as the inter-cluster medium (ICM). The temperature and density of the gas can be deduced from the surface brightness and spectrum of the X-ray emission [24]. Such high temperatures are thought to be achieved by the release of gravitational energy as material falls towards the galactic centre. The temperatures obtained are expected to be high enough for the heated material to achieve the escape velocity of the individual clusters. That the material remains bound suggests a large dark matter component providing additional 'gravitational attraction'. The heat created ensures hydrostatic equilibrium within the cluster but also the emission of X-rays via Bremsstrahlung and atomic de-excitation.

X-ray observations of galaxy clusters have enabled constrains to be placed on Ω_m (where $\Omega_m = \Omega_b + \Omega_c$) and Ω_{Λ} and at times question cosmological models [25]. The Chandra X-ray Observatory ([26], and references therein) and BeppoSAX (Satellite per Astronomia X) [27] are the leading telescopes in

X-ray observation. Recent values for Ω_m, have been calculated by including known values for a mean baryon density Ω_b. From BeppoSAX data (2002) $\Omega_m = 0.34^{+0.11}_{-0.05}$ and $\Omega_m = 0.33^{+0.07}_{-0.05}$ for a flat universe. More recent results (2009) are obtained from the Chandra data [26], where $\Omega_m = 0.35^{+0.03}_{-0.04}$ and $\Omega_\Lambda = 0.59^{+0.44}_{-0.56}$ (for $H_0 = 72 \pm 8$ kms^{-1} Mpc^{-1} and $\Omega_b h^2_{70} = 0.0462 \pm 0.0012$) and $\Omega_m = 0.32^{+0.04}_{-0.05}$ when a flat universe is considered. These results are compatible with WMAP results of ~ 0.28 (model dependent).

1.2.1.2 Rotational velocity of spiral galaxies

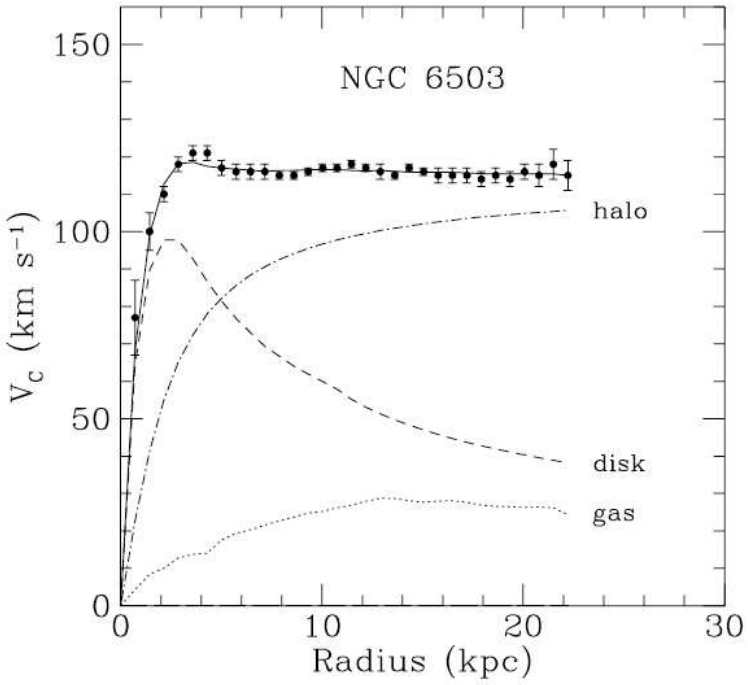

Figure 1.8: *An example of a rotation curve for the spiral galaxy NGC6503. The data points are the measured rotational velocities of objects from the galactic centre. The dotted and dashed lines are contributions from the disk and gas showing a difference between the observed velocities. The line labelled halo is the dark matter contribution required to explain this difference. Figure taken from [28]*

The methodology of observing the dynamics of objects to infer their total mass content has also been applied to the stars and material within individual

galaxies. Vera Rubin was the first to pioneer the technique by taking measurements of the velocity distributions of spiral galaxies by observing the Doppler shifted 21 cm emission lines from neutral hydrogen [29]. Using Kepler's law, the mass ($M(R)$) can be obtained from the velocity measurements ($v(R)$) by equating Newton's second law of motion to his law of gravitation,

$$v(R) = \sqrt{\frac{GM(R)}{R}}. \tag{1.14}$$

A galaxy rotation curve (see Figure 1.8) showing velocity of rotating matter as a function of radius from the centre of the galaxy, can be produced. Comparing observation to theory (i.e. Equation 1.14) highlights an interesting discrepancy at higher radii where the velocity is observed to reach a maximum and then remain constant. A $r^{-1/2}$ velocity dependence would be expected if one were to assume that all matter present was in the form of luminous matter. To account for these observations it is expected that a large gravitational mass is present throughout the galaxy and extends beyond the luminous matter forming an extended isothermal 'dark matter' halo.

1.2.1.3 Rotational Velocity of Elliptical Galaxies

Calculating the mass of elliptical galaxies requires a different approach to that previously outlined. Elliptical galaxies fail to have an obvious rotation within a single plane. The distance-velocity dependence of the mass content of an elliptical galaxy can be revealed through the Doppler shifted spectral lines of the random motion of individual stars as a function of distance from the galactic centre. Studies observing neutral Hydrogen have also been employed due to the observation of large, faint disks in some elliptical galaxies. Measurements of NGC 612 [31] indicate a large rotation disk of H up to velocities of 850 kms^{-1}, which require a dark matter component to explain these velocities. Observations of NGC 2974 using the Very Large Array [30] also detected a H_I disc in the galaxy and discovered that the mass-to-light ratio of NGC 2974 increased from 4.3 $M_\odot/L_\odot$ to 8.5 $M_\odot/L_\odot$ at larger radii. This analysis also used data from SAURON for the ionised gas content of NGC 2974 which allowed measurements of a rotation curve ranging from 100 pc to 10 kpc at the edges of the H_I. Different mass models and halo models were used to fit to the data (see Figure 1.9) with the best results obtained when accounting for a dark matter component.

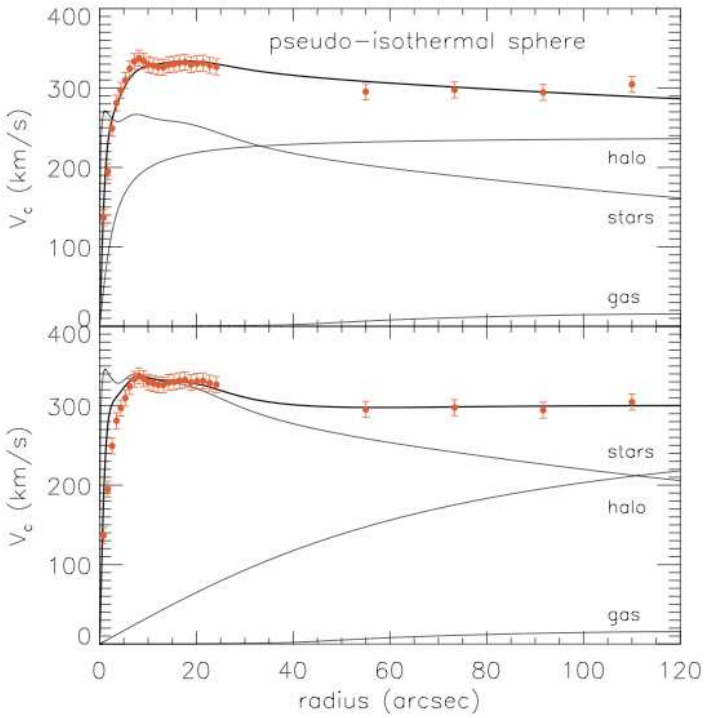

Figure 1.9: *Measurements shown in red are from an area of ionised gas ($r \leq 2.5$ kpc) and neutral hydrogen ($r \geq 5$kpc) in NGC2974. Rotation curves from separate components of the galaxy such as the halo, stars and gas are shown in grey. The bold line is a convolved rotation curve using the combined potential of the halo, stars and gas. A pseudo-isothermal sphere model is used for the the fit (bold line), which has the following density profile $\rho(r) = \rho_0/(1 + (r/r_c)^2)$, where ρ_0 is the central density and r_c is the core radius. Other profiles such as the NFW and MOND were also tested giving a less reasonable fit. [30]*

There is still controversy over the presence of dark matter halos in elliptical galaxies with some measurements indicating a null result [32; 33]. However, the evidence from galaxy and galaxy cluster dynamics has been irrefutable in showing the need to either accept and therefore detect this dark matter component or at least develop new theories of gravitation to explain these findings.

1.2.2 Gravitational Lensing

Gravitational lensing is a very different technique to those already discussed. It has provided an extra dimension to the growing support for dark matter. Gravitational lensing was predicted by Einstein as part of his theory of general relativity. The theory postulates that the path of a photon is deflected due to gravitating matter curving space-time, thus altering the time it takes for light to travel to an observer. The effect of this is to either magnify or distort the image of a background source. Gravitational lensing can be used as a tool for inferring the mass of astronomical objects and is also utilised to locate non-luminous matter.

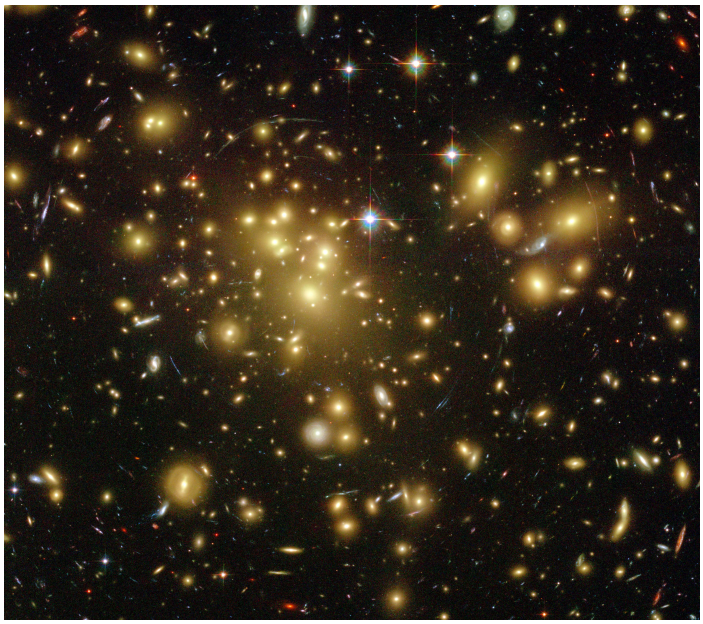

Figure 1.10: *Images taken by the Hubble Space Telescope have shown in Abell 1689 the effect of gravitational lensing. The multiple thin arcs are distorted images of more distant galaxies which have been magnified due to the effect of gravitational lensing from dark matter.[34]*

Gravitational lensing can be sub-divided into three separate categories, strong, weak and microlensing. Strong lensing occurs when the light source is close to a massive lens, resulting in observation of multiple images of the source. If the source, lens and observer are aligned, Einstein rings can form (see Figure 1.10), otherwise multiple arc shaped images will be observed. Using this information the mass of the distorting object can be calculated by measuring the distortion geometry. Considering the difference between the amount of visible matter to that calculated from the distortion geometry provides one estimate of dark matter components.

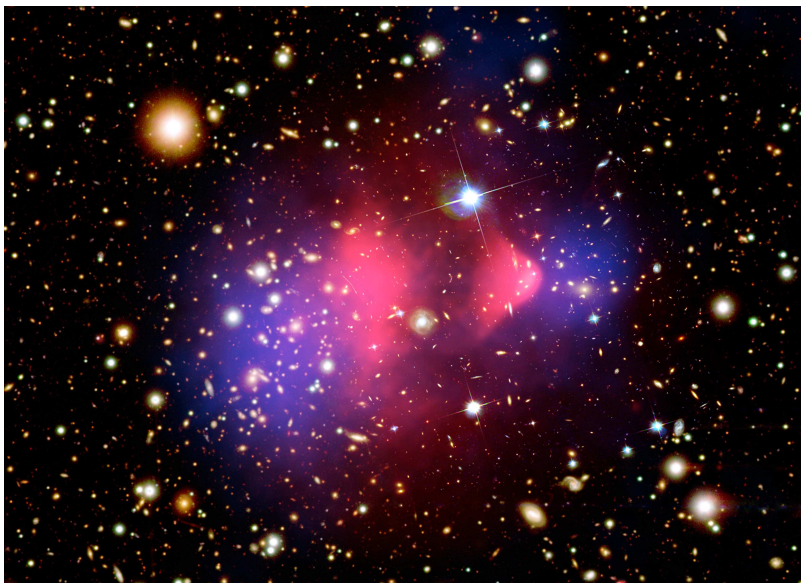

Figure 1.11: *Galaxy cluster 1E 0657-56 or the 'Bullet cluster' was formed after the collision of two Galaxy clusters. This Figure shows a composite image of the Bullet cluster, revealing a distribution of dark matter inferred using gravitational lensing (blue). The pink areas is the X-ray emitting baryonic material observed using The CHANDRA X-ray observatory. All luminous matter appears white. [35]*

Weak lensing is the effect interacting gravitating matter has on the image an observer sees of a large number of objects (see [36] for a review). The shape and orientation is measured and averaged, and then used to reconstruct the mass distribution in the vicinity of the objects. The third type of lensing is Microlensing. This occurs when the flux of light varies in time due to a lens cutting across the observer-source path. Microlensing has opened new possibilities for

astronomers to observe small dark objects which would otherwise be impossible to see. It is not wavelength dependent and objects of the size of planets can be detected (such as Exoplanets). Microlensing has also been used to observe Massive Compact Halo Objects (MACHOS) which were a serious candidate to account for dark matter.

There are a number of dedicated experiments exploiting gravitational lensing to infer the existence and mass of non-luminous objects. One such experiment was the Cosmic All Sky Survey (CLASS) which took observations during the 1990's using the Very Large Array (VLA) and discovered 22 lensed sources. They estimated the total matter density to be $\Omega_m = 0.31^{+0.27}_{-0.14}$ [37]. Other experiments such as the Optical Gravitational Lensing Experiment (OGLE), MACHO and superMACHO (the Massive Astrophysical Compact Halo Object) aimed to determine whether non-luminous baryonic matter could solve the missing mass problem (see Section 1.3.1.1).

Results from gravitational lensing have arguably contributed to the best observational evidence for the existence of dark matter. The Bullet cluster (1E 0657-56) is a fine example. It was discovered in 1995 and is composed from two colliding galaxy clusters. D. Clowe *et. al* [38] revealed a possible dark matter component using gravitational lensing techniques. These data are complemented by additional techniques to observe the bullet cluster. Data from CHANDRA and the HUBBLE Space telescope were used to observe the X-ray and visible regimes and hence determine where the baryonic matter resided. As a result of the two galaxies colliding the stellar component and X-ray plasma are very well separated. Hot gases from both clusters interact electromagnetically, altering velocities, leaving the observed stellar populations (in the visible regime) virtually unaffected during the collision. Using gravitational lensing the majority of the mass was found to be situated in two separate regions near the visible galaxies. The spatial offset of the centre of mass of the system requires either an alteration to current gravitational models (see Section 1.3.3.1) or highlights the necessity for a dominating dark matter component. In Figure 1.12 the weak lensing component is highlighted in blue. A second, similar study of two colliding galaxies was announced in 2008 called MACS J0025.4-1222 [39] pertaining to the same conclusions as with the Bullet cluster.

1.2.3 Large Scale Structure Formation

As mentioned in section 1.1.2.2, CMB observational experiments have indicated a possible dark matter component in the angular power spectrum. It is this dark matter component that may have seeded structure formation within the Universe leading to the formation of stars, galaxies and superclusters. The cosmological principle states that the Universe is homogeneous and isotropic; however, a better description would be 'granulated'. The universe is distributed with a large collection of galaxies, galaxy clusters and galaxy walls, all of which are separated by vast empty voids. The rise of these superstructures can be attributed to the inflation period of the Universe. Anisotropies observed today in CMB may have arisen from quantum fluctuations. These quantum fluctuations would be elongated through rapid expansion of the Universe with newer fluctuations continuously arising, experiencing the same effect, thus creating irregularities with varying length scales throughout the young universe. Quantum fluctuations would have also led to the production of particle-antiparticle pairs (e^+ and e^-), which would rapidly separate due to inflation, preventing total annihilation. Topological defects due to the GUT phase transition could have also contributed to observed anisotropies resulting in a collection of strings that would have attracted matter.

Gravity then plays the major role in the subsequent formation of structure. Structure formation occurs in a hierarchical format, whereby smaller structures are initially created leading to the formation of larger structures through the gravitational attraction of increased mass. Eventually the largest regions condense to form stars and galaxies.

The baryon component of the Universe is not large enough to account for the structures observed to date [1]. During radiation domination, prior to photon decoupling, baryon collapse below the Jeans mass would have been prevented by radiation pressure. Therefore a dark matter component would have been crucial in providing sufficient mass to ensure matter inhomogeneities existed, that grew out of gravitational instability. Hot Dark Matter (HDM) would have been (by definition) relativistic at this time, and therefore unable to provide the stabilising force required. However, cold dark matter (CDM) would have been non-relativistic and also unaffected by radiation pressure, only affected by gravity. A CDM component would have been vital for future structure development

and has already shown its effect in galaxy dynamics (as discussed in section 1.2.1).

Experiments such as Sloan Digital Sky Survey (SDSS) and Two Degree Field (2dF) Galaxy Redshift Survey have verified measurements made by WMAP of acoustic oscillations of large-scale structure. In particular, baryon acoustic oscillation (BAO) peak identification has been vital in showing that baryons and dark matter were essential for seeding the initial structures of growth in the early universe after photon decoupling and inflation, and proving predictions for a ΛCDM universe.

J. D. Einstein et. al [40] in 2005 used a sample of 46,748 luminous red galaxies observed with the Sloan Digital Sky Survey to study large scale structure. An acoustic peak was discovered at $100h^{-1}$ Mpc which correlated to the recombination epoch acoustic oscillations for the low-redshift clustering of matter. This demonstrated the linear growth of structure between $10 < z < 1000$. The amplitude of this oscillation feature does not meet the requirements necessary for a large baryon fraction of Ω_m, thus there is a requirement for dark matter. SDSS set a value of $\Omega_m = 0.24 \pm 0.002$, including WMAP data [41].

N-body simulations, such as The Millennium Simulation, simulate the the evolution of the matter distribution within the Universe. These have also shown the need for a dark matter component to aid structure formation within the Universe. To conclude, without a CDM component the Universe would not have developed into the 'granulated' species observed today, on this timescale, with the minimum scale size of objects.

1.2.3.1 Big Bang Nucleosynthesis

Observations of galaxy clusters and gravitational lensing measurements have shown that luminous matter contributes to a small proportion of the total matter required to obtain $\Omega_{tot} = 1$. However, some of the mass contribution could be in the form of non-luminous baryonic matter that has yet to be detected. One method to determine the amount of baryonic material within the Universe is to understand the processes surrounding its creation. The current abundance of light elements such as ^{4}He, ^{2}H, ^{3}He, and ^{7}Li can be compared to those created at the beginning of nucleosynthesis. According to big-bang theory the baryons would have formed after the GUT phase transition, as constituent quarks and gluons became subjected to confinement, leaving protons and neutrons (as well

as electrons, positrons and neutrinos) in equilibrium due to the hot dense nature of the Universe at that time. Equilibrium was maintained through the influence of the weak force governing the following interactions;

$$\begin{aligned} p + e^+ &\longleftrightarrow n + \nu_e \\ n + e^+ &\longleftrightarrow p + \overline{\nu}_e \end{aligned} \tag{1.15}$$

The equilibrium between protons and neutrons are governed by Maxwell Boltzmann factors since the temperatures would have been non-relativistic ($kT = 20$ MeV). The ratio between neutrons and protons is then given by,

$$\frac{N_n}{N_p} = exp\left[-\frac{(M_n - M_p)c^2}{kT}\right] \tag{1.16}$$

where M_n and M_p are the neutron and proton masses. Equation 1.16 shows a strong dependence between the nucleon ratio and the temperature, hence, as the temperature cools, the ratio will increasingly become unbalanced. At ~ 1 s the production of e^+ and e^- pairs become so reduced, that continuation of the reactions presented in 1.15 is prevented. This resulted in the n to p ratio freezing out at $\sim 13\%$ and $\sim 87\%$ receptively (conversion of $n \rightarrow p$ is easier as $m_n > m_p$). The neutron abundance then decreased further by decay to protons, although neutrons did not disappear completely. The temperature fell below the deuterium binding energy ($Q = 2.22$ MeV) creating the deuterium bottleneck where a large number of photons caused photodisintegration. At a temperature of $\sim kT = 0.05 - 0.06$ MeV nucleosynthesis could begin.

Primordial abundances can be observed in a variety of astronomical objects, and in particular old objects such as quasars. Values for the baryon density have been quoted at $\Omega_B h^2 = 0.021 \pm 0.001$ [42] which is constrained by deuterium. Deuterium is ideal for such measurements as it has a low binding energy and is therefore not easily produced in stellar nucleosynthesis. Measurements from WMAP using the CMB power spectrum state a value of $\Omega_B h^2 = 0.02267^{+0.00058}_{-0.00059}$ [1]. Recent measurements of the individual nuclei abundances can be found in the following recent reviews [42; 43]. The primordial nucleosynthesis measurements are similar to WMAP indicating that baryons could not contribute substantially to $\Omega_{tot} = 1$. Nucleosynthesis also provides further evidence for the standard big bang model.

1.2.4 Indirect Dark Matter Detection

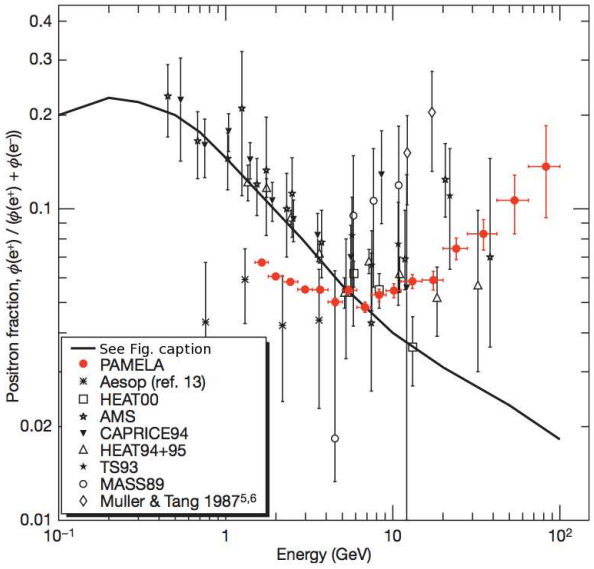

Figure 1.12: *The measured PAMELA positron fraction compared with other experimental data [44]. The solid line is the expected rate of positron production due to secondary sources (ISM etc.) only. It is clear that there is a positron excess eluding to primary production processors.*

Recent cosmic-ray data has alluded to the possibility that dark matter may have been indirectly detected. Cosmic-rays are energetic particles that have originated from space. They range from relatively low kinetic energies up to extremely high energies, with the most energetic being in excess of a few $\times 10^{20}$ eV, significantly greater than anything that is reproduced today in collider experiments. There are a number of experiments studying cosmic-rays in an attempt to understand their origin and the mechanisms that can create these high energy particles. Cosmic-rays can be subdivided as those (such as positrons) produced by the likes of stellar nucleosynthesis or dark matter annihilation ('primary source') and those originating from cosmic-ray nuclei interacting with the interstellar medium (ISM) ('secondary source').

Experiments such as PAMELA (a **P**ayload for **A**ntimatter **M**atter **E**xploration and **L**ight-nuclei **A**strophysics) measure the ratio between the primary and secondary nuclei. This can provide information on the encountered amount of matter (e.g. in the ISM). PAMELA recently released data alluding to the possibility

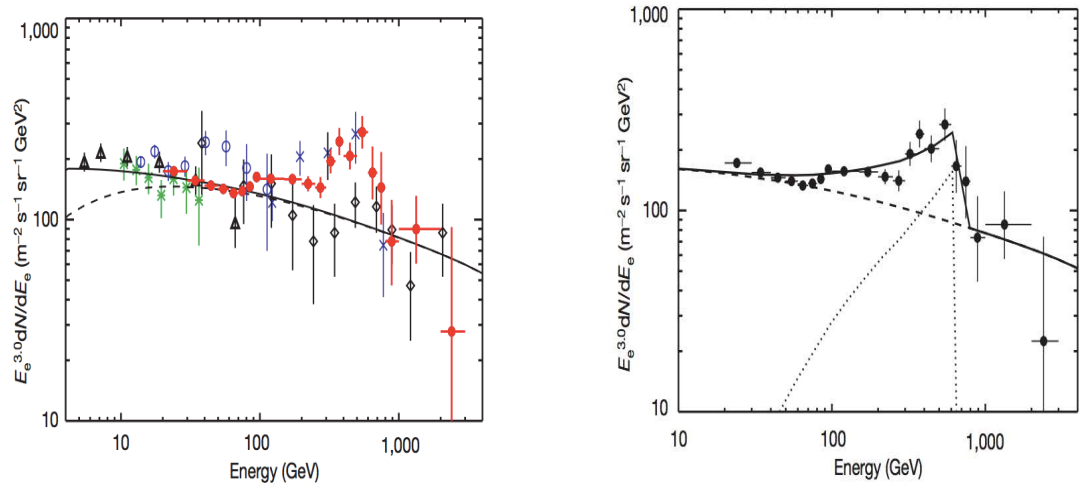

Figure 1.13: *The left figure shows the electron differential energy spectrum as measured by ATIC (red filled circles), the Alpha Magnetic Spectrometer AMS (green stars), HEAT (open black triangles), BETS (open blue circles), PPB-BETS (blue crosses) and emulsion chambers (black open diamonds) and the GALPROP code calculated spectrum (solid line). Both ATIC and the PPB-BETS data observe an enhancement above 100 GeV. The right hand figure shows that assuming an annihilation signature of Kaluza-Klein dark matter the data can be reproduced. The solid line is a combination of the GALPROP (dashed) general electron spectrum and the propagated electrons from the Kaluza-Klein particle (dotted) [45].*

that the products expected from dark matter annihilation had been observed. PAMELA [44] has measured the ratio of the positron and electron flux for an energy range of 300-600 GeV and discovered that the positron fraction increases between 1.5-100 GeV. The origin of the positron excess is unclear. It is possible that nearby sources such as pulsars and micro-quasars could accelerate cosmic particles, which can eventually cause an electromagnetic cascade contributing to the electron and positron components. However WIMP annihilation through leptonic channels (producing $e^{\pm}$) could also account for the observed excess.

The ATIC (**A**dvanced **T**hin **I**onization **C**hamber) instrument has also observed an excess of galactic cosmic-ray electrons at energies of $\sim 300-800$ GeV [45] (see Figure 1.13). This is again indicative of a nearby source (such as the Geminga pulsar) producing energetic electrons. However the calculated flux for the Geminga pulsar is about a factor of 60 too low to explain the observations from ATIC. An alternative explanation again involves the annihilation of dark matter particles such as WIMPs or Kaluza-Klein (KK) particles (which have developed from extra dimensional models). Both WIMPs and KK particles can annihilate through leptonic channels or produce gamma-rays. The left hand plot in Figure 1.13 shows the model which includes the electron spectrum and the expected electron rate from KK annihilation. This reproduces the ATIC data very well.

Despite the observations made by PAMELA and ATIC, the H.E.S.S (**H**igh **E**nergy **S**tereoscopic **S**ystem) data cannot confirm the excess observed by ATIC. H.E.S.S data [46] do not show an excess or sharp cutoff between 300-800 GeV but do confirm the falling electron spectrum above 1 TeV (see Figure 1.14). The H.E.S.S data are also consistent with those measured by the FERMI gamma-ray telescope up to 1 TeV [47]. Thus, it is currently unclear as to whether there is an excess in the cosmic-ray electron energy spectrum and if there is, what the origin of such an excess is. Dark matter annihilation is one possibility that could account for some of these observations.

To conclude this section, we state that the evidence for a dark matter component is very strong. Observations using a variety of techniques have arrived at similar conclusions, that there must be some type of non-luminous, dark matter component that would lead to the observations in rotation curves, gravitational lensing and could aid large scale structure formation. Baryonic matter does not

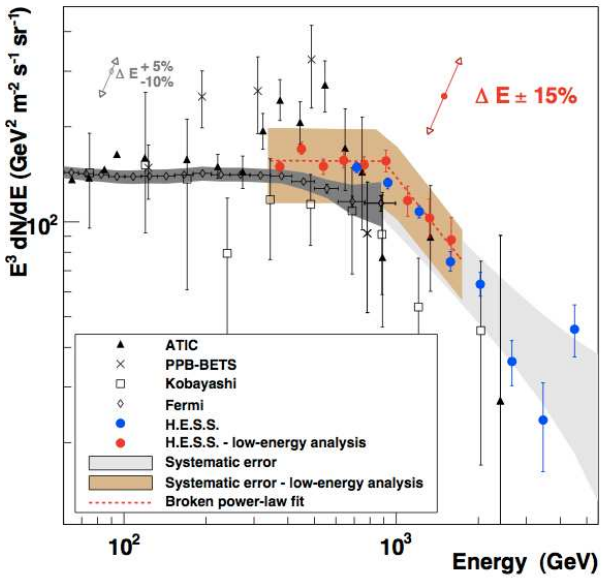

Figure 1.14: *The energy spectrum $E^3\,dN/dE$ of cosmic-ray electrons as measured by various experiments (indicated in the Figure) [46]. The H.E.S.S data does not confirm the excess observed by ATIC and PPB-BETS. The FERMI data is more consistent with H.E.S.S data.*

seem to provide the solution since studies of MACHOS and big bang nucleosynthesis cannot contribute the required amount. The next section will describe possible dark matter candidates.

1.3 Dark Matter Candidates

The beginning of this chapter has focused on presenting the reader the case for dark matter. The evidence is vast and is reinforced by the variety of complementary observational techniques employed. Current measurements suggest that only $\sim 4\%$ of the critical density is in the form of baryonic matter, with $\sim 73\%$ in the form of dark energy. The missing mass ($\sim 23\%$) is thought to be in the form of dark matter. But, what is dark matter? There are a number of candidate particles and theories to explain its nature with the most compelling discussed in more detail within this section. To date the WIMP (Weakly Interacting Massive Particle) has become the favoured candidate, a particle developed separately in SUSY models which happened to fit precisely the requirements for

a possible dark matter candidate.

1.3.1 Known Candidates and their limitations

There have been a number of suggestions in the form of particles already understood by the standard model of particle physics. These will be discussed in further detail.

1.3.1.1 Baryonic Dark Matter

It was initially considered that non-luminous baryonic dark matter could contribute to the missing dark matter component. However, dedicated research in this area, particularly in relation to BBN, has yet to provide a significant enough component to rectify the missing mass problem. One solution explored further was that matter could exist in the form of MAssive Astrophysical Compact Objects (MACHOS). Microlensing has been implemented to search for MACHOS which are thought to exist in the form of Brown dwarfs, white dwarfs, M dwarfs, red dwarfs, neutron stars and also black holes. However the most recent results published by the MACHO collaboration have placed constrains on the contribution of MACHOs to the galactic dark matter halo of $\sim 18\%$ and determined that MACHOs could not contribute $\sim 100\%$ of the mass [48]. The EROS project also found similar results quoting only $\sim 25\%$ of MACHOs could contribute to the galactic halo [49]. Recent results from the EROS-2 survey from the Large Magellanic cloud stated an $\sim 8\%$ contribution can only be considered [50].

Constraints made by big bang nucleosynthesis have also set primordial elemental abundances on baryonic matter (see Section 1.2.3.1). Therefore the requirement for non-baryonic dark matter is still extremely favourable. WMAP measurements (see Table 1.3) and cluster measurements (Section 1.2.1) have also placed constrains on the total baryonic matter which are still significantly lower than is required to account for the missing mass.

1.3.1.2 Neutrinos

It is expected that a dark matter candidate particle will interact with matter gravitationally and possibly weakly. From current candidates that adhere to these rules neutrinos might appear to fit the description. Neutrinos are fundamental spin 1/2 fermions, that interact via the weak force, are electrically

neutral and exist in three flavours, the τ, μ and electron. Neutrinos are also abundant (comparable to the photon density of 411 cm^{-3} [17]) and recently, through the observation of neutrino oscillations [51], they have been found to have mass. There are a number of experiments trying to place constraints on the mass of the neutrino.

The Mainz Neutrino Mass Experiment can set neutrino mass limits by studying the shape of the β spectrum of tritium around its endpoint and has set an upper limit of $m(\nu_e) \leq 2.3$ eV/c^2 at 95% confidence limit [52]. The Heidelberg-Moscow experiment has also placed constrains on the upper limit of the effective Majorana-neutrino mass of 0.35 eV at 90% confidence limit [53]. This experiment also has the potential to observe neutrinoless double beta decay and claims to have found evidence for its observation [54]. If the neutrino is a majorana particle then this interaction is conceivable and would produce two spectral lines from the release of two electrons providing the means to obtain excellent mass measurements. Other methods include studies performed on reactor and solar neutrino data. The neutrino mass scale is currently unknown. Therefore neutrino mass values can also be quoted in terms of the differences in the mass squared of mass eigenstates. The most recent results from the KamLAND experiment are $\Delta m^2_{21} = 7.59^{+0.21}_{-0.21} \times 10^{-5}$ eV^2 [55] using a combination of reactor antineutrino and solar neutrino data. Measurements from the MINOS collaboration have determined $\Delta m^2_{32} = 2.74^{+0.44}_{-0.28} \times 10^{-3}$ eV^2 [56].

WMAP has also set neutrino mass limits. The 5-year WMAP data on the neutrino content of the Universe have been set at $\Omega_\mu h^2 < 0.0076$ implying a neutrino mass < 0.23 eV [5]. According to [17] a total neutrino mass of all three flavours needs to be comparable to the critical density with a value of ~ 47 eV hence the neutrino has too little mass to be a sufficient contributor to dark matter.

Another problematic issue for neutrinos is that they would have been relativistic when matter began to form structures. Therefore it would be considered hot dark matter and thus, unable to partake in structure formation (as observed in the Millennium simulation). Neutrinos also de-coupled from matter before the CMB was created and were frozen out when temperatures fell below 3 MeV.

1.3.2 Theorised Candidates

As no currently known particle has the complete set of properties required to be dark matter, some theorised candidates have been suggested.

1.3.2.1 Axions

Axions were originally postulated in response to CP-violation having not been observed in quantum chromodynamics (QCD) and are 'strongly' expected to exist. In electro-weak theory the CP-symmetry can be easily broken and has been observed in neutral kaon decay whereas this is not the observed case in strong interactions. If CP violation were to occur in the strong sector, the electric dipole moment of the neutron would be significantly larger than current experimental bounds of $\sim 10^{12}$ [17]. To explain the absence of strong CP violation, a new global symmetry was proposed by Pecci and Quinn in 1977 which can be spontaneously broken. This leads to the production of the axion, which, although having a small predicted mass of 10^{-6}-10^{-3} eV/c^2, would be sufficiently abundant to contribute significantly to the dark matter density. Due to the weakness of axion coupling it is expected that they would have formed during the inflation period of the Universe as a boson condensate of dark matter. Experimental searches for the axion are still ongoing and are a promising candidate as they are also predicted to be cold and non-baryonic, although they may not be massive enough to contribute fully to the total dark matter content.

1.3.2.2 MSSM and Weakly Interacting Massive Particles (WIMPs)

The standard model (SM) has experienced relative success in explaining the nature of the fundamental particles in the Universe and also the forces and exchange particles that govern interactions (see Table 1.4), but problems have arisen requiring an extension to the SM. The SM's initial failing is its exclusion of the gravitational force (only accounting for the weak, electromagnetic and strong forces.) It does not allow for the experimentally proved neutrino mass, nor has it provided a solution for the gauge hierarchy problem. Finally, it does not provide an opportunity for the grand unification of the fundamental forces. Supersymmetry (SUSY) claims to solve these problems and also reveals a promising dark matter candidate. The problems of the SM and the SUSY solution will be discussed below and the SUSY dark matter candidate. (Detailed

discussion is beyond the scope of this thesis but further information on the SM and SUSY extensions can be found in for example [57], [58]).

The hierarchy problem

One of the main issues of the SM is the question of why the electroweak interaction energy scale is significantly smaller than the Planck energy scale of $\sim 10^{19}$ GeV. This question is also referred to as the hierarchy problem. Table 1.5 gives all particle interactions with the corresponding mediating exchange particles. The type of exchange particle is dependent on the type of interaction, for example, an electromagnetic interaction is governed by photons. The four fundamental forces (electromagnetic, weak, strong and gravitation) all interact at vastly different ranges (see Table 1.5) which relates to the mass that accompanies the exchange particles. The electromagnetic force is governed by the exchange of massless photons and therefore has a larger range than the weak force which is governed by massive Z and $W^{\pm}$ bosons ($80-100$ GeV). The range of any interaction is thus dependent on the mass of the governing exchange particle. If all bosons had zero mass then symmetry would be preserved; however, this is not the case. The question arises as to how particles acquire mass and why are some bosons massless when others are not?

Family	Particle	Charge	Interaction
Leptons	Electron neutrino	} 0	} Weak
	muon neutrino		
	Tau neutrino		
	Electron	} -1	} weak & electromagnetic
	muon		
	Tau		
Quarks	Up	+2/3	} electromagnetic, weak & strong
	Down	−1/3	
	charm	+2/3	
	Strange	−1/3	
	Top	+2/3	
	Bottom	−1/3	

Table 1.4: *Standard model particles and their interactions*

Exchange Particle	Mass (GeV/c^2)	charge	Interaction	Range (m)
8 gluons (g)	0	0	Strong	10^{-15}
Photon (γ)	0	0	Electromagnetic	∞
Vector Bosons (W$^{\pm}$, Z^0)	80-100	± 1	Weak	10^{-18}
Graviton (g,G)	0	0	gravity	6×10^{-39}

Table 1.5: *A list of force carriers and their ranges within the standard model*

The Higgs Boson

To explain how particles acquire mass a scalar field with non-zero vacuum expectation ($< \Phi > \neq 0$) and four scalar components was postulated in SM theory. This is now more affectionately known as the Higgs field and has an associated exchange particle, the elusive Higgs boson. If the Higgs field were to permeate through all of space, then as particles travel through this field they may interact with it. From this interaction particles appear to gain mass.The Higgs field has four real components, three of which couple to the W$^{\pm}$ and Z bosons with the last coupling to the Higgs boson (self interaction). Without the Higgs field the masses of the W$^{\pm}$ and Z bosons would be significantly smaller, where the quarks and leptons would be massless. One of the issues with the current mass calculations of the Higgs boson is that it should be comparable to the Planck mass of 10^{16} TeV/c^2, but is in fact 16 orders of magnitude lighter. To remedy this issue an extension to the SM was proposed.

Supersymmetry

From quantum mechanics and the uncertainty principle, short-lived virtual particles can be spontaneously produced and promptly annihilate with momentum approaching infinity, contributing logarithmically to the energy of the system. Major radiative corrections arise from the influence of loop diagrams involving these virtual particles and Higgs boson exchanges. However these interactions are based on the electroweak mass scale. If there are more massive, currently undetected particles above this scale, at M$\simeq$M$_{GUT}$, then they would contribute as virtual particles in the electroweak scale and radiative corrections of the standard model parameters of the order M$^2_{GUT}$ are necessary. Corrections of the order 1 part in 10^{14} [57] would be required to prevent the quadratic divergence of the Higgs mass. To prevent the requirement for serious fine-tuning, Supersymmetry (SUSY) is proposed which introduces fermion and boson superpartners.

SUSY is as yet unproven but serves as an elegant solution to the problems of the standard model. SUSY predicts that for every boson or fermion there is a superpartner relating matter and force particles. Therefore a fermion would have a bosonic superpartner (the fermion name but prefixed with an 's') and a boson would have a fermionic superpartner (the boson name but with 'ino' appended to the end). Since fermions and boson loops have opposite signs, their virtual superpartners should cancel with the SM particles providing the one-loop correction to the Higgs mass of the form,

$$\Delta m_H^2 \sim \left(\frac{\alpha}{\pi}\right)(m_F^2 - m_B^2) \tag{1.17}$$

where m_F and m_B is the fermion and boson mass respectively, and m_H is the Higgs boson mass.

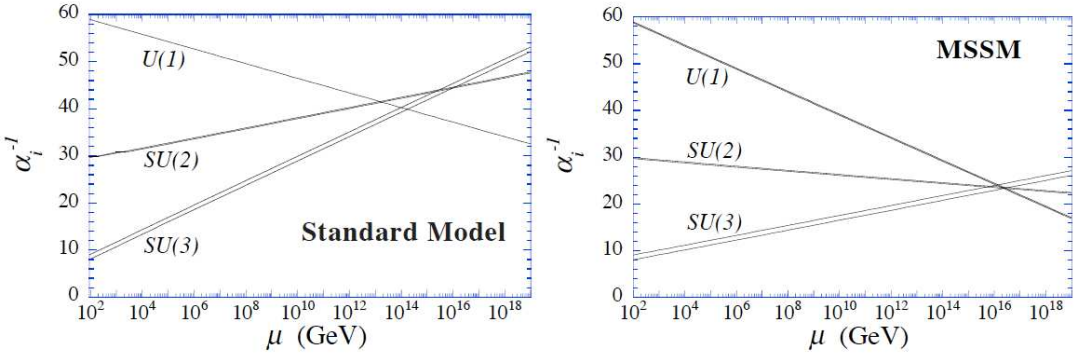

Figure 1.15: *Extrapolation of the gauge running couplets back to a point of possible grand unification. The SM (left) show poor convergence of gauge couplings, whereas the MSSM (right) shows excellent convergence at* 10^{16} *GeV [59].*

Grand Unification Theory

SUSY also enables the observed strengths of the electromagnetic, weak, strong and gravitational interactions to be modified, enabling a grand unification to occur at energies of 10^{16} GeV, when the strengths of these interactions become comparable at short distances. Due to the convergence of the electroweak force it is expected that the strong force may also converge at higher energies (i.e U(1)×SU(2)×SU(3)) to form a unified GUT model. Based on the SM, observing the evolution of the gauge couplets to higher energies displays poor convergence

(see Figure 1.15); however with the introduction of SUSY the modified gauge running couplets converge at $\sim 10^{16}$ GeV.

The shifting of the GUT scale also resolves issues with the lifetime of proton decay. The predicted lifetime for proton decay is $10^{(30\pm0.5)}$ years [17]; however experimental lower limits set the half-life for proton decay to be at least 10^{33} years. With SUSY extensions this issue is resolved where the proton decay lifetime is now estimated to be $10^{34} - 10^{38}$ years [17].

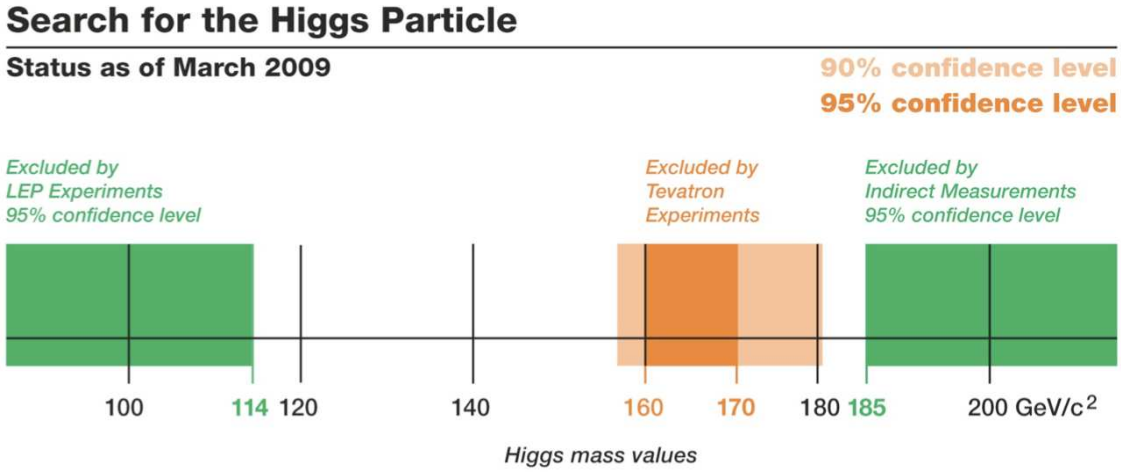

Figure 1.16: *Current experimental constrains on the Higgs mass from indirect searches, the Tevatron and LEP experiment at CERN indicate a mass within the range* $\sim 114 - 160$ *GeV/c*^{2}*. The Large Hadron Collider will probe this region from 2010 with the aim of detecting the Higgs Boson [60].*

Despite the successes of SUSY there are still problems with the theory. If SUSY were an exact symmetry then SM particles and their superpartners would have the same exact mass. Experimentally this is not observed indicating that there must be some form of symmetry breaking. Including symmetry breaking terms, SUSY particles are expected to have masses in the TeV scale and should therefore be detected when the Large Hadron Collider (LHC) starts taking data in 2010. 90%-95% confidence limits for the Higgs mass are shown in Figure 1.16 [60], revealing a mass range between $\sim 114 - 160$ GeV/c^2.

MSSM and a Dark Matter Candidate

The Minimal Supersymmetric standard model (MSSM) is the supersymmetric extension of the standard model with minimal particle content. The MSSM

introduces soft symmetry breaking operators in an attempt to explain the theoretically larger s-particle masses. A consequence of this is the appearance of over 120 free parameters. To reduce the number of free parameters assumptions on the mass of gauginos and sferminos are assumed (i.e. they are equal at GUT scales). MSSM also introduces the notion of R-Parity. The SM already possessed the ability to conserve both lepton and baryon terms; however with the introduction of the SUSY Lagrangian violation of baryon and lepton number could now occur. R-parity is introduced to prevent this, by essentially constructing a barrier between SM and SUSY particles. R-parity introduces a new multiplicative quantum number for SUSY particles and appears in the form,

$$R = (-1)^{3b+l+2S} \tag{1.18}$$

which protects the proton from decaying via intermediate SUSY loops. In Equation 1.18 S is spin, b is baryon number and l is lepton number. This ensures that the SUSY particles are produced in pairs with R=±1, enabling a quark antiquark pair to annihilate a squark-antisquark pair.

SM particle	**Superpartner**	**Spin**	**R-Parity**
Quark (q)	squark ($\tilde{q}$)	0	-1
Lepton (l)	slepton ($\tilde{l}$)	0	-1
W (W)	Wino ($\tilde{W}$)	1/2	-1
B (B)	Bino ($\tilde{B}$)	1/2	-1
Gluon (g)	Gluino ($\tilde{g}$)	1/2	-1
Higgs Boson (H_u, H_d)	Higgsinos ($\tilde{H}_u$, $\tilde{H}_d$)	1/2	-1

Table 1.6: *Corresponding superpartners for the standard model particles. Details of spin and R-parity of each superpartner is also shown*

With the inclusion and conservation of R-parity, SUSY particles decay into lighter SUSY particles in pairs. When a cascade of decays has occurred the chain stops at the Lightest Supersymmetric Particle (LSP). The LSP becomes frozen out of the decay process as it is energetically unfavourable for further decays to occur leaving a stable SUSY particle. With R-parity conservation the LSP will also be unable to decay into SM particles. It is this LSP that may hold the key to the missing dark matter mass problem.

There are a number of SUSY dark matter candidates that are suitable to explain cosmological observations outlined in this chapter. Particles such as

gravitinos and sneutrinos (see reference [61] and references therein) are postulated as possible candidates however, the most compelling is the neutralino (χ). The main requirements for a dark matter candidate is that it is massive, stable and weakly interacting. The neutralino ticks all of these boxes. The neutralino is a majorana particle and exists from a superposition of two gauginos, $\tilde{B}$ and $\tilde{W}_3$ and two Higgsinos, $\tilde{H}_1^0$ and $\tilde{H}_2^0$. There are four neutralinos each with different mass eigenstates, the lightest mass eigenstate is the LSP. In the early Universe it is expected that these particles existed in equilibrium by undergoing the following reversible reaction;

$$\chi + \bar{\chi} \rightleftharpoons P + \bar{P} \text{ (or } \gamma + \gamma) \tag{1.19}$$

where $\bar{\chi}$ is the neutralino antiparticle and $P+\bar{P}$ is a particle-antiparticle pair. As the Universe expanded and the temperature decreased the neutralino will have become frozen out from interactions. The temperature for freeze-out to occur would be on the weak scale $T_f \simeq m_\chi/20$ meaning that the neutralino would then be non-relativistic and thus provide the seeds for structure development within the Universe. The cosmological relic abundance can then be expressed as [62];

$$\Omega_\chi h^2 = \frac{m_\chi n_\chi}{\rho_c} \simeq \frac{10^{-27} c m^3 s^{-1}}{< \sigma_A v >} \tag{1.20}$$

The neutralino is expected to be detected in the energy range of 10-1000 GeV/c^2 (accelerators contrain this to be $\sim$ 46 GeV/c^2). The beauty of MSSM and the neutralino is the fact that the prediction of the neutralino was made separately to the dark matter problem and yet independently MSSM provides a perfect particle candidate for detection. The neutralino should also be able to 'feel' the weak force and so could scatter off baryonic nuclei, one avenue currently explored in direct detection experiments.

1.3.3 Alternatives to Dark Matter

1.3.3.1 MOND

There have also been non-particle related alternatives proposed to solve the missing mass problem. One controversial theory was originally proposed by Mordehai Milgrom in 1983, [63]. The theory, known as MOND (MOdified Newtonian Dynamics), attempts to modify gravity to fit with observations of rotation

curves as discussed in section 1.2.1. Milgrom proposed that small accelerations experienced by orbiting bodies deviated from that predicted by Newtonian dynamics. MOND predicts that in the limit of small accelerations (such as those experienced by stars and galaxies where the gravitational force is acting on large distances) the force experienced is vastly reduced compared to that calculated in Newtonian dynamics.

Newton's second law of motion states that an object with mass m, must undergo an acceleration $\vec{a}$ when a force $\vec{F}$ is applied,

$$\vec{F} = m\vec{a}. \tag{1.21}$$

Milgrom modified Equation 1.21 to include a new constant of acceleration,

$$\vec{F} = m\mu\left(\frac{a}{a_0}\right)\vec{a} \tag{1.22}$$

For accelerations vastly greater than a_0, $\mu = 1$ and thus $\mu\left(\frac{a}{a_0}\right) = 1$ restoring Equation 1.21 to its typical form. Newtons laws have been well tested in the laboratory and on Solar system scales for large accelerations, but for smaller accelerations where the gravitational force is extremely weak, verification is required.

There are a number of issues with MOND in particular MOND has been created in response to observed rotation curves and thus was developed to fit the data without any explanation of why Newton's laws should change for small accelerations. Measurements from WMAP (not dependent on rotation curves etc.) shows a CDM component is necessary to obtain $\Omega_{tot} = 1$ and gravitational lensing has also shown possible dark matter regions in the Universe, such as the Bullet cluster, where a dark component was resolved. From the bullet cluster findings, new theories involving both MOND with a dark matter component (in the form of massive neutrinos) [64] have come to light since MOND was unable to fully explain the observations.

MOND is not the only theory of gravitation there are other examples such as, Non-symmetric Gravitational Theory which modifies Einstein's theory of general relativity and extensions to MOND such as Tensor-vector-scalar theory (TeVs) (see [65] for a review). There is still a vast catalogue of evidence supporting the necessity of a dark matter component although alternatives should be investigated until a positive dark matter result is observed.

1.4 Summary

A vast array of evidence indicates we live in an expanding, flat, ΛCDM dominated universe. The evidence for a missing mass component is compelling and necessary to explain findings from galaxy and galaxy cluster observations, gravitational lensing, WMAP and big bang nucleosynthesis. Without a cold dark matter component it is apparent that structure formation would not have occurred to the level observed today. The search for this dark matter has become one of the greatest goals of modern physics. Some known particle candidates have been suggested, such as neutrinos or baryonic matter; however these do not seem to be able to meet the requirements of a suitable candidate. Therefore scientists have to reach beyond the standard model to SUSY to find a suitable candidate in the form of the Lightest supersymmetric particle. The neutralino, also known as the WIMP (Weakly Interacting Massive Particle) has now become the prime target for most dark matter searches, such as that by ZEPLIN-III. The next chapter will discuss how to detect a WIMP and the dark matter searches currently undertaken in the world.

Chapter 2

The Methodology of WIMP Dark Matter Detection

2.1 Introduction

A convincing case for dark matter, especially in the form of weakly interacting massive particles (WIMPs) has already been presented in Chapter 1. This chapter will focus on the techniques for direct WIMP dark matter detection. Detecting WIMPs is by no means simple it is; however expected that WIMPs should interact with ordinary matter and may also undergo annihilation or decay, producing detectable products. Over the last two decades, this has sparked an intense period in detector development and construction pertaining to WIMP searches, either directly or indirectly (via their annihilation products or missing mass such as in collider experiments like the LHC). This chapter will focus on direct dark matter searches, where the detection method of WIMP-induced nuclear elastic recoils is exploited. The WIMP-nucleon interaction is described taking account of the types of available interaction channels based on target material. Also discussed are limiting factors that can effect the sensitivity dark matter detectors and the methods employed to improve on these. Section 2.3 provides an overview of some of the current dark matter detectors, in particular xenon based detectors with brief explanations of the extensive array of technologies implemented.

2.2 WIMP-Nucleon Interactions

One of the principal aims for most dark matter detectors is to detect, or set sensitivity limits on, WIMP-induced nuclear elastic recoils. WIMP-induced nuclear elastic recoils occur when a WIMP weakly interacts with a target nucleus, generating a small energy deposition that may be observed in the form of photons (scintillation), charge (ionisation) or heat (phonons). Many experiments exploit at least one of these techniques; others, use a combination of methods to improve event discrimination. All dark matter experiments, regardless of the method of observation, are subject to similar problems and issues. These issues relate to understanding the differential energy spectrum of these nuclear recoils, which is expected to be featureless and smoothly decreasing with energy, taking the form:

$$\frac{dR}{dE_R} = \frac{R_0}{E_0 r} e^{-(E_R/E_0 r)} \tag{2.1}$$

where R is the event rate per unit mass of the target, R_0 is the total event rate, E_R is the recoil energy and E_0 is the most probable incident kinetic energy of a WIMP of mass M_χ and r is the kinematic factor given by

$$r = \frac{4 M_\chi M_t}{(M_\chi + M_t)^2} \tag{2.2}$$

for a target nucleus of mass M_t.

The expected energy deposition from a typical nuclear-recoil is in the range of 1-100 keV assuming a Galactic velocity of $\sim 10^{-3}c$, and a WIMP mass of 10-1000 GeV/c^2. The primary experimental objective is to reduce or reject background rates so as to observe any WIMP-induced signal. This, in effect, refers to the left-hand side of 2.1; the right-hand side however, requires detailed corrections to account for the practicalities of observing a WIMP-nucleon interaction. Such corrections are:

1. The position of the detector is not stationary relative to the galactic rest frame. As such, the motion of the Earth relative to the Galactic rest frame must be taken into account.

2. The quenching factor. The detection efficiency for nuclear recoils will be different to that which is observed for electron recoils, where the difference

is described by the quenching factor. This is defined as the ratio of ionisation produced by a recoil nucleus to the amount of ionisation produced by an electron of the same energy.

3. The target medium may consist of more than one species hence, for each contribution to the target separate calculations are performed to determine WIMP-nucleon cross-section limits.

4. The detector will naturally be subject to experimental constraints, such as energy resolution and threshold effects.

5. The physics of the WIMP-nucleon interaction is unknown it could couple to either the spin or the mass of a nucleus. These two cases are referred to as spin-dependent and spin-independent interactions. The magnitude of the interaction cross-section differs in either scenario.

6. A form factor correction is required to account for the effect of the finite size of the nucleus; in general this is dependent on the nuclear radius and the recoil energy.

Considering the above corrections, Equation 2.1 can be re-written as

$$\frac{dR}{dE_R}|_{observed} = R_0 S(E) F^2(E) I \tag{2.3}$$

where F is the form factor correction described in point 6, I is the interaction function, involving spin-dependent or spin-independent factors and S is the corrected spectral function. R remains defined as the unmodified rate for a stationary Earth.

2.2.1 Wimp-nucleon Cross-sections

In WIMP or neutralino search experiments the aim is to determine the probability of a WIMP-nucleon recoil. The likelihood of such an interaction is described by the total WIMP-nucleon cross section, σ_A. This can be estimated by considering different parts of the interaction, that is, sequentially addressing the fundamental forces at play during a WIMP-nucleon interaction. A more thorough treatment of this methodology is provided in [62].

Firstly, neutralino interactions with quarks and gluons are considered. This is described using an effective Lagrangian, utilising one-loop amplitudes (as often depicted in Feynman diagrams) to calculate various coefficients.

$$L_{eff} = f_q(\chi\overline{\chi})(\overline{q}q) + d_q(\overline{\chi}\gamma^\mu\gamma^5\chi)(\overline{q}\gamma_\mu\gamma^5 q) + ... \tag{2.4}$$

where d_q is a coupling f_q is the quark coupling shown in [62]. Equation 2.4 shows a simplified version of the effective Lagrangian of the system where the first term relates to scalar interactions (spin independent) and the second term relates to axial vector interactions (spin dependent). Other terms (noted with the +...) are not considered here. In the non-relativistic limit certain terms, such as the vector and pseudoscalar terms are negligible, therefore, only the axial vector and scalar components contribute. These contributions also add incoherently and so can be approached separately.

Despite the lack of any experimental observation of a neutralino, Feynman diagrams can be used to predict the type of neutralino-quark couplings, including any internal quark loops that can increase the scalar interaction cross-section. The next step is to evaluate these quark-gluon interactions using the matrix elements of the operators in a nucleon state. Thirdly, the spin and scalar components of the nucleons are added coherently to give the matrix elements for the WIMP-nucleus cross sections as a function of momentum transfer.

For a WIMP-nucleus elastic scatter, the cross section (σ_A) depends predominately on the the WIMP-quark interaction and the momentum transfer (q) during the interaction. In this case the differential cross section can be expressed as

$$\frac{d\sigma}{dq^2} = G_F^2 F^2(q)\frac{C_A}{u^2} = \frac{\sigma_A}{4\mu_A^2 u^2}F^2(q) \tag{2.5}$$

where σ_A can be defined in the limit where $q \to 0$;

$$\sigma_A = 4G_F^2\mu_A^2 C_A \tag{2.6}$$

and u is the WIMP speed relative to the target nuclei and $F(q)$ is the q dependent form factor. G_F is the Fermi weak-coupling constant, which describes the strength of a weak interaction. $\mu_A = \frac{m_t m_\chi}{m_t + m_\chi}$ is the reduced mass of the WIMP-nucleus system, and C_A describes the enhancement factor. The enhancement factor depends on the nature of the interaction, i.e. spin-dependent or spin-independent, and also the WIMP composition.

2.2.2 Spin-Dependent and Spin-Independent Interactions

Different calculations of the enhancement factor are necessary depending on the interaction involved. Generally, for heavier nucleons ($A \geq 30$), spin-independent interactions dominate; however in some SUSY scenarios it is also possible for axial vector or spin-dependent interactions to dominate. Detectors such as ZEPLIN-III, which uses xenon as a detector target material, can exploit this interaction channel as half of the natural abundance of Xe is ^{129}Xe and ^{131}Xe, which consist of odd-nucleon protons.

2.2.2.1 Spin-Independent Interactions

In spin-independent interactions the entire nucleus is involved in the scattering. This results in a coherent summation of the A scattering amplitudes (where A is the number of nucleons) at sufficiently low momentum transfer ($qr_n \ll 1$). Therefore the interaction cross section is expected to be proportional to A^2. In the spin-independent case the scalar neutralino-nucleon interaction arises from several sources. There are contributions from the following;

- Squark and Higgs exchanges.
- One-loop amplitudes for interactions of neutralinos with gluons.
- Other higher order terms, generally of less importance.

Interactions between neutralinos and hadrons are mediated by the the exchange of squarks and the Higgs boson. There are also contributing loops from gluonic interactions that also need to be considered (Feymann diagrams for a number of gluonic interactions are shown in [62]). It has been shown [67], through derivation and evolution of the effective Lagrangian, that neutralinos can couple to gluons via heavy quark loops and squark exchange (see Figure 2.1). In the limit of heavy squarks, neutrino-gluon coupling through Higgs-boson exchange can occur [67]. The Higgs boson (and therefore, also the Higgsino) couples proportionally to the mass of the particle involved in the interaction, such as quarks. [68] then showed that the heavy quark contributions can cancel out leaving a light quark term, and more importantly, a gluon term. The gluon term is therefore responsible for the mass of the nucleon leaving the possibility of gluon-neutralino coupling. Therefore the neutralino coupling is proportional

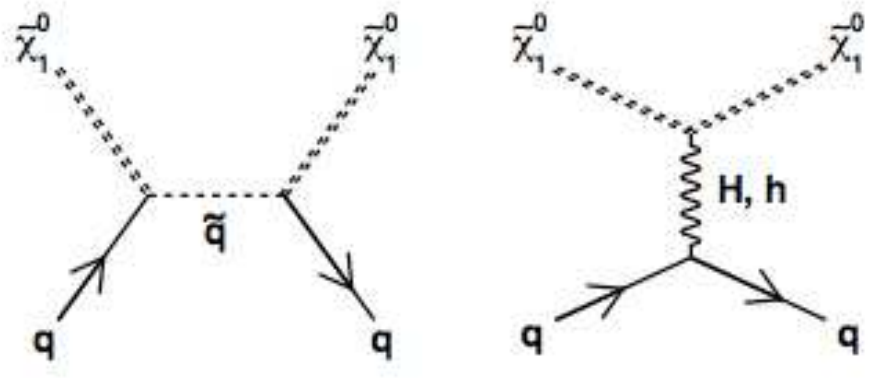

Figure 2.1: *Feynman diagrams showing the contributions of the spin-independent elastic scattering amplitudes. Shown is the neutralino-quark interaction. Figure taken from [66].*

to the mass of the nucleon not to the quark mass. By summing over all the nucleons within the nucleus and by calculating the matrix elements of the quark and gluon operators, $< n, p|m_q\bar{q}q|n, p >= m_{n/p}f_{Tq}$ (where f_{Tq} are the nucleon parameters), it is possible to obtain the spin-independent cross section [62; 67],

$$\sigma_{SI} = \frac{4G_F^2\mu_A^2 C_{SI}}{\pi} \tag{2.7}$$

where

$$C_{SI} = \frac{1}{G_F^2}(Zf_p + (A - Z)f_n)^2. \tag{2.8}$$

Here f_p and f_n are the effective WIMP-proton and WIMP-neutron couplings. Z is the number of protons, and $(A - Z)$ is the number of neutrons. If, as predicted, neutralinos are Majorana particles, then, $f_p \approx f_n$ and $C_SI \propto A^2$, thus to reiterate, a heavier target nuclei would increase the probability for a WIMP-nucleon interaction. The average momentum transfer to a target nuclei of mass m_t is,

$$q = \sqrt{2m_t E_R} = \mu v_0 \tag{2.9}$$

and the characteristic interaction length λ is given by $\lambda = h/q$. Typically values of m_t range between $10 - 1000\ GeVc^{-2}$, and a relative velocity of the two particles, $v_0 \simeq 10^{-3}c$, is assumed. The interaction length, λ, is typically $10^{-14} - 10^{-15}$ m, i.e the nuclear radius. Therefore the interaction will occur

with all the nucleons in the nucleus. The nucleus can only recoil coherently if $qr << 1$, where r is the nuclear radius, otherwise there is a suppression factor or form factor. The total event rate R_0 of the WIMP-nucleon cross-section can thus be derived for the dominant spin-independent interaction [69],

$$R_0(SI) \simeq 1.2r\left(\frac{N}{2}\right)^2 kg^{-1}d^{-1}. \tag{2.10}$$

R_0 can be normalised for different targets by dividing by N and then multiplying by A^2, to compare the rate to a reference nuclei.

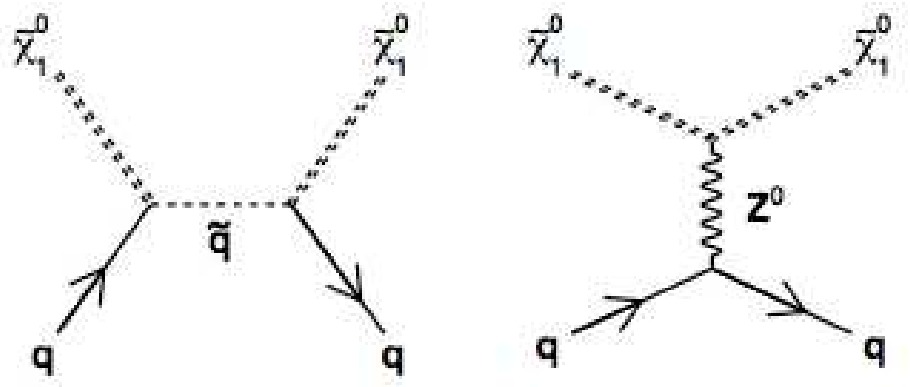

Figure 2.2: *Feynman diagrams showing the contributions of the spin-dependent elastic scattering amplitudes. Contributions to the spin-dependent interaction can be principally attributed to Z_0 exchange and squark exchange. Figure taken from [66].*

2.2.2.2 Spin-Dependent Interactions

Spin-dependent interactions differ from scalar interactions as they do not involve the entire nucleus. Instead, because the scattering amplitudes change sign and spin direction, when coherent scattering occurs only unpaired nucleons contribute to the scattering amplitudes with zero contributions from the paired nucleons. Scattering is therefore proportional to the total nuclear spin J. Spin-dependent interactions will generally occur where the nucleon has an odd number of neutrons and/or protons (all ground state even-even nuclei are spinless).

Contributions to the spin-dependent interaction can be principally attributed to Z_0 exchange and squark exchange for neutralino-quark scattering. As previously described in Section 2.1, it is possible to calculate matrix elements to determine the neutralino-nucleon cross-section.

$$< p(n)|\mathcal{M}_{SD}|p(n) >= 4\mathbf{S}_\chi \mathbf{S_q} \sum_{\mathbf{q}\in\mathbf{p(n)}} \mathcal{A}_\mathbf{q} \mathbf{\Delta q}^{\mathbf{p(n)}} \tag{2.11}$$

where $\mathbf{A_q}$ encompasses all the SUSY dependent terms over the sum of all quark contributions within the nucleon. $\mathbf{\Delta q}$ is the fraction of the nucleon spin carried by quark q. $\mathbf{S}_\chi$ and $\mathbf{S_q}$ are the neutralino and nucleon spin operators. To obtain the spin-dependent cross section the resultant matrix element is squared and summed over the initial spin states. The averaged final spin states are then calculated to give σ_{SD}, where:

$$\sigma_{SD} = 4G_F^2 \mu_A^2 C_{SD} \tag{2.12}$$

where C_{SD} refers to the quark spin content of the nucleus. This is given by

$$C_{SD} = \frac{8}{\pi}\Lambda^2 J(J+1) \tag{2.13}$$

and

$$\Lambda = \frac{1}{J}[a_n < S_n > + a_p < S_P >]. \tag{2.14}$$

Λ encompasses the total angular momentum of the nucleus. a_p and a_n give information of the WIMP couplings to protons and/or neutrons where the expectation value for the spin content of neutrons is given by $< S_n >=< N|S_n|N >$ and for protons, $< S_p >=< N|S_p|N >$.

The absolute cross section for a nucleon, scattering with a neutralino in the spin-dependent scenario, can be estimated as follows. Assuming a relic density of $0.1 < \Omega_\chi h^2 < 0.3$ and $\tan\beta = 3$ [70], σ_{SD} would yield values of $10^{-3} - 10^{-5} pb$. The spin-dependent cross section needs to include contributions from both the proton and neutron terms. This is also the case when calculating the form factor (see Section 2.2.3). With the choice of a suitable nuclear models σ_{SD} is given:

$$\sigma_{SD}(\tilde{\chi}N \to \tilde{\chi}N) = \frac{\mu_N^2}{\mu_p^2}\frac{C_N}{C_p}(\tilde{\chi}p \to \tilde{\chi}p). \tag{2.15}$$

2.2.3 Nuclear Form Factor Corrections

When elastic nuclear recoils occur, the interaction is modified by a form factor due to the momentum transfer. Form factors account for any reduction in the scattering cross-section from a value calculated for a point-like nucleon. The nuclear form factor can be written as $F(qr_n)$ and modifies the differential event rate by $F(q^2)$. The effective cross-section rapidly decreases as the momentum (q) transfer increases. When the momentum transfer q is small enough, the de-Broglie wavelength (h/q), is comparable to the nuclear radius r_n, and the effective interaction cross-section of scattering from the nuclei $\sigma(qr_n)$ is reduced by a factor $F^2(qr_n)$.

$$\sigma(qr_n) = \sigma_0 F^2(qr_n) \tag{2.16}$$

where σ_0 is the fundamental cross-section in the limit of zero momentum transfer i.e if $q \to 0$, the nuclear form factor need not be accounted for.

The Born approximation is employed to describe the situation. In this case the incident beam of particles can be described by a plane wave, except in the vicinity of the scatterer where the potential is zero. Using a plane wave approximation, $F(q)$ can be further interpreted as a loss of coherence in the scattering amplitudes for $q > 0$; they are either in or out of phase with each other. $F(q)$ may then be expressed as the Fourier transform of $\rho(r)$, which is the density distribution of the nuclear scattering centres;

$$F(q) = \int \rho(r) e^{i\mathbf{q}\cdot\mathbf{r}} d^3r = \frac{4\pi}{q} \int \rho(r) \sin qr dr. \tag{2.17}$$

The effect of $\rho(r)$ on the form factor can be further emphasised by considering the Fourier transform of a solid sphere for the spin-independent case, and a thin shell for the spin-dependent case. For the spin-dependent case the thin shell approximates an outer shell nucleon producing the resultant form factor:

$$F(qr_n) = \frac{sin(qr_n)}{qr_n} \tag{2.18}$$

The Fourier transform result for the spin-independent case is;

$$F(qr_n) = \frac{3}{(qr_n)^3}[\sin(qr_n) - qr_n \cos qr_n] \tag{2.19}$$

Both Equations 2.18 and 2.19 are commonly approximated using Equation 2.20

$$F^2(qr_n) = e^{-\alpha(qr_n)^2} \tag{2.20}$$

where, the exact form for a Gaussian scatterer of $r_{rms} = r_n$ is $\alpha = 1/3$, which is an adequate approximation to Equation 2.18 for small qr_n. A reasonable approximation for the spin-independent case (Equation 2.19) includes $\alpha = 1/5$ for $qr_n < 3 - 4$.

Further consideration is required for the spin-dependent case where the model is further complicated due to the outer shell nucleon. A complete study of this is given in [71] where it is shown that the zeroes of the Bessel function of Equation 2.18 are partially filled and the coupling to all 'odd group' nucleons are accounted for. A suitable approximation can be made whereby,

$$F^2(qr_n) = \begin{cases} (\frac{sin(qr_n)}{qr_n})^2 & 4.5 < qr_n < 2.55 \\ \sqrt{0.047} & 2.55 \leq qr_n \geq 4.5 \end{cases} \tag{2.21}$$

Accurate calculations have been performed for the spin-dependent case that include all contributions from the nucleus. Here the form factor is represented as having three parts, the neutron, the proton and the interference terms. The interference terms can be isoscalar $(p+n)$ and isovector $(p-n)$. In the isovector case $F^2(qr_n) = S(q)/S(0)$, where $S(q)$ folds the spin structure functions $S_{ij}(q)'$;

$$S(q) = a_0^2 S_{00}(q) + a_1^2(q) S_{11} + a_0 a_1 S_{01}(q) \tag{2.22}$$

Using shell model calculations for a specific nucleus the S_{ij} can be deduced. a_o and a_1 are the WIMP-nucleon coupling constants.

2.2.4 Detection Efficiency for Nuclear Recoils

The corrections calculated so far apply to an idealised detector with 100% efficiency. In reality this is not the case as there will be additional corrections, intrinsic to detector efficiency. This section discusses such corrections.

2.2.4.1 Detector Energy Efficiency and Threshold

For scintillation and ionisation detectors the apparent observed nuclear recoil energy E_v is some fraction of the true energy deposited, E_R. The type of recoiling particle, i.e. nuclear or electron recoil, can also effect the fraction of energy deposited. The ratio of the amount of ionisation produced by a recoiling nucleus

to the amount produced by an electron is further defined as the 'quenching factor', f_n. The difference emerges due the mechanism by which the recoil slows within the detector medium. An electron recoil energy deposition is more effective at producing scintillation and charge than a nuclear recoil of a similar energy. This leads to the use of two different energy scales depending on the type of interaction; keV electron-recoil equivalent energy (keVee) for electron-recoil events and keV nuclear-recoil equivalent energy (keVnr) for nuclear recoil events. The relationship between E_R, E_v and f_n can be defined as,

$$E_v = f_n E_R, \tag{2.23}$$

The keVee energy scale is often determined by taking gamma-ray calibration data and establishing the total number of photoelectrons detected by a photo-multiplier tube for a single energy point (often 122 keV gamma-rays from ^{57}Co). This scale if often used as a reference point for all other measurements. Determination of the keVnr energy scale is more complicated and requires calculation of the relative scintillation yield of nuclear recoils. This will be discussed further in Section 2.2.4.2.

By allowing for the dependence of f_n with E_R,

$$\frac{dR}{dE_R} = f_n \left(1 + \frac{E_R}{f_n}\frac{df_n}{dE_R}\right)\frac{dR}{dE_v}. \tag{2.24}$$

it is expected that when E_R drops below a threshold value, where the maximum energy transferred to electrons is less than the excitation energy (E_g), there will be a rapid drop in ionisation and/or scintillation and the detector will not produce an observable signal. For nuclear recoils this minimum energy is of the order E_C given by

$$E_C = \frac{m_t}{4m_e}E_g, \tag{2.25}$$

where m_t is the target nucleus mass and m_e is the electron mass. For electron recoils,

$$E_C = \frac{m_t}{4m_e}\left(\sqrt{E_e + E_g} - \sqrt{E_e}\right)^2 \tag{2.26}$$

where E_e is the typical kinetic energy of electrons in the atoms or molecules in the target volume.

2.2.4.2 Xenon Detector Thresholds

For liquid xenon, the 'quenching factor' must also be considered. The quenching factor of xenon is currently subject to much discussion based on recent measurements [72; 73], indicating an energy dependence for scintillation detectors below 15 keVnr.

The 'quenching factor' implies a comparison of the relative light yield of the nuclear recoil energy to the light produced from an electron recoil of the same energy. Although, in most xenon based detectors ℓ_{eff} is often preferred which is the measured (effective) light yield of nuclear recoils compared to an electron recoil measurement at zero field and at a single, fixed energy. In the ZEPLIN-III [72] experiment, the electron recoil energy reference was taken at 122 keV. This is achieved by using 122 keV gamma-rays emitted by a ^{57}Co source. The energy threshold of a detector can be determined by the light collection efficiency for primary scintillation photons (S1) and the effective scintillation yield of nuclear recoils. ℓ_{eff} is defined by the following equation;

$$\ell_{eff} = \frac{S1}{L_y}\frac{S_e}{E_{nr}S_n} \tag{2.27}$$

where S_e and S_n are the suppression factors in the scintillation output for 122 keV (L_y) gamma-rays and nuclear recoils at a particular electric field strength. E_{nr} is the nuclear recoil energy. Until recently there was not sufficient information on the conversion between the keVee and keVnr energy scales at low energies and thus it was assumed to be linear around $E_{nr} \sim 20$ keV, meaning ℓ_{eff} was assumed to remain constant at ~ 0.19 [74]. Using data from the ZEPLIN-III FSR it appeared that S_n or ℓ_{eff} do not have a linear dependence below ~ 15 keVnr.

In Figure 2.3, taken from [72], the differential energy rate has been plotted against simulated GEANT4 data. Once software and hardware efficiencies are accounted for the differential spectrum observed during nuclear-recoil calibration can be compared to Monte Carlo simulation. The energy scale of the simulated data has been converted from keVee to keVnr by dividing by 2.09, calculated using Equation 2.27 and accounting for the field strength of the experiment (3.9 V/cm in the liquid phase). It is clear from Figure 2.3 there is a mismatch between the solid-line simulation curve and AmBe calibration curve below ~ 20 keVee. This indicates that, as a result of the non-linearity, the energy conversion at lower energies is significantly affected, resulting in an efficiency

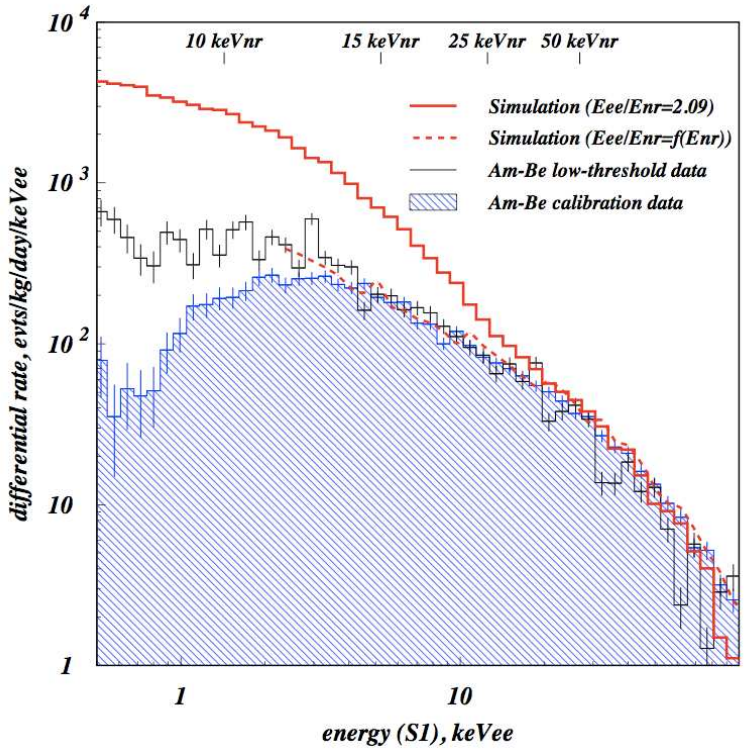

Figure 2.3: *Differential energy spectrum for the AmBe elastic recoil population. There are two AmBe data sets. The blue dataset was obtained at a higher hardware threshold compared to the black lined data set. The solid red line represents the Monte Carlo simulation which is scaled with a constant factor of* $E_{ee}/E_{nr} = 2.09$ *which displays a non-linearity below* 15 *keVnr. The red dash line is the resulting analysis to account for this non-linearity below these energies.[72]*

loss for the nuclear recoil detection. The ZEPLIN-III collaboration performed extensive independent testing of various efficiency factors that could have contributed, including independent verification of the relevant physics processors of the GEANT4 simulation toolkit, by employing alternative simulation packages and exploring all contributing factors. This discrepancy has now also been observed, in XENON10 where ℓ_{eff} was shown to vary from 0.16 - 0.194 within an energy range of $2-15$ keVnr [73]. To account for the observed non-linearity both XENON10 and ZEPLIN-III used a maximum-likelihood technique to derive a function that best matched the AmBe data to simulation.

Independent testing of ℓ_{eff} for xenon nuclear recoils below 10 keV was also performed [75] by firing a neutron beam at a xenon target for varying scattering angles. If the neutron (mass M_n) produces only a single scatter in the target (mass M_{Xe}) then the xenon recoil energy is given by;

$$E_R = T_n \frac{2M_n M_{Xe}}{(M_n + M_{Xe})^2}(1 - \cos\theta) \tag{2.28}$$

where T_n is the incident neutron energy, θ is the angle in the centre of mass frame and E_R is the nuclear recoil energy. The scintillation yield can then be compared to one another at each energy. The relative scintillation efficiency for nuclear recoils of 5 keV is 0.14 staying constant up until 10 keV where above this they achieved 0.21, consistent with previous data of 0.19.

It is currently unclear why the behaviour of ℓ_{eff} changes below energies of 15 keVnr. Akira Hitachi [76] proposed that the variation in ℓ_{eff} could be attributed to bi-excitonic collisions, where there is a collision between two 'free' excitons. These emit an electron with a kinetic energy equivalent to the difference between twice the excitation energy and the band-gap energy of LXe. Therefore, only one photon is produced for two excitons. This results in a reduction of the number of excitons available. However Aprile *et al.* [75] found that for energies below 10 keVnr the Hitachi model does not compare well to data.

A more recent measurement down to 4 keV has been undertaken [77] again confirming a variation in ℓ_{eff} at energies below 20 keVnr and also producing data inconsistent with the Hitachi model. Therefore the model has been further adapted to incorporate an extra component.

$$\ell_{eff} = q_{ncl} \cdot q_{el} \cdot q_{esc} \tag{2.29}$$

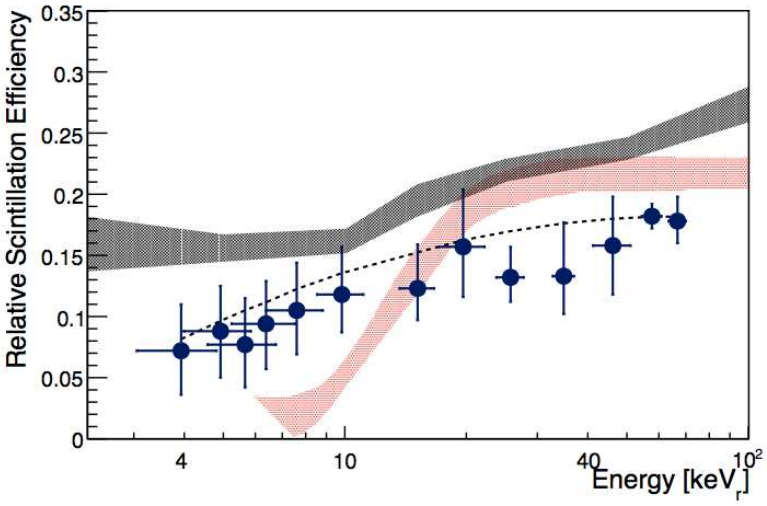

Figure 2.4: *The scintillation efficiency for nuclear recoils as measured by A Manzur et al. [77] (blue circles) XENON10 (top shaded area) and ZEPLIN-III (bottom shaded area). The dashed line is the theoretical model as described by Equation 2.29. Figure taken from [77].*

Equation 2.29 gives a theoretical expression for ℓ_{eff}, where q_{ncl} is the Lindhard factor, which describes how a large fraction of energy in a nuclear recoil is dissipated into atomic motion or heat. The Hitachi model is incorporated using the second term, q_{el}. q_{esc} describes the reduction in scintillation light yield due to escaping ionisation electrons which have thermalised outside the Onsager radius (the radius by which electrons with a thermal energy have an equal probability to either recombine or escape). This effect has only been applied recently to nuclear recoils due to the high ionisation yield normally observed. From Equation 2.29 q_{esc} can be expressed as a ratio between the initial number of excitons and electron-ion pairs $\alpha = N_{ex}/N_i$, and the fraction of of escape electrons, $\beta = N_{esc}/N_i$.

$$q_{esc} = \frac{\alpha + 1 - \beta_{NR}}{\alpha + 1 - \beta^{122}} \tag{2.30}$$

where β^{122} is the fraction of escape electrons for 122 keV electron recoils. Figure 2.4 shows the results from the work described in reference [77] compared to data produced by ZEPLIN-III and XENON10. Also shown is the theoretical model described here (dashed line). Data taken by A Manzur *et al.* sits (at times) within the middle of the ZEPLIN-III and XENON10 data. The differences between the data sets could be attributed differences in the detector set-ups and and the values of ℓ_{eff} used to correct the data; however this is still unclear.

2.2.4.3 Detector Resolution

If a monoenergetic beam of radiation was fired at an ideal detector the response would be a sharp delta-function peak. In reality, however, a Gaussian-like structure is observed with finite width. This is principally due to the fluctuations in the number of ionisations and excitations and other effects that can be attributed to non-ideal electronics. In Xe detectors the standard deviation, δ, in the number of N electron-ions pairs produced by an ionising particle is given by the following equation (originally observed by Fano in 1947) [78];

$$\delta^2 =< (N - N_i)^2 >= F \times N_i \tag{2.31}$$

where F is the Fano factor which depends on the ratio of excitations to ionisations and the stopping material itself. Fano demonstrated that the detector response would be different from the Poisson distribution by a factor of F. In LXe F is quoted as 0.059 [79]. The ionisation yield is defined as the electron ion pair production based on the unit energy absorbed. This is often quoted as the W-value which is the reciprocal of the average number of electron-ion pairs produced per 100 keV. Both the Fano factor and W-value can be used to calculate the ultimate energy resolution achievable in a xenon detector.

The energy resolution of a detector is often experimentally determined by measuring the full width half maximum (FWHM) of an energy peak. The FWHM of an energy deposition peak ΔE_{tot} has various contributions including electronic noise, ΔE_{en}, and fluctuations associated with the light collection of scintillation photons ΔE_c.

$$\Delta E_{tot} = \sqrt{\Delta E_0^2 + \Delta E_{en}^2 + \Delta E_c^2} \tag{2.32}$$

The best achievable energy resolution can therefore be given as [78];

$$\Delta E_0(keV) = 2.355\sqrt{FW(eV)E(MeV)} \tag{2.33}$$

where ΔE_0 is the energy resolution and E is the incoming ionisation radiation. This is also known as the Fano limit and has yet to be attained experimentally.

2.2.5 Target Mass Fractions

For most detectors the target material is composed of more than one element. As previously discussed, different target species will produce different recoil energies. Therefore a sensitivity cross section for each target species should be determined. The differential rate 2.1 can be expressed, for an element A which contributes a fraction f_A to the target volume as.

$$\frac{dR}{dE_v}|_{observed}(A) = f_A R_0 S_A F_A^2 I_A \tag{2.34}$$

The recoil rate can be given by

$$R_0 = \frac{2}{\sqrt{\pi}} \frac{N_A}{A} \frac{\rho_0}{m_\chi} \sigma_0 v_0 \tag{2.35}$$

where N_A is the Avogadro's number, ρ_0 is the local mean WIMP density, v_0 is the velocity of the Earth relative to the WIMP wind. It is then possible to obtain scattering cross sections for each element, summing them to produce a total cross section σ_{tot}.

$$\frac{1}{\sigma_{tot}} = \sum_A \frac{1}{\sigma_A} \tag{2.36}$$

2.2.6 Corrections Due to the Motion of the Earth

The rate of WIMP-nucleon interactions are also dependent on the position of the detector within the galaxy, the WIMP velocity distribution and WIMP particle density. In addition, while the detector is stationary on the Earth, the Earth rotates about the sun and the sun rotates around the galaxy in a relatively circular orbit. The speed at which the 'WIMP wind' will be observed by the sun is relatively constant, but the Earth's motion around the sun will cause an increase/decrease on an annual basis. The WIMP wind is expected to be at the maximum in June and at a minimum in December. Consequently an annual

modulation signal is a strong indicator of a dark matter presence within the galaxy. The WIMP motion in a halo at a velocity $f_{gal}(\mathbf{v})$, relates to the WIMP differential cross section through a form factor $d\sigma/d|\mathbf{q}|^2 \propto F^2(Q)$

The nuclear recoil energy E_R, that is deposited in the detector due to the scattering by a WIMP of mass m_χ from a target nuclei of mass m_t, is given by

$$E_R = \frac{q^2}{2m_t} = \frac{\mu_A^2 v^2}{m_t}(1 - \cos\alpha) \tag{2.37}$$

where $|q|^2 = 2\mu_A^2 v^2(1 - \cos\alpha)$, is the momentum transferred in the centre of mass frame according to the scattering angle α, where $\mu_A = m_\chi m_t/(m_\chi + m_t)$. The kinetic energy of the incoming particle is $E_\chi = \frac{1}{2}m_\chi v^2$ with velocity v. The total incoming rate is determined by integrating the differential rate dR, given by [62],

$$dR = \left(\frac{\rho_o}{m_\chi m_t}\right) v f_\oplus(\mathbf{v}, t) \left(\frac{d\sigma}{d|\mathbf{q}|^2}\right) d|\mathbf{q}|^2 du \tag{2.38}$$

where $\rho_0 = n_0 m_\chi$ is the local WIMP density. Integrating 2.38 over the WIMP velocity distribution, the differential recoil spectrum can be expressed as,

$$\frac{dR}{dE_R} = \frac{\rho_o \sigma_o}{2m_\chi \mu_A^2} F^2(E_R) \int_{v_{min}}^{v_{max}} \frac{f_{gal}(\mathbf{v} + \mathbf{v}_E)}{v} d^3\mathbf{v} \tag{2.39}$$

where $v_{max} = v_{esc}$ and $v_{min} = \sqrt{(E_R m_t)/2\mu_A^2}$ is the minimum velocity required for the generation of nuclear recoils. A precise value for v_{esc} is unknown; [80] assumes a value of 650 km/s, [69] used 600 km/s whilst recent limits from [81] have values between $498 < v_{esc} < 608$ km/s. With the application of the Maxwellian velocity distribution in accordance with the Standard Halo Model, hence assuming the dark matter distribution as an isothermal halo, (further discussion of different halo models and their impact on differential cross section are discussed in section 2.3.2.2) to Equation 2.39, yields the following result,

$$\frac{dR}{dE_R} = \frac{\rho_o \sigma_o}{2m_\chi \mu_A^2} F^2(E_R) \frac{\left\{\frac{1}{4\mathbf{V}_\odot}\left[erf\left(\frac{v_{min}+v_E}{\bar{v}}\right) - erf\left(\frac{v_{min}-v_E}{\bar{v}}\right)\right]\frac{1}{\bar{v}\sqrt{\pi}} e^{\frac{-v_{esc}^2}{\bar{v}^2}}\right\}}{erf\left(\frac{v_{esc}}{\bar{v}}\right) - \left(\frac{2v_{esc}}{\sqrt{\pi}\bar{v}}\right) e^{\left(\frac{-v_{esc}^2}{\bar{v}^2}\right)}} \tag{2.40}$$

where σ_o is measured in pb, m_χ is measured in GeVc^{-2} and ρ_0 is measured in GeV$c^{-2}cm^{-3}$, The rate can then be given, in units of kg^{-1}d^{-1} as [62]

$$R = 4.9 \frac{\rho_0 \sigma_o}{m_\chi m_t} g(\overline{v}, v_E, v_{esc}) \tag{2.41}$$

In the instance of xenon based WIMP detectors the recoil spectrum tends to reach a maximum below ∼100 keV with a predicted event rate of <0.01 kg^{-1} day^{-1}. Equation 2.40 will also differ for models which do not follow the Standard Halo Model assumptions. This would change the event rate for particular detectors. However, all detectors generally employ this model to enable comparison between different datasets.

2.3 WIMP Dark Matter Experiments

There are many experiments around the world devoting their efforts to the discovery of dark matter. Each experiment, although they may differ in techniques, all encounter similar issues when trying to detect these elusive particles. Some of these issues have already been discussed in Section 2.2. The main problems to overcome when designing and building a dark matter detector are as follows,

- Heavy nuclei are preferred to match the expected WIMP mass, thus maximising the kinematic factors.
- The type of limit to be set, whether it is a spin-independent or spin-dependent limit.
- The bigger the size of the detector mass the improved chance there is of WIMP detection. With an expected rate of $\lesssim 0.01$ kg^{-1} day^{-1} most dark matter detector collaborations are already proposing tonne scale or larger detectors.
- The WIMP-nucleon recoil energy will be very small, therefore an extremely low threshold is required.
- The removal or identification of unwanted background is vital. With an extremely low threshold more unwanted events will be observed. This is discussed further in this Section (2.3.1), including a detailed discussion on techniques that can be employed to discriminate against certain types of unwanted background.

2.3.1 Background in Dark Matter Detectors

Eliminating background in dark matter detectors is of utmost importance due to the low rates of interactions leaving energy depositions. The predominant sources of background arise from,

1. Cosmic muons
2. Neutrons and gamma-rays from detector or laboratory materials
3. Radon progenies, from detector components or laboratory materials

Cosmic muons arise from cosmic-ray spallation in the Earth's atmosphere. These are produced when the incoming cosmic ray produces secondaries commonly in the form of pions (π^+, π^- and π^0). The charged pions can then decay to muons and neutrinos; $\pi^+ \rightarrow \mu^+ + \nu_\mu$ and $\pi^- \rightarrow \mu^- + \bar{\nu}_\mu$. These Muons can interact with nuclei, ultimately leading to the emission of neutrons, a major background source. The most popular method for shielding against muons and muon induced events is by positioning dark matter detectors deep underground. This serves to attenuate the muon flux. Figure 2.5 shows the muon flux for various underground laboratories. Due to the extremely low cross-sections of WIMP-nucleon interactions, positioning dark matter detectors underground would have little impact on their detection. WIMPs are expected to penetrate through the rock and then to the detector, unaffected by the rock overburden.

Neutrons and gamma-rays are another source of background limiting dark matter detectors. The main sources of neutrons and gamma-rays are the laboratory structure and surroundings, and the materials used to build the detector. Naturally occurring uranium and thorium isotopes present in the laboratory building can decay to produce neutrons and gamma-rays observed in the detector. These backgrounds are predominantly reduced using neutron and gamma-ray shielding. Neutrons can be effectively thermalised and absorbed by hydrocarbon plastic or water shielding where capture onto hydrogen occurs. To reduce the gamma-ray flux lead or copper is normally implemented.

Although external sources of radiation can be relatively successfully reduced, removing internal sources of background emanating from detector components is a far greater challenge, especially as dark matter detector sensitivities become increasingly background limited. To improve the level of contaminants, detector

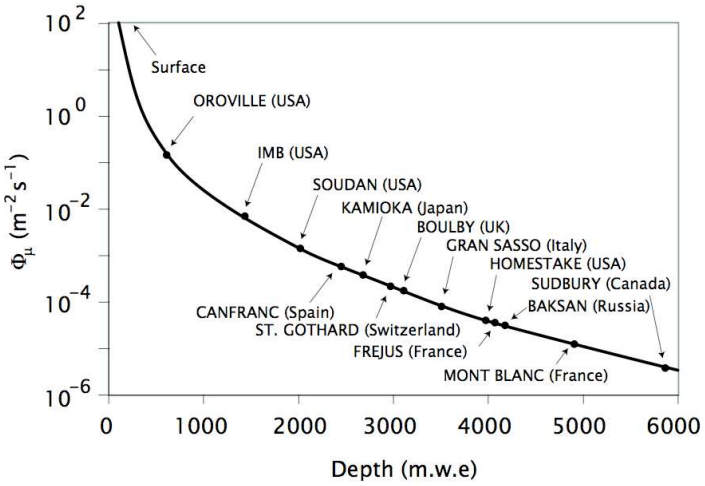

Figure 2.5: *Measurement of the muon flux taken from [82]. Various measurements from different underground laboratories of the differential muon flux as a function of depth.*

components are often specially selected, for example the ZEPLIN-III detector [83] employed pure copper for the vaccum jacket and target vessel construction. All detector components were also tested using a dedicated underground high-purity Germanium (HPGE) detector to determine the activity of components. Materials are selected and rejected based on these background measurements. In the ZEPLIN-III First Science Run (FSR) the major source of background emanated from the photomultiplier tubes (PMTs). One of the main objectives of the Second Science Run (SSR) is to reduce this by up to a factor of 30 with the implementation of new lower background PMTs. Despite the extreme efforts employed by numerous collaborations to remove background there are limits to which this can be successfully achieved, therefore identification and discrimination between background and WIMP events is a necessary extra measure.

Event discrimination can be successfully achieved through the study of signals produced by different particle species. Electron recoils would have a longer range, but a lower mean charge distribution compared to nuclear recoils. This knowledge is effectively exploited in various detectors to discriminate between electron recoils and nuclear recoils. If good discrimination is achieved then total rejection of electron recoil events can occur, leaving only nuclear recoil events. This pure signal can be further analysed to look for WIMP induced nuclear

recoils. Since neutron interactions cannot be well distinguished from WIMP interactions, it is vital to minimise the neutron background either by shielding and/or veto techniques. If the observed background rate for nuclear recoils matches the rate experimentally measured then a background subtracted limit can be set whereby no WIMP signals have been observed above this threshold (but with worsened statistical significance).

2.3.2 Current status of Dark Matter Detection

The typical methods currently utilised in direct dark matter experiments are,

- Phonon detection
- Ionisation detection
- Scintillation detection

Typically, many projects have elected to use a combination of two methods to improve event discrimination. Below is a summary of past, current and future dark matter detection projects that have impacted or may impact on the field.

2.3.2.1 UK Dark Matter Collaboration, Boulby Mine, UK

The Boulby Laboratory is situated at a working salt and potash mine in the county of Redcar and Cleveland, on the North East Coast in England. It is operated by Cleveland Potash Ltd [84] and has played host to numerous experiments from 1987-present. From 1987-2007 Boulby mine was the main experimental facility for the UK Dark Matter Collaboration (UKDMC), and since the dissolvement of the UKDMC, dark matter projects such as DRIFT and ZEPLIN still operate successfully underground. More recently, non dark matter related projects such as SKY-ZERO have made Boulby their home. The main laboratory is situated in a cavern at a vertical depth of 1100 m underground providing a 10^6 muon flux attenuation.

NaIAD

The NaIAD (**NaI A**dvanced **D**etector) programme operated from 2000 - 2003.

The NaIAD array consisted of eight NaI(Tl) crystals, contributing a total target mass of 46 kg. Each NaI module was mounted in a 10 mm thick polytetraflouroethylene (PTFE) reflector cage and then coupled to two quartz waveguides. Coupled to the end of each waveguide were 5" low background PMTs. NaIAD worked on the principal of observing scintillation light emitted from possible WIMP-nucleon interactions. Pulse shape analysis was performed to distinguish between electron recoil pulses and slower nuclear recoil pulses. NaIAD also possessed the advantage of having sensitivity to spin-independent and spin-dependent targets due to the presence of ^{22}Na and ^{127}I respectively. The NaIAD project collected a total of 44.9 kg years of data during the period of 2000-2003 and achieved the worlds best spin-independent limits on the WIMP-nucleon cross-section as referenced in [85] and displayed in Figure 2.10. For further reading see [85; 86; 87].

ZEPLIN

The ZEPLIN (**Z**on**E**d **P**roportional scintillation in **LI**quid **N**oble gases) project exploits the scintillation properties of liquid xenon. There have been three ZEPLIN detectors built throughout the project with ZEPLIN-III being the latest. All ZEPLIN detector targets utilise cryogenic liquid xenon as their main target volume. Xenon is an excellent dark matter target due to its high mass of A$\sim$ 131, its sensitivity to both spin-dependent and spin-independent measurements through the isotopes Xe^{129} and Xe^{131} and high light yield of $\sim$ 40 photons/keV.

ZEPLIN-I operated in Boulby mine during 2000 with its primary aim to display proof of concept for xenon detector suitability for dark matter searches. ZEPLIN-I operated as a single phase detector, unlike its successors, where scintillation light produced from either nuclear or electron recoils were analysed using pulse shape discrimination (PSD). PSD can be employed due to the way Xe interacts and decays from a nuclear or electron recoil. By observing the difference in the scintillation pulse time constant revealed a factor of 2-3 difference between the pulse produced by an alpha particle to one produced by an electron recoil due to the density in the ionisation track deposited by each particle species (see Chapter 3 for more information on the particle interactions with Xe). ZEPLIN-I housed 5 kg (3.2 kg fiducial) of liquid xenon in an ultra pure copper vessel, surrounded by a Compton veto and lead shielding. Three low background

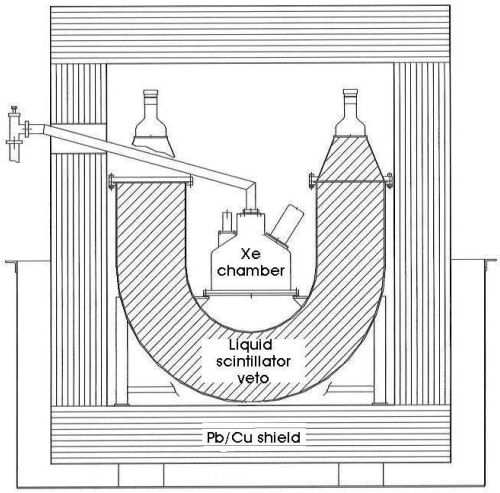

Figure 2.6: *The ZEPLIN-I detector [88]. The xenon chamber is shielded with liquid scintillator and lead and copper to attenuate the neutron and gamma-ray flux.*

PMTs obtained $\sim$ 293 kg·days data giving an at-the-time world leading spin-independent WIMP-nucleon cross-section of 1.1×10^{-6} pb at a WIMP mass of 50 GeV [89]. This limit can be observed in Figure 2.10.

The second phase of the ZEPLIN project was ZEPLIN-II. The main differences between ZEPLIN-I and ZEPLIN-II was an increased LXe target volume to 31 kg and the presence of an electric field and two phase operation (gas and liquid). The electric field enabled measurements of both primary scintillation and ionisation. The ionisation charge is extracted from a LXe phase and accelerated into a gaseous phase producing electroluminescence. Using a two phase operation improves the discrimination between particle species that interact within the target volume. The proportion of vacuum ultraviolet (VUV) scintillation light and ionisation charge produced will differ according to a particular particle species. These processes that occur due to particle interactions within the xenon are discussed in further detail in Chapter 3.

The ZEPLIN-II detector was designed with seven ETEL (Electron Tubes Enterprises Ltd) low background PMTs which view the LXe target mass from above. The target vessel was composed from copper. Further information on the

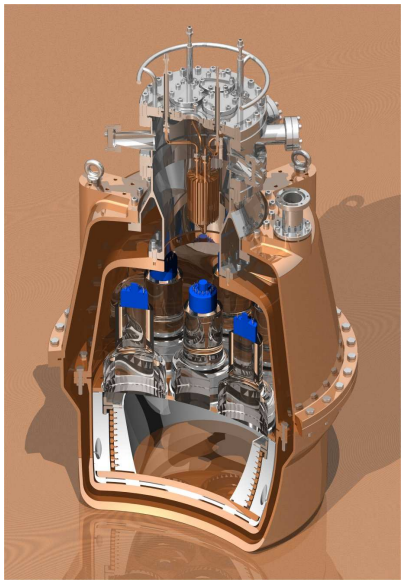

Figure 2.7: *The ZEPLIN-II detector. Scintillation photons produced in the xenon target are observed by seven PMTs. ZEPLIN-II uses a two phase system to improve particle discrimination.*

ZEPLIN-II data acquisition (DAQ) and analysis procedure can be found in this reference [90] and Figure 2.7 shows the inner details of the detector. ZEPLIN-II acquired a total of 225 kg days of data with a fiducial mass of 7.2 kg, after the application of analysis cuts, and achieved a WIMP-nucleon cross-section of 6.6×10^{-7} pb [91], third best in the world at the time (see Figure 2.10).

ZEPLIN-III is the third phase of the project. ZEPLIN-III improves on previous ZEPLIN detector designs by adopting the two-phase particle species discrimination technique [83] but also learning from systematic problems that arose in the previous detectors. A comprehensive overview of the ZEPLIN-III detector and current status can be found in Chapter 3. The ZEPLIN-III collaboration recently completed the first science run (FSR) achieving a WIMP-nucleon elastic scattering spin-independent cross-section of 8.1×10^{-8} pb for a WIMP mass of 55 GeV/c^{-2} [72], placing ZEPLIN-III as the second best in the world with the best noble gas detector result. The 2008 ZEPLIN-III FSR limit in shown in Figure 2.10. ZEPLIN-III also set a 90%-confidence upper limit of a pure WIMP-neutron spin-dependent cross section of 1.9×10^{2} pb for a 55 GeV/c^{2} WIMP mass.

DRIFT

The DRIFT (**D**irectional **R**ecoil **I**dentification **F**rom **T**racks) programme utilises low pressure time projection chambers (TPC) filled with a mixture of target gas with an aim to detect low-energy nuclear recoils with a uniquely directional signature. These are produced by the elastic scattering of WIMPs with atomic nuclei. DRIFT is a directional detection program with an ambition to observe an annual and diurnal modulation signal produced by the relative motion of the Earth travelling through the galaxy and the non-rotating WIMP halo. DRIFT utilises negative ion time projection chamber (NITPC) technologies [92] and uses CS_2 gas filled vessels equipped with multi-wire proportional counters (MWPCs). With the application of an electric field primary ionisation electrons produced from a recoil event, are captured by the electronegative gas which are drifted to an anode. The use of a heavier target enables good track reconstruction from the impact point and reduces the diffusion of the track. Directional information is obtained by reconstructing the track. Good background discrimination can be obtained between electron and neutron recoils by exploiting the lower dE/dX of electrons and rejecting electron recoils based on their longer ionisation tracks.

DRIFT-I operated in Boulby mine during 2000-2001 and served as a proof of concept [93]. DRIFT-I also aided improvements for the DRIFT-II module, which was installed in Boulby mine in 2005 [94]. DRIFT-IIA is the first of a possible 20 modules that can be placed in Boulby mine and has successfully taken 16 kg·days of data. Despite the fact that no sensitivity limit has been set for DRIFT-II, it has been able to demonstrate a number of important features required by a directional dark matter detector. Reconstruction of the full recoil direction vector to distinguish the 'tail' from the 'head' is useful for providing directionality and background rejection. Using the DRIFT-IIC module (the same design as DRIFT-IIA) it was possible to reconstruct sulphur recoil tracks induced by ^{252}Cf neutrons [95]. Directionality has also been demonstrated [96] by placing a ^{252}Cf neutron source at three different positions around the detector to see if the x, y and z axes of a recoil can be resolved. It seemed that the x and z axes were easier to resolve than the y axes; however with reductions to the noise produced in the grid readouts, information regarding the y orientation may be improved.

No sensitivity limit has been set, but operations at Boulby mine have primarily focused on developing the technology for future modules.

2.3.2.2 Gran Sasso National Laboratory (Italy)

The Gran Sasso National Laboratory (**L**aboratori **N**azionali Del **G**ran **S**asso (LNGS)) is situated in Italy, about 120 km from Rome. LNGS is located beneath the Gran Sasso mountain with an average of 1400 m of rock coverage, reducing the muon flux by $\geq 10^6$. Access to the facility is provided via a 10 km freeway tunnel crossing the Gran Sasso mountain. For further information see [97].

XENON

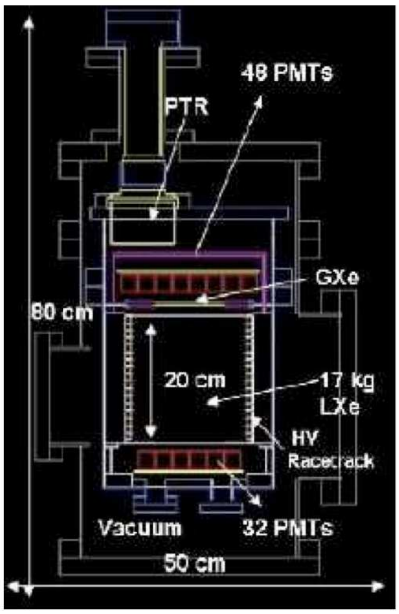

Figure 2.8: *The XENON10 vessel [98] displaying the upper and lower PMT arrays, that both look upon the xenon target.*

The XENON programme [99] relies on the same principles as the ZEPLIN II & III projects to search for WIMP events. XENON10 uses LXe and runs a two-phase operation and has served as a proof of concept for future tonne scale xenon detectors. The XENON10 module has a 15 kg detector volume and can discriminate signal from background down to 4.5 keVnr. The XENON10 detector utilises a dual phase (liquid/gas) operation where direct scintillation (S1) in the liquid and proportional scintillation in the gas (S2) are measured. The XENON10 construction includes a 20 cm inner diameter and 15 cm high

Teflon cylinder which defines the active volume. Four electrodes, two in the liquid and two in the gas phase, define an electric field which drifts ionisation electrons for extraction in the gas phase. The drift field in the liquid is quoted as 0.73 kV/cm, much lower than in ZEPLIN-III detector. XENON10 uses PMTs to observe signals produced by incoming events. Both ZEPLIN-II and III used a single PMT array to observe events whereas XENON10 uses two arrays of PMTs, above and below the LXe (see Figure 2.8). 41 PMTs are positioned in the liquid and are therefore situated at the bottom of the detector, 1.5 cm below the cathode mesh. The top array includes 48 PMTs in the gas phase and observes the majority of the scintillation light. Using both PMT arrays it is possible to obtain improved event location position sensitivity in the XY plane. The third co-ordinate is inferred from the electron-drift time through the liquid xenon.

The XENON10 collaboration acquired 58.6 days of data with a fiducial mass of 5.4 kg. XENON10 presented a WIMP-nucleon spin-independent cross section of $\sigma = 8.8 \times 10^{-44}$ (4.5×10^{-44}) cm^2 for a WIMP mass of 100 (30) GeV/c^2 [100] (see Figure 2.10). This has been revised to recognise new physics with the varying ℓ_{eff} values (see Section 2.2.4.2) to $\sigma = 9.9 \times 10^{-44}$ (5.6×10^{-44}) cm^2 for a WIMP mass of 100 (30) GeV/c^2 [75]. XENON10 have also recently published a WIMP-proton spin-dependent limit of 5×10^{-39} cm^2 for a WIMP mass of 30 GeV/c^2 [101].

The next phase of the project is XENON100 which is currently under construction in LNGS. XENON100 aims to achieve a WIMP-nucleon cross-section of 2×10^{-45} cm^2.

DAMA, LIBRA and XeDAMA

The DAMA (particle **D**ark **MA**tter searches with highly radio-pure scintillators at Gran Sasso) programme was first proposed in 1990 and published their first major results in 1998. The DAMA project has caused much controversy over the last decade in claiming a positive dark matter result from data published between 1998-2003 (accumulated data), and 2008. DAMA has utilised various detector target materials to search for an annual modulation dark matter signal, as were the objectives of NaIAD (2.3.2.1). DAMA/NaI was the first DAMA detector [102], which deployed nine 9.70 kg NaI(Tl) crystals. DAMA/NaI is similar in design to NaIAD but does not use pulse shape discrimination to reject recoil

events. Instead, DAMA/NaI analyses events in energy bin ranges, particularly in the WIMP candidate range of 2-6 keV. The main analysis involves removing the flat rate (noise) from the residual rate of single-hit events within a particular energy bin.

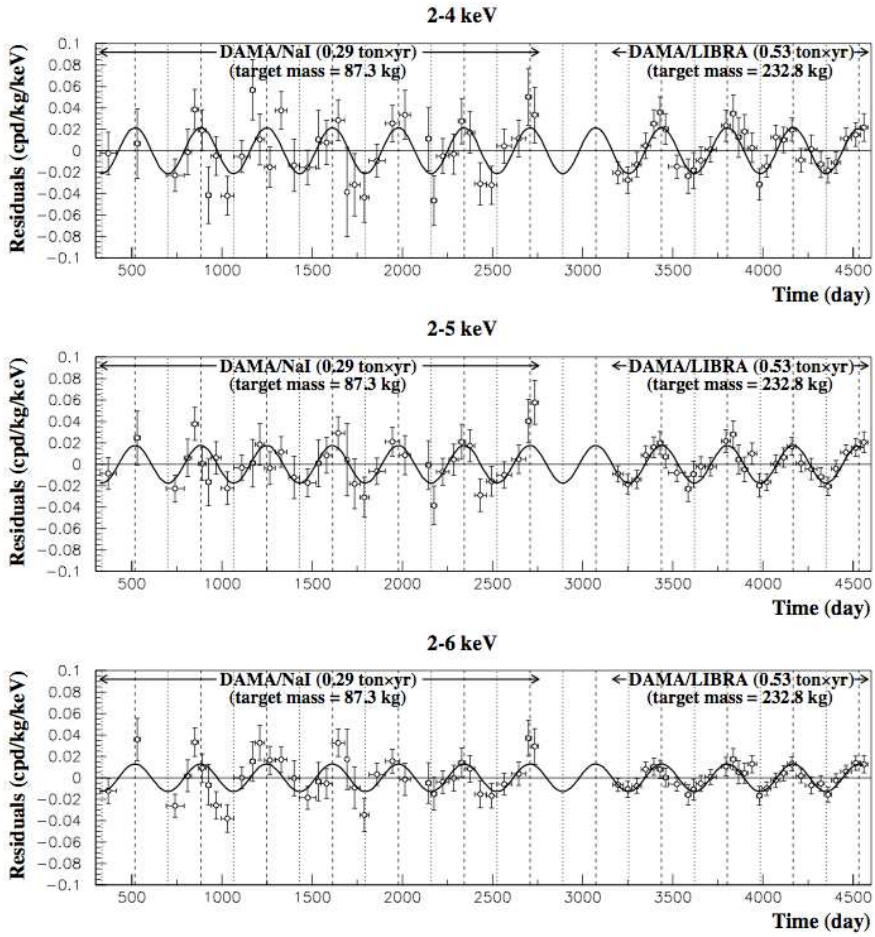

Figure 2.9: *Experimental residual rate for single-hit events in the 2-4, 2-5 and 2-6 keV energy intervals. Time is measured in days from January-1st of the first of seven years of data taking. Up to day* $\sim$ 2750 *data has been obtained from DAMA/NAI. From day* $\sim$ 3000 *onwards is data from the DAMA/LIBRA experiment. The black line is a superimposed co-sinusoidal function in accordance from what is predicted for a typical annual modulation signal for WIMPs. [103]*

DAMA/NaI completed operations in 2002 with a total exposure of 107731 kg·days collected over seven annual cycles, [104; 105]. A modulated cosine-like behaviour was observed at 6.3σ C.L. The residual count rate can be observed in

Figure 2.9 (between days 0 to $\sim$ 2500) and has been fitted with a co-sinusoidal function, the type of behaviour expected from a WIMP signal. The DAMA collaboration interpret this as a WIMP-nucleon spin independent cross section of 6×10^{-6} pb. There were a number of issues expressed by other collaborations with this result including the fact that others (CDMS, EDELWEISS and ZEPLIN-I) had already surpassed this cross section also due to the absence of PSD, separation into electron and nuclear recoil contribution is not possible, but there was, at that time no other detector similar in terms of detector material and also sensitivity as DAMA/NaI that could unequivocally disprove their claims. More subtle effects could be exhibiting themselves which only DAMA is sensitive to.

In March 2003 the DAMA programme started taking preliminary measurements with DAMA/LIBRA (**L**arge sodium **I**odide **B**ulk for **RA**re processors) the next phase of the DAMA programme. The aim of DAMA/LIBRA was to develop a detector with a mass of $\sim$ 250 kg. DAMA/LIBRA [106] has 25 highly radiopure NaI(Tl) detectors, arranged in 5×5 columns. DAMA/LIBRA released results in 2008 [103] after acquiring an impressive 0.53 ton·yr data over 4 annual cycles. Including the DAMA/NaI data this equates to a total exposure of 0.82 ton·yr. From these results DAMA claimed they had again observed an annual modulation signal in the 2-6 keV energy range (see Figure 2.9 from days > 3000)

Some proposals have been suggested to explain the DAMA results. One such idea is inelastic dark matter ("idm"). The kinematics of a WIMP interaction can be altered if the dark matter particle, having scattered from a nuclei is left in an excited state. Equation 2.39 in Section 2.2.6 describes the differential event rate for a WIMP nucleus scattering on a target nuclei. In the idm scenario, the minimum relative velocity for scattering has an extra dependence, δ, whereby the dark matter particle χ has an excited state χ^*, with a mass $\delta = m^*_\chi - m_\chi \sim$ 100 keV. This leads to a low energy cutoff in recoil spectrum not present in elastic scattering scenarios. Another effect of the idm scenario is the increased annual modulation signal as a fraction of the total signal due to the higher minimum velocity required. The minimum velocity cutoff may also be lower for heavier target nuclei which could have important consequences for some detectors such as CDMS-II where Ge (atomic mass 72.61 amu) is the target mass. If δ is varied for $\delta \sim 130$ keV [107] based on a small WIMP mass (≤ 100 GeV) the exclusion limits set by experiments are at times in agreement with the DAMA results.

However, at larger WIMP masses experiments such as CRESST-II and CDMS-II still exclude the DAMA result. Also, recently D. Cline *et.al* [108] re-analysed ZEPLIN-II data to look for any indication of idm induced background with the final conclusion of a null result; an analysis from the ZEPLIN-III FSR is in preparation.

Another proposed explanation is based on the current assumption that to help solve Equation 2.39 the WIMP velocity distribution is described by the Standard Halo Model (SHM). A variation from the SHM could greatly effect the differential event rate as observed by a detector on Earth. The SHM assumes a Maxwellian WIMP velocity distribution but there is little evidence to fully support this model. Other models have been implemented based on the Via Lactea simulation and Dark Disc numerical calculations. Reference [107] took to varying δ and applied both types of velocity distributions to different experimental data sets to compare with the DAMA/LIBRA results. In some scenarios it is possible that ZEPLIN-II and III, XENON-10, CRESST-II and CDMS-II do not exclude the DAMA preferred region of parameter space. Other possibilities to account for the DAMA signal includes the detection of mirror dark matter and Axions. Until a similar experiment can confirm or other more sensitive experiments can deduce a similar signal the DAMA debate will undoubtedly continue for some time.

The third phase of the project is DAMA/LXe which, as the name suggests, uses LXe as its target medium. DAMA/LXe has a $\sim$ 6.5 kg LXe target where scintillation is observed by three 3 inch PMTs. Numerous upgrades and R&D programmes have been realised since DAMA/LXe's conception in the 1990s. Further information can be found in reference [109] and references there-in.

2.3.2.3 Soudan (USA)

The Soudan Underground Laboratory is located in the Soudan Mine State Park, Minnesota, USA and has a depth of 780 m which reduces the muon flux by a factor of 5×10^4.

CDMS

The CDMS (**C**ryogenic **D**ark **M**atter **S**earch) collaboration currently holds the worlds best spin-independent WIMP-nucleon cross-section limit. CDMS employs low-temperature germanium (Ge) and silicon (Si) detectors to search for

WIMPs and can discriminate between different particle species through simultaneous ionisation and phonon detection. CDMS-I was part of the first phase of the project which was located in a tunnel at Stanford University, USA. Originally two types of detectors were used, BLIP (Berkeley Large Ionisation and Phonon mediated) and ZIP (Z-sensitive Ionisation and phonon-mediated) detectors. CDMS-II uses only ZIP detectors, therefore discussion will focus on these, further information on BLIP detectors can be found in the following reference [110] and references there-in. CDMS-I [111] acquired data throughout 2002 whilst at Stanford university until the CDMS project was moved to Soudan underground Laboratory in 2003.

CDMS-II [112] has improved on the first phase of the project to become world leaders in the field in terms of dark matter sensitivities. CDMS-II uses ZIP detectors which are cylindrical high purity Ge or Si crystals 1 cm thick and 7.6 cm in diameter. Each Ge (Si) ZIP detector has a mass of 250 g (100 g). Situated on each of the crystals are two concentric ionisation electrodes and four independent phonon sensors. The CDMS set-up involved stacking these ZIP detectors 2 mm apart. Close packing of the detectors increasing the ability to observe multiple scatters, (an indicator of a non-WIMP event) and shields the detectors from low-energy electron surface events. The CDMS ZIP detectors observe events via two channels, either electron recoils where electrons can Compton scatter through K shell capture, and nuclear recoil events. The interactions deposit energy via phonons or charge excitations. The ZIP detectors are able to measure both ionisation and phonon energy enabling discrimination between the type of incoming particle causing the interaction. Nuclear recoils produce less ionisation energy than electron-recoils and can thus be discriminated from each other. CDMS-II published a spin-independent WIMP-nucleon cross-section of 4.6×10^{-8} pb at 90% CL for a WIMP mass of 60 GeV/c^2 [113] in 2008, as shown in Figure 2.10. They also published a spin-dependent WIMP-nucleon cross-section of 1.8×10^{-3} pb at 90% CL for a WIMP mass of 60 GeV/c^2 [113]. More recently the final CDMS-II results have been published. A raw exposure of 612 kg·days was analysed with two events observed within the WIMP signal region. They claim that the probability of observing these two background events is 23%, hence these two events are inconsistent with background to the 77% level. CDMS-II do not have sufficient evidence to claim that these two events are WIMPs; however they can not completely rule them out. CDMS-II

set a spin-independent WIMP-nucleon cross-section of 7.0×10^{-8} pb at 90% CL [114] for a WIMP mass of 70 GeV/c^2. Combining these results with previous CDMS-II data a spin-independent WIMP-nucleon cross-section of 3.8×10^{-8} pb for a WIMP mass of 70 GeV/c^2 is attained, maintaining their position as the most sensitive dark matter detector in the world.

2.3.2.4 Other Experiments

In addition to the dark matter experiments already mentioned above there are numerous other ongoing or planned experiments. The XMASS [115] (**X**enon **MASS**ive detector) programme is a single phase, self-shielding xenon based dark matter detector currently under construction at the Kamioka Underground Observatory in Japan. XMASS expects to set a WIMP-nucleon spin-independent limit of 10^{-9} pb (see Figure 2.10) in their first stage of operation.

The LUX (**L**arge **U**nderground **X**enon) experiment is another xenon based programme to construct a 1-10 tonne two phase liquid/gas xenon detector at DUSEL in Homestake mine. The two phase design follows current experiments such as ZEPLIN II & III and XENON. The initial phase of the LUX detector will contain 300 kg of LXe and will be surrounded by a $\sim$ 200 tonne water shield. Using the XMASS principle, 200 kg of the LXe target will be used for self-shielding purposes. 122 PMTs will observe any scintillation and ionisation produced by an incoming recoil event and are arranged in arrays above and below the LXe volume. The Laboratory is currently under construction and the detector is in an R&D/construction phase. The goal of LUX is to achieve a WIMP-nucleon cross section of $\sim 7 \times 10^{-9}$ pb after one year of operation. See references [79; 116] for more information.

The EDELWEISS (**E**xperience pour **DE**tector **L**es **W**imps **E**n **S**ite **S**outerrain) experiment [117] is situated in Modane, France and uses cryogenic high purity Ge bolometers to measure both phonons and ionisation produced from a WIMP-induced recoil. The first phase of the programme was EDELWEISS-I and achieved a a WIMP-nucleon spin-independent cross section of the order 10^6 pb. EDELWEISS-II is the second phase of the project which uses a larger fiducial volume, whilst improving on problems discovered in the first phase of the project [118]. EDELWEISS-II achieved a spin-independent sensitivity limit of 1.0×10^{-7} pb (90%CL) for a WIMP masses $\sim$80 GeV/c^2 [119].

Another European based programme is CRESST (**C**ryogenic **R**are **E**vent **S**earch using **S**uperconducting **T**hermometers) which uses sapphire cryogenic calorimeters to simultaneously detect both scintillation light and non-thermal phonons. CRESST-I achieved a spin-independent WIMP-nucleon cross section limit of $\sim 10^3$ pb and a spin-dependent WIMP-proton cross section limit of $\sim 10^1$ pb [120]. CRESST-II set a WIMP-nucleon spin-independent limit of 4.8×10^{-7} pb, for a WIMP mass of ~ 50 GeV [121]. For further information see [122] and [123]. The EDELWEISS programme is set to merge with CRESST to form EURECA (**E**uropean **U**nderground **R**are **E**vent **C**alorimeter **A**rray), which will be situated in Modane laboratory. EURECA [124] aims to explore scalar cross-sections in the $10^{-9} - 10^{-10}$ pb range using a 1-tonne target mass in a modular design.

Other searches include DEAP [125; 126] which utilises liquid argon as it's detector medium. ORPHEUS [127; 128], ELEGANT V (NAI) [129], NEWAGE (CF4) [130], PICASSO (Superheated Fluid) [131], WARP [132], HDMS (Ge) and GENIUS [133]. For a review of the above and other experiments not mentioned here see [134]. For a review of xenon dark matter detectors see [79; 135].

2.3.3 Summary

There is a large and exciting world wide effort to detect WIMP events using the method of observing WIMP-induced nuclear recoils. The mechanisms for such an observation chosen by numerous collaborations are similar. Such methods include observation of ionisation, scintillation or phonons. Often a combination of two methods is employed to aid in event discrimination, a vital tool when one of the main missions of such detectors is in background reduction. Building and designing a dark matter detector is a difficult task when dealing with the requirement of very low background environments and materials, low detector thresholds and large detector volumes. Currently the most sensitive detectors are CDMS-II, XENON10 and ZEPLIN-III, with XENON10 and ZEPLIN-III using a xenon target mass, proving that xenon is an extremely promising and competitive detection medium. Proposed tonne scale xenon detectors will undoubtedly start to push into the predicted theoretical sensitivity region expected for a positive WIMP result within the coming years.

Despite the positive claims from DAMA no other experiment in the world has yet been able confirm their result, with many detectors 100 times more sensitive than the DAMA/LIBRA detector. It is possible that those detectors are not as sensitive to dark matter as with DAMA, due to the detection medium employed. Further theoretical study may also be required to look at a better defined WIMP Halo model and also inelastic dark matter models which could explain the positive result. CDMS-II have also stated they may have observed a signal inconsistent with background; however there is not enough evidence to confirm this as a WIMP result. In any case more work is required and until another detector makes the leap and publishes a positive result, these questions will remain unanswered.

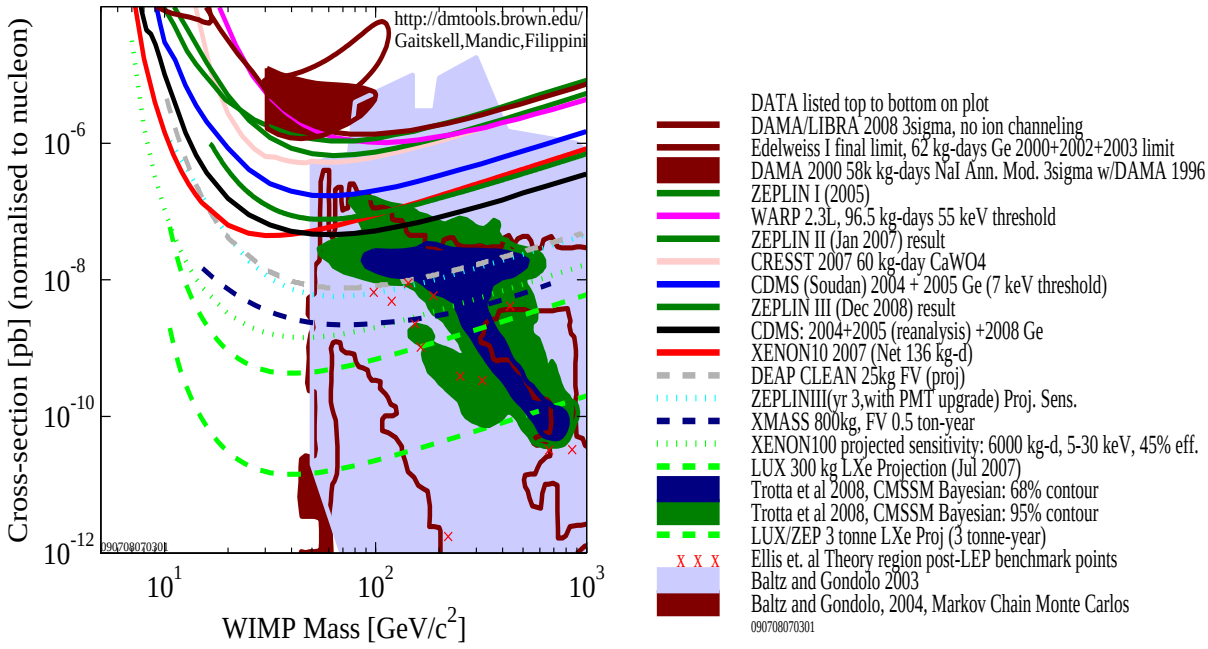

Figure 2.10: *Summary of the past, present and future dark matter detector spin-independent WIMP-nucleon cross sections. For Spin-dependent results see Chapter 3, Figure 3.29*

Chapter 3

ZEPLIN-III and the First Science Run

3.1 Introduction

The ZEPLIN-III detector is an effective, low background high sensitivity dark matter device utilising xenon as a target medium. This chapter will introduce to the reader the ZEPLIN-III detector design and physics behind the device. In addition the results and analysis programme from the ZEPLIN-III FSR is also discussed. During the FSR 847 kg·days of data were acquired between February 27th 2008 and May 20th 2008. With no WIMP signal observed, ZEPLIN-III has excluded a WIMP-nucleon spin-independent cross section above 8.1×10^{-8} pb (90% confidence limit) for a WIMP mass of 60 GeV/c^2 [72] and also set an upper limit of a pure WIMP-neutron spin-dependent cross section of 1.9×10^{-2} pb (90% confidence) for a 55 GeV/c^2 WIMP mass [136]. An overview of the analysis procedure employed to develop these limits is given. This includes details on the reduction software, cuts applied to the data and calibration of the FSR data and the author's contribution to the analysis effort. This included profiling the historical evolution of the electron lifetime throughout the FSR, and using this to improve the data quality by applying a continuous correction to all the data of the FSR. The results from this investigation and effects on the FSR sensitivity limit are also shown.

3.2 The ZEPLIN-III xenon detector

ZEPLIN-III, like its predecessors, utilises liquefied xenon (Xe) as a target mass. In accordance with theoretical models [137] a WIMP-nucleon cross-section of at least 10^{-10} pb should be probed for a realistic chance of WIMP detection. This is a difficult technical challenge, requiring impeccable identification and discrimination between particle species and the realisation of an extremely low background environment. To achieve the latter, ZEPLIN-III is situated 1100 m below ground in a salt mine (Boulby mine) in the county of Cleveland and Redcar; this attenuates the muon flux induced from cosmic ray spallation by a factor of 10^6. ZEPLIN-III has also been constructed from radiologically pure materials, of which samples have been tested in a dedicated germanium detector situated underground, to ensure that the materials employed have suitably low radiological content. Particle discrimination was achieved by the the application of high electric fields and two phase (gas/liquid) running of ZEPLIN-III target.

Xenon as a target medium has proved to be very competitive in the world rankings for setting dark matter sensitivity limits. The ZEPLIN projects [89; 91] and XENON10 have historically produced some of the best limits in the world. Currently ZEPLIN-III [72] and XENON10 [75] are two of three most sensitive dark matter detectors, with only CDMS-II [113] with a better sensitivity.

3.2.1 Xenon Physics

Liquid Xe is utilised as a detector target medium. Noble gas detectors were a popular area of research particularly in the 1970s and have since made a resurgence due to their applicability to rare event searches (dark matter, neutrinos), medical physics and as radiation detectors amongst others (see [79; 135] for reviews). Xenon, as a detector medium is favourable for the following reasons;

- High stopping power to radiation due to high atomic number ($Z = 54$) and density (as a liquid ~ 2.953 g/cm^3, STP Xe gas 5.858 g/l)
- High ionisation and scintillation yield
- Generates both ionisation electrons and scintillation photons to facilitate signal response
- Can be purified relatively simply

- Transparent to UV wavelengths
- Different Xe isotopes are useful for spin-independent and spin-dependent searches
- The absence of any long lived isotopes

Vital to dark matter detectors is the ability to detect WIMP events and to be able to identify and discriminate between different types of background. Background relates to neutrons and gamma-rays that deposit energy within the target volume. Xenon based technologies have attained levels of discrimination between particle species of the order of 99.99% [72] (with ZEPLIN-III currently the best in the world) in the region of interest for WIMP searches.

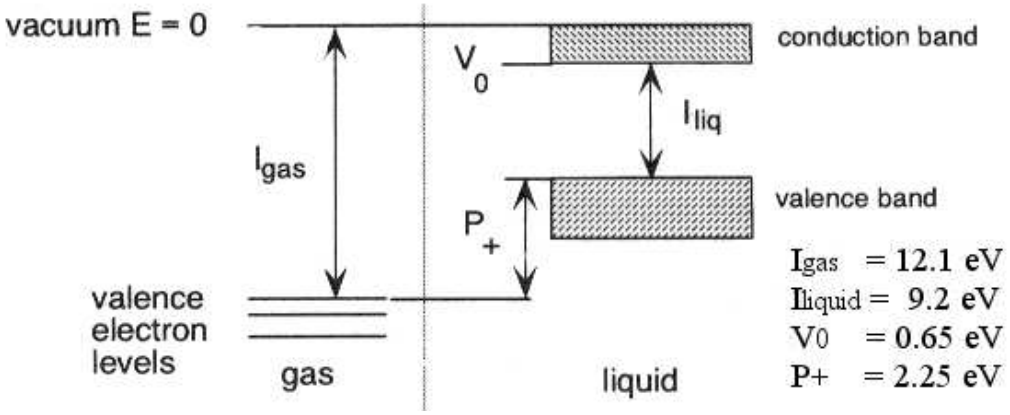

Figure 3.1: *The bandstructure of liquid and gaseous Xe from [138]*

Xenon is also an excellent insulator due to its electronic band structure. The band structure of liquid Xe is shown in Figure 3.1, where I_{liq} is the energy difference between the valance and conduction bands (this will be referred to as E_g for the remainder of this thesis). When energy is deposited in Xe both ionisation and scintillation can occur, a characteristic that has been fully exploited in Xe based dark matter detectors.

3.2.1.1 Two phase emission

Xenon detectors used for dark matter searches generally employ two phase systems in an attempt to improve discrimination between different incoming particle

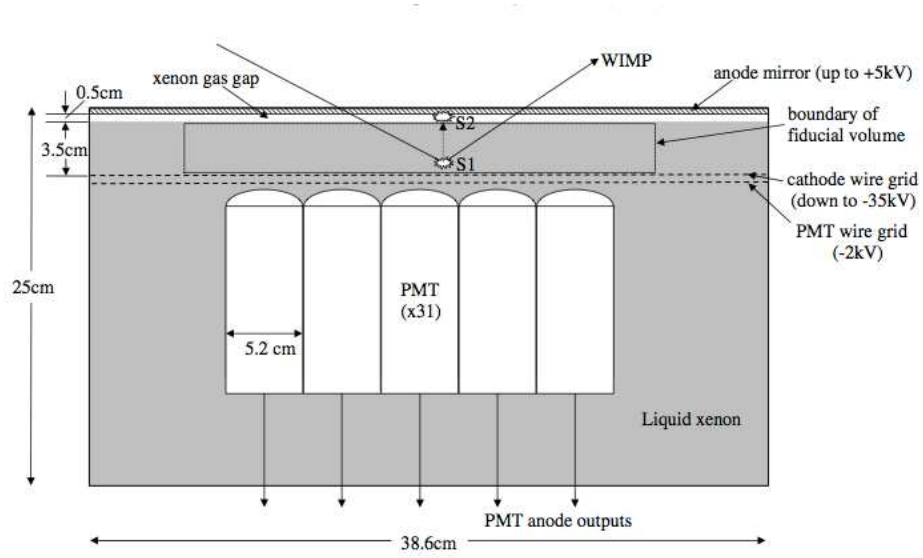

Figure 3.2: *The ZEPLIN-III Xe target [83]. The ZEPLIN-III PMTs are positioned within the liquid Xe. The active liquid Xe region is 3.5 cm in height. Positioned above this is the 0.5 cm Xe gas gap. The primary scintillation occurs in the liquid phase (denoted S1 in the figure) and the secondary scintillation occurs within the gas gap (denoted S2).*

species; ZEPLIN-III uses liquid and gaseous Xe. Displayed in Figure 3.2 is the central Xe target vessel of the ZEPLIN-III detector. There is an active liquid Xe region of length 3.5 cm and a Xe gap gap above this of 0.5 cm. An anode mirror is situated above the gas gap and a cathode grid within the liquid phase. The PMTs are used to observe any scintillation light.

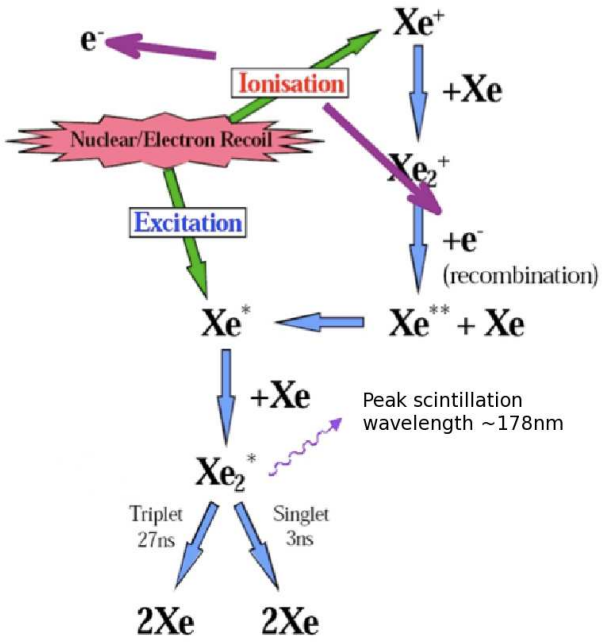

Figure 3.3: *The interaction process in liquid Xe due to an electron or nuclear recoil.*

There are three important physics processes that dominate a two phase time projection chamber such as ZEPLIN-III.

1. Scintillation in the liquid phase
2. Ionisation in the liquid phase
3. Electroluminescence in the gas phase

When an incoming particle deposits energy within the liquid Xe, Xe atoms can become excited and ionised. Figure 3.3 gives a diagrammatic view of the interaction process. An excited or ionised Xe atom can eventually produce vacuum ultraviolet (VUV) scintillation light. Both the excitation and electron-ion recombination leads to the formation of excited dimers. An excited Xe atom

can combine with an unexcited Xe atom to form an excited dimer as shown below;

$$Xe^* + Xe \rightarrow Xe_2^* \tag{3.1}$$

Xe_2^* can then decay to give

$$Xe_2^* \rightarrow 2Xe + hv. \tag{3.2}$$

In this process a photon is emitted from the decay of Xe_2^* with a peak wavelength of 178 nm. In addition to the above, in the absence of an electric field, an ionised Xe atom can recombine through the following mechanism;

$$\begin{aligned} Xe^+ + Xe &\rightarrow Xe_2^+ \\ Xe_2^+ + e^- &\rightarrow Xe^{**} + Xe \\ Xe^{**} &\rightarrow Xe + heat \end{aligned} \tag{3.3}$$

the resultant excited Xe dimer decays as shown in Equations 3.1 and 3.2 to produce a 178 nm photon.

The scintillation light produced at zero field from relativistic electrons has a time constant of 45 ns probably due to the slow recombination of electrons and ions [139] (shown in Equation 3.3). However in the presence of an electric field this component is quenched [140]. With an applied field two photons are observed that are attributed to singlet and triplet states of the excited dimer that have decay times of $\sim$ 3 ns and $\sim$ 27 ns respectively. These decay times have been found to differ for different particle species due to the energy deposited. This difference can be utilised to discriminate between particle species using pulse shape analysis techniques, as was applied in the ZEPLIN-I experiment [89].

Ionisation

The Platzman Equation [141] describes the processors that occur in Xe when energy is deposited (E_0) from a particle.

$$E_0 = N_i E_i + N_{ex} E_{ex} + N_i \epsilon \tag{3.4}$$

where N_i is the number of electron-ion pairs of mean energy E_i, N_{ex} is the number of excited atoms of mean energy E_{ex} and ϵ is the average kinetic energy of the sub-electrons. For solid or liquid Xe Equation 3.4 can be re-written as;

$$\frac{W}{E_g} = \frac{E_i}{E_g} + \left(\frac{E_{ex}N_{ex}}{E_g N_i}\right) + \frac{\epsilon}{E_g} \tag{3.5}$$

where the W-value ($W = E_0/N_i$) is the average energy required to produce one electron-ion pair, and the band structure within liquid and solid Xe allow the use of E_g, the band gap energy (see Figure 3.1). The W-value for liquid Xe is 15.6 ± 0.3 eV where $E_g = 9.28$ [79]. However, as previously discussed, without the application of an electric field almost 100% of electron-ion pairs will recombine.

Secondary scintillation

In the ZEPLIN-III experiment the primary scintillation (denoted S1) is detected by the PMTs immersed in the liquid Xe. Under the application of an electric field some of the free electrons produced from the initial interaction are drifted towards the gas phase, where an electric field of 7.8 kV/cm is present. The field has to be larger in comparison to the liquid phase; this ensures good extraction and acceleration of the electrons. Within the gas phase, the ionising radiation is effectively amplified through a process called electroluminescence. In the presence of an electric field, electrons can gain sufficient kinetic energy to cause ionisation or excitation of atoms. If the electron is below the energy of ionisation then is will cause excitation of the Xe atoms and the eventual emission of VUV photons as shown below in Equation 3.6;

$$\begin{aligned} e + Xe &\rightarrow e + Xe^* \\ Xe^* + 2Xe &\rightarrow Xe_2^* + Xe \\ Xe_2^* &\rightarrow 2Xe + hv \end{aligned} \tag{3.6}$$

Another possible channel is through the excitation of free dimers, particularly in dense gases such as Xe, where;

$$e + Xe_2 \rightarrow e + Xe_2^*$$

$$Xe^* + Xe_2 \rightarrow Xe_2^* + Xe$$
$$Xe_2^* \rightarrow 2Xe + hv \tag{3.7}$$

At even greater densities other channels can become available which are discussed further in [78]. As a consequence of the acceleration of the free electrons and then emission of secondary electrons, an avalanche multiplication is observed. A signal proportional to the width and the initial electron extraction at the gas phase is then produced (denoted as S2).

The signals produced by each incident particle species have different S2/S1 ratios, where the time constant of the scintillation signal is affected by the charge collection. This enhances the ionisation signal at the expense of the scintillation signal. The large initial linear ionisation density of an alpha-particle signal would result in a relatively larger S1 compared to the S2. The energy loss (dE/dx) of a charged particle at high energies be described by the Bethe-Block equation. As the particle moves through the xenon it can interact with the xenon electrons, exciting or even ionising them. At higher energies, it has been observed that particles will lose most of their energy at the end of their range, following a relatively constant rate along their track prior to this point. This is because the interaction cross section for a charged particle ionising atoms in the medium increases with decreasing energy, as described by the Bethe-Bloch formula. This gives rise to a characteristic feature known as the Bragg peak. For low energy particles the Bethe-Block formula begins to break down when charge exchange between the particle and he absorber become important. The Bragg peak has yet to be observed at these energies therefore there is no general consensus on whether a low energy recoil should deposit a disproportionate amount of energy at the start or end of the track, or if it should be linear along the entire track.

For a gamma-ray interaction S2/S1 ratio is reversed. A less dense ionisation track is produced, making it easier for the electric field to separate out and drift electrons to the gas phase producing a relatively smaller S1 and larger S2. Figure 3.4 shows a typical neutron recoil event. There is an initial small primary pulse (S1) and a larger secondary pulse (S2). The S2/S1 ratio is calculated and this is used to discriminate against electron recoil induced events. Generally the S2/S1 ratio is lower by a factor ~ 2 for nuclear recoils compared to electron recoils. Further information on the analysis techniques used to extract a sensitivity limit

and determine the discrimination between neutron and electron recoils can be found in Section 3.3

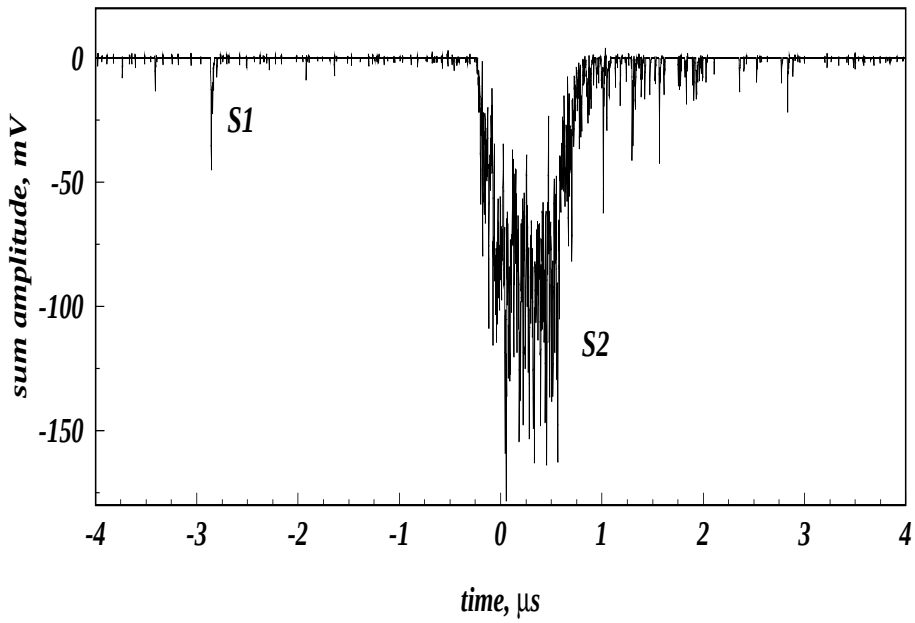

Figure 3.4: *A typical neutron induced event in ZEPLIN-III [72]. Two-phase technologies produce two signals, an S1 from the primary scintillation in the liquid Xe and an S2 due to electroluminescence from ionisation electrons that have been accelerated in the gaseous Xe phase.*

The ZEPLIN-III collaboration was able to achieve a gamma-ray rejection factor of 5×10^3 between 2-16 keVee by using two-phase technologies. The identification and removal of background using the above technique significantly improves the sensitivity of the detector. Once all non-WIMP events are identified and thus removed any remaining events could indicate the presence of a WIMP signal. It is also expected that WIMPs would produce recoil spectra similar to neutrons, therefore background reduction is extremely vital in the case of neutrons. The inclusion of a veto sensitive to internal and external neutrons would also improve particle discrimination (see Chapters 4, 5 and 6).

3.2.2 The ZEPLIN-III Detector

ZEPLIN-III can be described as a detector in three parts all working collectively, producing the optimum conditions for WIMP detection. The target vessel is at

the heart of ZEPLIN III, where particle interactions with the Xe target occur. The second component of ZEPLIN-III is the cooling system, which cools Xe to its liquid and gaseous states. LN_2 is used by means of an internal LN_2 reservoir located beneath the target vessel. The third component of ZEPLIN-III is its gas system which purifies and transfers liquid Xe to and from the target vessel.

Critical to the construction of any dark matter detector is the requirement for components to exhibit low levels of radio-impurities hence, all materials undergo radiological testing. Techniques for building components such as the target and vacuum vessels were also adapted to reduce the materials used in construction and therefore possible points of contamination. In the FSR the ZEPLIN-III photomultiplier tubes were the largest contribution to background. In the second science run (SSR), as part of the upgrade (including the veto) they will be replaced with up to 30× lower background PMTs.

3.2.3 The ZEPLIN-III Target Vessel

The liquefied and gaseous Xe target can be found within the target vessel. The target vessel is constructed from ultra-pure copper using electron beam welding to reduce the number of impurities being introduced. Figures 3.5 and 3.6 show the internal structure of ZEPLIN-III. Top centre of Figure 3.5 is the ZEPLIN-III PMT array which sits within the target vessel and liquid Xe (blue). The target vessel is positioned above the LN_2 reservoir which cools the Xe to a liquid state (the ZEPLIN-III cooling system is discussed in section 3.2.4). Surrounding the entire device is the vacuum vessel, also built using ultra pure copper. Its main purpose is to create vacuum conditions within the device.

3.2.3.1 The Photomultiplier Tubes

The ZEPLIN-III PMT array is positioned within the target vessel; and is shown in Figure 3.7. The array consists of 31 PMTs and is immersed in the liquid phase of the Xe within the target vessel. The PMTs look up towards an anode mirror positioned above the 5 mm Xe gas gap. VUV light emitted from scintillation processors can be reflected back into the target by the highly polished anode mirror to be observed by the PMTs.

Each PMT within the array includes 15 separate pins for power and signal retrieval. The large numbers of connections required is itself a concern, because

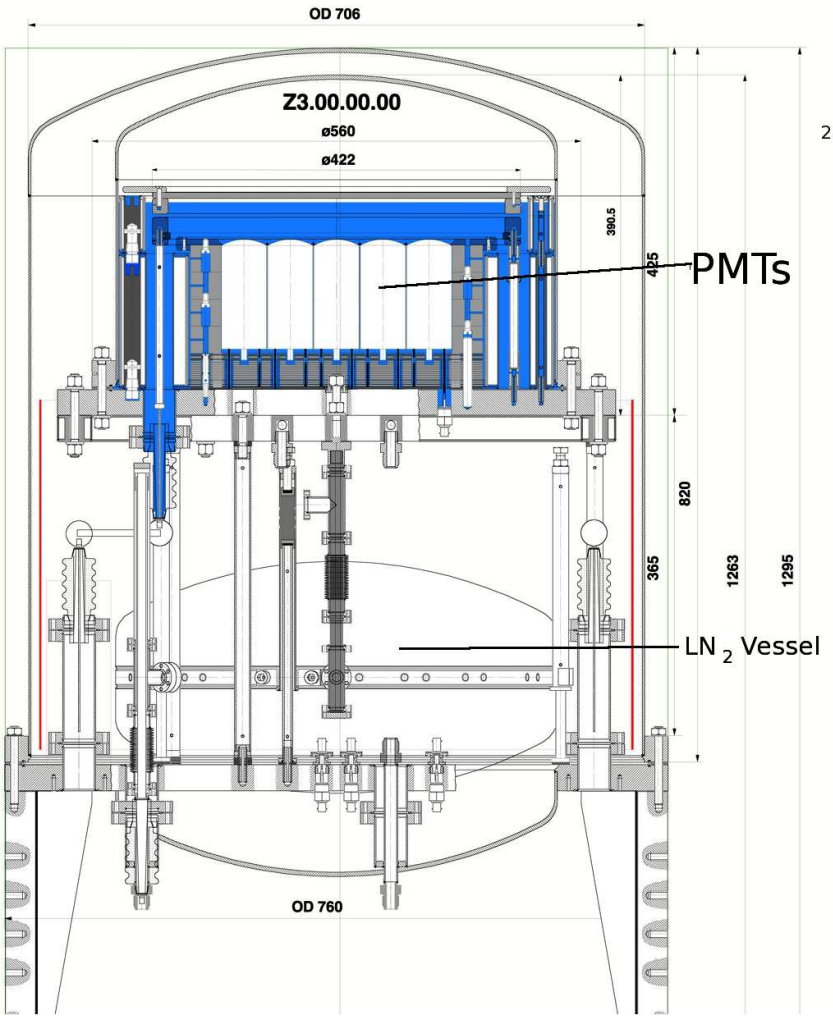

Figure 3.5: *A CAD drawing of the ZEPLIN-III detector showing details of its inner components. Top centre is the PMT array surrounded by the target vessel. Below this is the LN_2 reservoir used for detector cooling.*

Figure 3.6: *The internal structure of the ZEPLIN-III device. The top dome object is the target vessel. Below this is LN_2 reservoir.*

Figure 3.7: *The ZEPLIN-III PMT array. The array include 31 PMTs positioned within the ZEPLIN-III target vessel and immersed in liquid Xe.*

it can lead to an increase in background from the wires and connectors. Therefore a method was devised to power the entire PMT array through a common voltage supply and dynode distribution system, reducing the total number of feed-throughs to 47. To do this, 16 2 mm thick copper plates, separated by quartz spacers were positioned below the array. Only certain PMT pins connect to particular copper plates corresponding to a particular voltage. The anode connection is made using a generic coaxial connector.

Figure 3.8: *The complete construction of the ZEPLIN-III detector. The majority of components cannot be viewed due to the vacuum vessel dome covering these. At the bottom of the figure are pipes which connect to the LN_2 vessel and other pipes that enter the target vessel Xe filling.*

3.2.3.2 Operation at high fields

Section 3.2.1 discussed the requirement for electric fields to suppress recombination of electrons and ions, and to facilitate drift of electrons from the liquid Xe phase to the gaseous phase in order to obtain a secondary signal (S2). Therefore a high extraction field is present throughout the target volume. The electric field is supplied across the anode mirror and a wire plane (cathode grid) positioned

40 mm below the anode mirror in the Xe liquid phase. A second wire grid (PMT screen) is also positioned above the PMT grid and below the cathode grid. This creates a region where the internal PMT fields can be separated from the influence of the high electric field throughout the Xe and it also serves to prevent S2 signals from gamma-ray interactions near the PMTs, below the screen (these gamma-rays are emitted by the U, Th and K in the PMTs). The electric fields present throughout the target volume serve three crucial purposes. Within the liquid phase is enables free electrons to be drifted from an interaction site to the gas phase for extraction. At the liquid/gas interface a higher electric field is required to prevent electron trapping. Once in the gas phase the electrons are then accelerated by the electric field where electroluminescence is produced (S2). The electric field was run continuously throughout the FSR, attaining field strengths of 3.9 kV/cm and 7.8 kV/cm in the liquid and gas phase respectively. The different field strengths are achieved due to the differing dielectric constants of Xe liquid and gas.

Much has already been discussed about liquid and gaseous Xe serving as a target medium. However the melting point as STP for Xe is 161.4 K thus cryogenic technologies are necessary.

3.2.4 Cooling System

The ZEPLIN-III cooling system uses an internal LN_2 reservoir, located beneath the target vessel. The LN_2 reservoir is a dome shaped container (displayed in Figures 3.5 and 3.6) and is a completely separate system to the Xe target vessel. To cool the Xe, the reservoir is filled with LN_2 by an external dewar on a daily basis throughout detector operation. Two thermal links are connected from the cryogenic reservoir to the target vessel. The first of the thermal links are attached to the underside of the target vessel, with its other end situated in the LN_2, in the reservoir. The second link provides contact between the nitrogen reservoir and a cooling flange on the underside of the target vessel. During operation 'boil-off' gas from LN_2 is utilised to provide cooling.

There are four pipes within the reservoir, two are open to the top of the reservoir with one serving as the delivery pipe. The other two pipes are connected to the thermal links and are fitted with control valves that regulate pressure and flow rate. The valves are operated using an external temperature control

unit that monitors temperature and pressure within the vessel; increasing or decreasing the N_2 vapour flow based on the input set-points. Heaters are also available if necessary. Stable cooling throughout detector operation is therefore maintained.

3.2.5 Gas system

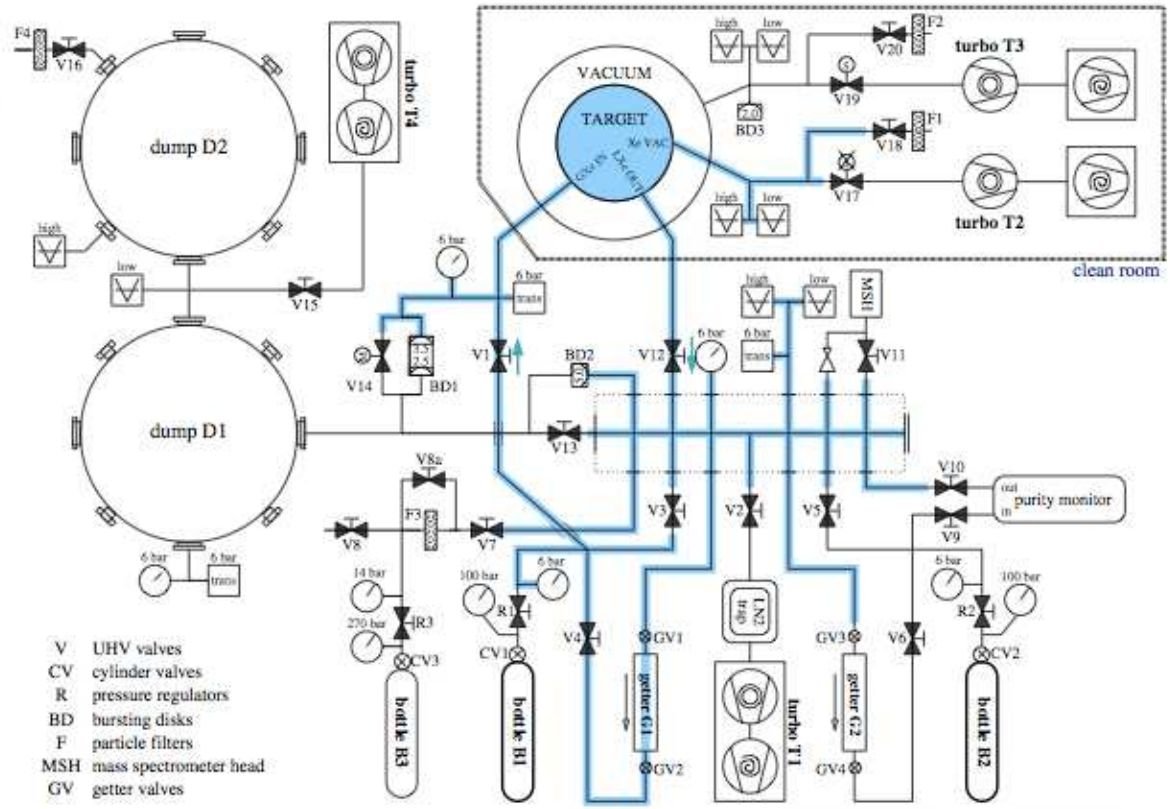

Figure 3.9: *Schematic of the ZEPLIN-III gas system during the FSR. The SSR uses one less dump and includes a hot getter.*

The ZEPLIN-III gas system serves multiple purposes; Firstly for Xe purification and secondly, for the movement of the Xe gas in out out of the target vessel. A schematic diagram of the ZEPLIN-III gas system (as in the FSR) is shown in Figure 3.9. The Xe is typically stored in either of the two bottles (bottles $B1$ and $B2$ in Figure 3.9) when not in the target vessel. The Xe can be purified by cryo-pumping between the bottles $B1$ and $B2$ through the SAES getters [142]

(getter G1 and G2 in Figure 3.9). The getters can remove impurities such as N_2O, O_2 and CO_2, which can severely limit the purity of the Xe and thus the S2 signals obtained from particle interactions (see section 3.3 for more information). Prior to operation of the detector, the purity can be tested using a device known as the electron lifetime monitor (ELM). The ELM can be attached to dedicated pipes shown in Figure 3.9. The ELM can only be used when the Xe is not in the target volume. Once in the target volume the Xe may be monitored by taking calibration data which is discussed in further detail in Section 3.3.

Other attributes of the ZEPLIN-III gas system include the ability to obtain samples of the Xe through pumping to bottle B3, which can be removed from the entire system, and a number of safety devices in the event of target failure. If the pressure in the target rises too rapidly, a series of burst disks from the target to the dumps (labelled Dump D1 and D2 in Figure 3.9) are in place. The Xe gas can then be 'released' into these dumps where it will can be reclaimed at a later time.

3.2.6 Slow Control

Monitoring of the system throughout detector operation is achieved using the 'slow control' (SC) software. SC monitors pressures, voltages and temperatures relaying them to the user. SC also alerts users when pressures, temperatures etc. rise or fall outside of safe operating parameters. There are pressure and temperature sensors positioned throughout the system monitoring everything from the target vessel, LN_2 reservoir, the gas system and the outer target jacket. The cathode, anode and PMT voltages are also monitored. If the PMT current exceeds safe operating levels they will automatically switch off, preventing any discharge or damage. The PMTs can then be set to automatically ramp back up after a specified time period.

The first priority of SC is the safety of the detector; however all information relating to the activities of the system is continuously recorded. These data can then be used in the data analysis programme; for example, when the PMTs tripped during the FSR the slow control data records the time of the failure. All data files affected by this were subsequently removed from the WIMP data. The pressure of the system was also monitored and analysed to determine whether

a correction to the WIMP data was necessary. In the FSR the variation in pressure proved too insignificant for any correction to be applied.

3.2.7 Data Acquisition System

All 31 PMT signals were input to an dual dynamic range data acquisition system (DAQ). Each PMT signal is sent to both Low sensitivity (LS) and high sensitivity (HS) channels. The HS amplify the signal by a factor of $\times 10$. This provided high and low sensitivity readouts to enable observation of small pulses of only a few photoelectrons and also large secondary pulses without saturation. The 62 channels were input into 8-bit ACQIRIS digitisers and sampled at 500 MS/s.

The trigger on ZEPLIN-III works by using the signals output from the HS. These signals pass through to a summer, creating one signal input into a discriminator. The threshold of the discriminator is set to reduce noise. If the summed signal goes above threshold the discriminator sends a signal to the trigger inputs of the ACQIRIS and the DAQ triggers. Once the DAQ has triggered it records the event introducing a period of dead time. Nuclear recoil events were triggered using the S2 signal for energies of $S1 = 40$ keVee. Here the trigger threshold was set at ~ 0.2 keV for electron recoils or ~ 11 ionisation electrons.

3.2.8 Shielding

To reduce background within the ZEPLIN-III detector it has been situated underground in a mine and constructed with extremely radio pure materials. However, further shielding is required around the ZEPLIN-III detector to reduce the neutron and gamma-ray flux emanating from the laboratory walls (60, 130 ppb U and Th and 1130 ppm K [143]). In the FSR the ZEPLIN-III detector was surrounded with 30 cm thick polypropylene shielding and 20 cm thick lead shielding, providing 10^5 attenuation factors for both external gamma-rays and neutrons. In addition to this, further shielding was positioned at the base of ZEPLIN-III; this included a 10 cm thick copper plate and individual sheets of polypropylene sheet with a total thickness of 30 cm.

For the second science run (SSR) more complex shielding has been designed. This is the primary subject of this thesis and is discussed in later in Chapter's 4, 5 and 6. The remainder of this chapter will discuss the FSR results and analysis.

3.3 The First Science Run of ZEPLIN-III

The aim of any dark matter detector is to observe a positive WIMP signal. To ensure observation of a true WIMP signature, data has to undergo a rigorous analysis procedure, including the application of strict data selection criteria. If after data analysis, a WIMP signal has not been observed, all is not lost. The detector can then be seen as constraining the allowed theoretical parameter space by producing sensitivity limits based on these data. This section discusses the data analysis performed for the FSR.

3.3.1 WIMP Search Data

WIMP-search data were obtained for 83 days of operation throughout the ZEPLIN-III first science run (FSR). With 84% live time this equates to 847 kg·days of raw data. In addition to the WIMP-search data numerous calibration data-sets were also obtained. ^{137}Cs and AmBe data were acquired before and after the FSR to examine the electron and nuclear recoil response. Daily calibration data were also taken with ^{57}Co to set energy scales, check the Xe purity and the detector tilt. Initially, 10% of the total FSR WIMP-search data were used to develop the data analysis and selection criteria. Data selection was performed with the implementation of the 'golden code' software that retains data meeting the WIMP-search criteria (discussed in section 3.3.3.2). The aim of the data-analysis is to define boundaries for a WIMP search box, by establishing the extent of nuclear recoil signals and the level of the electron-recoil background. Within this box one hopes to observe events, that on further analysis are recognised to be successful WIMP candidates. Even if events are not observed, defining such a WIMP search area and attaining good discrimination between neutrons and gamma-rays can push the level of observed parameter space for a meaningful null result.

3.3.2 Calibration of WIMP Search Data

To calibrate the WIMP-search data, AmBe, ^{137}Cs and ^{57}Co data-runs were acquired. These were used to ascertain the performance of the ZEPLIN-III detector to gamma-rays and neutrons. The discussion here is an overview, further detail can be found in reference [72].

3.3.2.1 ^{57}Co Calibration Data

^{57}Co is an isotope that emits 122 keV and 136 keV gamma-rays with intensities of 85.6% and 10.7% respectively. ^{57}Co calibrations were performed daily throughout the FSR and used for the following:

1. To monitor any movement of the detector (the tilt effects the S2 width by changing the size of the gas gap).
2. To normalise the measured response from each PMT (also known as 'flat fielding' the PMT array).
3. To monitor the purity of the Xe.
4. Determination of any variation in the average light and ionisation yields by fitting to the areas of the S1 and S2 pulse spectra and setting energy scales.

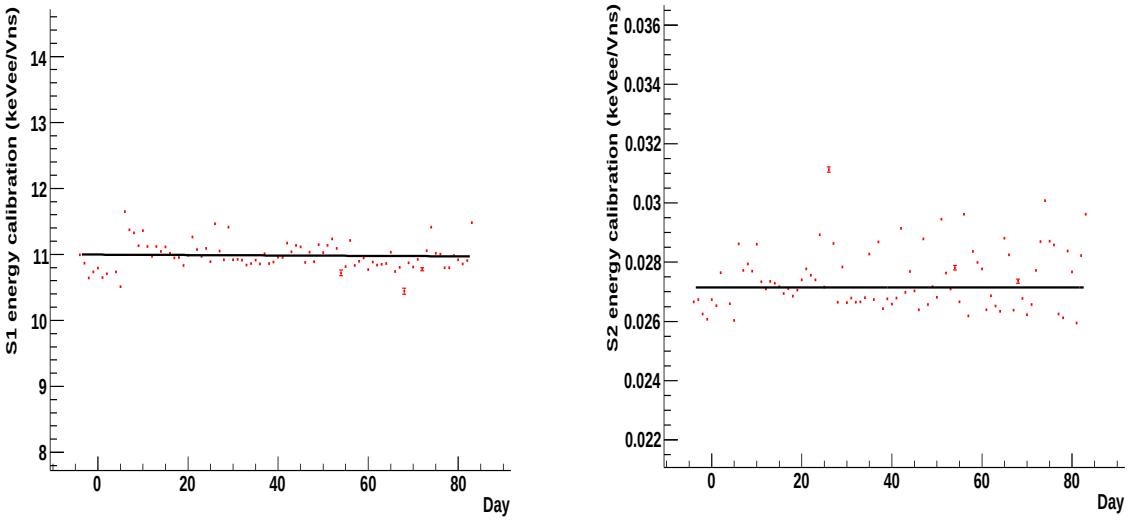

Figure 3.10: *Variation in the S1 and S2 energy calibration during the FSR. Two graphs are shown, the left graph is the energy calibration for an S1 peak and right for the S2 peaks as a function of FSR day. A straight line is fitted to both data sets for reference.*

Point 3 will be covered later in this chapter. The evolution of the tilt (movement of the detector due to geological factors within the mine environment) was found

to be negligible making correction unnecessary (having levelled the detector prior to the FSR); the same is true for point 4. Here the entire FSR ^{57}Co data set has been fitted to ascertain the S1 and S2 energy calibration (given in keVee/Vns), by fitting to the 122 keV and 136 keV gamma-ray peaks in these data. Although there is an obvious deviation from the reference line (standard deviation of data in the left plot from Figure 3.10 is 0.21; for the right plot it is 0.00103) the scale of the deviation was insufficient to necessitate a daily correction, therefore mean values for the S1 and S2 energy calibration of the entire WIMP data were used. This is shown in Figure 3.10.

Another important usage of ^{57}Co calibration data is in determining the electronic recoil energy scale. This is characterised by the parameter ℓ_{eff}, which was discussed in detail in Chapter 2.27.

3.3.2.2 AmBe and ^{137}Cs Calibration Data

The response of ZEPLIN-III to neutrons is measured using an AmBe calibration source ($^{241}Am \rightarrow {}^{237}Np + \alpha$, then $\alpha + {}^{9}Be \rightarrow {}^{12}C + n$). Figure 3.11 displays a scatter-plot of log10(S2/S1) as a function of energy in keVee. Two separate bands can be observed in the plot. The first is situated between 2-60 keVee and has relatively small values of S2/S1. This can be attributed to elastic recoils. The second band between energies of 40-70 keVee, and having larger S2/S1 values is due to inelastic scattering of neutrons from the ^{129}Xe nuclei. The remainder of the events populating the plot are due to gamma-ray interactions. The red and blue lines were produced by slicing these data into 1 keVee bin histograms of the energy calibrated S2area/S1area, and then fitting the nuclear elastic band with a log-normal distribution. The mean of the fitting procedure is displayed in red, whilst the blue line represents the mean $\pm 1\sigma$.

The response of ZEPLIN-III to gamma-rays was established using a ^{137}Cs source. By examining Compton scattered events from the ^{137}Cs source, it is possible to probe down to energies of $\sim$ 2 keVee. The ^{137}Cs data were sliced in 1 keVee bins and fitted using a skew-Gaussian function. The low S2/S1 tail of this function could then be used to estimate the number of electron-recoils leaking into the WIMP search area. However due to the ^{137}Cs data not truly mimicking the WIMP data accurately [72] an overestimate of WIMP events in the box resulted. As a fall back measure, the FSR WIMP data was used to

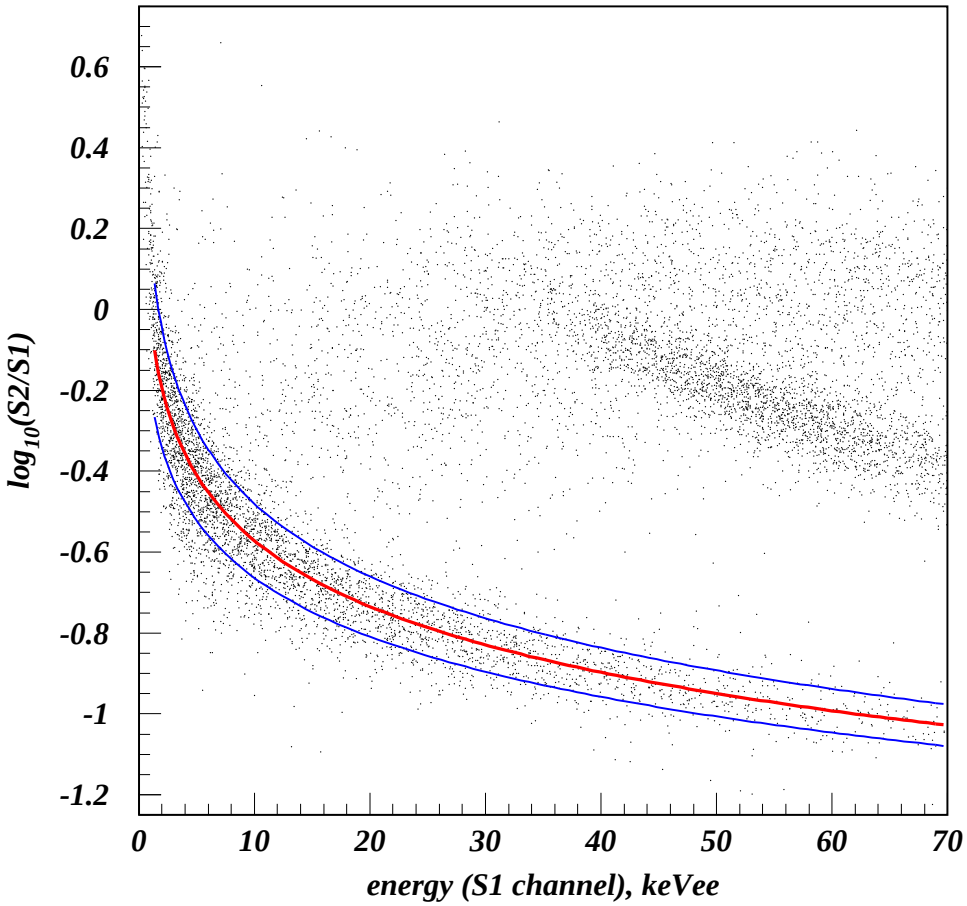

Figure 3.11: *AmBe calibration scatter plot detailing the response from the ZEPLIN-III detector. Log_{10}(S2area/S1area) is plotted against electron-equivalent energy using S1 signals calibrated by ^{57}Co. The population >40 keVee, and larger values of S2/S1 is due to inelastic scattering of neutrons from the ^{129}Xe nuclei. The red and blue lines are the mean and sigma fits of 1 keVee bins to the elastic recoil band [72].*

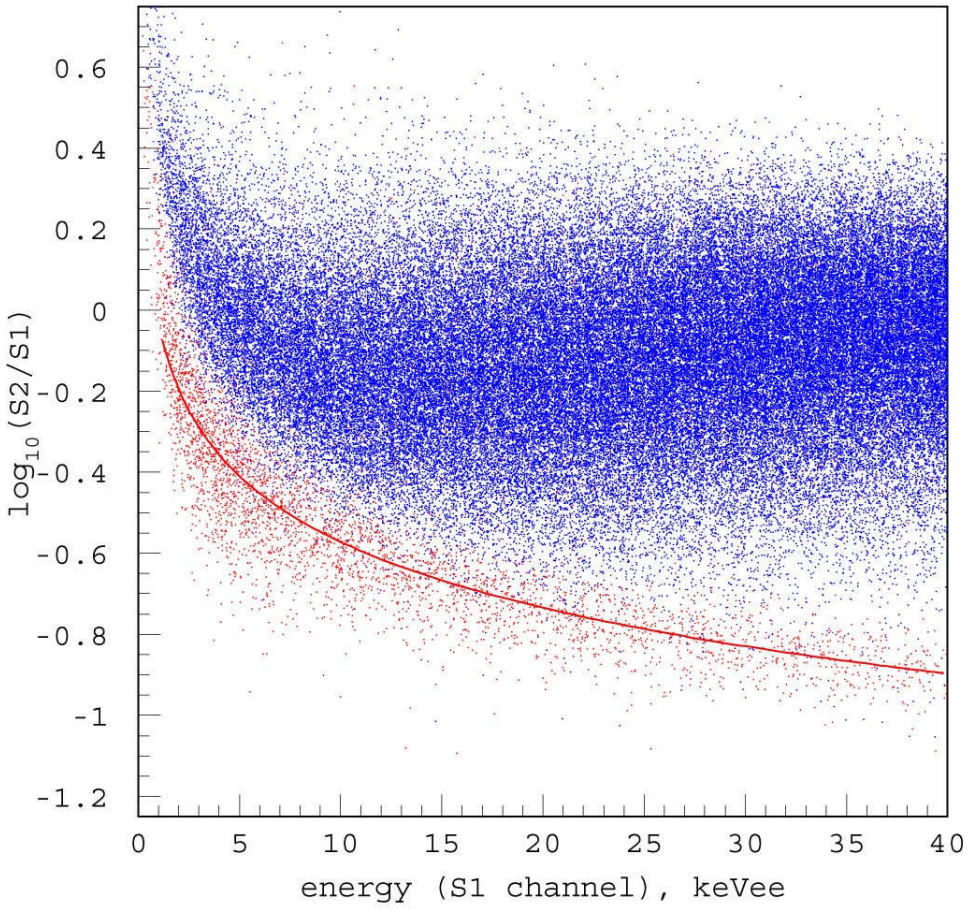

Figure 3.12: *The response of ZEPLIN-III to the irradiation of AmBe (red) and* ^{137}*Cs calibration sources [72].*

predict the expected number of electron-recoil events leaking into the WIMP search box.

Using both the AmBe and ^{137}Cs calibration datasets, the ability of ZEPLIN-III to discriminate between electron and neutron-recoils was measured. This separation between the populations is the key factor used to define the nuclear recoil search box for potential WIMP events. The WIMP search box was defined as $(2 < Energy < 16)$ keVee and $(\mu n\text{-}2\sigma) < log10(S2/S1) < \mu$n, where μn is the energy dependent mean of the nuclear recoils; this definition results in an acceptance of 47.7%. The fraction of gamma-rays that fall within this region implies an average gamma-ray rejection factor of 5×10^3, as illustrated in Figure 3.12, where the blue data points are gamma-rays emitted from the ^{137}Cs data and the red data points are attributed to neutron-recoil events from the AmBe data.

To define the WIMP search box and prepare the FSR data for analysis two programs were used. These were ZE3RA which identifies pulses using peak finding algorithms and the ZEPLIN-III 'golden code' which applies fiducial and multiplicity cuts and corrections to the data.

3.3.3 Data Analysis Procedure

The process of deducing whether the raw recorded data indicates the presence of galactic dark matter requires several phases of analysis. The first two phases are, (i) identification of S1 and S2 signals from the raw waveforms; (ii) determination of whether the event as a whole is consistent with what would be expected from a WIMP interaction. For this, two analysis programmes have been created, ZE3RA and the 'golden code'.

3.3.3.1 ZE3RA

Initially, raw data files were input into a program called ZE3RA (**ZE**PLIN **3** **R**eduction **A**nalysis). ZE3RA reads the raw data and identifies pulses with specific pulse finding algorithms. ZE3RA then defines the pulses as either an S1 type or an S2 type based on their pulse widths. Scintillation pulses (S1) have a much shorter time constant than electroluminescence pulses (S2) making it possible to discriminate between the two. ZE3RA also outputs other characteristics of the S1 and S2 pulses including pulse amplitude and area, decay time of a

waveform and the time when an event was recorded. The main use of ZE3RA is in characterisation of events, it does not make selection cuts or apply corrections to the data, this is left to the second stage of analysis using a programme known as the 'golden code'.

3.3.3.2 The ZEPLIN-III golden code.

The 'golden code' has been designed to ensure that events that would meet the WIMP search criteria are retained for analysis and output in the form of ntuples. The main criteria for positive WIMP candidates is that an event should contain only one S1 signal and one S2 signal. Multiple scatters may validly be rejected due to the low probability that a WIMP would interact more than once with the Xe target. Events are also removed if inconsistencies are present in their waveforms or the ZEPLIN-III PMTs had tripped during data acquisition. The golden code also corrects the daily background data for such things as pressure changes in the detector and changes in the electron lifetime. These types of variations cannot be controlled externally during data acquisition; however such changes can be monitored throughout the science run and later corrected in software.

The development of the golden code was a rigorous, iterative procedure. It was initially tested on 10% of the FSR to optimise the code for identification of useful events. The author's contribution to the development of the golden code involved profiling the electron lifetime over the FSR and creating a correction to be applied to the entire FSR data.

3.4 Electron Lifetime

The purity of Xe plays a significant role in the operation of a Xe detector and for this reason the purity was monitored throughout the FSR. Impurities can originate from a number of sources and much is done to prevent their presence, including the choices of materials used for detector construction and various methods of Xe purification. As already discussed in this chapter, the light and charge produced by an ionising particle are used to characterise interaction events in ZEPLIN-III. If significant quantities of impurities are present, the amount of charge or light collected can be reduced. The impurities discussed include electronegative molecules that trap electrons and prevent them from

drifting to the gas phase of a two-phase detector. If this happens the S2 signal will be significantly reduced if not completely lost. Much work is performed prior to running a detector to ensure high levels of purity (impurity concentrations $<$ 1 ppb [79] are required); this can often be a limiting factor in detector sensitivity, as poor purity will result in the deeper volume of the detector becoming invisible.

Throughout the FSR ^{57}Co data were taken to monitor the electron lifetime. It was observed that the electron lifetime in the Xe improved over time. This was not expected, indeed many experiments such as [99; 144] expecting the purity to worsen, employ active recirculation to improve the purity of the Xe through the duration of the science run. In ZEPLIN-III the Xe was purified prior to the FSR using gas-phase purification through external 'getters', and was not actively purified during the FSR. It was expected that either the electron lifetime would remain constant or reduce over time, as stated, but it appeared to improve. Regardless of an improvement or worsening of the lifetime, that the purity is changing implies that the number of electrons recovered from events has changed during the FSR. A correction to account for this change was therefore necessary. The author was responsible for identifying and implementing the required algorithms.

3.4.1 Electron Lifetime Theory

The electron lifetime can be described as the average time period in which an electron remains free prior to attachment to an electronegative impurity within the detector. Interactions between a free electron and an electronegative ion can result in the following scenarios [78];

Radiative attachment

$$e + AB \rightarrow AB^- + h\nu \tag{3.8}$$

Dissociative attachment

$$\begin{aligned} e + AB \rightarrow AB^* + e \rightarrow A^+ + B^- + e \\ e + AB \rightarrow AB^- \rightarrow A + B^- \end{aligned} \tag{3.9}$$

Three body attachment

$$\begin{aligned} e + AB \rightarrow (AB^-)^* \\ (AB^-)^* + X \rightarrow A^+B^- + X \end{aligned} \tag{3.10}$$

where A and B symbolise the electronegative ions, examples of which include CO_2 and N_2O. Since interaction 3.8 has a small cross section it does not contribute significantly to the reduction in the electron lifetimes. Reaction 3.9 shows how an electron can be captured by non-electronegative particles resulting in the production of electronegative molecules. Equation 3.10 describes the energy released when an electron is attached to a neutral atom or molecule, where X in this case would be Xe. The energy released due to the interaction given in Equation 3.10 is also known as the electron affinity. In all scenarios capture of an electron by an impurity results in the formation of negative ions.

The lifetime of an electron can be modelled as a survival probability, i.e.,

$$N(t) = N_0 exp(-t/\tau) \tag{3.11}$$

where N_0 is the number of original electrons and $N(t)$ is the number of free electrons that remain in the Xe target after a time t. τ, the mean electron lifetime before capture, is related to the number of impurities within the target by,

$$\tau = \frac{1}{\sum k_s n_s} \tag{3.12}$$

where k_s is the electron capture cross section for different impurities and n_s is the concentration of the various impurities. A more useful description of the electron capture can be described as the attenuation drift length L, given by;

$$L = v_d \tau \tag{3.13}$$

where v_d is the electron drift velocity. This quantity is determined by looking at the difference between the time of observation of the S1 and S2 signal as a fraction of depth. Knowing the length of the Xe target, the electron lifetime can then be determined.

Changes in the electron lifetime effect the S2 signal, which relies entirely on free electrons produced at the particle initial interaction site. With the application of an electric field, these electrons are drifted through the liquid phase to the gas phase. If impurities are present within the detector volume, many of these electrons can be captured before reaching the gas gap. The size of the S2 signal will therefore be significantly effected, hence the requirement

for a correction within the golden code to normalise and factor out the time evolution.

3.4.2 Daily Evolution of the Electron Life-time

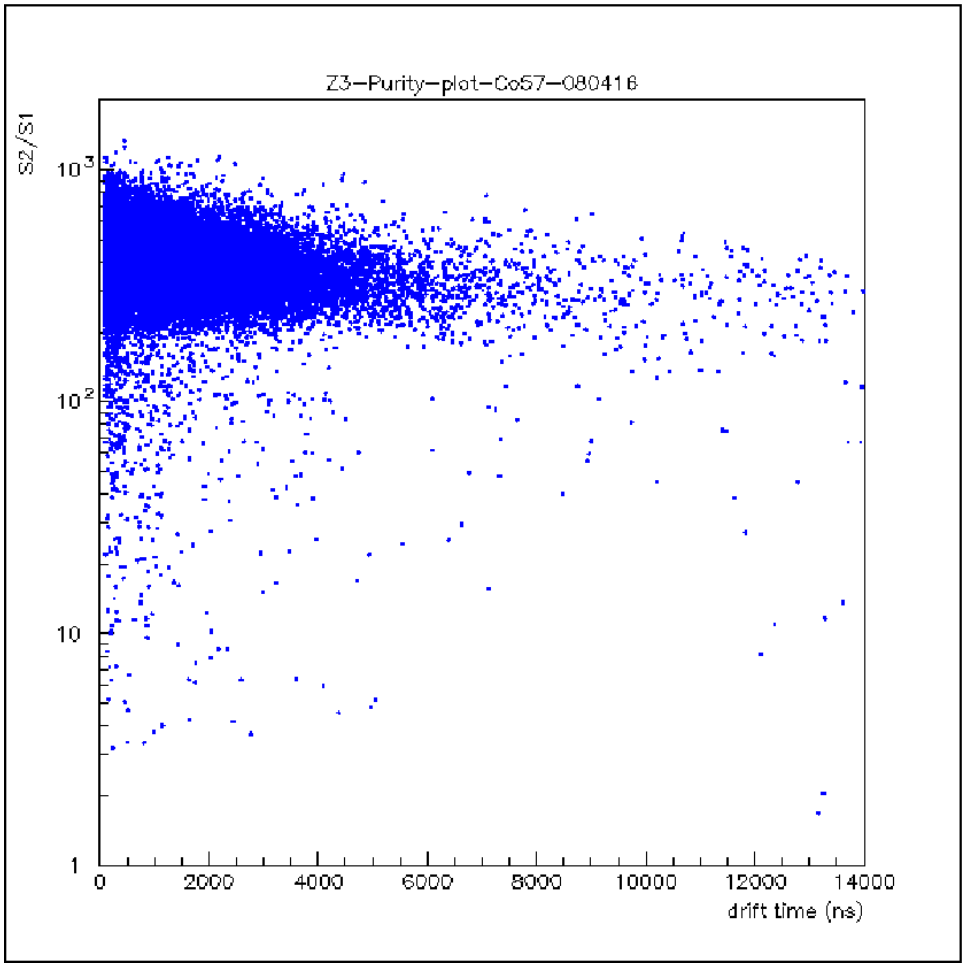

Figure 3.13: *$Log_{10}(S2/S1)$ versus drift time for ^{57}Co calibration data. Higher drift times indicate a reduction in the S2 signal size.*

The electron lifetime in the Xe target was determined using ^{57}Co calibration data. Figure 3.13 is a plot of $Log_{10}(S2/S1)$ versus electron drift-time ($dtime$), where S2 and S1 are the energy calibrated areas of the S1 and S2 pulses. The area of both the S1 and S2 signals and electron drift-time are all output by the golden code. The drift time($dtime$) is the time difference between an observed S1 (at time $S1time$) and S2 (at time $S2time$) signal associated with an event

i.e. $dtime = S2time - S1time$. More simply, it is the time for a liberated electron from the site of primary scintillation (due to an electron/nuclear recoil event) to move to the gas phase of the detector, where the S2 signal is observed via electroluminescence. The ratio of the primary to secondary signal areas is dependent on the ionisation density of the track i.e. dE/dX, thus enabling discrimination between incident particle types. Here the logged ratio between the secondary signal ($S2$) and the primary signal ($S1$) is used.

Figure 3.13 shows data from events occurring within the ZEPLIN-III volume due to the irradiation of a ^{57}Co source. The downward trend of the blue data-points shown in Figure 3.13 indicates a reduction in the size of the S2 signal observed with increased depth. For corrected electron lifetime S2 signals, such a downward slope would not be observed.

To obtain the electron lifetime for a particular day the data displayed in Figure 3.13 were sliced into one-dimensional histograms of number of events versus $Log_{10}(S2/S1)$, for various drift-time ranges. Each slice was then fitted with a Gaussian function, from which the mean is obtained. Logging the data is the equivalent of fitting a Log-normal distribution (chosen due to its excellent representation of the data). Figure 3.14 displays an example of the slicing and fitting procedure for the ^{57}Co calibration data-set obtained on April 16th, 2008. Most fits are reasonable until the drift-time extends beyond 6000 ns, where there the statistics become poor. Each data range was fitted to twice. The first fit used an estimate of the fit range whilst the second fit computed a more suitable fit range based on output fit parameters of the first fit. Although the variation between the mean values obtained by the Gaussian fit is small at lower drift times (0.004% difference between the means values) this difference increases at higher drift times when the statistics are reduced (0.2% difference between the mean values). Due to the large volume of data the fitting was automated, using this multiple fitting technique ensured that data were fitted as accurately as possible, particularly at higher drift times when there were lower statistics.

The purity analysis has been conducted on data that successfully passed through the golden code, i.e. all signals were consistent with one S1 and one S2 event. This ensured that only high quality events were being analysed. However, although the statistics would be reduced as a result of this, there are other benefits to this process. Any data that was taken before and after the PMTs had tripped would have been removed, also all data would be energy calibrated

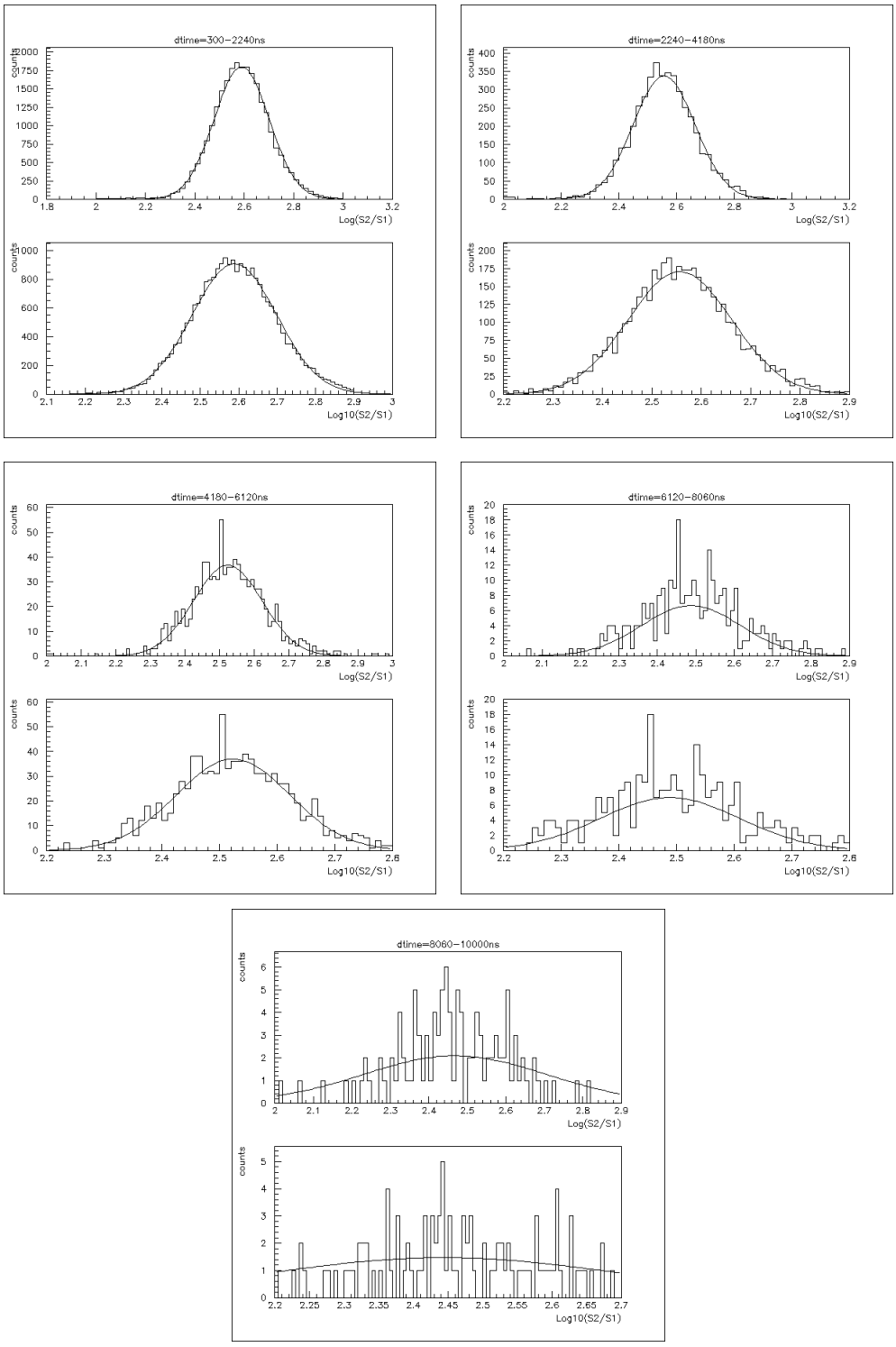

Figure 3.14: *Figure 3.13 has been sliced into 1-d histograms of* $Log_{10}(S2/S1)$ *for different drift time ranges. Each* $Log_{10}(S2/S1)$ *histogram for a drift time range is fitted twice with a Gaussian. The first fit uses an estimate for the fit range (x-axis) whilst the second fit uses the parameters obtained from the first fit to fit to a more accurate range in the x axis. The mean from each fit is used to calculate the electron lifetime. For drift times* $\geq 6000ns$ *there is less data, hence a poorer fit with observed.*

and 'flat fielded' using this code. Data is also output in a convenient format for plotting. If any additional cuts were required to the data this can be applied later, in analysis. The purity analysis imposed a further cut on the data beyond those imposed in the golden code; only events with energy depositions of $<$ 200 keVee were retained.

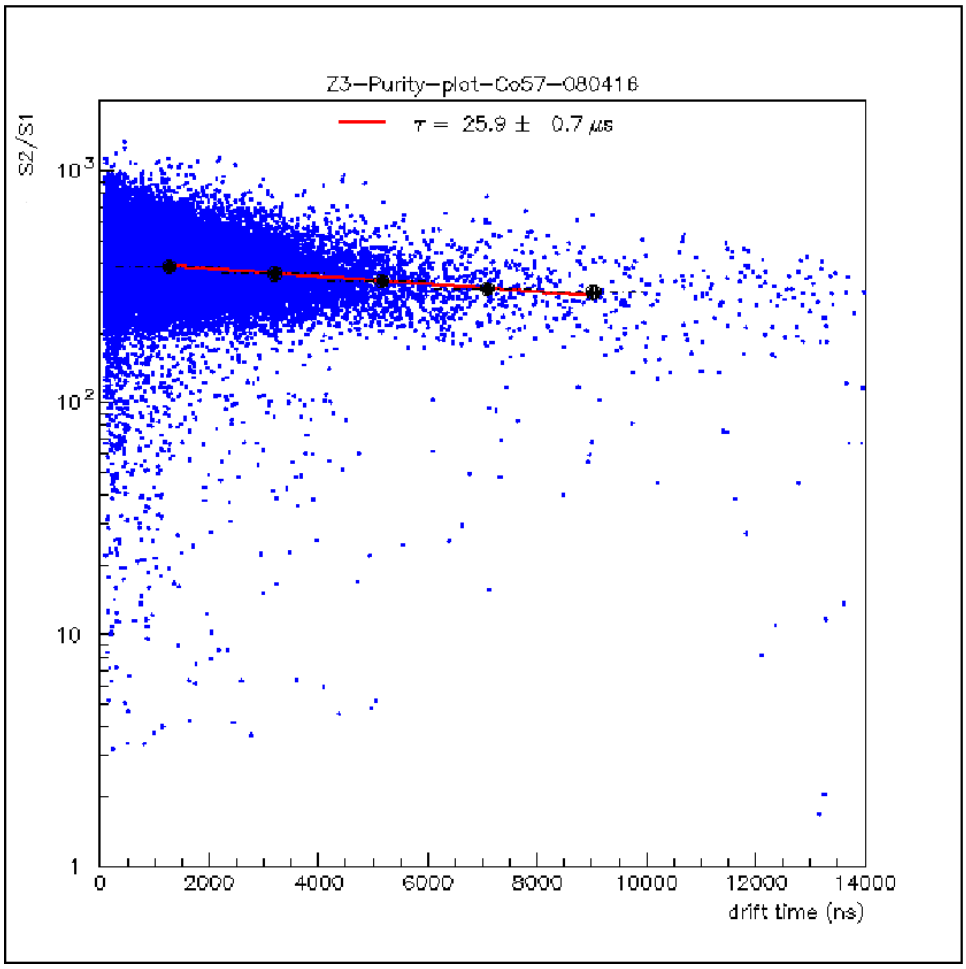

Figure 3.15: *Fitted electron lifetime data, produced using a* ^{57}Co *source. The black data points were obtained using the technique displayed in Figure 3.14. The data is fitted with the exponential function* $exp(p1 + p2 \cdot x)$.

Results from the fitting of the sliced data are shown in Figure 3.15. The mean values obtained from the one-dimensional histogram fits are shown in black. These mean values are fitted with an exponential ($exp(p1 + p2 \cdot x)$), shown in red so as to extract their dependence as a function of drift time. The

electron life-time (τ) is determined from the slope in the fit (i.e. $p2$), where $\tau = -1/p2$.

3.4.2.1 Improving the Analysis

It is obvious that slicing and fitting to data at higher drift times becomes more difficult due to poorer statistics, so the analysis was improved by concentrating on the $300 - 6000$ ns drift times only. The energy range was also tightened to only retain events between 100-150 keV. This is reasonable since ^{57}Co emits 122 keV and 136 keV gamma-rays. Figures 3.17 and 3.16 show the improved fits and a slightly higher purity, corresponding to a mean lifetime, of $\tau = 26.2 \pm 1.0 \mu s$ compared to the original value of $\tau = 25.9 \pm 0.7 \mu s$. Results are consistent (within errors), which is expected since the majority of gamma-rays originate from the ^{57}Co source (although the application of strict energy cuts may have reduced the impact of background gamma-rays within the data set resulting in a biased electron lifetime value.)

3.4.2.2 Creating a Historical Electron Lifetime Profiled for the FSR

All ^{57}Co daily calibration data from the entire FSR were analysed using the above technique. Figure 3.18 displays a small sample of analysed ^{57}Co data sets for six days from April 18th to April 28th 2008. Even from this small sample it is obvious that the electron lifetime is increasing over time, therefore a simple correction was devised in order to correct the S2 signal in the FSR WIMP data, based on the day the background data was obtained.

The correction was determined by fitting to all electron lifetime results, as a function of day in the FSR. Figure 3.19 shows these data with the following fitting function applied;

$$\tau = p0 \times exp(day \cdot p1) \tag{3.14}$$

where τ is the electron lifetime as a function of FSR day, with the parameters of the fitting routine $p0$ and $p1$. The positive gradient of these data indicates that the purity of the Xe had improved during the FSR.

Equation 3.14 is based purely on ^{57}Co data, in an energy range of 100-150 keV; however the energy regime we are interested for WIMP searches is lower, at 0-40 keV. If the electron lifetime is energy dependent, an energy correction need also be applied.

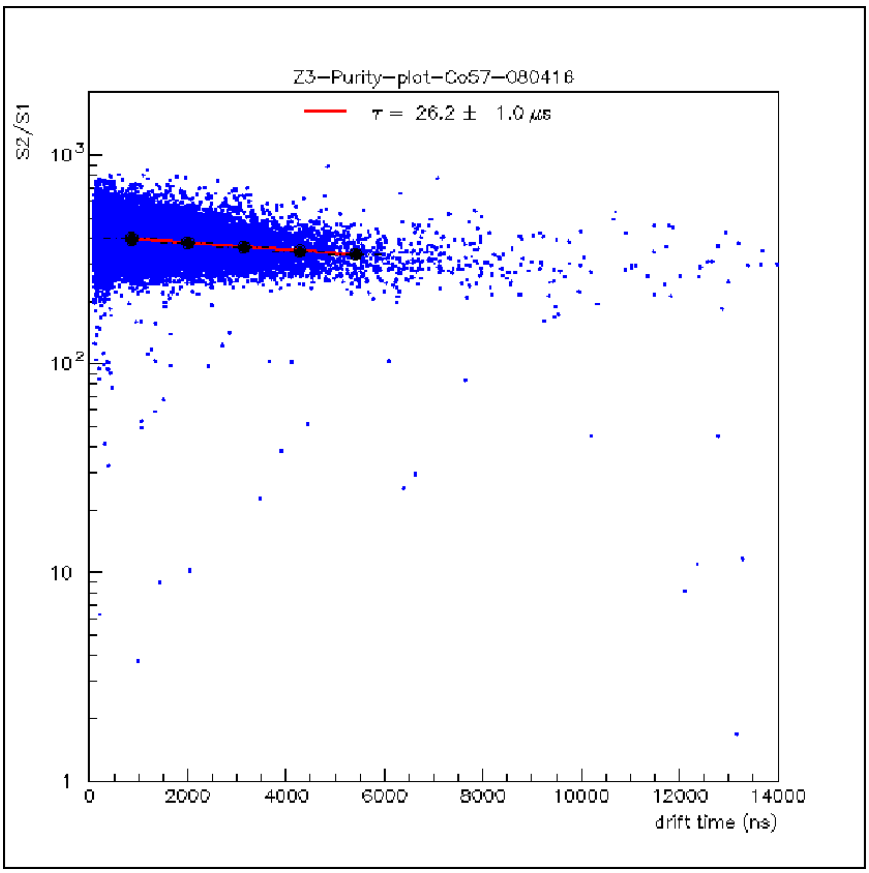

Figure 3.16: *Fitted electron lifetime data, with tighter energy and drift time cuts. The black data points were obtained using the technique displayed in Figure 3.14. The data is fitted with the exponential function* $exp(p1 + p2 \cdot x)$.

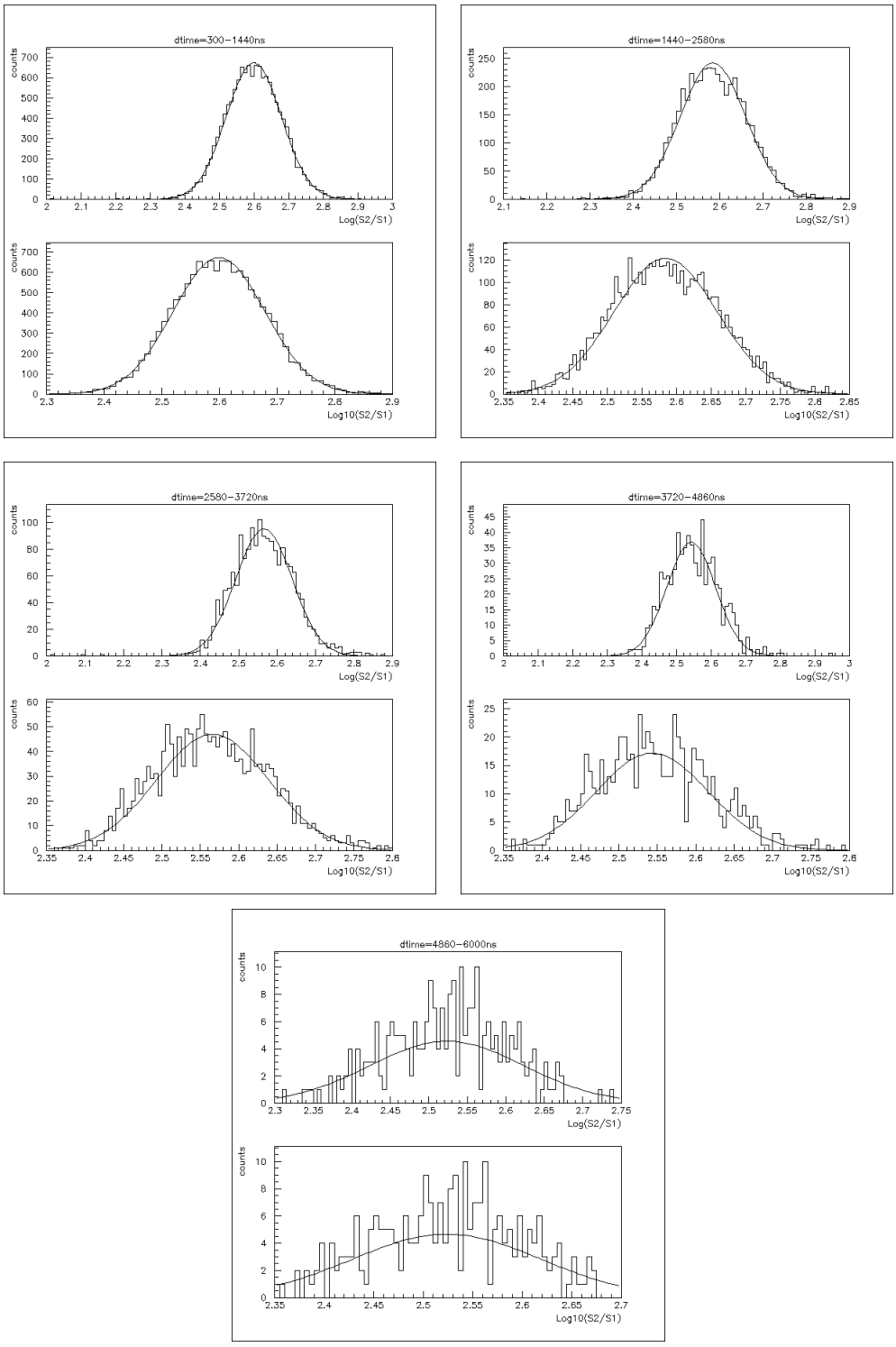

Figure 3.17: *Here Figure 3.13 has been sliced into 1-d histograms of* $Log_{10}(S2/S1)$ *for different drift time ranges. Each* $Log_{10}(S2/S1)$ *histogram for a drift time range is fitted twice with a Gaussian. The first fit used estimated parameters whilst the second uses parameters obtained from the previous fit.*

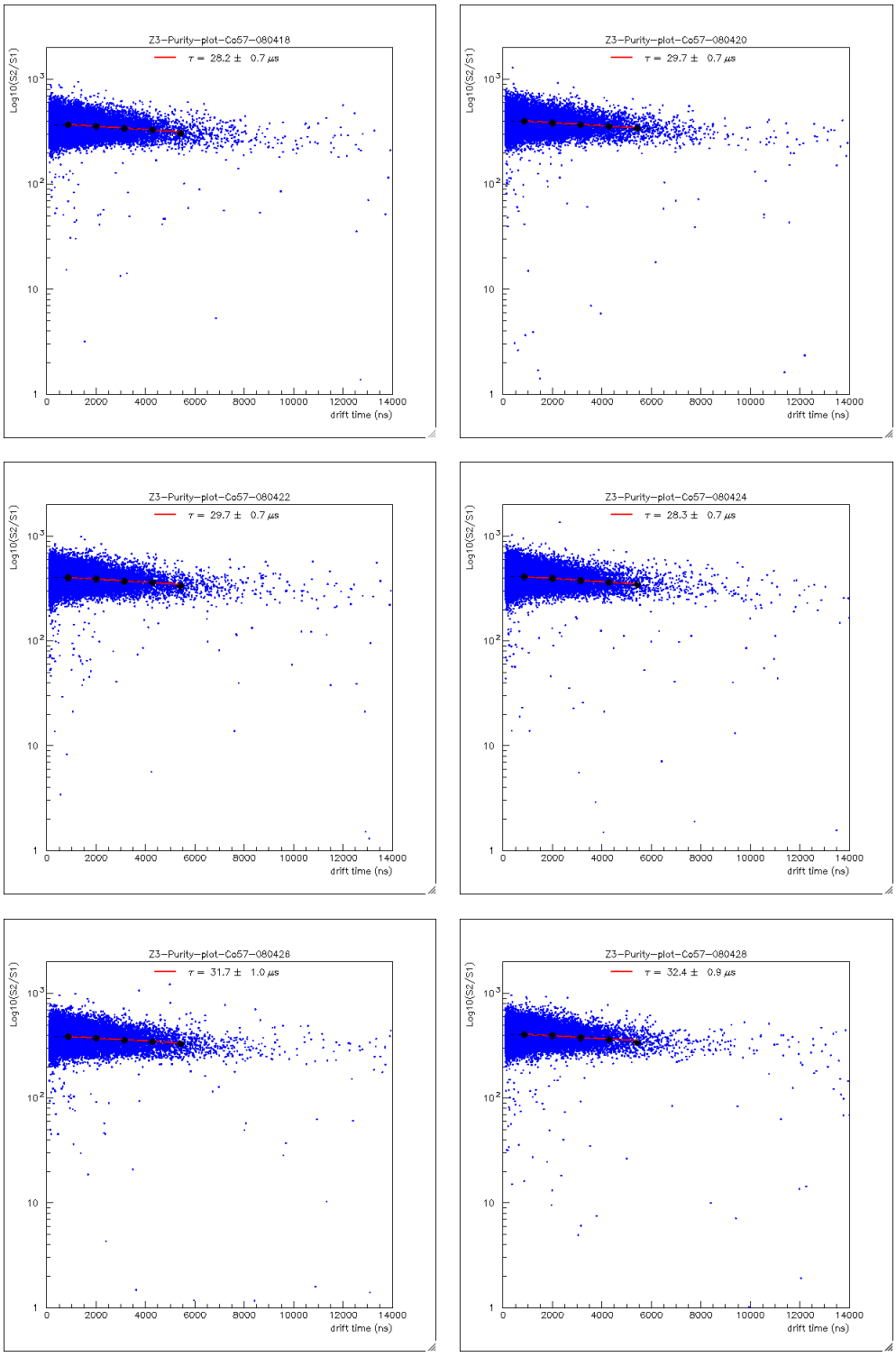

Figure 3.18: *Six electron lifetime datasets are shown from a total of 88 up to and including 5 days prior to the start of the FSR. After 12 days there is an apparent improvement in the electron lifetime.*

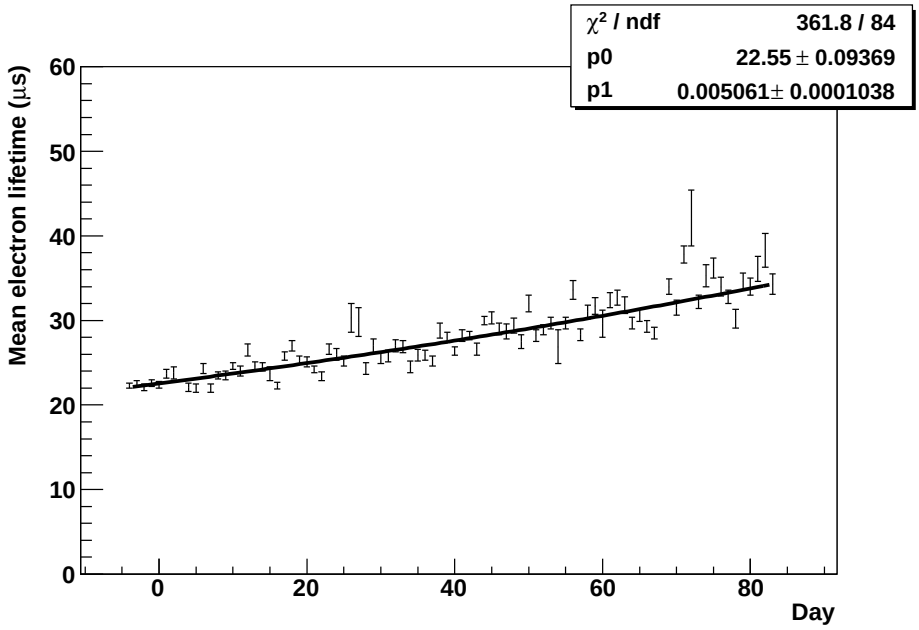

Figure 3.19: *The historical profile of the electron lifetime throughout the FSR. The data was fitted using function 3.14. The parameters obtained with this fit are used as a daily correction in the golden code.*

3.4.2.3 Energy Dependence of Electron Lifetime

The possibility that the electron lifetime may depend on energy was investigated. This required a different approach to the analysis already undertaken. Figure 3.20 shows a typical $Log_{10}(S2/S1)$ versus drift time plot with different colours highlighting the energy of events observed. The majority of the events lie within the energy range of 100-150 keV (red), as expected. There are poorer statistics for events within the 40-70 keV (green) and 0-40 keV (blue) energy ranges and the majority of low energy events are only observed towards the top of the Xe target (i.e $dtime \leq 2000$). All gamma-ray calibration sources were positioned above the ZEPLIN-III target vessel, and since low energy events are less penetrating, a smaller number of signals were observed from deep within the Xe target.

To obtain reasonable statistics for data analysis, particularly for energies $\leq$ 40 keV, an alternative calibration source was used; ^{137}Cs. By examining Compton scattered events from the 662 keV gamma-rays emitted by ^{137}Cs, it is possible to probe down to energies of $\sim$ 2 keVee. Although ^{137}Cs data were

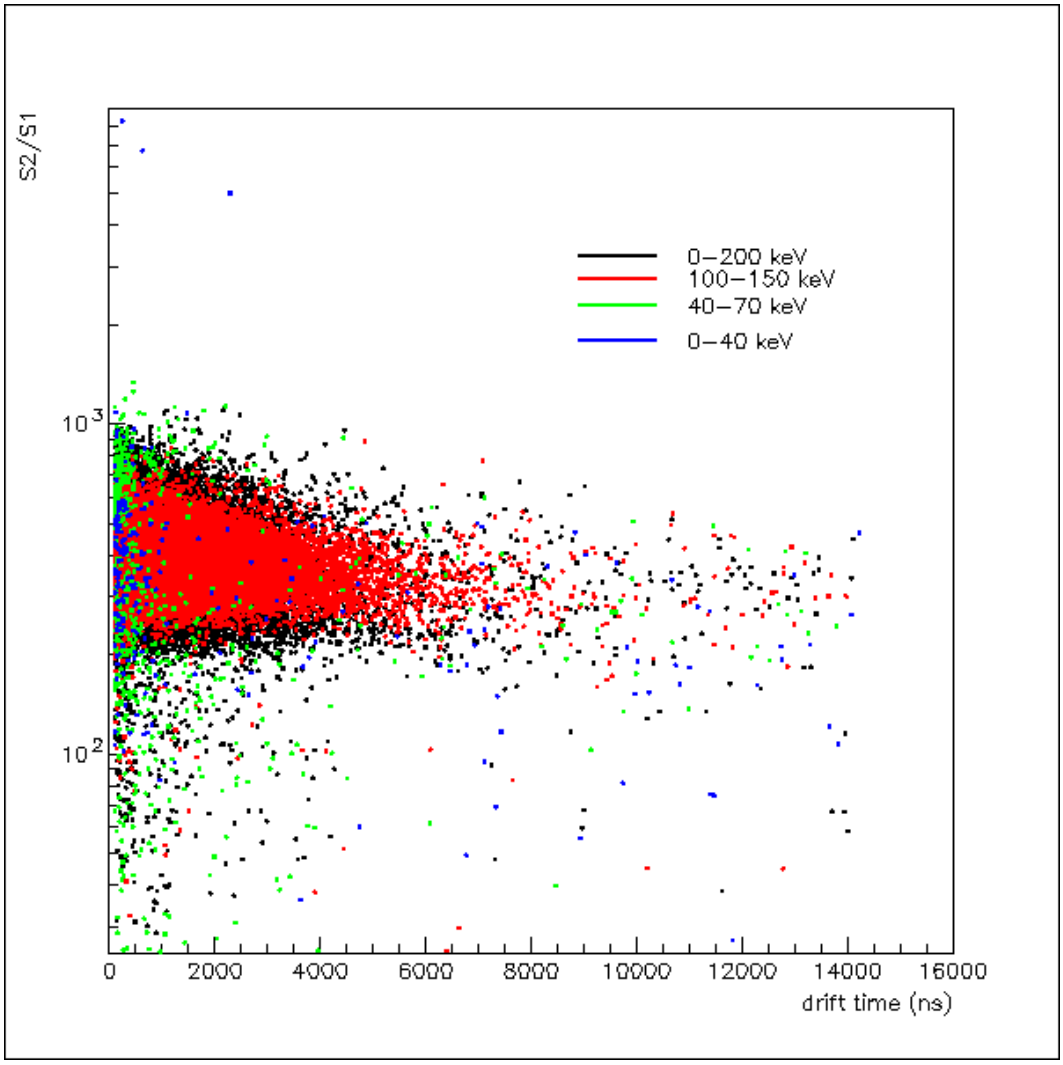

Figure 3.20: *Scatter plot showing the energy profile of* ^{57}Co *events. The majority of the* $0-200$ *keV (black) events have been coloured for different ranges; all events on this figure are within the* $0-200$ *keV energy range. As expected the majority of events are within the energy range* $100-150$ *keV (red).* ^{57}Co *emits 122 keV and 136 keV gamma-rays with intensities of 85.6% and 10.68% respectively.*

not taken as part of the daily calibration, data does exist for dates before and after the FSR and the number of files obtained for each day is at least double that taken for the ^{57}Co data sets. The ^{137}Cs data were analysed using the same method as for the ^{57}Co data. Saturation cuts to remove events that were so large that they extended beyond the range of the acquisition or PMT were applied in the data acquisition software made it difficult to compare electron-lifetime measurements above energies of 100 keV. For three days these saturation cuts were relaxed, allowing for higher energy data from these days to be considered.

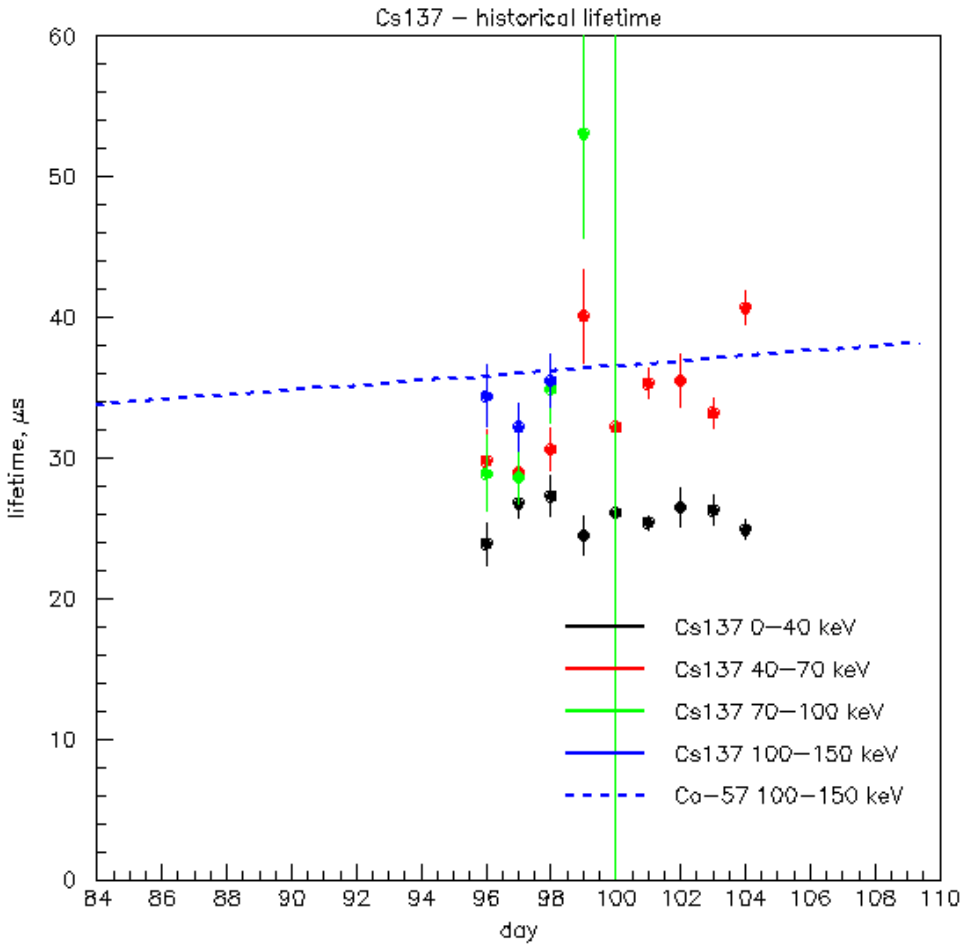

Figure 3.21: *Results displaying the energy dependence of electron lifetime, based on ^{137}Cs data. Also displayed is the ^{57}Co trend line reproduced from Figure 3.19*

Figure 3.21 displays the results of the ^{137}Cs analysis at various energy ranges

between the dates of June 2nd (day 96) - June 11th (day 104) 2008. The energy ranges chosen for study are between $0-40$ keV, $40-70$ keV, $70-100$ keV and for three days $100-150$ keV. For days 96-98, the electron-lifetime is shown for the $100-150$ keV energy range. This provided an opportunity to confirm similarity between the results measured with ^{57}Co. The $100-150$ keV ^{137}Cs data points are shown in blue and compare exceptionally well to the blue ^{57}Co prediction using the Function 3.14. Data after day 98 at energies greater than 70 keV became too difficult to analyse. This was due to the implementation of the saturation cut, which had the effect of removing larger events from the dataset.

There is a clear increase in purity values from the 0-40 keV range (black points) and the 40-70 keV range (red points), albeit lower than that from the 100-150 keV data; the electron lifetime does appear to exhibit an energy dependence. Using the results obtained from the ^{137}Cs data for the energy range of $0-40$keV, it was possible to include an energy correction in Equation 3.15. ^{57}Co data were unavailable for the dates when the ^{137}Cs data were obtained, but using 3.14 it was possible to extrapolate values for the electron lifetime for these days. The ratio between the electron lifetimes for ^{57}Co data $(100-150$ keV) and ^{137}Cs data $(0-40)$ provides the energy correction factor. The results are displayed in table 3.1; the mean correction factor (mean of the forth column) is 0.77.

Day	**τ based on ^{57}Co data μs**	**^{137}Cs measured τ μs**	**Correction factor**
96	33.5	23.9	0.71
97	33.6	28.5	0.85
98	33.8	28.5	0.84
99	33.9	24.5	0.72
100	34.1	26.1	0.77
101	34.2	25.4	0.74
102	34.4	26.5	0.77
103	34.5	26.3	0.76
104	34.7	24.9	0.72

Table 3.1: *The energy correction factor is calculated by extrapolating the ^{57}Co trend line to the dates when the ^{137}Cs data were taken and analysed for the 0-40 keV energy range. The ratio between the two daily values are used to develop a correction factor.*

FSR S2 data could then be corrected by implementing 3.14 and using the following;

$$S2area_{corr} = S2area_{uncorr} \times exp(dtime/(\tau \times E \times 1000) \tag{3.15}$$

where $S2area_{corr}$ is the corrected S2 event, $S2area_{uncorr}$ is the uncorrected S2 event and τ is produced from Equation 3.14 and is multiplied by 1000 to convert to nanoseconds. This is the variation in the electron lifetime as a function of day. The factor of E is an energy correction of 0.77 for the electron lifetime for energy depositions of $0 - 40$ keV.

3.4.3 The Variational Analysis Method

To ensure the integrity of the findings a different analysis technique was also employed to test the data, called the variational method. Originally the variational method was tested with the ^{57}Co data to overcome the poorer statistics at lower energies; however, it remained unsuccessful. This method was therefore only used for the ^{137}Cs data-sets.

The variational method involves projecting an entire ^{137}Cs data set as a one-dimensional histogram of $Log_{10}(S2area/S1area)$ and then multiplying $S2area$ with the following function;

$$S2area \times exp(dtime/\tau \times 1000). \tag{3.16}$$

Individual τ values are input into the projected histogram in accordance with Equation 3.16. The one-dimensional histogram was fitted with a Gaussian function. With an increase in τ, the width (σ) of the Gaussian fit decreases to a minimum point, indicating the optimum correction achievable. σ will increase once again when τ becomes less favourable.

Figures 3.22 and 3.23 show examples of the result of application with the variational method. σ versus τ is plotted, and the minimum that is clearly observed is equivalent to the electron lifetime for that particular data-set. The following function was fitted to the data, so that the minimum of the graph could be output and to aid in error analysis;

$$\frac{P3}{P0 \times \tau} + P1 \times (1 - exp((\tau - P4)P2)) \tag{3.17}$$

Results from variational analysis for ^{137}Cs data taken on June 5th 2008 (day 99 of the FSR) for an energy range 0-40 keV are shown in Figure 3.22. The minimum of the fit applied is found at 24.658 ± 0.006 μs. Using the previous method a value of $24.5 \pm 1.4\mu$ s has been obtained, showing excellent agreement. Figure 3.23 displays results for ^{137}Cs data taken on June 7th 2008 (day 101 of the FSR) for an energy range 40-70 keV. The minimum of the fit applied is given as 31.449 ± 0.004 μs. Using the previous method a value of $35.3 \pm 1.1\mu$s has been obtained which is in reasonable agreement, where any variation can be ascribed to differences in the analysis procedure.

The errors calculated for the variational method electron lifetime result have been determined using partial differentiation of the function 3.17 with respect to the parameters, $P0, P1, P2, P3$ and $P4$ inclusive of their corresponding errors. The errors calculated are very small; however the fitting procedure worked remarkably well (as can be observed in figures 3.22 and 3.23.)

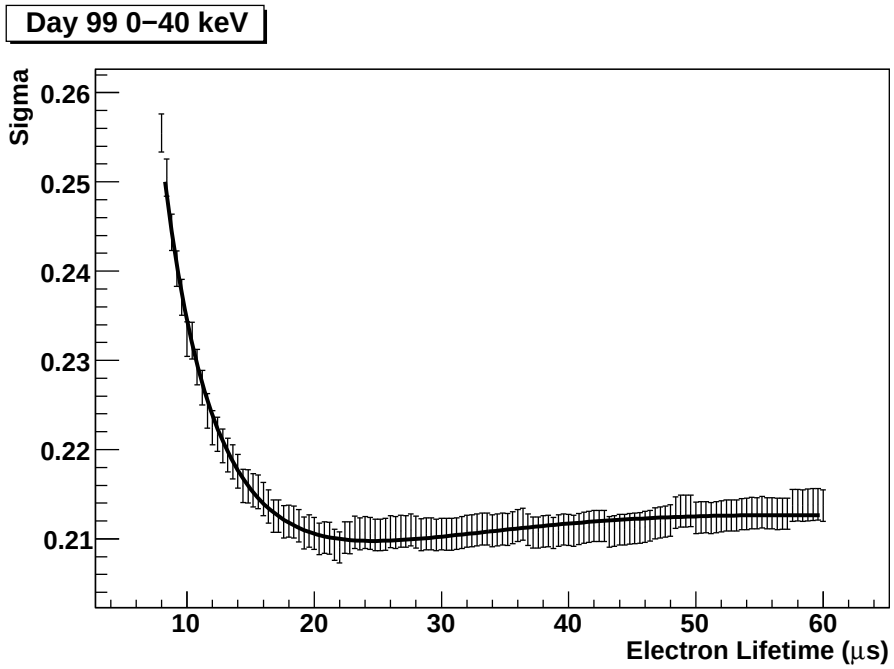

Figure 3.22: *Example of data analysed using the variational method. The minimum occurs at 24.8 μs, which is equivalent to the electron lifetime of that dataset.*

A comparison of the two techniques for all ^{137}Cs data can be found in Figure 3.24 for energies of $0-40$ keV and $40-70$ keV. The agreement between the two

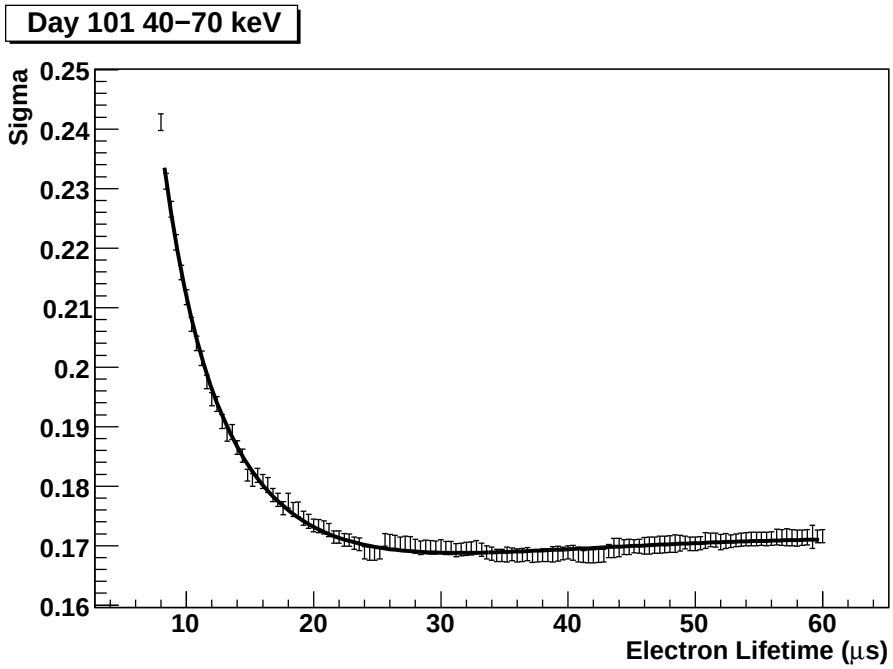

Figure 3.23: *Example of data analysed using the variational method. The minimum occurs at* $31.4\mu s$*, which is equivalent to the electron lifetime of that data-set.*

techniques is good, hence demonstrating that the observed improvement in the electron lifetime is not simply a consequence of the analysis method employed.

3.4.4 Conclusions

The evolution of the electron lifetime shows a daily improvement during the FSR. The initial electron lifetime attained prior to the FSR was 22.3 ± 0.3 μs which increased to a values of 34.3 ± 1.2 μs, based on energies of 100-150 keV. A further correction factor of 0.77 has been identified for application to lower energies of interest for WIMP searches, i.e., $0 - 40$ keV.

The observed increase in the electron lifetime indicates an improvement to the purity of the Xe. The true cause of this improvement is unclear; one might have expected the purity to either remain constant or degrade over time. The fact that Xe-friendly materials were used in the construction of the ZEPLIN-III Xe vessel may have helped in retaining the purity levels observed at the start of the FSR. Also, continuous application of the electric fields higher than those applied in previous dark matter detectors ([91; 99]) may have aided in the contin-

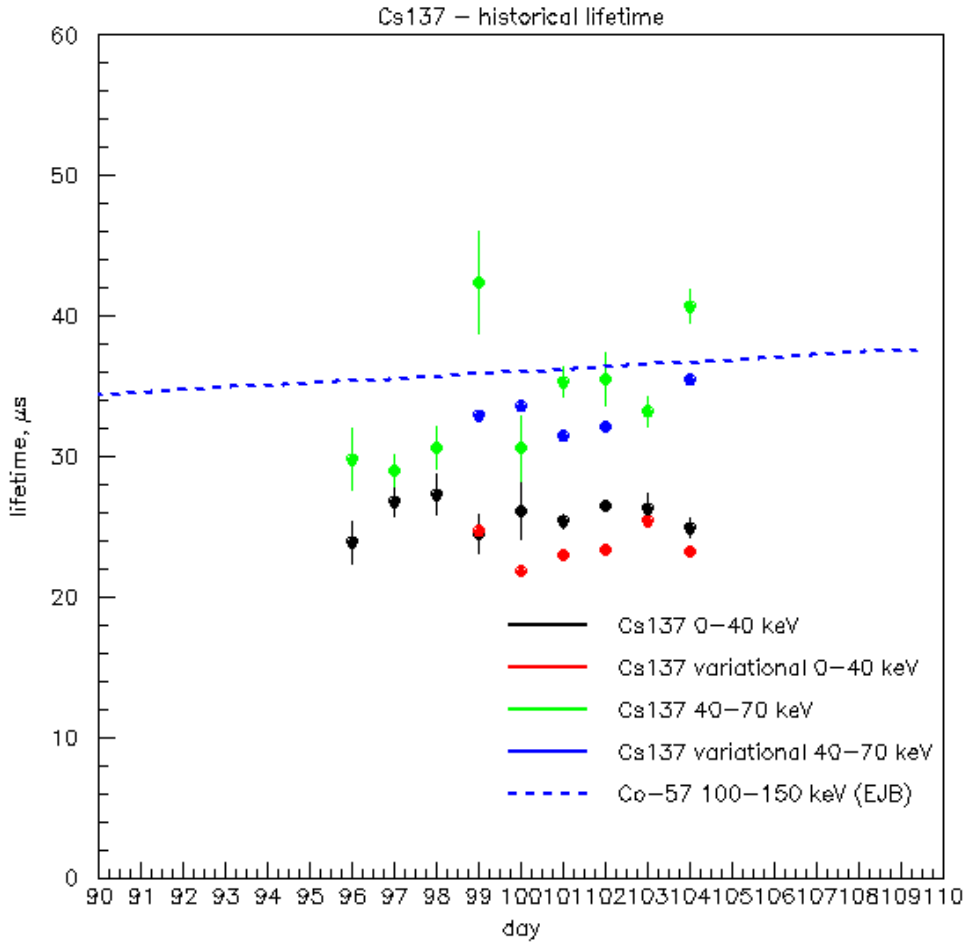

Figure 3.24: *Comparing analysis techniques for data of energies 0-70 keV. Comparison between the two techniques is good.*

ued improvement of the electron lifetime levels. Application of a strong electric field may have removed electronegative impurities from the Xe, by forcing them to attach to the copper target instead of remaining in the liquid.

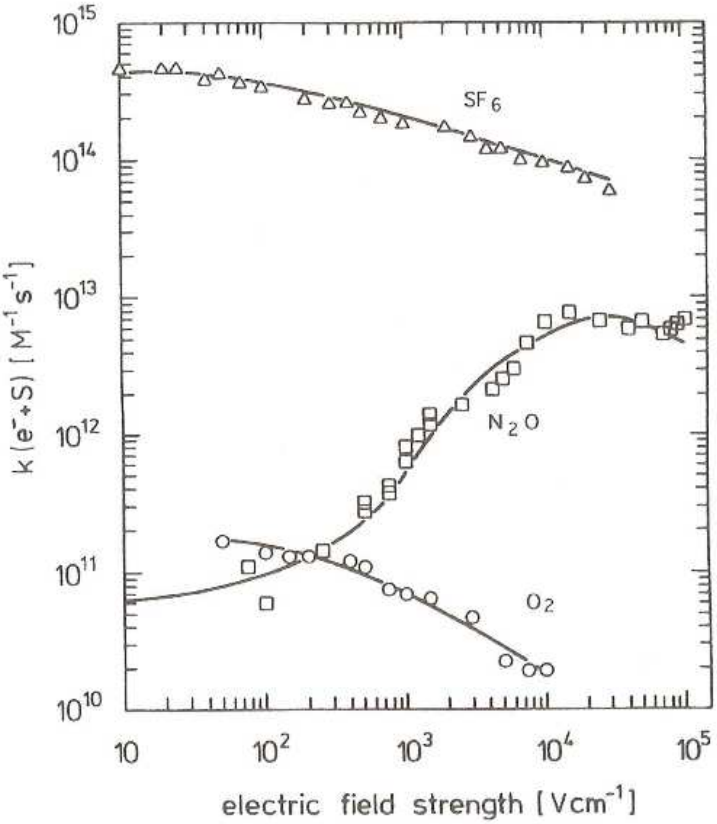

Figure 3.25: *Rate constant of the electron attachment in liquid Xe for SF_6, O_2 and N_2O obtained from [145]*

Bakale *et. al* [145] have explored the electric field dependence of electron attachment to impurities. Figure 3.25 displays the rate of attachment to electrons to SF_6, N_2O and O_2 molecules in liquid Xe as a function of electric field strength. It is shown that there is a distinct field dependence for certain molecules, such as SF_6 and O_2, whereby the electron attachment cross section (k_s) decreases with increasing electric field, because the electron lifetime and k_s are inversely proportional to one another as shown in Equation 3.12. ZEPLIN-III used an electric drift field of 3.9 kV/cm, where there is an order of magnitude reduction in the attachment of electrons to SF_6 and O_2 molecules in Xe. However

at these fields there is a significant increase in the attachment of electrons to N_2O, again by an order of magnitude, therefore perhaps negating the previous. Unfortunately direct measurement of the N_2O (or other) contaminant species is not possible. This would require the Xe to be removed from the target vessel where the purity can be significantly affected when entering different areas of the ZEPLIN-III gas system.

3.5 First Science Run Results

Implementing the golden code with the electron lifetime correction now applied, the results from the FSR were obtained. The results of the FSR are described in [72] and Figure 3.26 displays the WIMP data inclusive of data cuts and corrections; the WIMP search box is drawn in red. Seven events were observed in the WIMP search box; 11.6 ± 3.0 were predicted. Initially these data remained un-blinded and selection cuts were tightened based on 20% of the FSR data; however with the un-blinding of these data more events were originally observed in the WIMP search box. These were attributed to multiple-scintillation single-ionisation (MSSI) events. MSSI events are double-Compton interactions with at least one vertex in a dead region in a detector. These events originally fulfilled the WIMP selection criteria since there is no S2 pulse from the dead region and the coincident scintillation pulses are added together in a single S1. To remove these the entire FSR data set was analysed to tighten cuts to remove MSSI events.

Figure 3.26 is culmination of the above analysis. The events can be observed near the top of the WIMP search box suggesting leakage from the electron-recoil band. Figure 3.27 shows the same data with the electron lifetime correction removed. The S2 signal is increased by the inclusion of the correction serving to increase the S2/S1 ratio. Without the correction significantly more events leak into the the WIMP search area.

Using the results obtained from the FSR the sensitivity of the ZEPLIN-III detector to WIMP like dark matter can be determined. This is shown through limit curves using the signal energy distribution from the theoretical WIMP spectrum discussed in Chapter 2. To calculate the sensitivity of the detector the likelihood that the seven events indicates the presence of WIMPs above the level expected from the background is calculated. The various software and

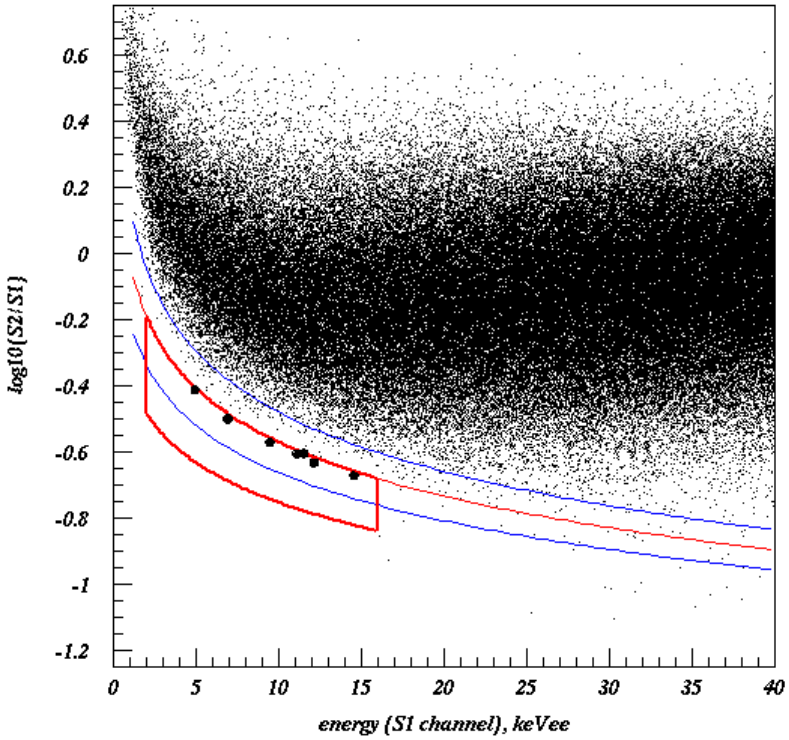

Figure 3.26: *FSR results displaying a scatter plot of the FSR data. 7 events are observed within the defined WIMP box (red).*

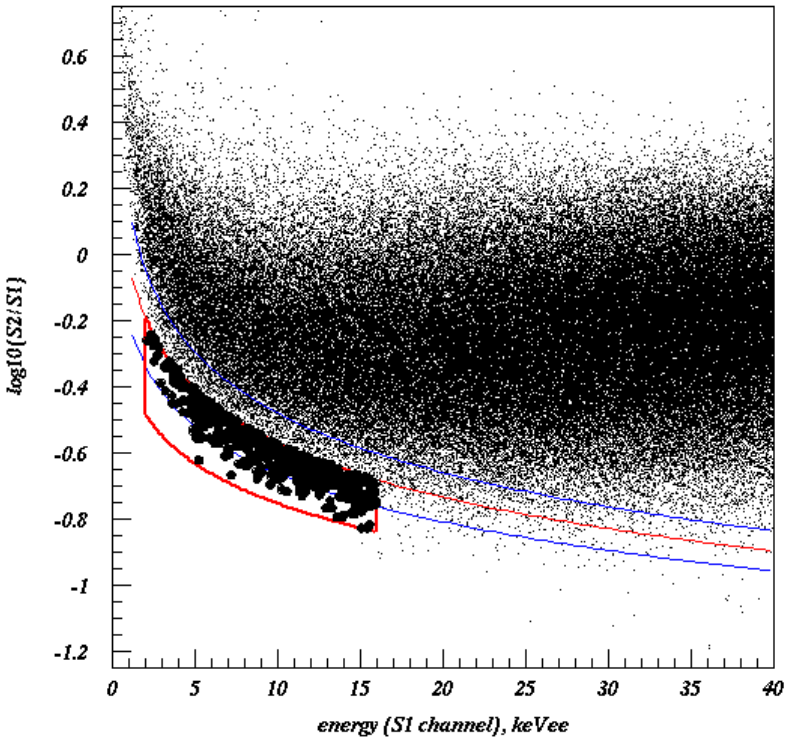

Figure 3.27: *FSR WIMP data without the electron lifetime correction. A significantly large number of events are now observed within the defined WIMP box (red).*

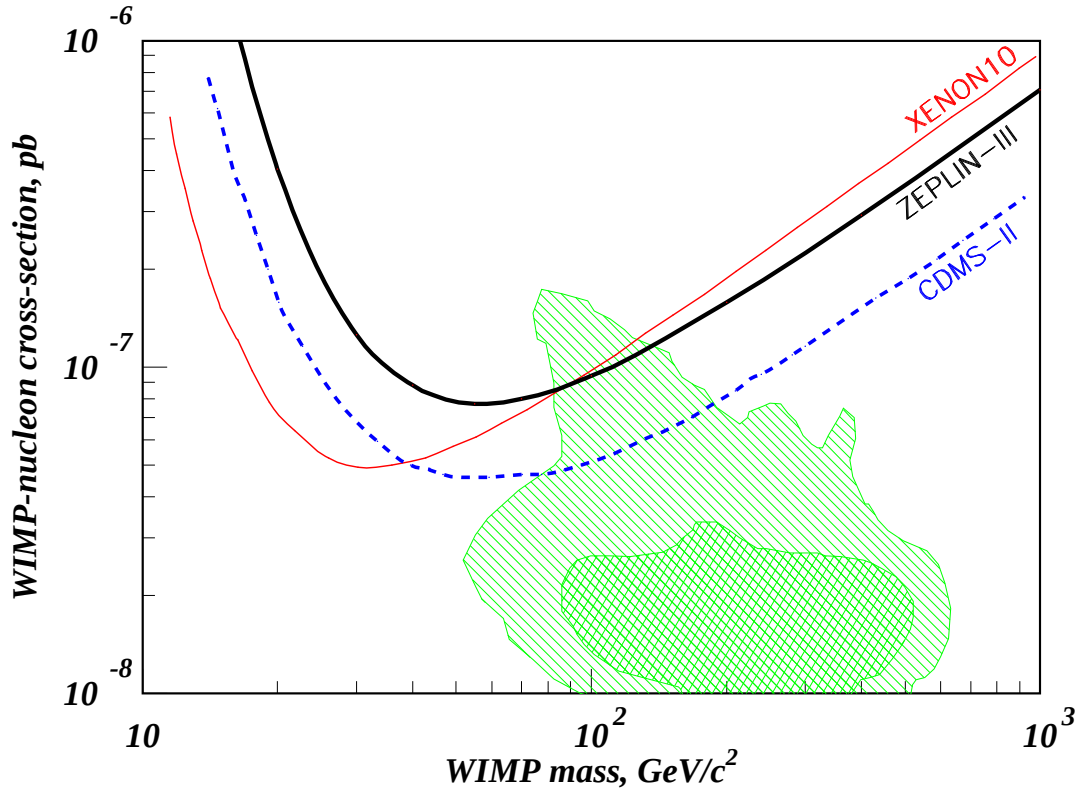

Figure 3.28: *The spin independent WIMP-nucleon cross section for the ZEPLIN-III [72]. Also shown are results for XENON10 and CDMS-II. The XENON10 result is a one-sided limit corresponding to an 85% (CL) two sided limit, whereas the CDMS-II and ZEPLIN-III results are 90% (CL) two sided limits.*

hardware detector efficiencies are also included in the final calculation of the ZEPLIN-III limit. This includes the efficiency loss due to the varying ℓ_{eff} at low energies. Further information on the limit calculation and discussion of the various detector efficiencies are found in reference [72].

To calculate the limit, the WIMP search box was divided into two areas, so that the seven observed events would reside in the top box. The expectation is then calculated that 10% of repeated experiments would produce seven events in the top box and zero events in the lower box. Based on the data, repeated simulations showed that a division between the upper and lower boxes placed such that the lower (empty) box contained 10% of the parameter space, was consistent with this requirement. The Feldman Cousins two-sided limit on an observation of zero events is 2.44 events. Since this corresponds to an 80% box, the sensitivity limit from the FSR data was based on 2.44/0.8 = 3.05 events. Then using the theoretical WIMP spectrum discussed in Chapter 2, based on the isothermal galactic model and inclusive of the values ρ=0.3 GeVcm^3 , V_o =220 km/s, V_{esc}=600 km/s and V_E=232 km/s, the spin independent WIMP-nucleon cross section for the ZEPLIN-III detector FSR is given as 8.1×10^8 pb for a WIMP mass of 60 GeV/c^2.

The WIMP-neutron and WIMP-proton spin dependent limits were also calculated using the FSR results; however the cross section is calculated separately to the spin-independent cross section to reflect the type of interaction involved (see Chapter 2, section 2.2.2.2 for further details). Different models are used to calculate the cross sections with different experiments quoting different methodologies. However, a WIMP-neutron cross section of 1.9×10^{-2} pb for a 55 GeV/c^2 WIMP mass [136] is given setting the best limit in the world above 100 GeV/c^2.

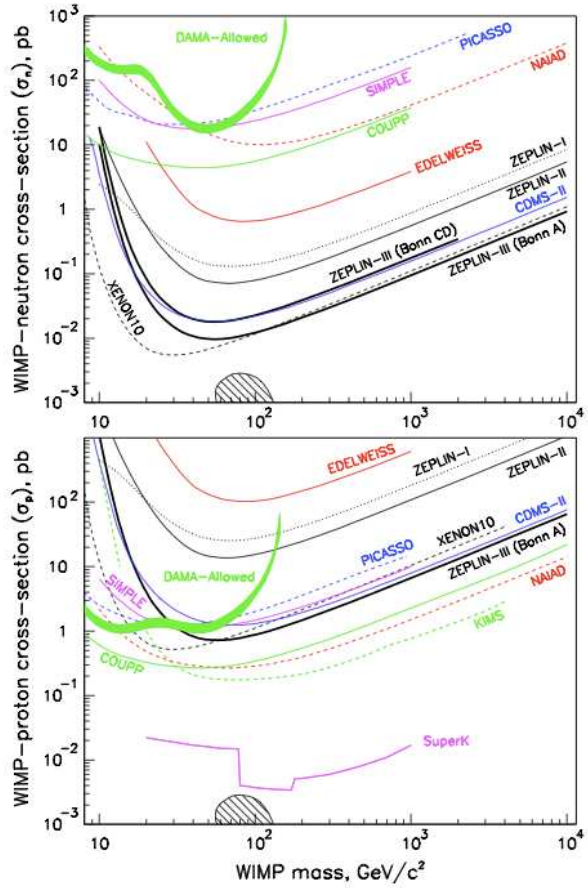

Figure 3.29: *The spin dependent WIMP-neutron and WIMP-proton cross section for the ZEPLIN-III [136]. Various experiments are displayed as shown on the diagram.*

Chapter 4

The ZEPLIN-III veto and the Second Science Run

4.1 Introduction

The ZEPLIN-III collaboration has already achieved excellent results in the FSR; however this was always only the first stage of the project. The aim of the second science run (SSR) is to improve on these results by reducing or improving identification of background within the detector. For this the ZEPLIN-III detector has undergone various modifications for the SSR. The ZEPLIN-III PMTs were replaced with $\sim 30\times$ lower background PMTs and an active veto was retrofitted to the device in place of the FSR polypropylene neutron shielding. The veto is itself the subject of this thesis. The purpose of the veto is to reduce and detect neutrons and gamma-rays in coincidence with the ZEPLIN-III target and thus identify them as background events. It is a relatively low cost device utilising plastic scintillator and gadolinium loaded polypropylene neutron shielding to improve the sensitivity of ZEPLIN-III. The veto can also serve as a diagnostic tool of the local radioactive environment and to confirm understanding of neutron backgrounds, particularly important in scenarios of a positive WIMP signal. In light of the latest CDMS-II results [114], identifying background events from candidate WIMP signals is essential. The veto will have the ability to tag neutrons but not WIMPs adding extra weight to any claim.

4.2 Veto Design

The principle purpose of the veto is to reduce and detect non-WIMP events that deposit energy in the ZEPLIN-III detector. The veto can be categorised into two sections, one active and one passive. The passive section has been designed using gadolinium (Gd) loaded polypropylene shielding and is positioned around the ZEPLIN-III detector. Neutrons that enter the passive shielding are moderated and then captured onto Gd or hydrogen (H) with the subsequent emission of gamma-rays. The emitted gamma-rays may then enter the active component of the veto, designed using 52 separate sections of plastic scintillator. Each section of plastic has a corresponding PMT to detect scintillation light produced by the incoming gamma-rays.

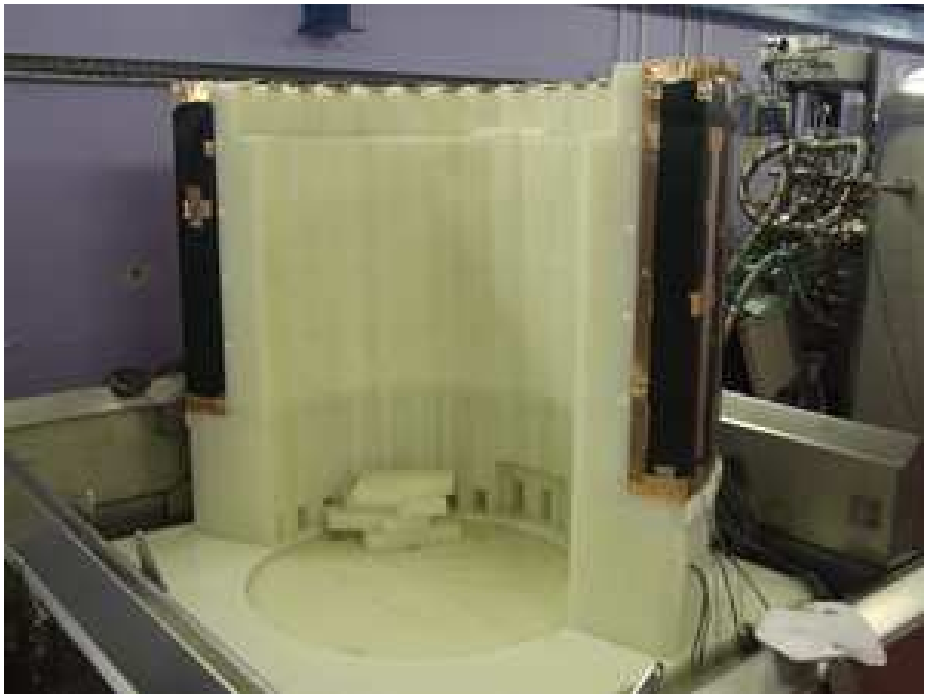

Figure 4.1: *The active (black) and passive (white) components of the veto are displayed in situ. The ZEPLIN-III detector would sit at the centre of the veto where the circular cut-out section can be observed in the shielding base. Only 50% of the walls are shown in the figure, the entire veto system resembles a barrel type structure which surrounds the entire ZEPLIN-III vessel. The roof sections are also not shown.*

4.2.1 Gadolinium Loaded Neutron Shielding

The passive component of the veto consists of Gd loaded polypropylene neutron shielding situated between ZEPLIN-III and the lead shielding. Polypropylene is often utilised as neutron shielding due to its high H content. Neutrons that enter the shielding are scattered, losing energy until they can be captured onto hydrogen releasing 2.218 MeV gamma-rays. To maximise the energy released following capture, the polypropylene shielding has been loaded with Gd. Gd, in particular the isotope ^{157}Gd ($\sim$ 15% abundance) has a high neutron capture cross section ($\sim$ 242000 barns). Neutron capture onto ^{157}Gd is accompanied by the emission of up to 3-4 gamma-rays of energy totalling $\sim$ 8 MeV which can enter the active component of the veto. The gamma-rays excite the atoms and molecules of the plastic which results in the emission of scintillation light, that can be subsequently detected by the veto PMTs. The emission of multiple gamma-rays with energies above ambient background maximises the detection potential of an event. Monte Carlo studies of Gd loaded neutron shielding have shown there to be a significant improvement in detection efficiency with its introduction; from $\sim$ 55% (0% Gd loading by weight) to $\sim$ 81% (0.5% Gd loading by weight) (Monte Carlo studies are described in further detail in Chapter 6).

The polypropylene shielding was manufactured at Rutherford Appleton Laboratory (RAL) with input to the design from this work. There are four parts to the neutron shielding. The first is the flooring which is based on the design used in the FSR, although some re-machining was performed for the veto. The second part of the design is the base section shown in Figures 4.1, 4.2 and 4.3. The base section has a complex design for the following reasons:

1. Both the polypropylene and scintillator sections would rest upon it
2. The PMTs attached at the end of the scintillator sections would need space to fit.
3. Cabling from the PMTs would need to be passed out of the detector for attachment to HV, etc.
4. Pipes and wires from ZEPLIN-III would also need to be brought out of the system.

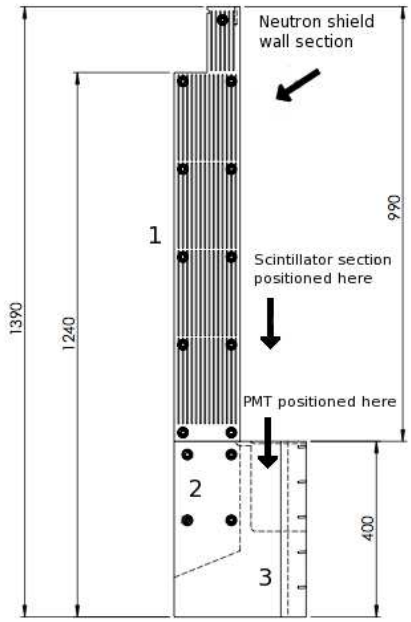

Figure 4.2: *CAD drawing of the neutron shield wall and base section. The numbered sections are discussed in the text. Some dimensions are also shown.*

Figure 4.3: *The base section of the passive veto shielding. The PMTs will sit within the cut out sections. A polypropylene back piece will seal in the PMTs.*

Figure 4.1 displays how the scintillator sections (in black) are positioned upon the passive shielding base section (in white). Figure 4.2 is a labelled schematic of a neutron shielding wall and base sections. Point one is the neutron shielding wall with dimensions shown. Point 2 is part of the base which is angled at the bottom where section 3 can be positioned. Section 3 contains a hole (also displayed on the diagram) to accommodate the PMTs. The scintillator blocks are positioned on top of section three, where their attached PMTs can fit within these holes. Figures 4.3 and 4.4 display the finished product.

The device is modular in design providing ease of movement. 32 standing trapezoid sections of height 990×150 mm comprise the passive shielding wall all of which are maintained in position using plastic screws, tightened to the point where no gaps are obvious. Remaining gaps have thin sheets of polypropylene inserted to reduce their size. An example of the PMT positioning is shown in Figure 4.4. A polypropylene back piece seals in the PMT, leaving space only for the wires to escape.

Figure 4.4: *Positioning of the veto PMTs in the base of the passive shielding. The scintillator section rests on top with room provided for its corresponding PMT. The PMT is sealed using a separate polypropylene back piece (not shown).*

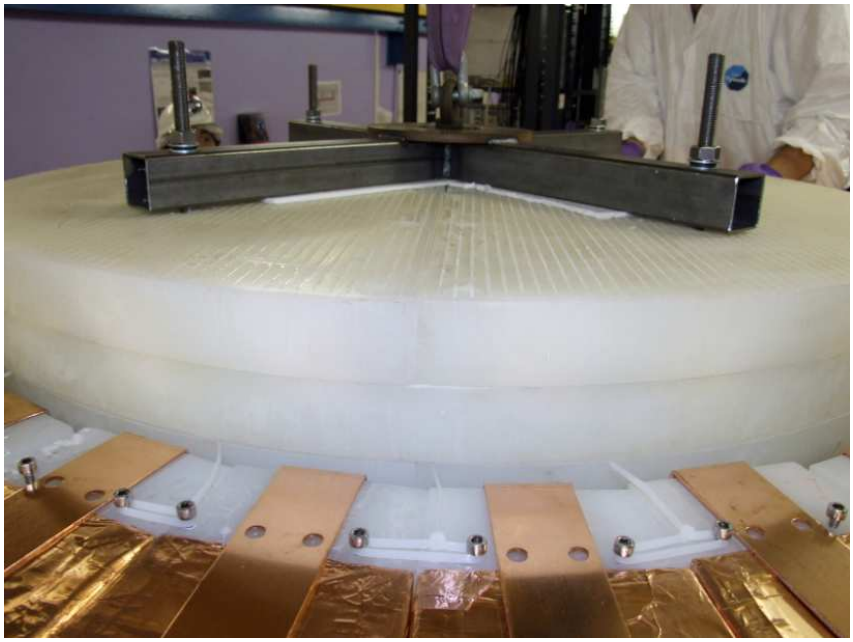

Figure 4.5: *The passive shielding roof section has a diameter of 115 cm and thickness of 15 cm. In this figure the roof is being placed with the aid of a specially created jig.*

Figure 4.5 shows the passive shielding disc shaped roof (115 cm diameter and 15 cm thickness). It is placed upon the passive shielding walls. At the top of Figure 4.2 a section of the passive shielding wall has been removed to create a step where the roof section can be rested.

The 0.5% (w/w) Gd loading is added in the form of $> 2.7\%$ (w/w) (10 μm) gadolinium oxide (Gd_2O_3) suspended in Rutherford Type 71 epoxy [146]. The mixture is poured into 2 mm wide, 10 mm pitch grooves machined within the wall and roof sections (the grooves are displayed as black lines in Figure 4.2). Only the roof and wall sections include Gd loading as Monte Carlo simulations of the veto structure revealed that there is little or no benefit to the overall veto efficiency by adding it to the base and floor sections. Monte Carlo studies were also used to determine the mass fraction and implementation of Gd loading to achieve acceptable detector efficiencies without compromising the cost effectiveness of the device (see Chapter 6).

4.2.2 The Plastic Scintillator

4.2.2.1 The Detector Material

The active shielding has been constructed using 1 tonne of UPS-923A plastic scintillator (2% p-terphenyl and 0.02% POPOP) produced by Amcrys-H, Kharkov, Ukraine [147]. The active shielding is positioned between the polypropylene and the lead castle. The basic properties of UPS-923A are displayed in Table 4.1.

Density	1.06 g/cm^3
Refractive index	1.52
Light output	60 % anthracene
Emission peak	425 nm
Rise time	0.9 ns
Decay time	3.3 ns
Bulk atten. length	50 - 300 cm

Table 4.1: *Properties of plastic scintillator UPS-923A as stated in [147]. The light output is given as a percentage of anthracene, where anthracene produces on average ∼20 photons/keV therefore, 12 photons/keV is expected from UPS-923A.*

The mechanical design of the active shielding consists of 32 standing trapezoid segments (length 98.5 cm parallel sides of 12.8 cm and 15.6 cm with a thickness of 15.0 cm) which combine to form a barrel structure with inner and outer diameters of 13.0 cm and 16.0 cm respectively. The active roof is positioned directly on top of the passive and active shielding walls and is constructed from another 20 scintillator sections of 4 separate geometries. Figure 4.6 shows a plan view of the roof displaying the four roof block geometries. The block lengths vary from 51.5 cm to 80.0 cm, with eight of the roof blocks being 80.0 cm in length whilst the other sets are produced as four's. The PMT positioning for each section is also shown in Figure 4.6.

The wall sections, are fixed into position onto the passive shielding using copper brackets; shown at the bottom of Figure 4.5. The scintillator construction is rotationally offset by 15° to prevent a line of sight straight through the passive and active shielding to the ZEPLIN-III detector. This is to ensure that external neurons will not be able to easily access the ZEPLIN-III detector, instead they should be thermalised and captured by H or Gd in the shielding. All scintillator

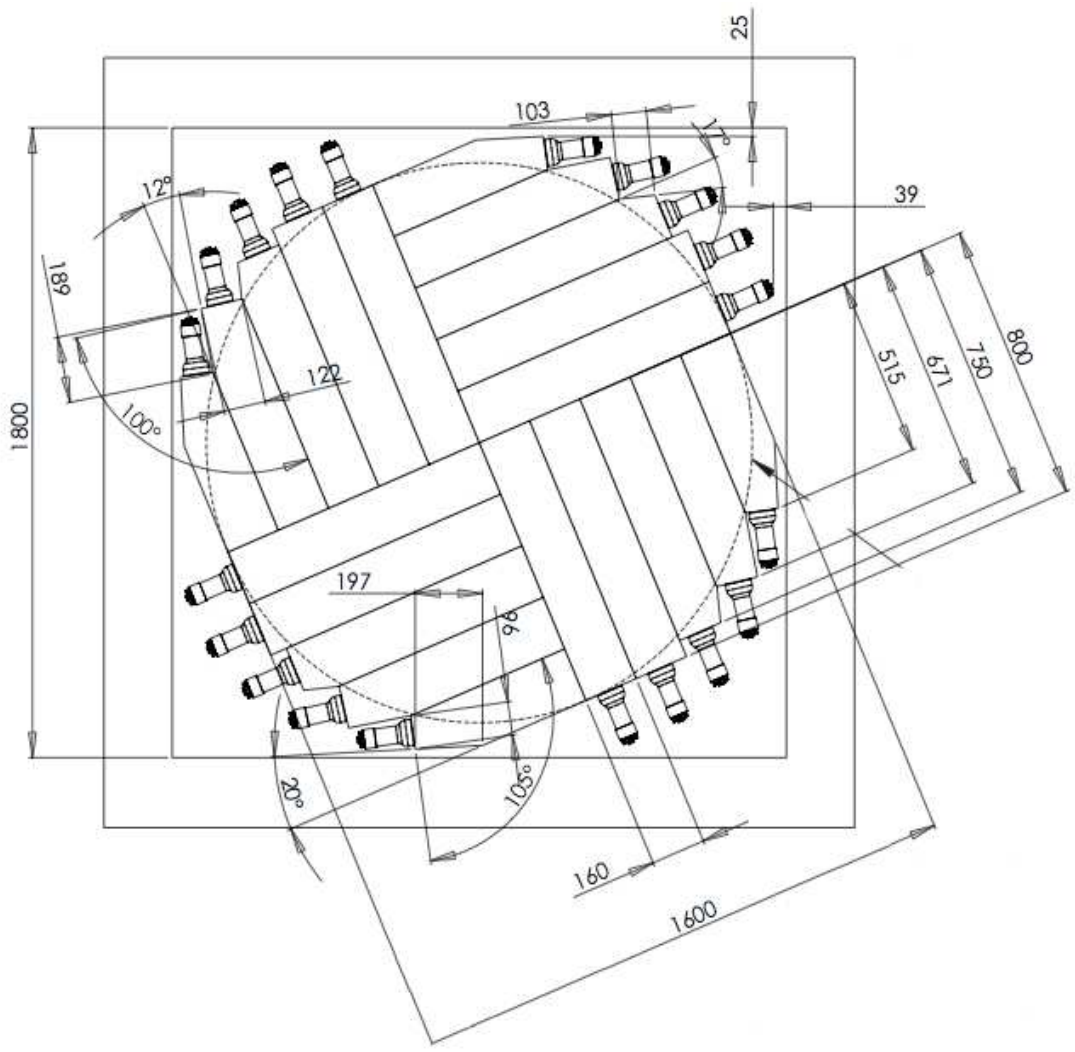

Figure 4.6: *Schematic of the veto roof comprising 20 blocks of scintillator. There are four separate geometries shown, some with angled cut-out sections. The positions of the veto PMTs are also shown (cylinders at the far end of each block). The dimensions are in mm and degrees.*

sections were tested to ascertain their performance which is described later in Chapter 5.

4.2.2.2 Improving the Light Yield

All scintillator sections were wrapped in two separate materials, PTFE and then black light tight wrapping. The PTFE is used to increase the effective light yield of a block, whilst the black wrapping prevents light from external sources entering the blocks, which could potentially damage the PMTs.

To select the most appropriate wrapping material a series of tests were performed on a sample scintillator block from Amcrys-H [147]. These tests were performed by myself with colleagues at the Institute of Theoretical and Experimental Physics (ITEP), Moscow and the University of Edinburgh and are discussed in the following publication [148]. The work performed at ITEP served multiple purposes. The veto performance could be predicted based on the quality of the sample material tested and a wrapping material could also be selected for use in the final detector design.

The cuboid scintillator block (100 x 15 x 15 cm) UPS-923A was placed in a light tight environment. It was optically coupled with a PMT (FEU139, 15% quantum efficiency) using optical grease (BC-603 purchased from Saint Gobain Crystals Ltd. [149]) and subsequently clamped in place. A blue light emitting LED was positioned at the opposite end of the block to the PMT, to be used to calibrate the experiment. Figure 4.7 shows the experimental set-up with the dark box opened. To the left is the PMT which was held in direct contact with the scintillator using a specially designed metal clamp. The scintillator block was tested with both cosmic ray muons and gamma-rays emitted from a ^{60}Co source with various wrapping materials. For gamma-ray measurements a NaI detector was implemented in coincidence with the scintillator block and PMT. For cosmic ray muon tests a larger coincidence circuit was utilised involving two PMTs attached to separate smaller pieces of scintillator positioned both above and below the scintillator block. Only events detected in coincidence between the scintillator PMT and either the NaI or Muon detectors were retained for analysis.

The light collection and linearity for each material were studied by measuring the number of photoelectrons detected as a function of distance from the scintillator PMTs. Calibration data was obtained by varying the voltage of the

Figure 4.7: *The experiment set-up at ITEP, Moscow. See text for details.*

blue LED prior to muon or gamma-ray data acquisition, as a cross check for consistency throughout all measurements. LED spectra were analysed by fitting a Gaussian and obtaining the position of the peak centroid (μ_e) and width (σ_e) from the fit. The results were plotted for peak amplitude versus channel number to confirm the linearity of the PMT. The noise corrected peak centroid values were then used in the following equation (Equation 4.1) to determine the number of detected photoelectrons.

$$\mu_{p.e} = \left(\frac{\mu_e}{\sigma_e}\right)^2 \tag{4.1}$$

Cosmic muon spectra were fitted using a Landau function accounting for the asymmetric distribution of energy loss. The long tail observed in the Landau distribution can be attributed to the the muon losing large amounts of energy (one-half the initial kinetic energy) as well as energy loss from Bremsstrahlung. Although highly improbable, they can occur resulting in the long tail to the high side of the energy distribution. The $\mu_{p.e}$ values for each data point was then plotted against the distance from the PMT, showing the number of photoelectrons detected as a function of distance. Next the plastic scintillator were then exposed to ^{60}Co gamma-ray source which produced a characteristic Compton edge

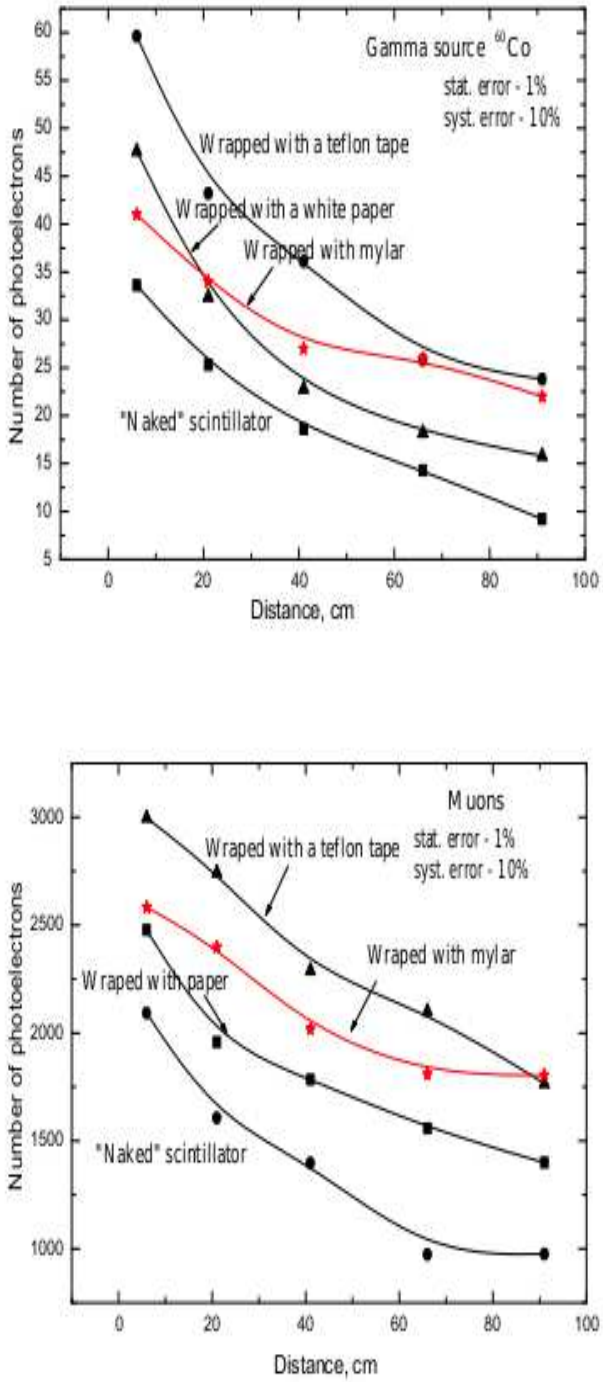

Figure 4.8: *Results from the scintillator wrapping tests. The top graph displays the number of photoelectrons as a function of distance from the PMT due to irradiation with gamma-rays. The bottom graph is for muons.*

that was fitted using a partial Gaussian. The peak position and σ_e defined from the fitting process was again used to calculate the number of photoelectrons.

The light collection and linearity were studied for various wrapping materials including a naked scintillator block, aluminized Mylar, white paper and PTFE. The results of which are shown in Figure 4.8. The top graph in Figure 4.8 shows a cross over between the mylar and white paper wrapped blocks data points. It is also apparent that the scintillator response changed between the ^{60}Co and muon data. Both of these effects can be attributed to variations in the PMT coupling to the scintillator. Each time the wrapping was changed the PMT had to be uncoupled completely from scintillator. The optical grease was also removed, only to be later re-applied after the wrapping was complete therefore changing the contact compared to any previous tests. In addition, the muon and ^{60}Co data-sets were not taken consecutively. Often the scintillator block may have been re-wrapped a number of times with different materials before the equivalent muon or ^{60}Co measurements were obtained (for a particular wrapping material). Despite the variations it was still possible to make a decision as to the type of wrapping material needed for the veto. PTFE tape was selected as it gave the best attenuation length (flattest curve) and is economical and quick to apply.

In addition to these tests a Monte Carlo of this experiment was also devised. The experimentally measured properties of the scintillator material were used in a Monte Carlo simulation. The geometry of the block tested in ITEP differed from the ones in the veto, hence by modelling the actual veto block geometries it was possible to predict the number of photoelectrons emitted as a function of distance from the PMT for each of the 52 scintillator blocks (accounting for five different geometries). These light curve equations were included in a larger Monte Carlo of the ZEPLIN-III detector with the veto geometry. This initial work on the Monte Carlo provided good preliminary estimates for the type of efficiencies expected from the veto. In Chapter 5 similar work was performed to characterise the actual scintillator sections used in the veto construction allowing better estimations of the veto efficiency.

4.2.2.3 Additional Components for the Scintillator Sections

The PMTs attached to each scintillator section are very sensitive to light, to the point where overexposure can cause permanent damage to the PMT photocathode. Hence, the scintillator sections were wrapped in black PVC sheeting

to reduce the amount of light from external sources entering the blocks. The PMT sensitivity is such that even pin-holes in the sheeting can cause signal saturation. To reduce this effect many hours were spent in darkened rooms with torches to determine their location and cover them using radiopure light-tight copper tape. The PMTs themselves were housed and supported using caps de-

Figure 4.9: *The PMT caps were glued onto the scintillator sections. The caps serve two purposes, firstly to protect the PMT from external light sources and secondly to hold the PMT into position.*

signed to fit around the veto PMTs. These caps were produced from a black PVC pipe and glued directly onto the scintillator. Figure 4.9 displays one of the caps undergoing attachment to a scintillator section. The caps serve two purposes, firstly to protect the PMT from external light sources and secondly to hold the PMT into position. The PMTs are optically coupled to the scintillator with optical grease (BC-603 purchased from Saint Gobain Crystals Lt [149]). All of the veto PMTs were positioned in such a way, that over time their own weight will cause them to move or pull away from the scintillator. The caps contain spring loaded screws that are attached to the PMT base and the PMT cap lid forcing the PMT into position, against the scintillator. Movement of the PMT will be significantly reduced with good optical contact maintained throughout veto operation.

Mylar mirrors were also placed at the far end (opposite to the PMT) of each scintillator section to improve linearity.

4.2.3 Construction of the Scintillator Sections

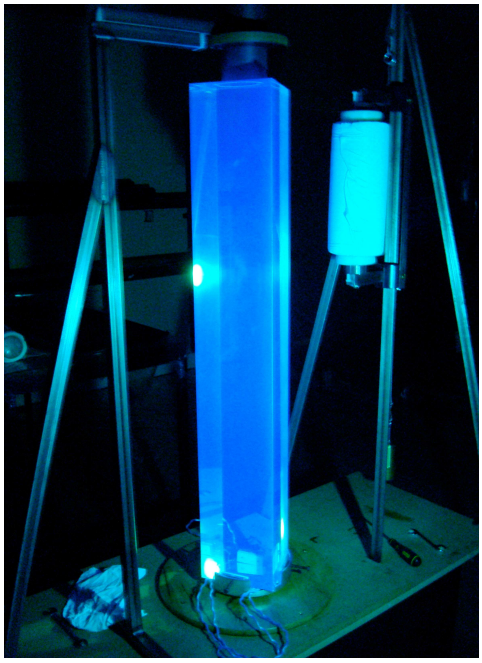

Figure 4.10: *The PTFE wrapping jig, with a scintillator block in place prior to wrapping.*

A clean room was established within the University of Edinburgh for veto construction. First, the PMT caps were attached to the scintillator ends, then the scintillator sections were wrapped with PTFE with the aid of a specially designed wrapping jig; this is shown in Figure 4.10. The bare scintillator block was mounted onto a turntable and held into place at its base and with its PMT cap. The PTFE roll was tensioned so that after one turn of the block it moved upwards until the top of the scintillator block was reached. Using the jig enabled the majority of the scintillator section to be wrapped uniformly and with speed. Some of the more intricate areas were wrapped manually.

The blocks were then wrapped in the black light tight sheet cut to the specifications of particular block geometries. Any holes in the wrapping were later plugged with copper tape. Once the preparation of all scintillator sections was

Figure 4.11: *Wrapping the scintillator sections. Here a scintillator block is undergoing wrapping with a black light tight sheet. This was performed after the PMT cap had been glued and after the block had been wrapped with PTFE.*

complete, testing of each section was initiated to ascertain their performance; this is discussed later in Chapter 5.

4.2.4 Photomultiplier Tubes

Attached to the far end of each of the 52 scintillator segments are low background PMTs. The photomultiplier tubes (model 9302KB) were supplied by ETEL [150] and are 113 mm in length with a 78 mm (3 inch) circular face. They have a blue-green sensitive balkali (K-Cs-Sb) photocathode, suitable for the UV emitting scintillator. They have nine amplification stages with a gain of 0.7×10^6 achievable [150], and a spectral range covering 285-630 nm, with the optimum response at a wavelength of $\sim$ 420 nm. These PMTs were chosen due to their low background construction with manufacturer quoted contamination levels of U, Th and K of 30 ppb, 30 ppb and 60 ppm, respectively. The radioactivity of a sample PMT was independently verified with testing performed at the low background counting facility of the Boulby mine (details given in Section 4.3 of this chapter).

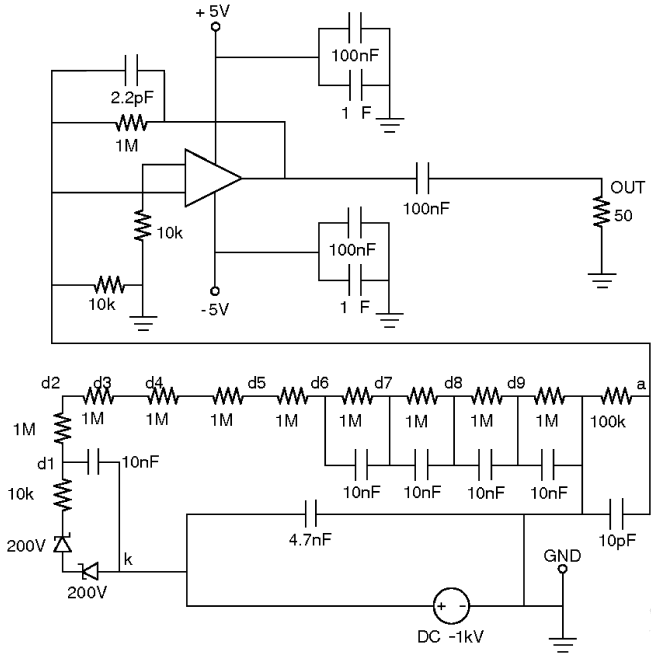

Figure 4.12: *Schematic diagram of the PMT electronics. Displayed is the voltage dividers network and pre-amplifier. k and a denote the cathode and anode locations, respectively.*

The aim of any PMT is to convert photons into a usable output signal. When a photon enters a PMT it impinges on photocathode (k) material where an electron can be emitted in accordance with the photoelectric effect. The remainder of the PMT generally contains a cathode, dynodes and an anode. When an electric field is applied across this system a potential ladder is set-up enabling photoelectrons produced at the photocathode to be accelerated and focused onto a dynode. These PMTs use linear focused SbCs dynodes. The impact of the incident electron transfers energy causing secondary electron emission. These liberated electrons are then accelerated to the second dynode, where more electrons can be liberated. This process is repeated multiple times depending on the number of dynodes present, creating an electron cascade. Eventually the electrons meet the anode and a current is produced, providing the output signal. There are various designs for dynodes, the design chosen for the veto PMTs is linear focused, due to the fast transit time of the electron through the multiplier structure and good linearity at high current. The ratio between the secondary and primary emission of electrons at a particular dynode not only depends on the energy of the incident electron but also on the potential present between each dynode. This is controlled by the voltage divider network.

PMT voltage dividers (ETL C647BFM2-01) were also supplied by ETL and are attached to the low background PMT bases (ETL model type B14A). The voltage divider accelerates and focuses photoelectrons onto the first dynode (d1 see Figure 4.12), and repeats the processes for each remaining dynode, until the last dynode is reached. The voltage between each consecutive dynode has to be greater than its predecessor to accelerate the liberated electrons.

In addition to the voltage divider, custom made pre-amplifiers were also built onto the PMT bases. They served two purposes, firstly to impedance match the signal from the PMTs to the DAQ digitisers and secondly to amplify signals with a gain of 11. The pre-amplifier boards were also constructed on low-background single sided resin bonded paper. Figure 4.12 displays the PMT electronics. The PMTs are powered with a negative bias.

All 52 PMTs were tested to ascertain their performance. The methodology and results are described in Chapter 4.

4.2.5 Additional Electronics

All veto PMTs are powered by Lecroy 1443F boards within a Lecroy 1440 HV voltage supply. Cabling for the PMTs and the DAQ are made-to-order [151] assuring consistency with the background requirements. A ±5V pre-amplifier power supply for the PMTs has also been custom built at the University of Edinburgh.

Each scintillator has been implanted with an optical fibre and then all optical fibres connected to a single UV LED. The LED is driven with a custom built (University of Edinburgh) unit that can flash the LED such that it emits a well controlled amount of light allowing a required number of photo-electrons to be generated as desired. It can also be pulsed at a wider range of frequencies, from single pulses to test functionality, or for a series of pulses to generate spectra, or to test for stability over longer periods. Together with occasional exposure to calibrated gamma-ray sources, this will allow any change in the performance of the plastic, or of the PMTs, to be monitored over the duration of the experiment.

4.2.6 Data Acquisition

The signal outputs from all veto PMT pre-amplifiers are input into one of seven 8-channel 14-bit CAEN V1724 ADCs situated within a VME8011 crate with CAEN V2718 PCI bridge. The DAQ communicates with a dedicated computer. Custom software has been developed using the libraries provided by CAEN for data acquisition. This enables the user to fully operate the device through software and change run parameters for various operation modes. The main attributes of the DAQ include the following;

- 100 Ms/s sampling rate simultaneously on each channel
- Internal buffering providing zero dead-time performance
- 2.25 Vpp ± input range of the digitisers
- 40 MHz bandwidth

To ensure synchronisation between the ZEPLIN-III detector and the veto, a unit has been specifically manufactured that can produce a digital trigger and time stamp all events. These time stamped events are then sent to both the ZEPLIN-III and veto DAQs so that the events can be correlated.

4.2.6.1 Triggering

The veto can be operated in two separate modes, the veto 'slave' mode and calibration/diagnostic 'master' mode. In the slave mode all DAQ modules take an external trigger from the ZEPLIN-III instrument. When energy is deposited within ZEPLIN-III the veto will record data. The benefits for this include;

1. Reduction in data volume
2. No efficiency loss at low energies (no veto threshold required)
3. Possibility to continuously monitor veto PMTs for any obvious variations
4. Monitoring of environmental background during acquisition

The last point is feasible due to the predictions made using Monte Carlo simulations of the veto (see Chapter 5). Simulations have shown that gamma-ray energy depositions within the veto of greater than 200 keV deposit more than 90% of their energy in less than six plastic scintillator sections. Hence, when the veto is triggered, the remaining sections will also record diagnostic information concerning the background present during the triggering event in ZEPLIN-III.

The expected time delay between signals in ZEPLIN-III and the veto was also determined with the aid of Monte Carlo simulations of the veto. Coincident gamma-rays will be effectively instantaneous; however single scatter neutron recoils within ZEPLIN-III would have a small time delay before detection by the veto PMTs. This time delay can be attributed to the neutron being thermalised in the polypropylene shielding prior to capture by Gd or H. Gamma-rays emitted due to neutron capture will then be detected by the veto PMTs. According to simulations (see Chapter 6) the time taken between an energy deposition in ZEPLIN-III to detection by a veto PMT has a mean difference of $\sim 35\mu$s, falling off exponentially. In ZEPLIN-III small signals are triggered by the S2 electroluminescence, hence a maximum time delay of 17μs is accounted for due to the time it takes for electrons to travel through the liquid phase to the gas phase (based on the length of the liquid phase). The veto, therefore has a pre-trigger of 20μs and a 300μs post-trigger.

The 'master' diagnostic/calibration mode is designed to record continuously with input of a fast external pulsed trigger. In this scenario a threshold signal may or may not be imposed, for example data may only be recorded when a

certain number of veto sections are above a defined threshold. This enables calibration of the veto device and for recording background data in all modules. As such the veto can effectively operate as a separate detector independently of the ZEPLIN-III instrument.

A combination of the two above scenarios will be implemented. The veto will trigger whenever energy is deposited within ZEPLIN-III, regardless of whether the veto observes the event. In addition to this, the veto will also trigger whenever signals above a threshold of 6 phe are observed in two scintillator sections. All events will be stored within the internal DAQ buffer (zero deadtime), therefore no ZEPLIN-III triggered event will be missed.

It is also possible to measure the cosmic muon flux through the laboratory by taking advantage of the segmented nature of the veto. The PMT outputs from the twenty roof sections are input into a dedicated triggering unit. These signals are passed to the ADC inputs where they are summed and the summed signal is shaped. If this summed signal meets the criteria for a cosmic muon event all 52 channels are triggered and the event is recorded.

4.3 Radiological Content of the Veto Components

Chapter 2 has already discussed in detail the importance of low background running of dark matter detectors. Consequently any material introduced to the ZEPLIN-III environment has to undergo radiological testing and the veto is not exempt from this.

The main radioactive contributions from the veto can be attributed to U and Th, which produce neutrons via (α,n) reactions (see Figure 4.13). There are also smaller contributions from fission, and from K via beta-decay, populating the 1.461 keV excited state in ^{40}Ca which then contributes to the gamma-ray background. Radon and its progenies also must be considered. To access the overall neutron and gamma-ray background contribution from the veto components, two methods of measurement were undertaken.

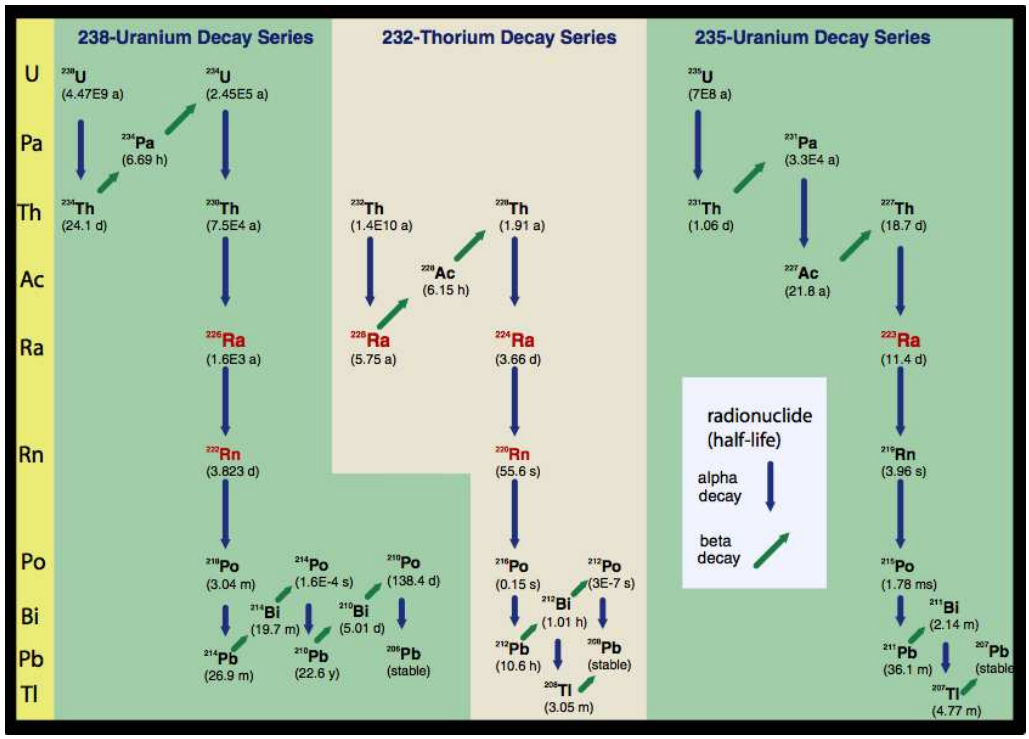

Figure 4.13: *The U and Th decay chains. The transitions are mediated by (α,n) reactions with the materials of the components. Neutrons produced may subsequently deposit energy within the ZEPLIN-III target. Image taken from [152].*

Component	Mass	Radiological content U (ppb)	Th (ppb)	K (ppm)
HPGe measurements				
Plastic scintillator	1057 kg	0.2 ± 0.3	0.1 ± 0.7	0.2 ± 0.6
PTFE Outer wrap	8.9 kg	1.3 ± 0.2	0.2 ± 0.5	1.2 ± 0.4
Silicone	103 g	2.9 ± 0.4	0.5 ± 0.8	5.7 ± 1.1
PTFE tape	3.1 kg	3.2 ± 1.3	6.1 ± 1.1	3.9 ± 1.0
Veto PMTs	6.2 kg	38.0 ± 0.8	21.1 ± 1.2	65.5 ± 2.4
PMT preamps	660 g	8.4 ± 1.7	13.2 ± 2.2	10.1 ± 1.7
PMT base	5.5 kg	12.7 ± 1.4	14.8 ± 2.4	20.2 ± 2.4
Epoxy	70 kg	2.5 ± 0.6	0.9 ± 0.3	0.6 ± 0.1
Gd oxide	8 kg	0.9 ± 0.1	1.2 ± 0.3	1.7 ± 1.1
Cavern rock	N/A	66 ± 6	145 ± 13	1130 ± 200
ICP-MS/OES				
Copper tape	26.0 kg	1.9 ± 0.2	2.9 ± 0.43	14.0 ± 2.0
PTFE inner wrap	8.8 kg	2.0 ± 1.0	5.0 ± 1.0	< 4
Veto PMTs	6.2 kg	30.2 ± 2.2	30.0 ± 3.7	60 ± 2.2
PMT preamps	660 g	10.3 ± 0.5	29.7 ± 3.2	24 ± 3.7
PMT base	5.5 kg	13 ± 3.4	19 ± 2.0	21 ± 3.0
Polypropylene	510 kg	<1	< 1	<5
PMT mounting	15.8 kg	30 ± 7.8	<10	10
Cabling	30.2 kg	110 ± 5.4	20 ± 3.2	29 ± 7.3
Connectors	2.1 kg	<10	<10	<4
Optical gel	260 g	<1	<1	<1
Gd oxide	8 kg	2.5 ± 0.5	3.4 ± 0.7	< 4.0

Table 4.2: *Radiological content of veto components as assessed either by direct observation of gamma ray emission or through inductively coupled plasma techniques. The gamma-rays emitted from the U, Th and K content in the laboratory rock were obtained from reference [143]. HPGe measurements and simulations pertaining to the Ge detector only, were performed by colleagues at the University of Edinburgh, but their impact on ZEPLIN-III was investigated by the author using the veto simulation as discussed in Chapter 6*

4.3.1 Direct Measurements of Radioactivity of Components

Direct measurements of the veto components were performed using a high purity germanium (HPGe) detector located in a dedicated low background counting facility at the Boulby mine. The HPGe detector head is encased in an inner copper and outer lead castle with dimensions $30 \times 30 \times 30$ cm^3. Prior to the testing of materials, the ambient gamma-ray flux within the HPGe box was measured. The sample material was then placed within the detector device and data acquired for approximately a week. The spectra produced were then background subtracted, revealing photo-peaks at energies corresponding to known gamma ray emissions from dominant spectral lines in particular U, Th and K.

To assess the quantity of an isotope that must have been present to generate the measured excess in the background-subtracted spectrum, a GEANT4 Monte Carlo of the testing facility was performed. The Monte Carlo was tailored for each test, for example the detector remained constant for all simulations, but if the veto PMTs were being tested a simulation of these PMTs was performed within the detector environment. Inputs to the Monte Carlo included the the test chamber, HPGe detector geometry and the test sample. The HPGe was calibrated using multi-line gamma-ray calibration sources positioned around the detector device from which the detector efficiency was determined. Sensitivities at the parts per billion level for U and Th, and parts per million level for K were achieved using this technique. A summary of the components tested and their measured activities is shown in Table 4.2. The conversion between gamma rays emitted from an isotope and the source contamination level is given using, for 1ppb U, 1ppb Th, and 1ppm K as 2310, 958, and 285 gamma rays per kg per day, respectively.

4.3.2 Mass Spectrometry Measurements of the Radioactivity of Components

To supplement and check the accuracy of the above gamma-ray measurements a selection of components were also measured using an alternative technique. Samples were tested by Geosciences Advisory Unit (GAU-Radoanalytical) at the University of Southampton. The samples were dissolved in acid and diluted in 2% HNO_3 and their activities of ^{232}Th, ^{235}U and ^{238}U were measured using

an inductively coupled plasma mass spectrometer. The potassium content was assessed using an inductively coupled plasma optical emission spectrometer. To calibrate the data a ^{236}U recovery tracer was added to the dissolved sample. The results from this process are also presented in Table 4.2 and are broadly consistent with the gamma ray measurements.

To assess the impact of the veto radioactivity levels on the ZEPLIN-III detector these were simulated in a Monte Carlo of the veto and ZEPLIN-III. This is discussed in further detail in Chapter 6. Using these simulations it was possible to provide a check as to whether the radioactivity levels of a particular component were acceptable to continue the low background running of the ZEPLIN-III device.

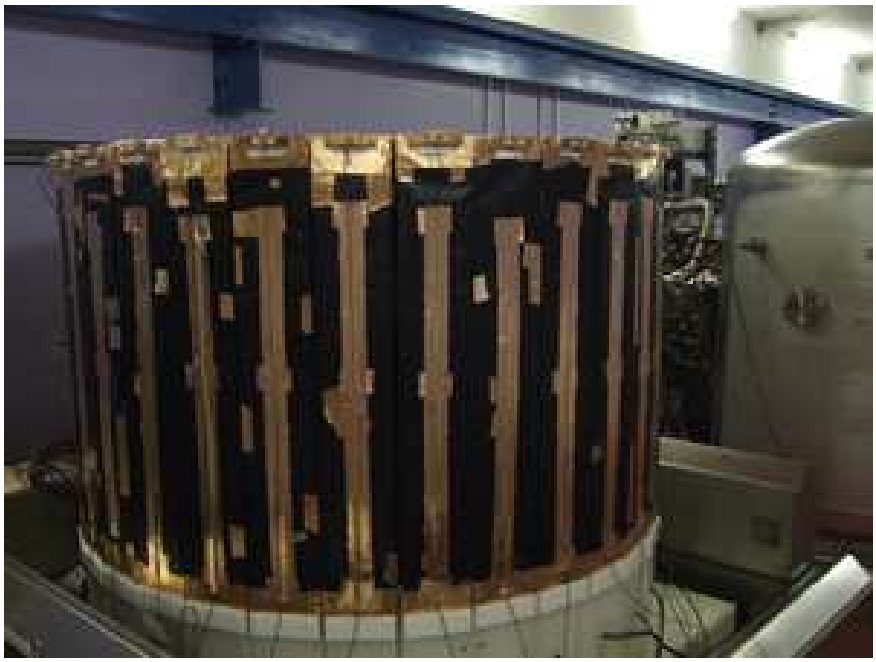

Figure 4.14: *The veto in situ, positioned around ZEPLIN-III underground in Boulby mine. The lead shielding (not shown) is positioned around the veto.*

4.3.3 Current Status of the Veto

As of February 2010 the veto has been built and tested underground. Figures 4.14 and 4.15 show the veto assembly. Figure 4.14 displays the veto without the roof sections and the lead shielding. Figure 4.15 shows a section of the veto

Figure 4.15: *The veto partially shielded with lead. The entire structure of the veto is surrounded by lead.*

structure with half of the lead castle built around it. The veto will be fully contained within the lead castle to reduce the external gamma-ray flux. For a background device, it is important to ensure extreme cleanliness to prevent dirt, etc. entering the system. As such, precautions such as thorough cleaning and gloved handling is mandatory for all systems in and around ZEPLIN-III.

The principle purpose of the veto is to reduce or detect non-WIMP events that deposit energy in the ZEPLIN-III detector. The veto has passive section designed using gadolinium loaded polypropylene shielding and an active section constructed with plastic scintillator. Neutrons that enter the passive shielding are moderated and then captured onto Gd or H with the subsequent emission of gamma-rays. The emitted gamma-rays may then enter the active component of the veto where they are detected by the veto PMTs. The veto will trigger when there is an event within ZEPLIN-III but it can also be used as a stand alone device to monitor background and take measurements such as the muon flux within the laboratory.

The veto will serve multiple roles, firstly to identify and remove coincidents with ZEPLIN-III and secondly to monitor the background environment. In

the SSR in the event of a non-zero observation the veto can prove to be a powerful tool to bolster the argument that the events observed are WIMPs and not background. $\simeq 0.4$ events per year are expected in ZEPLIN-III; however this can be reduced further to $\simeq 0.14$ due to the veto (see Chapter 6 for further details) a significant factor in the event of non-zero observation.

Chapter 5

Veto Construction and Testing

5.1 Introduction

Prior to the installation of the veto, all components underwent performance testing. Described in this chapter are the testing methodology and results for all 52 PMTs and scintillator blocks that comprise the veto. The results obtained from these experimental measurements have then been utilised to match scintillator sections to PMTs, where lower performance PMTs are optically coupled to high performance scintillator blocks and vice versa, improving uniformity across the array. In addition to the experimental tests, a Monte Carlo simulation of the scintillator block experiment has also been developed. This Monte Carlo served two purposes, firstly, to demonstrate understanding of the performance and secondly to aid in production of light curves for all scintillator blocks. The light curves give the number of photoelectrons per unit energy deposition for various positions along a particular scintillator section when particles interact with it. These light curves are designed for input into a larger Monte Carlo of the entire veto coupled to the ZEPLIN-III detector.

5.2 Photomultiplier Tube Testing

5.2.1 Introduction

Arguably the most important component of the veto are the PMTs, and therefore rigorous testing was required to ascertain their performance. The PMTs were purchased from ETEL [150] who provided operating voltages for 50 A/lm and 200 A/lm. These operating voltages were re-checked at the University of

Edinburgh as part of the testing programme. The PMTs were ranked according to their bias voltages by obtaining single photoelectrons spectra (SPE) for all PMTs. SPE data inherently provides an excellent indication of PMT response. In an idealised system, constant gain (amplification of the signal) from one PMT to another would be attained for a photon of a particular wavelength entering the PMT and hitting the dynode, generating an electron. However, in reality this will not be observed and the gain will fluctuate. This is predominantly due to variations inherent to the design of a PMT that will effect the emission of secondary electrons. SPEs essentially give the response of the PMT. Increasing the gain until the SPE is observed above background provides the optimum voltage the PMT should be set if low energy signals are to be detected. Below this voltage no signal will be observed (and significantly above this voltage there is a risk of PMT breakdown and permanent damage occurring. The SPE and can also be used for calibration of the detector.) The effective quantum efficiency (QE) was also determined for each PMT providing another measure of their quality. The QE is the average photoelectron yield from an incident photon, therefore for a PMT with 30% QE, an average of 3 out of every 10 photons will produce photoelectrons. This is crucial, as the QE essentially describes how efficient the detector is.

Tests performed at the University of Edinburgh were aimed at identifying the performance of each PMT based on the above criteria.

5.2.2 Ranking in Terms of PMT Gain

Spectra from all 52 PMTs were obtained in a custom built chamber providing a dark environment. The signals observed in these tests come from spontaneously emitted electrons from the photocathode, and thus coupling of the PMTs to the scintillator was not required (indeed, it would have caused additional signals that would have hindered the measurement). To observe an SPE spectrum the bias voltage of each PMT was increased until the SPE peak appeared in a particular ADC channel (channel number 130 was chosen). Due to low statistics the PMTs were then exposed to a pulsed blue LED light source, driven by a linear pulser unit giving pulses of $\sim$ 100 Hz, with a width of 85 ns. The LED voltage was set to only allow a small amount of light to be produced, hence the probability of inducing more than one photoelectron from the photocathode at a time was

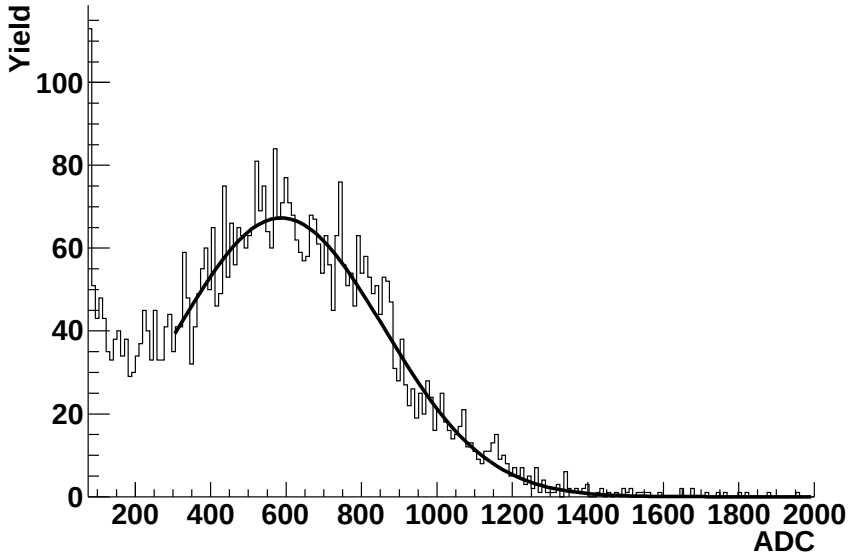

Figure 5.1: *A typical single photoelectron spectrum obtained from a veto PMT. This spectra were obtained with the presence of the blue light source and within a dark environment. The PMT was not attached to a scintillator section.*

small. Whilst keeping the PMT bias voltage constant, the voltage of the LED was varied until the peak produced by the LED was also observed in channel 130, thus indicating SPE generation.

Figure 5.1 shows a typical spectrum of events generated with a blue LED driven with a voltage corresponding to several photoelectrons. The width of the peak is dominated by the Poissonian statistics of the photoelectron emission where,

$$\sigma = \mu/\sqrt{N} \tag{5.1}$$

where σ is the measured width (1 s.d.), μ is the centroid of the peak, and N is the mean number of photoelectrons emitted for events in the peak. This relationship was used to calibrate, converting channel number to number of photoelectrons observed. The dependence observed between the centroid and the width from LED spectra was consistent with the observed position of the SPE peak in the absence of a light source confirming the validity of this approach.

Based on the ADC channel number where the SPE was observed, and the

gain required to drive the PMT, a ranking based on PMT gain was then produced.

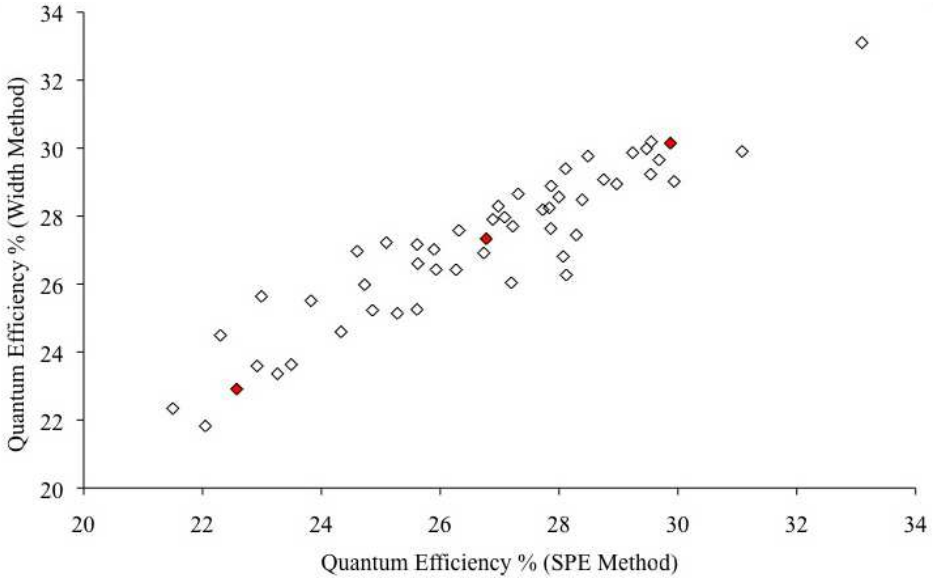

Figure 5.2: *The distribution of QEs, as determined using two methods for the estimation of the number of photoelectrons. The errors associated with the width method measurements are* $\sim 0.2\%$ *and with the SPE measurements is* $\sim 0.5\%$

5.2.3 Ranking in terms of Relative PMT Quantum Efficiency

All PMTs were also ranked according to their relative quantum efficiencies (QE). Again, the LED was used for these measurements, which were made relative to a single reference PMT to ensure environmental and electrical uniformity throughout testing. The reference PMT was randomly chosen from the set purchased from ETEL and had an operating voltage of 1126 V.

Both the reference PMT and the PMT to be tested were placed in a custom made chamber and the k-a voltage of the test PMT varied until the spectral peak position observed from single photoelectron emission from the photocathode was matched to that of the reference PMT. At this individual k-a voltage for each PMT, the photocathode was illuminated by the fixed voltage pulsed LED. The number of photoelectrons observed were calculated using the above calibration which uses the width dependence of the peak seen, but also estimated by simply

dividing the peak position of the LED spectrum by that obtained from the dark environment single photoelectron peak data.

The measurements confirmed the relative QEs between PMTs for sensitivities of 50 A/lm and 200 A/lm as quoted by the manufacturer. The measured response from all PMTs were then normalised to the absolute QEs by having the absolute QE of three of the 52 PMTs measured externally by ETEL. The mean QE of the PMTs at a wavelength of 360 nm was found to be 30.1% and at 420 nm is 27.1%. The PMTs were considered to show good performance and could therefore undergo optical coupling to the scintillator sections (once these had undergone testing). The distribution of QEs, as determined using either method for estimating the number of photoelectrons, is shown in Figure 5.2.

5.3 Characterising the Veto Scintillator Segments

All 52 scintillator sections, which comprise the veto, have undergone individual testing to ascertain the quality of the plastic and their response to gamma-rays and neutrons. Using a combination of experimental testing in a laboratory at the University of Edinburgh, and GEANT4 simulations, it was possible to characterise each scintillator section and then, based on this information make predictions as to how effective the complete veto construction would be in the finished detector environment. The key aims for this research were;

1. Determine which scintillator block should be matched to which PMT based on the quality of the plastic and the proximity of the scintillator block to the ZEPLIN-III active volume.

2. Predict the efficiency of the entire veto detector as a final product.

5.3.1 Experimental Determination of the Technical Attenuation Lengths of the Veto Scintillator Sections

All 52 scintillator sections were tested to ascertain their individual Technical Attenuation Lengths (TAL), a key property of plastic scintillator. The TAL of a plastic scintillator is defined as the length corresponding to a reduction in the light signal by a factor of $1/e$, accounting for the plastic scintillator thickness, geometry and reflective surface properties. As such, the TAL is a property of

the specific units produced, and indicates the likely observed performance. The manufacturer of the plastic scintillator, Amcrys-H [147] had provided information of the Bulk Attenuation Lengths (BAL) for 37 of the scintillator sections. The BAL, in accordance with the Beer-Lambert law, is described as the reduction from the initial light intensity by a factor of e, due to self-absorption by the molecules that comprise the plastic material. The main difference between the BAL and TAL measurements is that the BAL does not account for any surface reflections or the geometry of the material. The BAL is mainly dependent on the material purity, regardless of its implementation in a specific experiment. Hence, the measured TAL values of any scintillating material are expected, generally to be lower than the equivalent BAL values [153] [154], due to the inclusion of these surface effects. Moreover, the TAL is more experimentally crucial, as this would describe the actual observed detector performance.

5.3.1.1 The Experiment

Prior to testing, each scintillator section had been wrapped with three layers of PTFE and a final layer of black, light tight wrapping (see Chapter 4 for further details). A 3" ETEL PMT, with attached VDN pre-amplifier, was positioned at a scintillator section end, which was itself located in a light-tight black cylindrical casing (see Section 5.2 and Chapter 4 for further details on the PMTs). At the opposite end of each scintillator section to the PMT, a Mylar mirror was placed for reflecting light back into the block, increasing the effective light yield of the scintillator.

Measurements were performed in a surface laboratory of predominantly concrete construction, and thus, for plastic scintillators of this size, a high rate of background gamma-rays were observed. This is mainly due to isotopes such as ^{40}K which have a relatively high concentration in concrete. To reduce the background rate a coincidence circuit was employed. Events observed by the scintillator PMT were required to be in coincidence with a 3" diameter, 3" long sodium Iodide (NaI) detector. A ^{22}Na source was situated on top of the scintillator block at various positions along the block lengths (depending on the length of the block, see Table 5.1). The NaI detector was then located above the ^{22}Na source, with added collimation from two lead blocks to reduce the area of scintillator being exposed to gamma-rays. The ^{22}Na calibration source was chosen as it decays via the emission of a positron, which subsequently annihilates with an

electron to produce two back-to-back 511 keV gamma-rays. These gamma-rays are detected, in coincidence, by the NaI detector and the scintillator PMT. In addition to the 511 keV gamma-rays, the ^{22}Na decay process also generates a 1275 keV gamma-ray. However these gamma-rays are not produced back-to-back as are the 511 keV gamma-rays. Some 1275 keV gamma-rays will occur in coincidence with a 511 keV; however at a significantly reduced rate. Lead collimation will also serve to reduce the number of 1275 keV events observed. Hence, the resulting spectra of events have a high fraction of 511 keV events, allowing a known feature to be used in analysis.

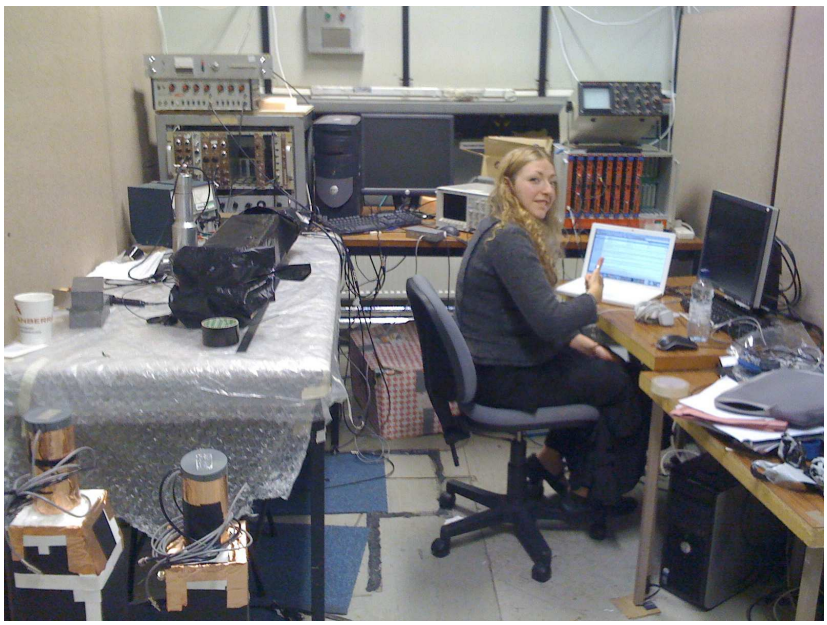

Figure 5.3: *The experimental set-up at the University of Edinburgh. To the left of the figure is a scintillator block within its light tight wrapping undergoing testing. At the back of the figure are the electronics and MCA readout (Maestro).*

For these tests the PMT was powered by a 415b HV supply. Optimal PMT performance at 420 nm was obtained by setting each PMT to a specific voltage, provided by ETEL. The PMT pre-amplifier was powered by a ±5 V Farnell L30AT power supply. The PMT signal was then input to an amplifier with a gain setting of 10, course gain of 0.3 and positive polarity for the procurement of ^{22}Na spectra. The unipolar output was fed into a Gate and Delay Generator (GDG). The delayed signal was input to a Multichannel Analyser (MCA) using a Maestro ADC and software [155] to acquire and visualise the spectra. The

NaI detector was powered using a 600 V supply. The signal was amplified by a custom-made pre-amplifier. This signal is then fed into an amplifier, converting the signal to positive output, and then fed into a GDG with a 1.4 μs delay. When the NaI detector was triggered, this then acted as a gate for the PMT pulse. Hence, only coincidence events between the PMT and NaI detector were observed. The width of the gate was adjusted to cover the entire PMT pulse, and the NaI gate signal was delayed to ensure it 'opened' in conjunction with the start of a PMT signal. The NaI gate and PMT signal were both input into the MCA, where only gated PMT events were registered.

All ^{22}Na spectra measurements were taken for a livetime of 600 s, with the ^{22}Na source and NaI detector positioned at various distances along the length of each scintillator section. Due to the variations in geometry and size of block types, the distance between each point and number of positions chosen varied, as displayed in Table 5.1.

To monitor PMT response throughout the testing, and to provide calibration data for conversion of data from channel number to photoelectrons, SPE spectra were obtained. All SPE measurements were taken before and after ^{22}Na measurements for a block. SPE readings were obtained by removing the coincidence circuit and inputting the PMT signal directly into the MCA. The gain on the PMT amplifier was increased to 100 to ensure true observation of the SPE, not noise. The analysis of the SPE data will be discussed later in Section 5.3.2.

Block Geometry	**Number**	**Block Length (cm)**	**Data points measured**	**Dist. between each point (cm)**
Trapezoid sections	32	98.5	9	10
Roof block 1	8	80.0	7	10
Roof block 2	4	75.0	9	8
Roof block 3	4	67.1	8	7
Roof block 4	4	51.5	7	5

Table 5.1: *Shown are the number of measurements taken in relation to the scintillator block length and geometry type. The label 'roof block 1' etc. refer to the different block lengths and geometries. Schematic diagrams of each block geometry can be found in Chapter 4.2.*

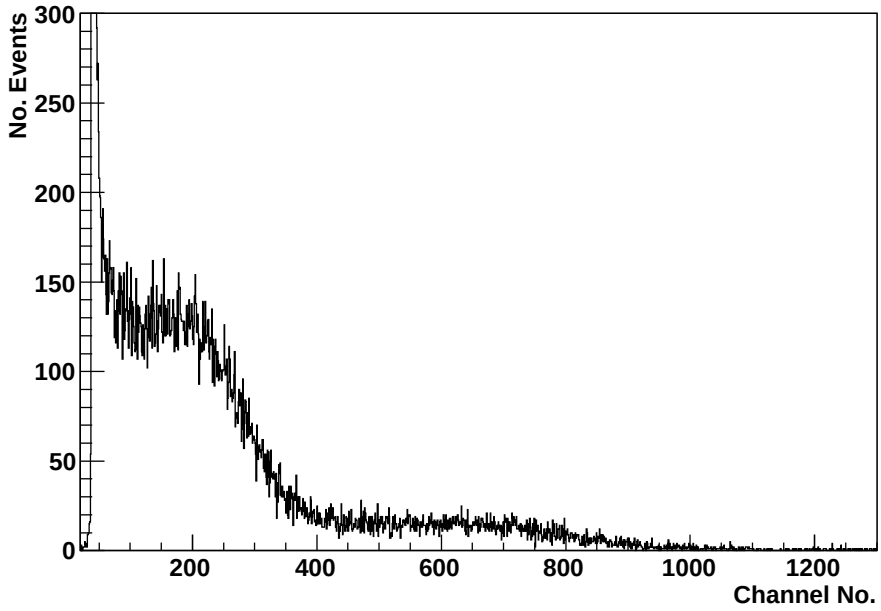

Figure 5.4: *A typical spectrum showing the response of a single barrel section of plastic scintillator to irradiation with a ^{22}Na gamma ray source at a horizontal distance of 80 cm from the PMT face.*

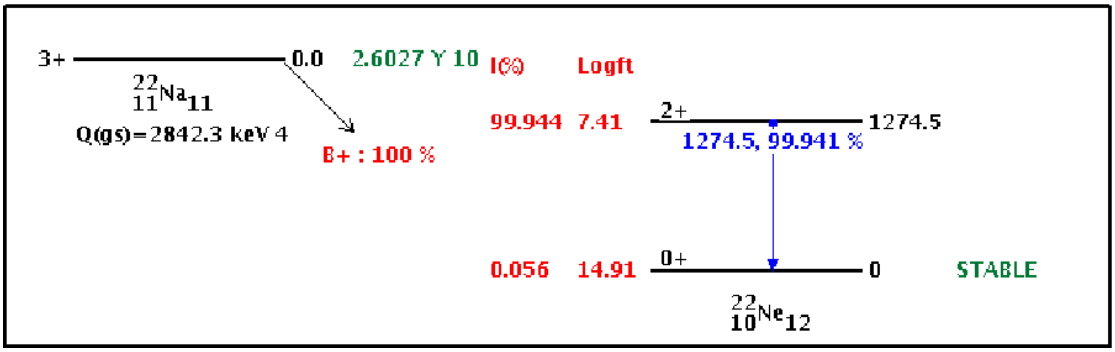

Figure 5.5: *^{22}Na decay scheme showing β^+ emission with an intensity of 100.0 %. The β^+ annihilates with an electron from the local environment to produce 511 keV gamma-rays. A 1275 keV gamma-ray can also be emitted with an intensity of 99.944% leaving ^{22}Ne in its ground state.*

5.3.2 TAL Data Analysis

5.3.2.1 Typical Spectra

A typical spectrum obtained from the irradiation of an ^{22}Na source 80 cm from the PMT face is shown in Figure 5.4, revealing a broad peak corresponding to the 511 keV gamma-rays (around channel 200). A second feature is observed between channel numbers 400-1000; this is attributed to 1275 keV gamma-rays, also emitted from ^{22}Na (see Figure 5.5 displaying the ^{22}Na decay scheme).

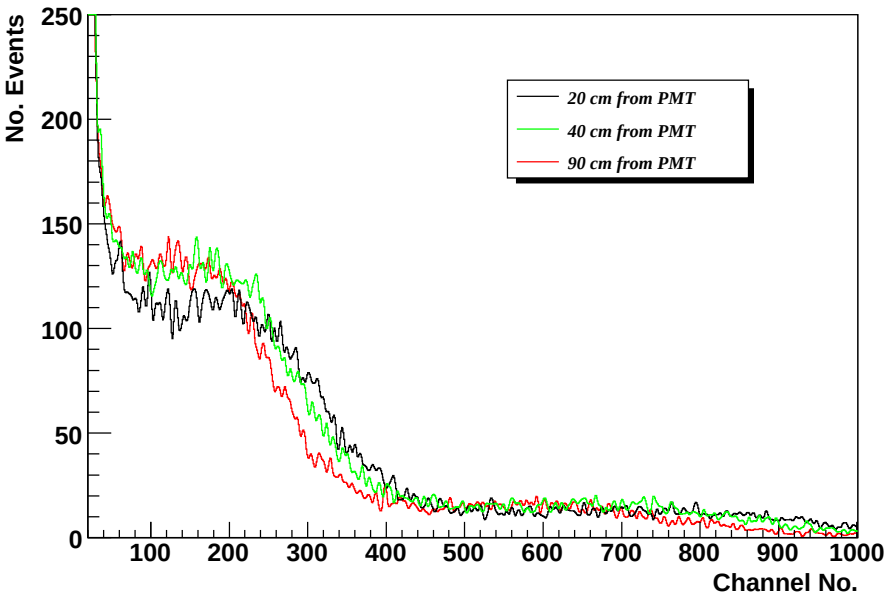

Figure 5.6: *Shown are three sets of data taken at 20 cm, 40 cm and 90 cm from the PMT face using a ^{22}Na gamma-ray source. The data is for barrel section 1-1-08-7 which has a BAL of 171 cm (Amcrys-H value). Notice how the broad peak due to 511 keV gamma-rays (between channel numbers 100-400) moves to the left as the source position moves away from the PMT face, signifying a reduction in light reaching the PMT. The data has been smoothed to provide the viewer with easier comparison between the different measurements.*

Figures 5.6 and 5.7 show spectra from two tested scintillator sections. Figure 5.6 displays three of a total of nine measurements taken for barrel scintillator section 1-1-08-7. The three different data sets relate to the position of the ^{22}Na source set at 20 cm (black), 40 cm (green) and 90 cm (red) from the PMT face. The quoted BAL for this scintillator block was 171 cm and can be assumed

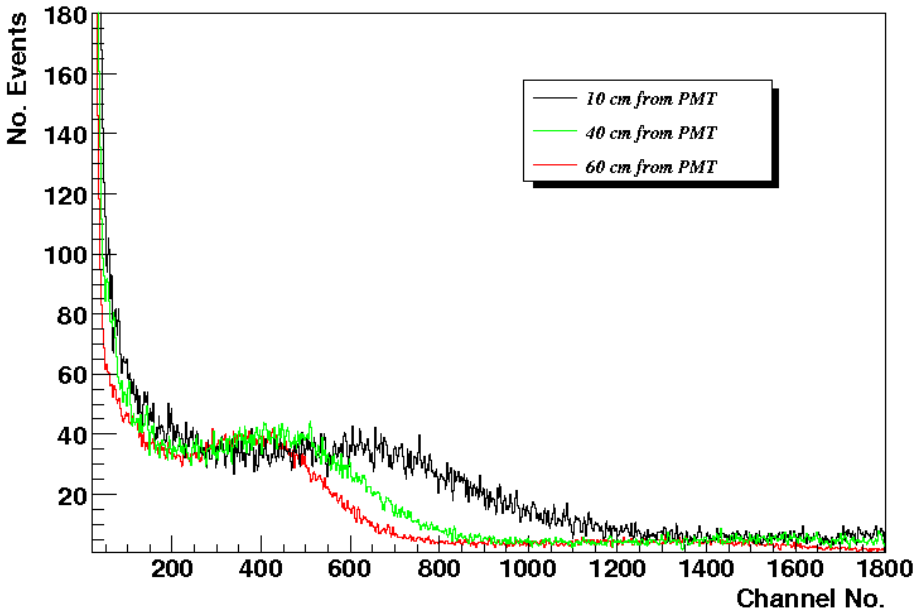

Figure 5.7: *The figure displays three sets of data taken at 10 cm, 40 cm and 60 cm from the PMT face using a ^{22}Na gamma-ray source. The data displayed is for roof section 61-4 of 80 cm length and with a BAL of 91 cm (Amcrys-H value). Notice how the broad peak due to 511 keV gamma-rays (between channel numbers 100-1200) shifts to the left as the source moved away from the PMT face. The data has been smoothed and also scaled in the y-axis to enable the viewer easier comparison between the different measurements.*

to be a medium to high quality scintillator section. The 511 keV peak moves to the left as the ^{22}Na source is positioned further away from the PMT face, indicating a reduction in light reaching the PMT. Figure 5.7 also shows three data sets (from a total of 7 data sets obtained) measured for an 80 cm length roof scintillator section. The three spectra correspond to measurements taken when the ^{22}Na was positioned at distances of 10 cm, 40 cm and 60 cm from the PMT face. These measurements were taken for block number 61-4 with a quoted BAL of 91 cm. Hence, this block can be regarded as lower in quality.

The BAL or TAL effect can be seen by comparing the difference of the 511 keV peak positions as a function of distance from the PMT face. Generally, a larger difference between peak positions (or reduction in light) is observed as a function of distance to the PMT face for lower quality (i.e lower TAL and BAL) scintillator segments. A high BAL or TAL reduces the difference between peak positions because of a more uniform light yield despite the distance between gamma-ray source and the PMT face. This difference is anticipated when referring to the TAL or BAL of a scintillator block, as photons will undergo reduced attenuation with a higher quality scintillator slab.

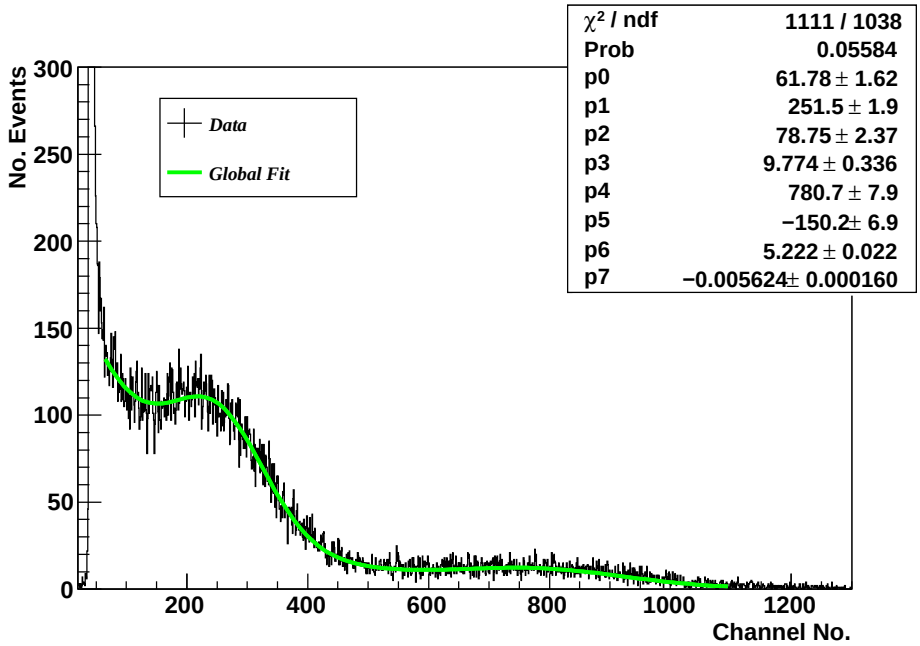

Figure 5.8: *Fitted spectrum of Figure 5.4. Data was fitted using a Gaussian + Gaussian + Exponential fit (green line)*

5.3.2.2 Experimental Data Analysis

The spectra from all 52 blocks were analysed to determine the peak position of both peaks attributed to the 511 keV and 1274 keV gamma-rays as a function of position from the PMT face. Figure 5.8 displays a typical spectrum of uncalibrated data (black) showing the response of a wrapped single barrel section of plastic scintillator to irradiation with a ^{22}Na source. The solid line (green) is the result of a fit to the data assuming partial Gaussians for the 511 keV and 1274 keV Compton edges and an exponential to describe the background. The fitting routine is utilised to identify the peak positions of the 511 keV and 1247 keV gamma-ray Compton edges. For a single scintillator section up to nine measurements with a ^{22}Na source are performed all of which have this fitting procedure applied. This allows the position of the peak-centroid of the Gaussian, as a function of distance from the PMT face, to be calculated and used to obtain a value for the scintillator section's TAL. Although background was minimised by employing a coincidence circuit it was not possible to remove the background due to electron noise hence the requirement for its characterisation using an exponential fit. All spectra were calibrated using single photoelectron spectra taken before and after all position measurements.

5.3.2.3 Calibration of Data

Figure 5.9 displays a typical SPE spectrum. The peak position was obtained by assuming a Gaussian fit to the signal (blue) and two exponentials to characterise the background (magenta and red). The parameters obtained are passed through to a larger fitting routine which employs a combination of a Gaussian and two exponentials. Figure 5.10 displays the result of such a fitting procedure. Information obtained from the fit is used to calculate a calibration factor for the conversion of channel number to photoelectrons.

Equation 5.2 gives the conversion factor to photoelectrons,

$$\mu_{p.e} = \left(\frac{\mu_e}{\sigma_e}\right)^2 \tag{5.2}$$

where μ_e is the mean position of the peak centroid and σ_e is the width (standard deviation) of the peak, both of which are values obtained using the fitting procedure described above (P1 and P2 fitting parameters as shown in Figure 5.10). $\mu_{p.e}$ is the number of photoelectrons per channel used to calibrate the

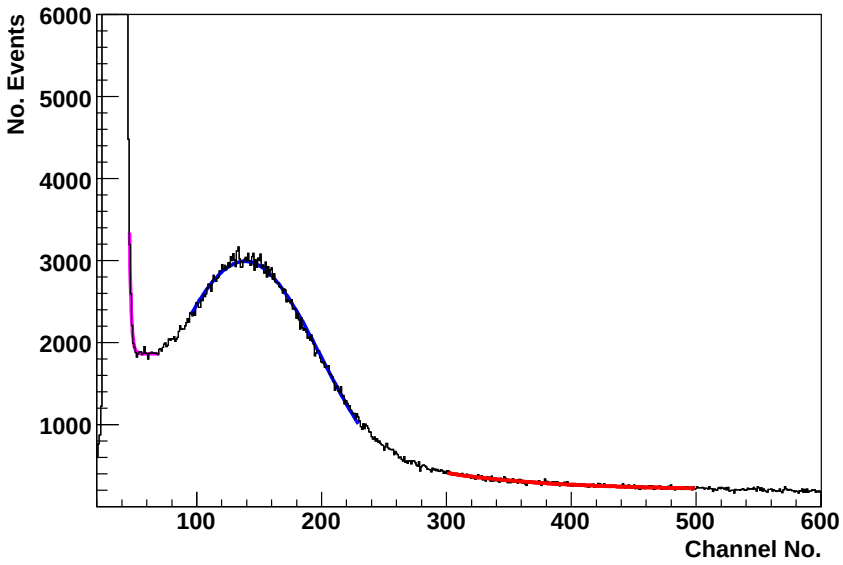

Figure 5.9: *An SPE spectrum displaying the individual fits to account for the signal and background. Data was obtained with barrel section 1-1-08-10.*

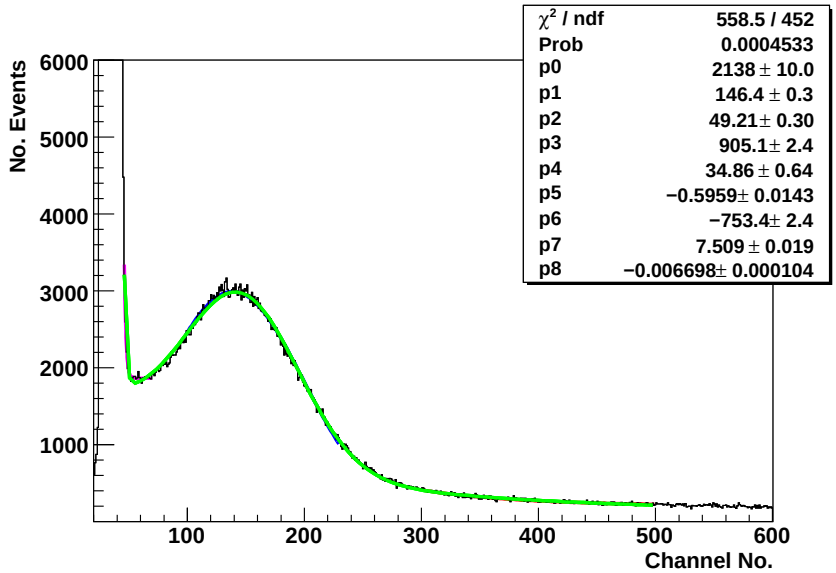

Figure 5.10: *A fitted SPE spectrum using a Gaussian + exponential+ exponential for barrel section 1-1-08-10. The parameters obtained from fitting to the signal and background, as shown in Figure 5.9, are fed into the total fitting function, shown in green.*

data. The origin of this equation relates to the assumption that the number of photoelectrons can be described using Poisson statistics with a mean μ and standard deviation of $\sigma_{p.e}$. Assuming a constant gain G, the charge distribution of the output signal can be expressed as,

$$\begin{aligned} \mu_e &= G\mu_{p.e}, \\ \sigma_e &= G\sigma_{p.e} \\ \sigma_e &= G\sqrt{\mu_{p.e}} \end{aligned} \tag{5.3}$$

which can lead to Equation 5.2 giving the mean number of photoelectrons. The SPE data obtained before and after TAL position measurements were fitted to also ensure accurate calibration.

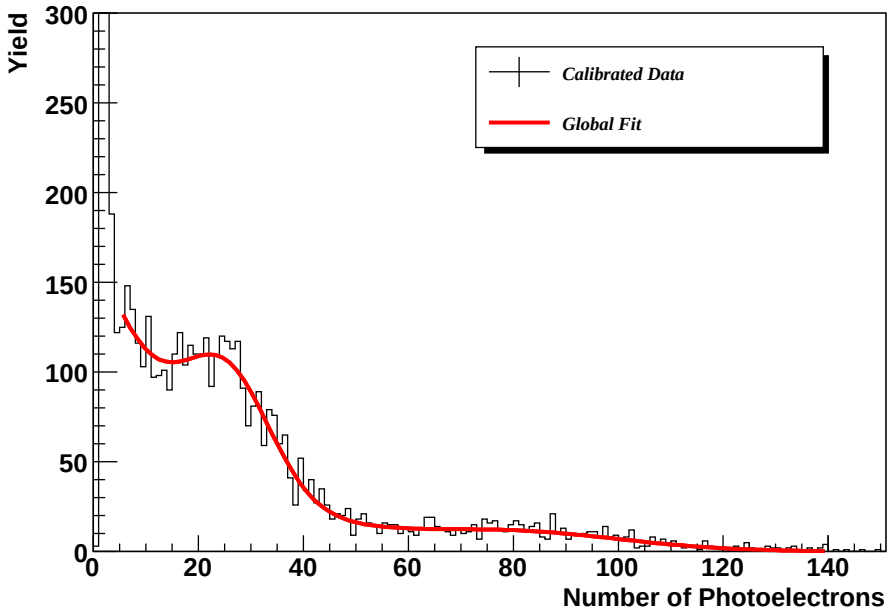

Figure 5.11: *A calibrated spectrum showing the response of barrel section 1-1-08-7 to irradiation with a ^{22}Na gamma-ray source positioned 20 cm from the PMT face. The uncalibrated spectrum of the same block was shown in Figure 5.4, here it has been re-bined. The calibration factor was calculated by fitting to SPE data as discussed in the text.*

A typical calibrated spectrum for a barrel scintillator section is shown in Figure 5.11 by applying a channel number to photoelectron conversion of $\mu_{p.e} =$

9.0 ± 1.1 channel/phe to the data shown in Figure 5.4. All data sets were individually calibrated using SPE data relating only to the scintillator block tested.

5.3.2.4 TAL Determination

The TAL of a scintillator block was determined by plotting the mean peak position of the 511 keV and 1274 keV peak centroids as a function of position. An example is shown in Figure 5.12.

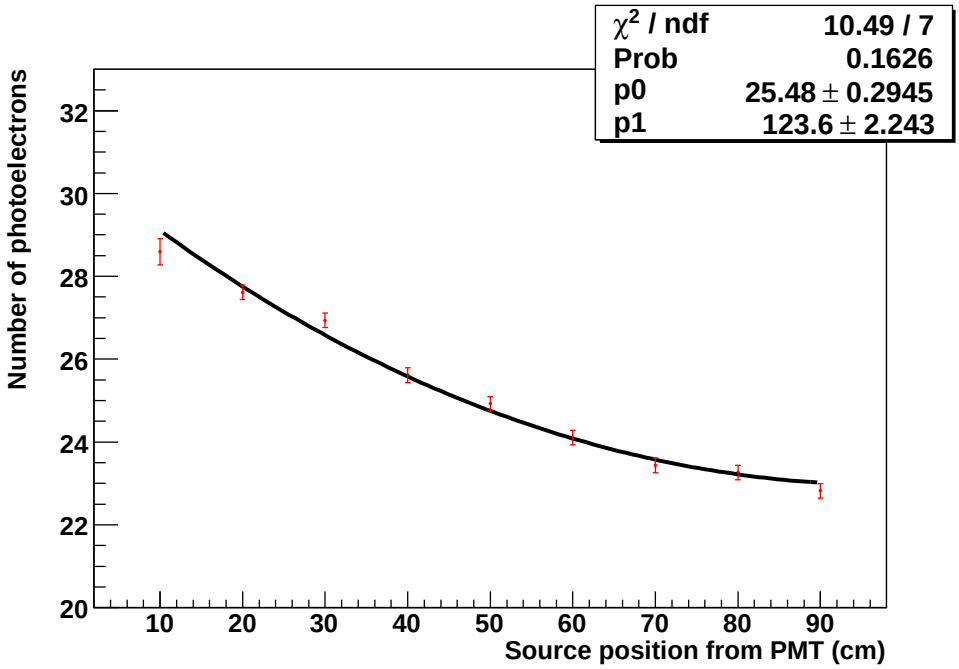

Figure 5.12: *The peak centroid of the 511 keV gamma-ray feature as a function of distance for barrel scintillator block 1-1-08-2. The fit applied to determine the TAL of the block is shown in Equation 5.4. To calculate the TAL, the effect of the Mylar mirror is taken into account in the fitting. The TAL is given by parameter P1, where a value of* 123.5 ± 2.2 *cm is concluded from the fitting routine. This compares to a quoted BAL of 145 cm by Amcrys-H.*

Figure 5.12 shows the peak centroids of the 511 keV gamma-ray Compton edge as a function of position of the ^{22}Na source from the PMT. It is also possible to use the 1274 keV Compton edge to determine the TAL of a scintillator section using the same analysis method described above. However, the peak attributed to the 511 keV gamma-rays is better defined and therefore better for data analysis.

To first approximation, the PMT response can be modelled as the sum of two exponentials, hence, the following function has been fitted to the data,

$$S(x) = I_0 e^{-x/TAL} + I_0 e^{-(2l-x)/TAL} \tag{5.4}$$

where $S(x)$ is the centroid of the measured photopeak, x is the distance from the PMT, l is the length of the scintillator block and I_0 is the maximum light yield when $x = 0$. The first exponent in Equation 5.4 describes the reduction of light due to the separation of the PMT and source position, i.e the amount of light attenuated before it reaches the PMT. The second exponent in Equation 5.4, models light reflections due to the Mylar mirror positioned at the far end of the block. This is assumed to be perfect which is somewhat inaccurate (i.e the coefficient of each term is I_0). While this will result in a slight underestimation of the TAL values of the blocks, the high reflectivity of the mirror ($\sim 95\%$ for light of this wavelength) coupled to the resolution of the experiment, meant extraction of a value different from I_0 was not possible.

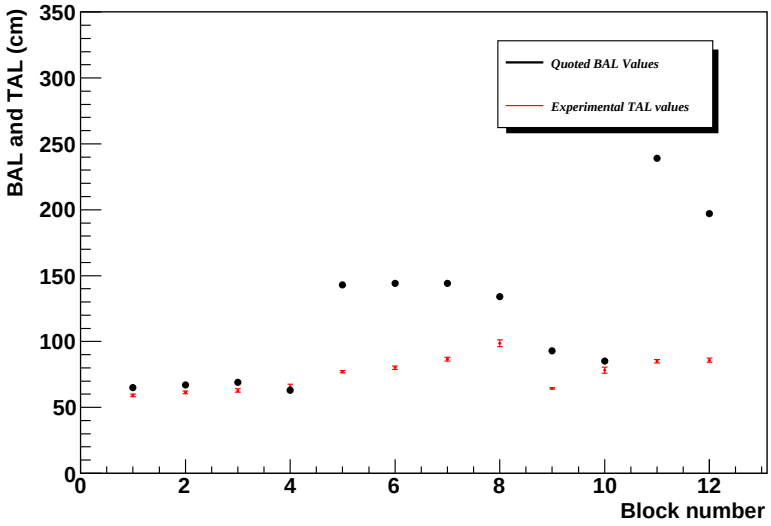

Figure 5.13: *Experimentally measured TAL (red) values from Edinburgh University and BAL values (black) for the blocks provided by Amcrys-H. These measurements are for the smallest 12 roof sections. From the x-axis, points $x = 1-4$ are results for the 51.5 cm scintillator blocks, points $x = 5-8$ are results for the 67.1 cm scintillator sections and points $x = 9-12$ are results for the 75.0 cm scintillator blocks.*

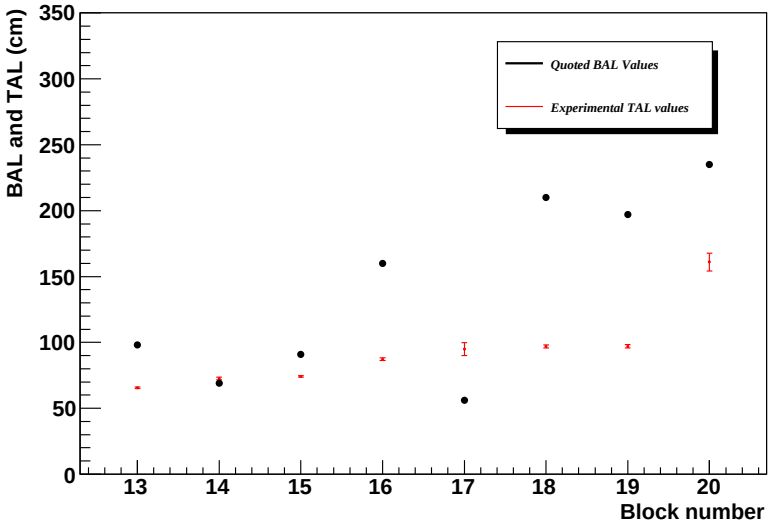

Figure 5.14: *Experimentally measured TAL (red) values from Edinburgh University and BAL values (black) for the blocks provided by Amcrys-H. These measurements are for the 80.0 cm roof sections*

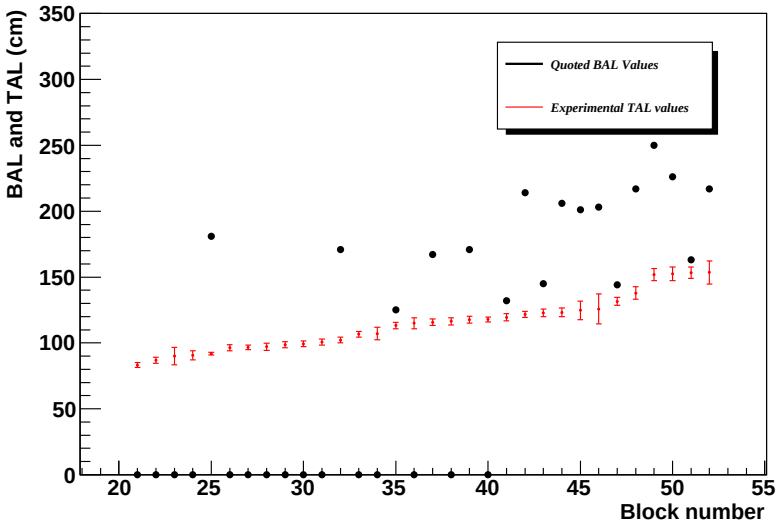

Figure 5.15: *Experimentally measured TAL (red) values from Edinburgh University and BAL values (black) for the blocks provided by Amcrys-H. These measurements are for the barrel sections of the veto. Zeros for the BAL values indicate that no value was provided by the manufacturer for these blocks.*

All scintillator sections have been analysed following this method, the results of which are shown in Figures 5.13, 5.14 and 5.15. These figures show the TAL values as measured at the University of Edinburgh and BAL values, as measured by Amcrys-H [147]. The results are separated into three different graphs to account for the different geometries of the scintillator blocks, which could effect the TAL measurements. There are a number of zero BAL values shown in Figure 5.15 where data were not supplied by Amcrys-H. There is some correlation between the TAL and BAL values, particularly in Figure 5.15. One would expect the TAL to increase as the BAL increased as better quality material would inherently improve the light yield, despite geometry. The TAL value is almost equal to the BAL value when the BAL $\leq$ 90cm (which can clearly be observed in Figure 5.13), this may be due to the fact that the blocks are so short that the effect of reflections from the surfaces are virtually removed. Points 9-12 from Figure 5.13 refer to scintillator roof sections 75.0 cm in length. The difference between points 9 and 10 are vastly different from points 11 and 12; however both pairs were produced in separate polymerisation processes which could contribute to the difference, particularly if the light yield differed between the material. There are obvious differences when obtaining TAL measurements, such as large reflections on the surfaces and five different geometries to consider. When the BAL is measured the nature of the scintillator is tested without the inclusion of surface effects and geometrical structure.

An additional tool was employed to confirm the experimental findings, Monte Carlo modelling of the experiment. Through Monte Carlo modelling it was possible for a given BAL to predict the scintillator TAL. This is discussed further in Section 5.3.3 and provided a useful insight into the experimental findings.

Despite the noticeable variation, the experimentally measured TAL values allowed for matching of individual sections of plastic scintillator to particular PMTs, providing a more uniform performance across the entire veto.

5.3.3 GEANT 4 Simulation of TAL Experiment

5.3.3.1 Modelling the experimental apparatus

The Monte Carlo method was utilised to estimate the TAL from a given BAL input by simulating the experiment and the ^{22}Na exposures. Figure 5.16 shows one of the simulated roof sections. All five different geometries were simulated

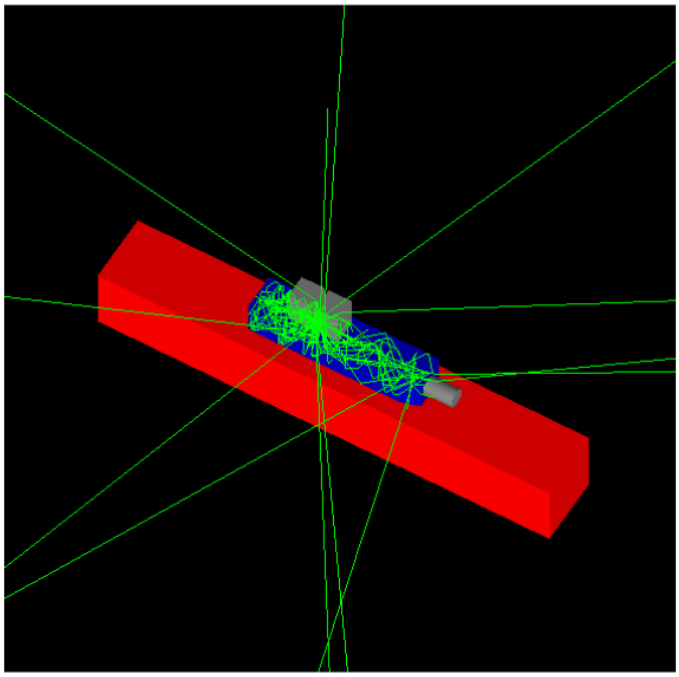

Figure 5.16: *The GEANT4 simulation of the Edinburgh TAL experiment. The position of the ^{22}Na source was moved to various distances away from the PMT face, above the scintillator block as in the experiment. A BAL value was input to the simulation. The TAL of the block for the corresponding BAL value is determined using the technique described for the real data. Shown here is the wooden table red), the scintillator block (blue), lead collimator (grey) and PMT (grey).*

using GEANT4 (see [156; 157; 158] for more details on GEANT4, including class structures). The simulation included details such as the wooden bench, laboratory (walls, floor and roof), 95% specular reflective Mylar mirror, PTFE wrapping, optical grease, lead collimators, ^{22}Na source and PMT. The PMT includes internal components such as a glass envelope, photocathode and internal elements. The optical properties of the scintillator material, PTFE wrapping, Mylar mirror and optical grease, such as refractive indices and reflective properties, were also included. For these simulations full tracking of scintillation photons from gamma-ray energy deposition through to incidence on PMT photocathode, and stochastic generation of photoelectrons was performed, allowing generation of spectra. Physics inputs include the QE of the PMTs and the BAL and light yield of the material. These three parameters can be adjusted to recreate specific experimental conditions (see Table 5.3 for a breakdown).

Parameter name	**Component**	**Value**	**Origin of value**
Quenching Factor	Scintillator	0.2	Amcrys-H
BAL	Scintillator	$50 - 350$ mm	Amcrys-H
Light yield	Scintillator	$5.5 - 8$ photons/keV	Literature and simulation
Quantum Efficiency	PMTs	$21 - 33\%$	ETEL manufacturer
Dimensions	All veto block geometries	various	Univ. Edi

Table 5.2: *Displayed is a summary of the physics inputs for the scintillator simulation. The inputs have been collated from a variety of sources, including manufacturer data sheets and specific tests performed at the university of Edinburgh or by the manufacturer.*

5.3.3.2 Optical Photon Modelling

Accurate modelling of the optical properties of the experimental materials was necessary to obtain a good comparison between experiment and simulation. Modelling the behaviour of light was crucial for four particular components of the experiment, these were the borosilicate glass in the PMT, the optical grease, the scintillator plastic and the PTFE wrapping. Modelling the interface between the PMT glass envelope, optical grease and the scintillator material could be simulated relatively simply. This will be discussed first.

For the boundary between the scintillator, optical grease and PMT, the only information required was the refractive indices at each of the surfaces. In this scenario, GEANT4 assumes a perfectly smooth interface between each of the dielectric materials. The action of utilising optical grease as a couplant between the PMT and scintillator would result in this effect in a real scenario. The well coupled interface between the PMT, grease and scintillator prevents any diffuse reflection back into the scintillator section and, more importantly, transmission of light in accordance with the Fresnel equations, which describe both transmission and reflection of light in accordance with the refractive indices of the interfaced material. For light incident normally onto an interface (such as the optical grease or the PMT) the following Equations (5.5, 5.6) can be used to determine the transmission (T) and reflectance (R) [159];

$$R = R_{\parallel} = R_{\perp} = \left(\frac{n_t - n_i}{n_t + n_i}\right)^2 \tag{5.5}$$

$$T = T_{\parallel} = T_{\perp} = \frac{4n_t n_i}{(n_t + n_i)^2} \tag{5.6}$$

There is a higher transmittance of light if the refractive indices are of the same or similar value, while if there was significant changes in the refractive index, as would be the case for an air gap, the transmission of light would be significantly reduced.

Component	**Typical Refractive Index**
Scintillator UPS 923A	1.52
Optical Grease BC-603	1.43
Borosilicate (PMT)	1.47
PTFE	1.30

Table 5.3: *Refractive indices of important materials in the GEANT4 simulation of the experiment.*

The PTFE and scintillator material were also implemented in the simulations in a way that included their optical properties; however the way in which light interacts between the diffuse PTFE wrapping and the scintillator material required more intensive modelling. There are three GEANT4 classes required for this.

1. The material properties class keeps information about the material itself, such as density, refractive index, etc.

2. The geometry class is employed, obtaining details of the touching physical volumes.

3. The G4OpBoundaryProcess class is also used to simulated the behaviour of the material at material boundaries.

Optical surfaces can be defined between either a metal-dielectric or dielectric-dielectric. Both the PTFE wrapping and the scintillator are dielectric materials, hence a dielectric-dielectric surface was specified. For such a surface, GEANT4 models the behaviour of light whereby the photon can undergo total internal reflection, refraction or reflection, depending on the photon's wavelength, angle of incidence, and the refractive indices on both sides of the boundary. Also, reflection and transmission probabilities are sensitive to the state of linear polarisation. In the case of a dielectric-dielectric interface the UNIFIED model [158; 160] can be employed (already built into GEANT4). This model attempts to simulate the passage of particles based on the surface and finish of the wrapping. The surface can be assumed either smooth (polished) or a diffuse reflecting material where Lambertian reflection occurs, i.e., assuming isotropic radiance. In this case a diffuse material was chosen in correspondence with the nature of PTFE.

5.3.3.3 Simulating the Experiment

The ^{22}Na exposures were recreated in the simulation by irradiating an emulation of the scintillator slab with a ^{22}Na source positioned at points along the length of a scintillator bar. The energy deposition within the scintillator block was converted to scintillation photons using estimates for the light yield. Taking other factors such as PTFE wrapping and the Mylar mirror, which would both serve to increase the effective light yield, values of between 5.5-8 photons/keV were used. The variation reflects the different polymerisation's for the different sets of scintillator materials. The photons are tracked in the plastic scintillator crystal with a varying bulk attenuation length (BAL) ranging from 50 cm to 300 cm based on measurements provided by Amcrys-H. Output recorded from the simulated events include energy of the initial particle, energy deposited within the

scintillator block, position of interaction, number of photons generated and number striking the photocathode. A global quantum efficiency was applied to the events that hit the photocathode, mimicking the PMT used. The number of photoelectrons generated was randomised in accordance with the stochastic nature of the process, with a Gaussian distribution used, unless the number of photoelectrons decreased below 15 in which instance the smearing was according to a Poisson distribution. The number of photoelectrons detected (absolute and per keV of energy deposited in the crystal) as a function of distance from the PMT was then calculated.

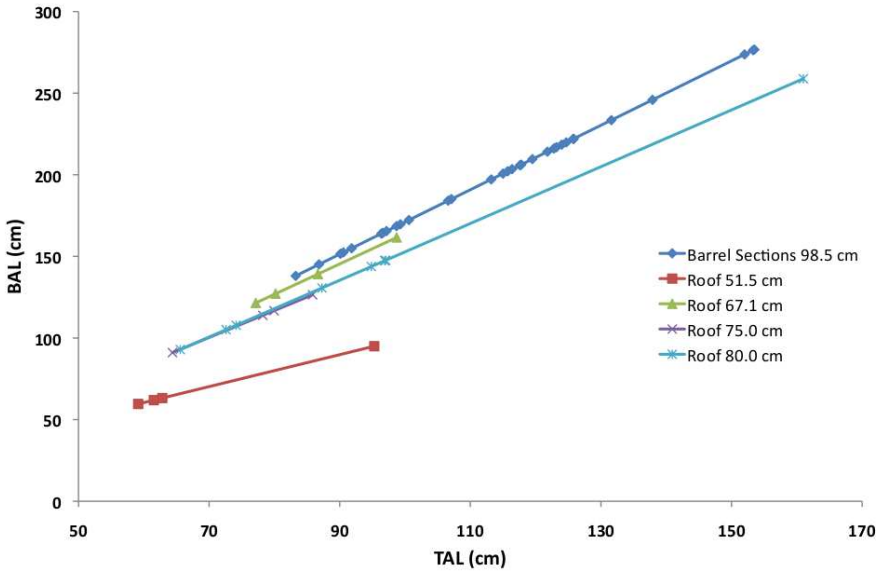

Figure 5.17: *The relationship between TAL and BAL measurements as devised from GEANT4 simulation. See text for details.*

With the physics parameters chosen, the functional form of the number of photoelectrons per unit energy deposition with distance from the PMT was calculated for all 52 sections by repeating the simulation for the 5 different geometries of scintillator material, with varying BAL values. The simulation data was analysed exactly as if it has been experimental data to determine the TAL for a particular BAL input.

To reduce the number of simulations required for comparison with all 52 scintillator blocks, the simulated TAL was obtained for BAL inputs of 100, 150, 200 and 250 for all five geometries. A relationship between the input BAL versus

simulated TAL (separately for all five block geometries) was characterised by fitting to the results. The fitting function and parameters of the fit applied could then be used to predict the BAL for a corresponding experimentally measured TAL. Figure 5.17 shows the predicted BAL versus the experimentally measured TAL value according to each block geometry.

The predicted BAL values are also shown in Figures 5.18, 5.19 and 5.20 as blue data-points, comparing directly with BAL values measured by Amcrys-H (black). The simulated BAL values rely on the experimental TAL input into the equation, therefore any deviation will vary in accordance to these TAL measurements.

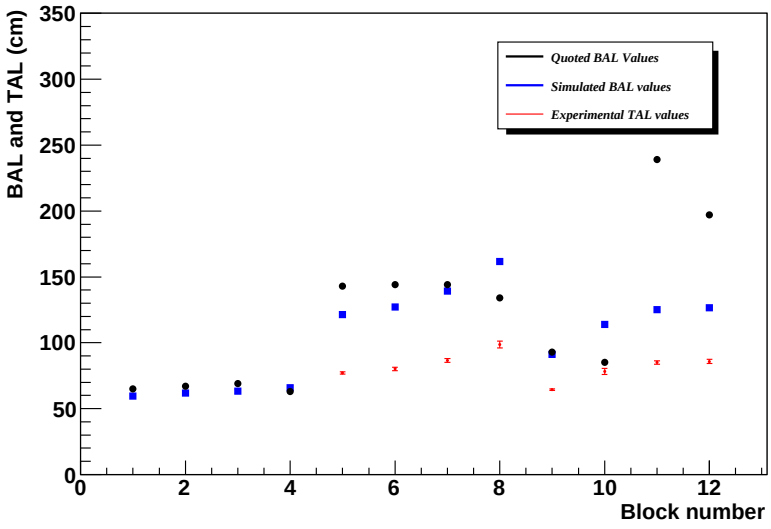

Figure 5.18: *Experimentally measured TAL (red) values from Edinburgh University and BAL values (black) for the equivalent blocks, provided by Amcrys-H. The blue data-points are the predicted BAL values based on the experimentally measured TAL. These measurements are for the smallest 12 roof sections. Points 1-4 from the x-axis are results for the 51.5 cm scintillator blocks; where the red data points are concealed by the blue data points. Points 5-8 are results for the 67.1 cm scintillator sections and Points 9-12 are results for the 75.0 cm scintillator blocks.*

In addition to the above simulation a selection of the blocks have been fully simulated based on the BAL as given by Amcrys-H. Figure 5.21 shows the measured and simulated number of photoelectrons as a function of position for the ^{22}Na exposures. The simulation agrees with the experimental data taken.

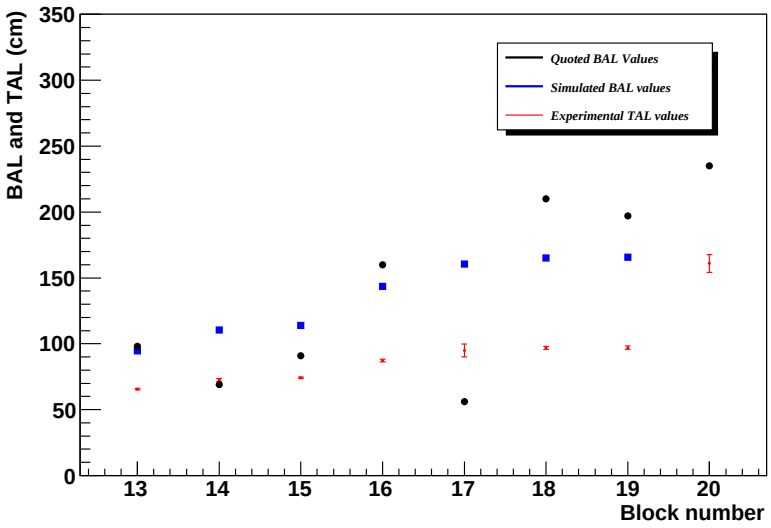

Figure 5.19: *Experimentally measured TAL (red) values from Edinburgh University and BAL values (black) for the equivalent blocks, provided by Amcrys-H. The blue data-points are the predicted BAL values based on the experimentally measured TAL. These measurements are for the 80.0 cm roof sections*

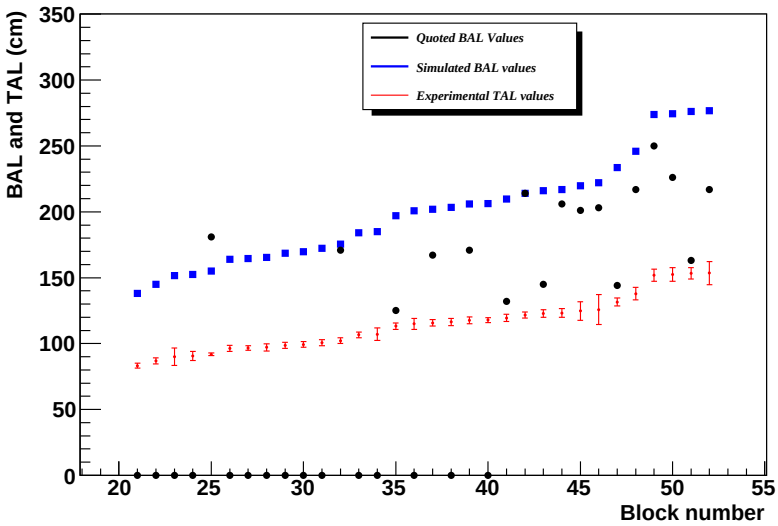

Figure 5.20: *Experimentally measured TAL (red) values from Edinburgh University and BAL values (black) for the equivalent blocks, provided by Amcrys-H. The blue data-points are the predicted BAL values based on the experimentally measured TAL. These measurements are for the barrel sections of the veto.*

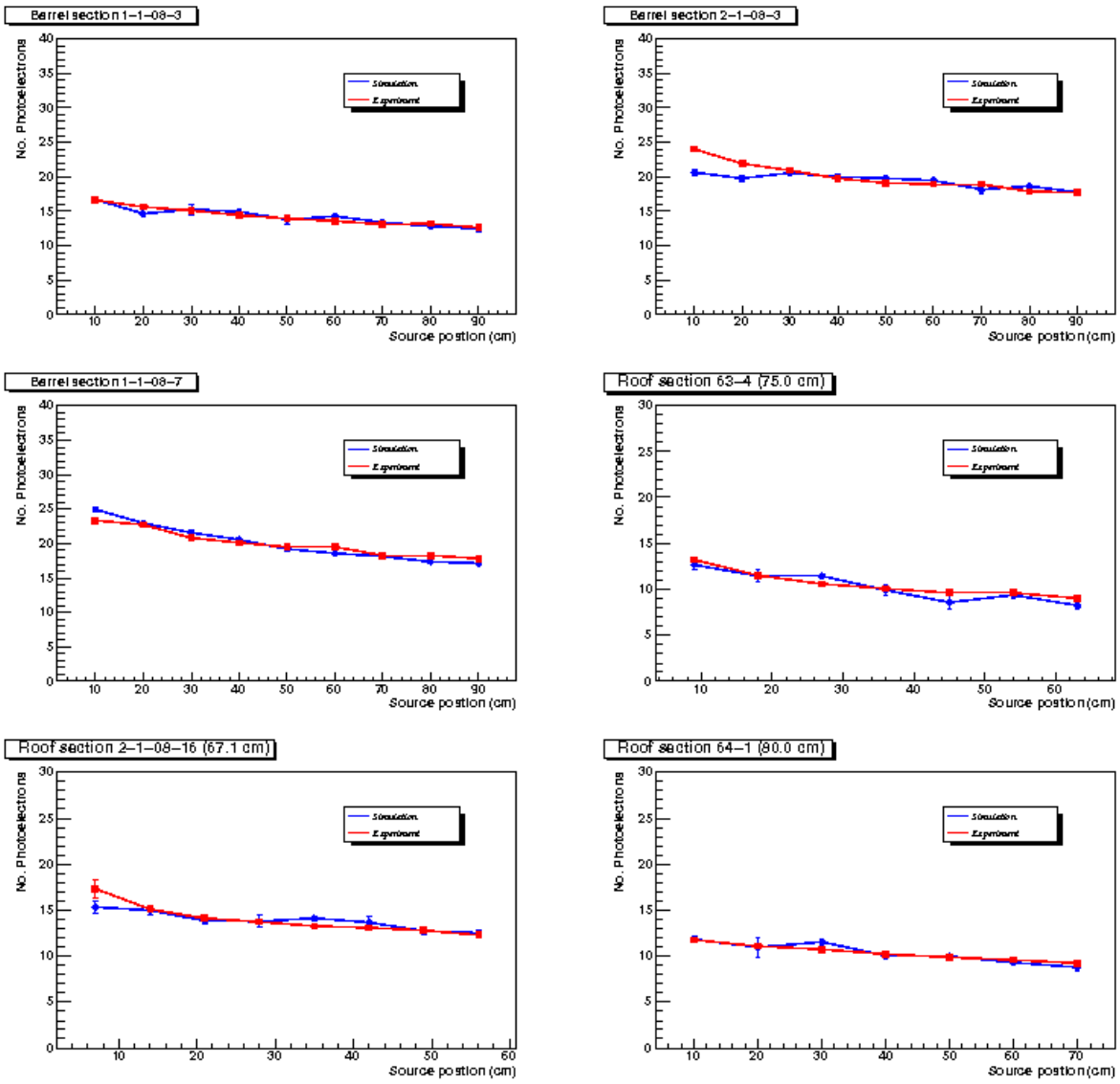

Figure 5.21: *A selection of simulated TAL and experimental TAL data from various scintillator sections. The fitted TAL results for both experiment and simulated data can be found in Table 5.4.*

Block Type	Block Name	Amcrys-H BAL (cm)	Experiment TAL (cm)	Simulation TAL (cm)
Barrel	1-1-08-3	125	113.2 ± 2.5	117.0 ± 5.6
Barrel	2-1-08-3	167	115.7 ± 2.4	134.5 ± 12.9
Barrel	1-1-08-7	171	102.2 ± 2.2	96.9 ± 1.9
Roof 75.0 cm	63-4	85	78.2 ± 2.2	83.6 ± 5.9
Roof 67.1 cm	2-1-08-16	144	86.7 ± 1.4	96.2 ± 8.8
Roof 80.0 cm	61-4	91	74.1 ± 0.6	93.9 ± 6.7

Table 5.4: *Displayed are Amcrys-H measured BAL and the experimental and simulated TAL values for a selection of scintillator sections. All TAL values compare well showing that the experimental measurements are accurate.*

A summary of the results are shown in Figure 5.21 and in Table 5.4. The experimental to simulated TAL values agree extremely well.

5.3.3.4 Comparing Simulation of Photoelectron Spectra to Experiment.

The second aim for testing the scintillator sections in Edinburgh was to supply the main veto simulation with accurate photoelectron modelling in the form of light curves for the individual scintillator sections. This required accurate comparison of the experimental data to simulation, firstly, to ascertain the accuracy of the data collected from scintillator testing and secondly to ensure the accuracy of the calibration data. Comparing the TAL and BAL values using GEANT4 simulations and experimental data had not required any detailed estimation of the light yield from the scintillator sections as the TAL can be determined purely by the fall in the exponential fit as displayed in Figure 5.12, and not the y intercept. However, it was now desired to see if individual spectra could be simulated in absolute terms to high accuracy. Therefore, a meticulous recreation of the experimental set-up was now necessary.

Figure 5.22 is an example of the initial comparison between simulation and experimental data. The data is from scintillator barrel section 2-1-03-8 and has a quoted BAL of 167 cm and an experimentally measured TAL of 115.7 ± 2.4 cm. For this simulation the BAL and a light yield of 8 photons/keV were used. The simulation did not initially include wrapping with PTFE, but it did include the optical grease coupling the PMT to the scintillator section and a Mylar mirror positioned at the far end to the PMT. The real scintillator section was

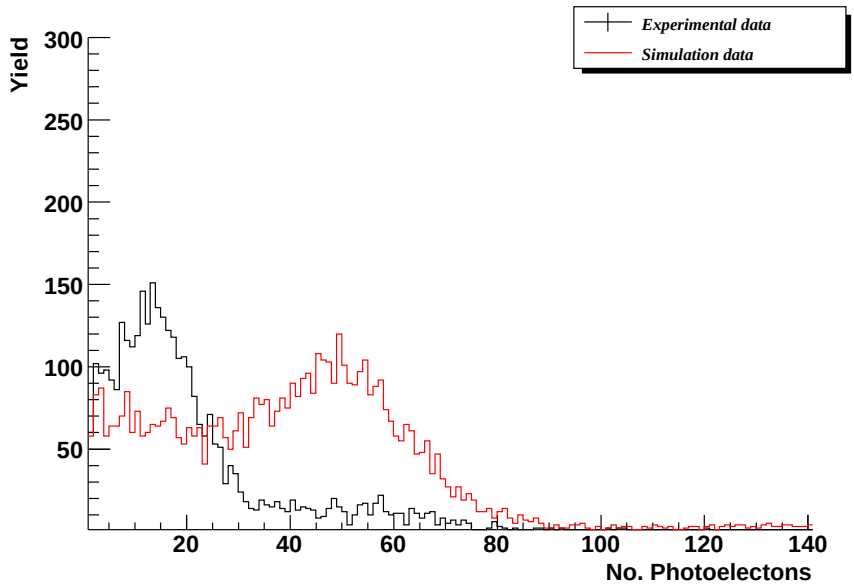

Figure 5.22: *Comparison between simulation and experimental data at a 40 cm distance from the PMT face. The data is from scintillator barrel section 2-1-03-8 and has a quoted BAL of 167 cm and an experimentally measured TAL of* 115.7 ± 2.4 *cm.*

wrapped and also included a Mylar mirror. The data has been calibrated using 10.3 ± 1.4 photoelectrons/channel, obtained as detailed in Section 5.3.2.3. From Figure 5.22, it is obvious there is a discrepancy between the data and GEANT 4 simulation where the simulation predicts a higher photoelectron response than that which had been experimentally measured. The reason for the discrepancy highlights the need for very accurate modelling of the system. To improve the discrepancy the following were considered more thoroughly;

1. The quantum efficiency (QE) of the PMT may have been set too high in the simulation.

2. The light yield may have been set too high in the simulation. In this example the light yield had been assumed to be 8 photons/keV.

3. The PTFE wrapping could have a larger effect than previously anticipated.

4. The use of optical grease may have been poorly simulated.

The effect of variation in the quantum efficiency (QE) of the PMT would have been minimal. PMT 1075 was used in the experimental measurement of block 2-1-08-3 and its corresponding QE of 29.6% was input into the simulation. The average QE of all 52 PMTs is 27.08% therefore any variation would have been minimal to the output from the simulation.

The light yield assumed has a direct impact on the observed light output. By reducing this parameter in the simulation to ~ 5.5 photons/keV, the simulation histogram (referring to Figure 5.22) would move to the left improving the comparison.

The omission of the PTFE in the simulation would be expected only to exacerbate the problem. If it were included in this particular simulation the effective light yield would be improved, resulting in a poorer comparison between simulation and experimental data.

To improve the simulation the above points were varied; however by removing the optical grease in the simulation the discrepancy was significantly improved. In the Edinburgh TAL tests it was required that the PMTs had not in fact been coupled to the scintillator with optical grease. This was necessary as the PMTs were yet to be matched to the scintillator blocks based on the measured TAL values. To minimise the risk of causing permanent contamination to the scintillator face, reducing good coupling between the PMT to the scintillator material, the majority of tests were performed without the presence of optical grease. Since Amcrys-H did not provide BAL data on 14 barrel scintillator sections these were the first to be tested. Time constraints resulted in some of the roof sections undergoing permanent coupling with their corresponding PMT early on into the scintillator testing phase and thus data for some of these were taken as such.

All points discussed above would contribute at some level to the discrepancy. This example highlights the accuracy with which everything had to be modelled and then validated before the final results were used to inform the full veto+ZEPLIN-III simulation.

5.3.3.5 Improving the Matching between Simulation and Experimental Data

Figure 5.23 displays results from two simulations for block 2-1-08-3. The physics inputs were kept constant with a BAL of 167 cm and a light yield of 8 pho-

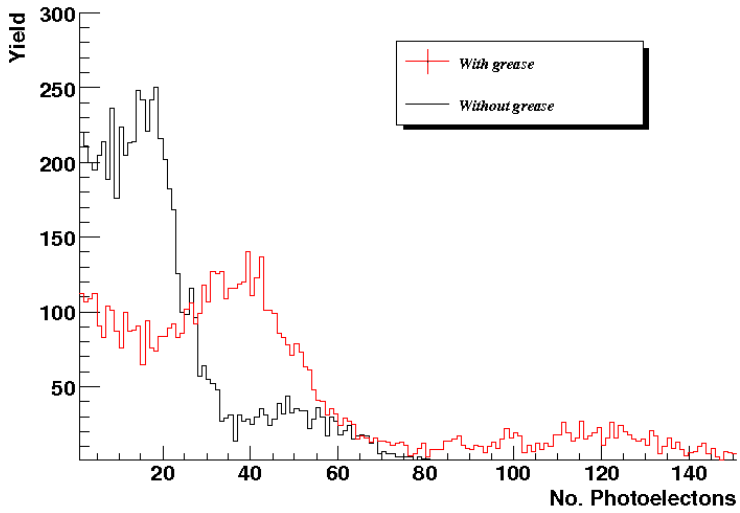

Figure 5.23: *This figure shows the results from two simulations of the irradiation of ^{22}Na source. The attributes of block 2-1-08-3 have been emulated in these simulations. A BAL of 167 cm and light yield of 8 photons/keV were input. The only difference between the two simulations is the presence of optical grease between the scintillator section and the PMT.*

tons/keV, the only difference between the two being the presence of optical grease. There is an obvious effect where the light yield is reduced by a factor of $\sim 50\%$.

As shown in Figure 5.24 (again block 2-1-08-3), the comparison between data and simulation is vastly improved (the calibration factor of 10.3 ± 1.4 channels/photoelectron was applied) with the removal of the optical grease in the simulation. Accounting for other effects such as variation in the light yield (i.e any deviation from 8 photons/keV), variation in the Mylar mirror reflectivity (100 % reflectivity is assumed in the simulation which is an overestimate) and the calibration factor uncertainty, the simulation can then be matched to the data precisely as shown in Figure 5.25. The experimental data in Figures 5.24 and 5.25 have both been background subtracted. A similar conclusion may be drawn by comparing experimental and simulation data for scintillator section 1-1-08-3. Figure 5.26 clearly shows an improvement in the comparison of experimental and simulation data with the removal of optical grease in the simulation.

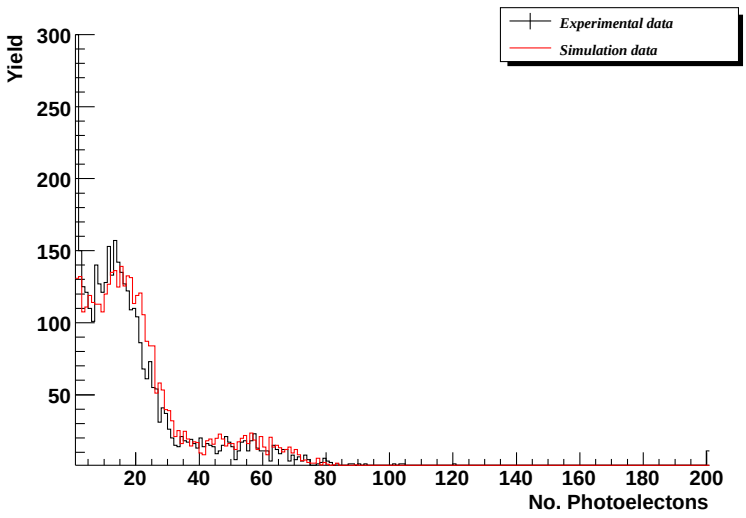

Figure 5.24: *This figure displays background subtracted experimental data for block 2-1-08-3 and the simulated equivalent (without optical grease).*

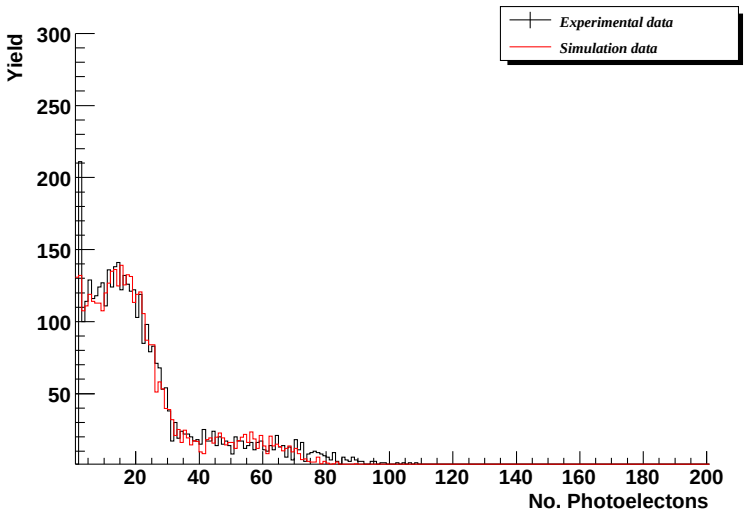

Figure 5.25: *This figure displays background subtracted experimental data for block 2-1-08-3 and the simulated equivalent (without optical grease). The calibration factor has been changed to 9.8 instead of the expected 10.3±1.4. This is within errors and variations in wrapping and light yield would result in such a difference.*

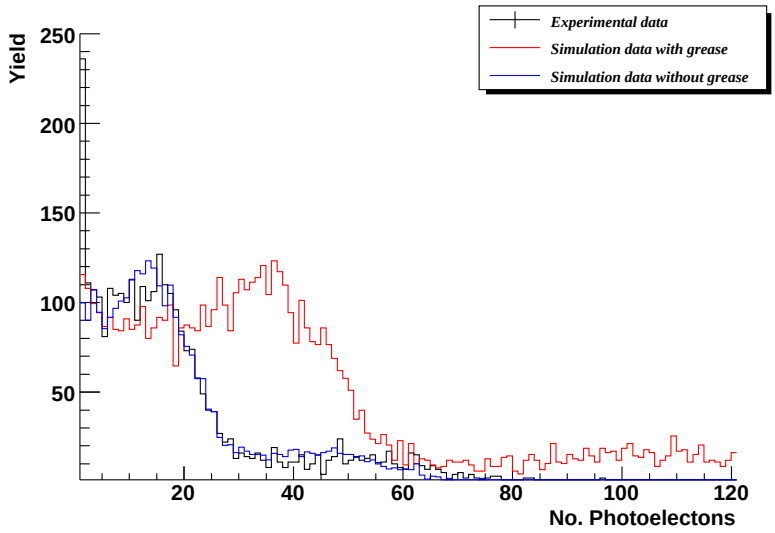

Figure 5.26: *Experimental and simulation data for block 1-1-08-3. The red histogram is simulation data when optical grease is present between the scintillator block and the PMT. The blue histogram is when there is no optical grease present in the simulation. The blue histogram matches the experimental data when the other effects such as the light yield and PMT position is accounted for.*

5.3.4 Modelling Light Output for the main Veto Simulation

Using a combination of simulation and experimental data, all scintillator sections have been successfully characterised. The final stage of this research is to create light curves for each scintillator block to be input into the main veto + ZEPLIN-III simulation. These light curves will be produced purely with the experimental TAL data; however a correction factor will need to be applied pertaining to blocks which were not tested whilst coupled to optical grease. Section 5.3.4.1 discusses the formulation of this correction factor, whilst Section 5.3.4.2 discusses the light model equations.

Using light curves based on experimental data alone will create a veto Monte Carlo that will best mimic the real scenario. Simulating fully the individual variations in the quality of PTFE wrapping, differences in the quantum efficiency of the PMTs and light yield of the scintillator would be extremely time consuming and in some cases not feasible. The experimental data will include all of these factors.

5.3.4.1 Correction to the Experimental Data

Simulations were performed for various scintillator sections both with and without the presence of optical grease. Figures 5.27 and 5.28 show these simulated results with and without the presence of optical grease coupling for block number 2-1-08-5. The data were fitted using the function applied in the experimental and simulation TAL tests. The centroid of the peak attributed to the 511 keV gamma-rays was recorded and the difference between the two calculated as a percentage.

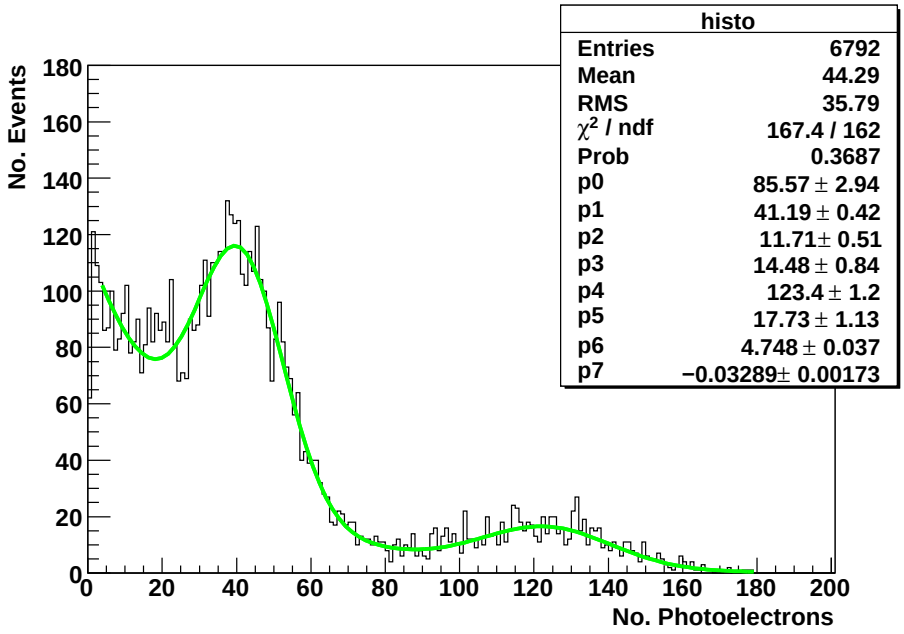

Figure 5.27: *Simulation of block 2-1-08-5 where the PMT has been optically coupled with the scintillator block*

This process was repeated to calculate an average correction factor. The results are displayed in Table 5.5. The average of these results were taken to be 48.6 ± 1.8 % (the error is given by the weighted standard deviation). The result for the 2-1-08-14 block is for an 80.0 cm block, which is slightly higher than the others. The average value excluding the 2-1-08-14 block is 47.0 ± 0.7 %. Therefore for scintillator sections experimentally tested without the presence of optical grease coupling the number of photoelectrons produced should be increased by a factor of ~ 2.

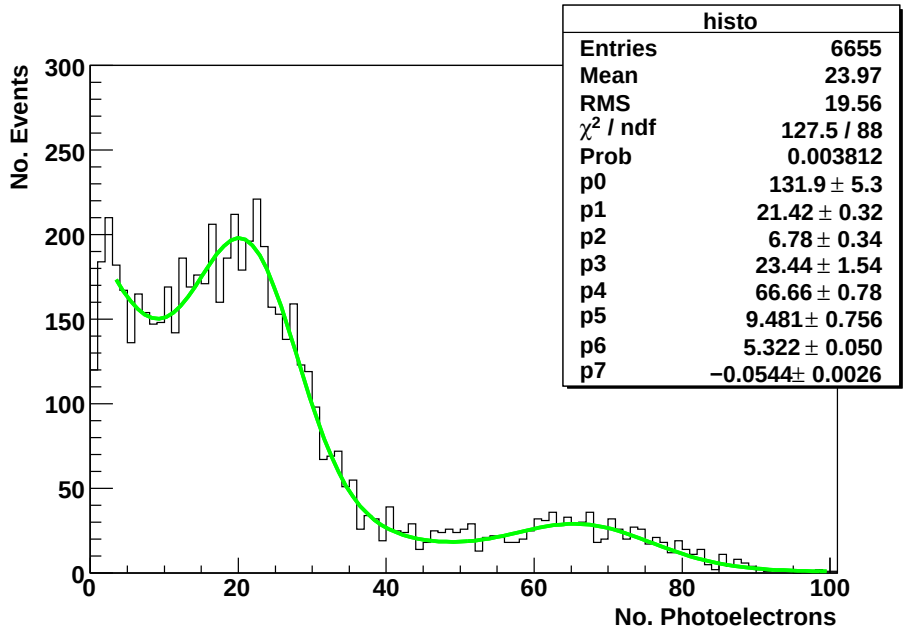

Figure 5.28: *Simulation of block 2-1-08-5 where the PMT has not been optically coupled with the scintillator block*

Block	511 keV mean with grease	511 keV mean without grease	Change
2-1-08-5	41.19 ± 0.42	21.42 ± 0.32	$48.0 \pm 0.9\%$
2-2-08-3	24.19 ± 0.36	12.49 ± 0.33	$48.4 \pm 1.5\%$
1-1-08-7	35.11 ± 0.42	18.62 ± 0.35	$47.0 \pm 1.0\%$
1-1-08-9	30.47 ± 0.37	16.72 ± 029	$45.1 \pm 1.0\%$
2-1-08-14	38.63 ± 0.39	16.98 ± 0.30	$55.7 \pm 1.1\%$

Table 5.5: *The measured variation in light output with and without the presence of optical grease to couple the PMT to the scintillator.*

5.3.4.2 Input into the Main Veto Monte Carlo

Using experimental data, calibration data and information obtained from simulation, it was possible to formulate equations for each scintillator segment to estimate the number of photoelectrons/keV emitted as a function of distance from a PMT face, individually for each scintillator section geometry type. All experimental data were calibrated using the method described in section 5.3.2.3 and analysed as discussed in Section 5.3.2.2. To model the scintillator response for input into the main veto Monte Carlo, the centroid values for the 511 keV

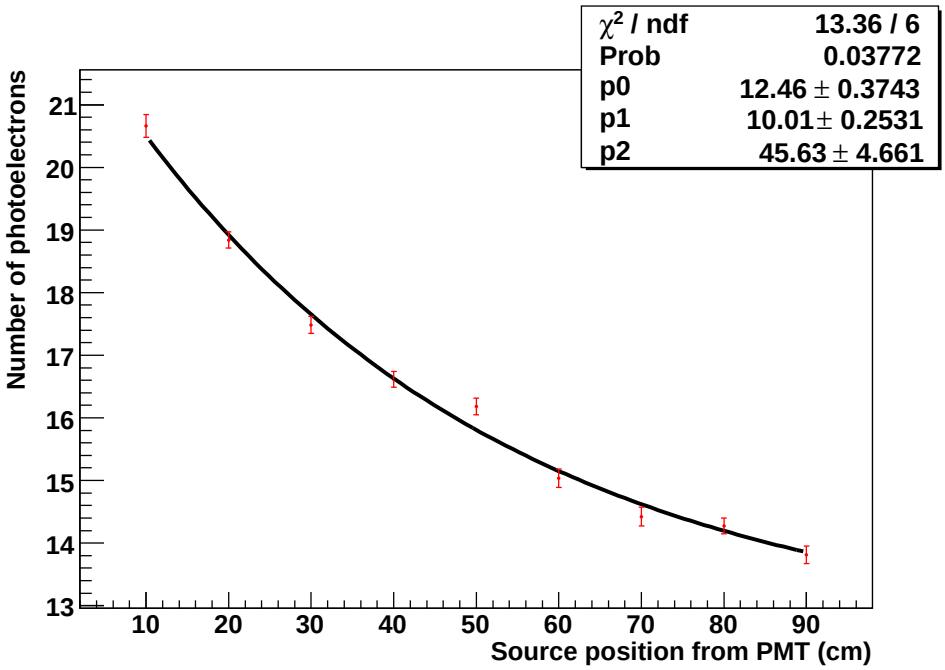

Figure 5.29: *The peak centroid of the 511 keV gamma-ray Compton edge as a function of distance for barrel scintillator block. The fit applied to provide data for light modelling is given in Equation 5.7. Here improvement in the effective light yield is accounted for unlike the TAL measurements.*

peaks were plotted as a function of distance from the PMT face, for all 52 scintillator sections and fitted using the following function;

$$M(x) = P0 + P1 \times exp(-x/P2) \tag{5.7}$$

where parameters $P0$, $P1$ and $P2$ were obtained from the fit and x is the position of the ^{22}Na source. Function 5.7 accounts for improvements in performance from the effect of the Mylar mirror, which is present in the real scenario, unlike the function used for TAL determination, which aimed to remove this effect. An example of fitted data is shown in Figure 5.29.

For scintillator sections where the PMT was not optically coupled to the scintillator a correction factor was applied to $P0$ and $P1$ ($P2$ only accounts for the rise or fall in the exponent). An average value of the parameters obtained for each of the five separate scintillator geometries was used to create five separate light curves for input into the main veto Monte Carlo. The parameters are summarise in Table 5.6 and are plotted as a function of distance in Figure 5.30.

Block type	**P0**	**P1**	**P2**
Barrel	35.95	21.17	51.47
Roof 51.5 cm	66.49	49.41	8.52
Roof 67.1 cm	89.02	52.05	23.89
Roof 75.0 cm	55.12	54.80	14.59
Roof 80.0 cm	57.09	44.65	30.10

Table 5.6: *Parameters obtained by fitting to each scintillator block data-set using the function 5.7. An average value was input into the main veto Monte Carlo depending on the geometry type.*

The observed trends in Figure 5.30 are as expected based on the dimensions and quality of the material for each geometry type. The 51.5 cm trend line appears to flatten nearer the PMT source, which may be attributed to the reduced distance to the Mylar mirror at the end of the scintillator section and the effect of a shorter scintillator section. One might also expect the 51.5 cm blocks to yield more light; however all four sections exhibited the worst BAL's ($69 \leq$ cm) and were more difficult to wrap with PTFE due to their size and angled cut out sections. The 67.1 cm scintillator sections give the best results

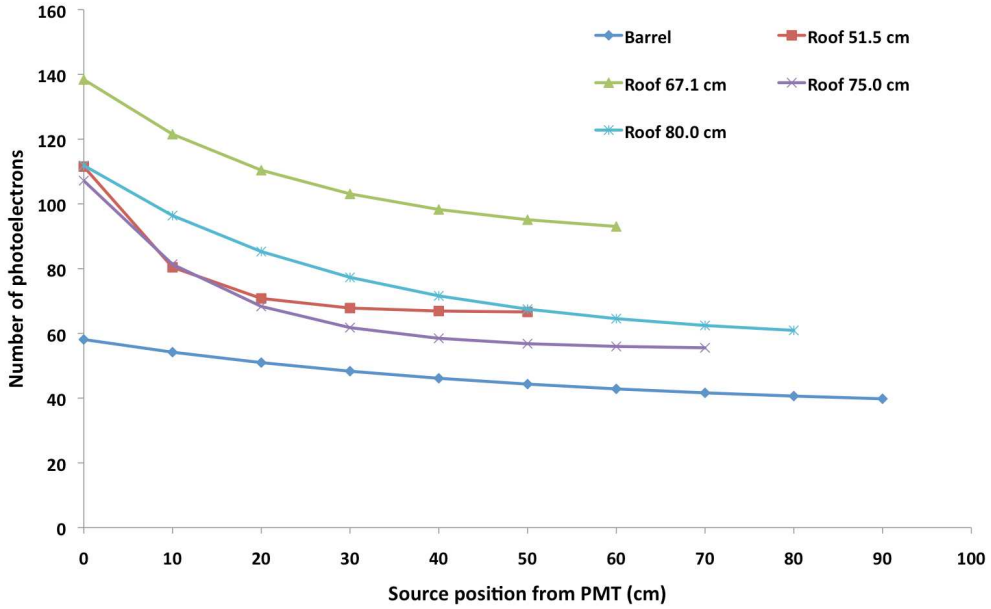

Figure 5.30: *The lightcurves produced using parameters shown in Table 5.6. These values were input into the main veto + ZEPLIN-III Monte Carlo.*

mainly due to their size but also as a result of an average BAL of 141 cm more than double the 51.5 cm roof sections.

The light curve equations were input into the main veto simulation as follows

$$Photoelectrons = (P0 + P1 \times exp(-x/P2)) \times E \tag{5.8}$$

where E is the energy deposition of the incident particle. The position, x, is where an event occurs within the scintillator section. This is output from GEANT4; however the position given is based within the co-ordinate system of ZEPLIN-III which is at the centre of the simulation ($x = y = z = 0$). Geometrical calculations were required to translate the position of an event back in terms of the co-ordinate system of the scintillator block where the PMT face of a scintillator section is given as $x = y = z = 0$. In this way, position of the event relative to the PMT face was determined and used in Equation 5.8.

5.4 Conclusion

All PMTs and scintillator blocks for the veto have been tested and matched based on each component's performance. The PMT's performances were ranked

in terms of gain and relative quantum efficiency. The scintillator sections were rated based on their Bulk Attenuation length (BAL) and Technical Attenuation lengths (TAL). The best performing PMTs were coupled to the roof sections due to their proximity to the ZEPLIN-III active volume and the fact that the roof sections are made from lower quality plastic, a fact that was beyond our control. The remainder of the PMTs were coupled to the barrel scintillator sections with the high performing PMTs coupled to the low quality scintillator blocks and vice versa improving uniformity across the veto detector. In addition to the experimental tests, Monte Carlo simulations were also performed to confirm the BAL and TAL measurements, especially as only 37 scintillator slabs had corresponding BALs provided by Amcrys-H. The agreement between the TAL and BAL measurements is reasonable; however comparison is difficult as the TAL measurements account for the scintillator geometry whereas BAL's which are based only on the purity of the material. The GEANT4 simulations of the experiment confirm the findings of the experimental tests. It was vital to include all processes to accurately model the experiment and extract parameters for the main veto+ZEPLIN-III simulation.

The second aim of these tests was to input light modelling of each scintillator block with specific PMT performance accounted for, into a larger Monte Carlo of the veto detector with ZEPLIN-III. These light curves were based purely on the experimental data obtained during the TAL measurements. The parameters extracted will also include variations in the veto PMTs. The light curves were subsequently input into the larger veto Monte Carlo which is discussed further in Chapter 6.

Chapter 6

Monte Carlo simulations of the VETO

6.1 Introduction

This chapter describes simulations for the design optimisation and performance evaluation of the veto, using the GEANT4 software package. The veto simulation has been incorporated with the existing ZEPLIN-III detector simulation, discussed in reference [161]. With the finalisation of the veto design, the contribution to background by the veto on the ZEPLIN-III detector, and the veto efficiency, was modelled using Monte Carlo methods. These two quantities are most important for dark matter detectors especially in the advent of the recent CDMS-II results [114].

6.2 Veto Simulations

Monte Carlo simulations were used extensively throughout the veto design process. All modelling of the veto was performed using the GEANT4 simulation package. GEANT4 is an object-orientated tool-kit, written in the C++ programming language, that can simulate the passage of particles through matter. Particle tracking and sensitive detector response are particular strengths of GEANT4 [156; 157; 158] making it well suited for the task in hand. GEANT4 also uses the most up to date particle data such as nuclear cross sections, to provide accurate information for particle interactions within a system.

The original ZEPLIN-III Monte Carlo simulation [161] was adapted to incorporate the veto design. The design of the veto simulation has been a constantly

evolving process, adapting to meet the findings from not only simulation work but also the changes required to meet the physical constrains of building such a device. The prominent changes to the original ZEPLIN-III simulation relate not just to the shielding, but also the addition of Boulby laboratory [66]. The main aim of this simulation was to accurately model the veto response in a 'mock up' of the live environment. It was therefore necessary to model all 52 veto channels, to record and output separate datasets providing the means to simulate coincidence events not only with multiple hits in the veto slabs from a single event, but also in coincidence with events occurring within the ZEPLIN-III target volume.

6.2.1 Features of the Veto Simulation

An iterative process of design and evaluation has been followed to arrive at a final veto construction. The version of veto simulation described here is based on the final veto detector design as described in Chapter 4.

6.2.1.1 The Plastic Scintillator (Active Shielding)

The simulation has assumed a geometry in which the veto surrounds the ZEPLIN-III detector. The active shielding has been modelled based on the dimensions and materials specified in Chapter 4. The segmented nature of the active plastic has also been modelled. The wall sections emulate the 32 standing parallelepiped segments (length 98.5 cm, parallel sides of 12.8 cm and 15.6 cm with a thickness of 15.0 cm) that form a barrel structure with inner and outer diameters of 13.0 cm and 16.0 cm. The veto PMTs that are attached to each end of the plastic scintillator have also been modelled including details such as a photocathode, envelope, internal components and PVC support structures as well has mimicking the metallic and glass properties of the real-life devices. The entire active wall structure (blue) is shown in Figure 6.1. The grey cylinders at the bottom of the plastic scintillator are the veto PMTs. The scintillator roof sits on top of the wall section and was recreated according to engineering specifications, by simulating the 20 cuboidal scintillator blocks (including the angled 'cut-out' areas; see Figure 6.2) again including their corresponding PMTs.

Light Collection Outputs

The real scintillator sections have been fully characterised; this work has been

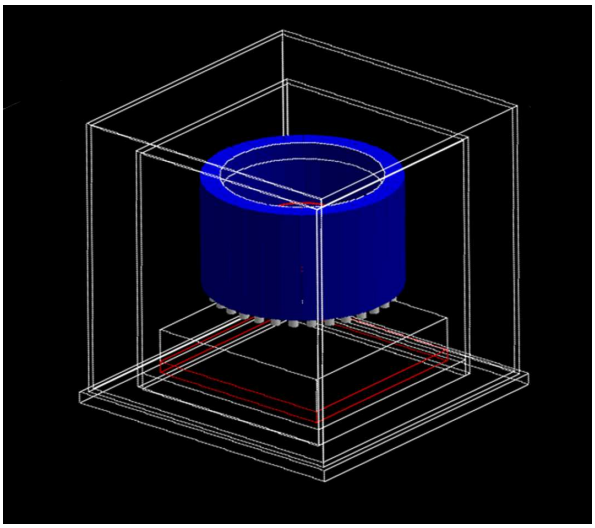

Figure 6.1: *The cylindrical object (blue) is the simulated veto wall section. This is comprised of 32 standing parallelepiped segments, together forming the barrel structure observed. At the lower end of each scintillator block are PMTs (white cylinders). The frame surrounding the veto indicates where other structures such as the lead shielding and neutron shielding base are positioned.*

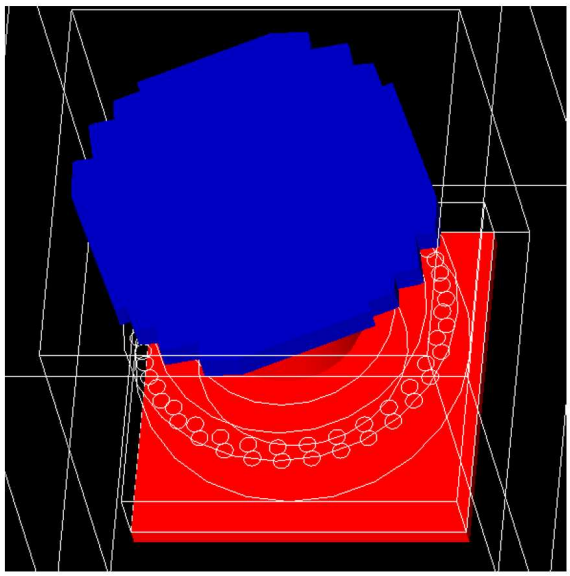

Figure 6.2: *The GEANT4 simulation of the veto roof (blue). This is comprised of 20 separate scintillator segments, with 5 separate geometry types.*

described in Chapter 5. Using experimental data obtained in Chapter 5, light curves detailing the number of photoelectrons produced when energy is deposited within a scintillator block (Section 5.3.4) as a function of distance from the PMT, have been implemented within the GEANT4 code. Two versions of the light curves have existed throughout this work. The first version was based on data obtained in the ITEP measurements, described in Chapter 4.2.2.2. However these results were based on one cuboid scintillator sample, not the actual plastic used in the ZEPLIN-III project. The latest version is based on work discussed in Chapter 5. The methodology is the same for both scenarios except the ITEP data are not strictly representative of the veto system, unlike the Edinburgh-based results.

The light curves are input into GEANT4 simulation in the form of equations, shown in Chapter 5.3.4 (Equation 5.8). When a particle interacts with the scintillator, the position and energy deposited (output by GEANT4) is converted to photoelectrons and directed to Monte Carlo output. Computationally, this provides a fast, efficient simulation process. Fully modelling each photon within GEANT4 is possible but is computationally expensive. The method discussed in this body of work produces realistic datasets at speed; and has the added benefit of including experimental details, which incorporate individual PMT responses.

6.2.1.2 Gadolinium Loaded Neutron Shielding (Passive Shielding)

The gadolinium (Gd) neutron shielding has also been simulated according to the details outlined in Chapter 4. The shielding is positioned between the plastic scintillator and ZEPLIN-III. The walls are 32 trapezoid sections, 15.0 cm thick and 83.5 cm in height, all of which rest upon a base section. The base section has been simplified for the simulation. It has a cylindrical geometry, 15.0 cm in height, with inner and outer diameter 65.0 cm and 80.0 cm, respectively; holes are simulated throughout the base where the veto PMTs are positioned.

The neutron shielding is composed of polypropylene ($(C_3H_6)_x$), density (1.06 g/cm^3). Material information such as the molecular formula and other attributes were input into the Monte Carlo having already created carbon and hydrogen as elements. The 2 mm thick slots which house the gadolinium (Gd) suspended in epoxy were recreated throughout the entire neutron shielding structure (with an 8 mm polypropylene layer and a pitch of 10 mm). The Gd and epoxy materials have also been simulated. The Gd, in the form of gadolinium oxide (Gd_2O_3) is

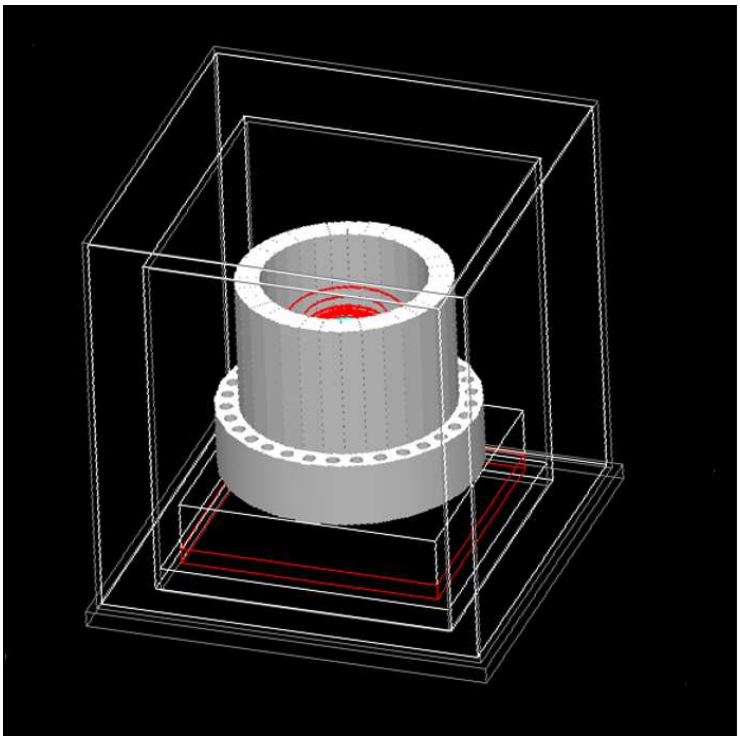

Figure 6.3: *Monte Carlo of the Gd loaded polypropylene neutron shielding (white). The ZEPLIN-III lead castle and plastic scintillator have been removed. The wire mesh represents other structures, left uncoloured to allow the reader to focus on the areas in question, but to still retain a sense of perspective for the entire device.*

suspended in epoxy. The Epoxy is a polymer with various fractions of H, C, O and Si. Gd by mass has to contribute 0.5% of the entire neutron shielding structure, therefore calculations were performed to determine the amount of Gd_2O_3 powder and epoxy required. The 0.5% figure had been arrived at using simulations to determine an optimum contribution. The results from these studies can be found later in this chapter.

6.2.1.3 Additional Shielding and Veto Components

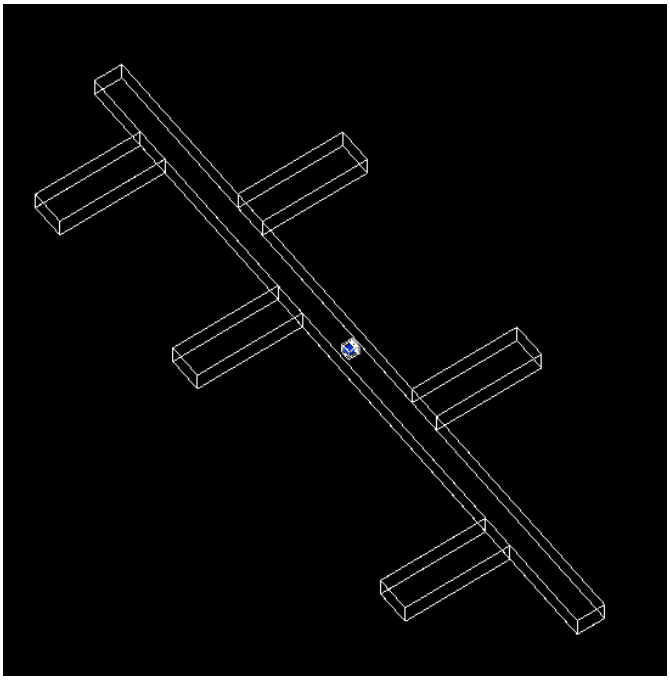

Figure 6.4: *Simulation the ZEPLIN-III detector within the Boulby Laboratory. The Boulby laboratory structure was originally designed by C. Ghag, see reference [66].*

The lead walls that surround the veto and the Boulby mine laboratory have also been included in the simulation [66], see Figure 6.4. The Boulby laboratory is simulated as walls of $\sim$ 10 m of rock salt (NaCl of density 2.17 kg m^{-3}), dimensions 6.5 m×4.5 m×80 m, and five stubs that lead off this main corridor with dimensions 25 m×4.5 m×8 m. The entire complex is filled with air at a pressure of 1.2 atmospheres. There is also CH_2 shielding under the laboratory floor, as in reality.

6.3 Simulating Gamma-ray and Neutron Exposures

GEANT4 is not well suited to the task of simulating the interactions from neutrons and gamma-rays emitted from materials used in the detector construction. All materials generally have various levels of contaminants such as ^{238}U, which can decay by alpha emission. This will give rise to (α,n) reactions with the surrounding material leading to the emission of neutrons at various energies. To model the decay of isotopes to this level (which is currently beyond the capabilities of GEANT4) a package called SOURCES [162] is employed. The molecular structure and level of contaminants in the material are input into SOURCES which will predict the processes that will occur. SOURCES then outputs a neutron energy spectra which is used in the veto Monte Carlo to assess the background impact of a particular detector component.

Gamma-rays emitted from a material can be released (after calculations to determine the daily rate) directly from the detector component without employing SOURCES. Gamma-ray calibration sources can also be reproduced by imputing the decay processors of an isotope and their intensities.

6.4 Feasibility Study

The first phase of simulations involved aiding design and estimating any impact of the veto on the low background running of ZEPLIN-III.

6.4.1 Veto Geometry Tests

The original concept design of the veto geometry was a single cylindrical shell. However difficulties arose relating to the feasibility of moving such a heavy object safely within the laboratory and the inability of Amcrys-h [147] to manufacture scintillator in this configuration. To remedy the situation, a segmented design for the veto was chosen. The benefits of such a design includes manoeuvrability and improved position resolution of energy depositions within the veto. The new geometry was tested within simulations to ascertain its performance, revealing no negative effect on the efficiency.

6.4.2 Positioning of the Veto PMTs

The impact of the veto PMT background to ZEPLIN-III was investigated. The majority of the observed background in ZEPLIN-III throughout the FSR can be attributed to the ZEPLIN-III PMTs, contributing ~ 10 dru (events/kg/day/keV) [163] due to their U, K and Th content. Using these numbers for the veto PMTs (the veto PMTs had not been purchased at this point), their background contribution to the ZEPLIN-III detector could be determined using Monte Carlo simulations. Positioning the veto PMTs away from the ZEPLIN-III target volume would reduce their total background impact; however this would have come at a cost of the veto efficiency. The bulk attenuation length of the scintillating material means that if the PMTs are set at the end of a block the light observed from an interaction with the plastic would be reduced as a function of distance. The majority of events observed in the plastic scintillator will be near the ZEPLIN-III target volume (noting that the veto will work in coincidence with the ZEPLIN-III detector), therefore the majority of events would occur at the top of the barrel wall sections and in the veto roof. Such considerations were tested to determine the optimum design without significantly compromising the veto efficiency and the low background running of the ZEPLIN-III detector.

The simulation at this stage was preliminary. The veto geometry consisted of the segmented wall sections, but with a disc-like roof. The scintillating material was assumed to have a BAL of 1.0 m and the light modelling discussed in the previous chapter was not implemented; this simplified model still gave a useful start point for further design iterations. Three positions were considered. The initial simulation had a PMT attached to the far end of each scintillator section (32 in total), the furthest position away from the ZEPLIN-III active volume. The other configurations examined had PMTs orientated perpendicularly at the top of the scintillator wall sections and in the middle. Six veto PMTs were also simulated for the roof section.

The simulated PMT design was based on the PMTs used in the first science run. The total number of gamma rays per day from the 38 PMTs is 4.4×10^6 for contamination levels of 250 ppm U, 290 ppb Th, and 1350 ppm K. Simulated gamma-rays emanating from the U and Th decay spectrum were fired isotropically from the veto PMTs.

Energy Range (keV)	Veto Threshold (keV)	Efficiency %	Un-vetoed Events
ZIII PMT γs (10 dru)			
2-20	100	20.8	2280
2-20	500	6.9	2680
Veto PMTs: Bottom (0.02 dru)			
2-20	100	50	2
2-20	500	50	2
Veto PMTs: Middle (0.03 dru)			
2-20	100	60	2
2-20	500	20	4
Veto PMTs: Top (0.05 dru)			
2-20	100	12.5	7
2-20	500	12.5	7

Table 6.1: *PMT position optimisation using GEANT4 simulations of ZEPLIN-III with the veto.*

Table 6.1 summarises the results from these simulations. The data were analysed to determine how many events that deposited 2-20 keVee energy within the ZEPLIN-III active volume (defined as a cylinder of xenon with dimensions of $0 < z < 35$ mm and radius$<$ 156 mm) and then within the veto.

It was found that the overall background contribution from the PMTs in each position were 0.02 dru (bottom), 0.03 dru (middle) and 0.05 dru (top), which were acceptable limits for the veto compared to the contribution from the ZEPLIN-III PMTs of $\sim$ 10 dru in the FSR. The veto efficiency for tagging events were 50% (bottom), 60% (middle) and 13% (top) for a veto threshold of 100 keV. Statistically the runs were poor (hence the future inclusion of the photoelectron light curve equations) though the results were sufficient to draw some conclusions and were significant for the continuation of the veto project. If the contribution from the veto PMTs was significant, a serious design rethink would have been necessary. It was decided to place the PMTs at the bottom of the scintillator blocks. Further improvement of light collection could be achieved with the introduction of Mylar mirrors and wrapping of the scintillator blocks (see Chapters 4 and 5). This also resolved any space issues within the design.

6.4.2.1 Veto Roof Design

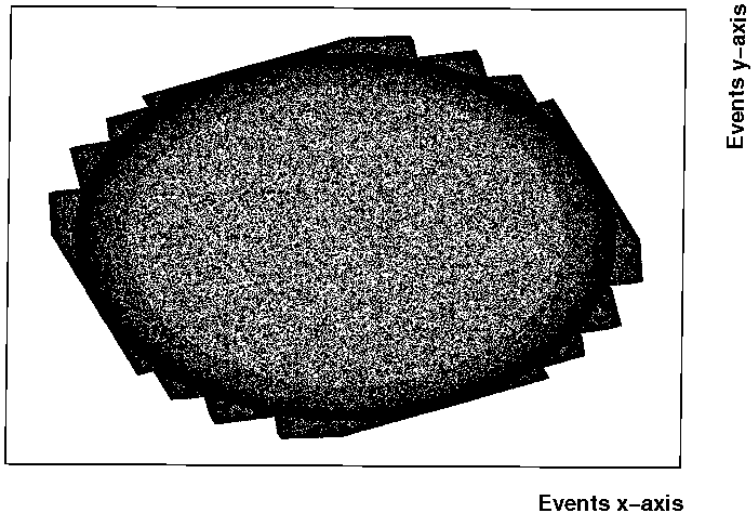

Figure 6.5: *Simulated gamma-rays detected by the veto roof. The shape of the roof can be clearly defined.*

The veto roof design has also evolved over time following space and safety considerations. Space between the ZEPLIN-III detector and lead shielding is limited, therefore a segmented design was considered because the roof would have to be lifted into position manually. With a predicted weight of 200 kg, this would not have been possible if not segmented. Figure 6.2 displays the final version implemented in the veto Monte Carlo. Simulations were performed to access if this was viable in light of background considerations. Gamma-rays were released isotropically from the 20 veto roof PMTs. It was found that the total rate detected by ZEPLIN-III was 0.023 dru, which was viable for continuation of the veto design. Figure 6.5 show the response of the roof to internal gamma-rays emanating from the ZEPLIN-III PMTs using the GEANT4 Monte Carlo. The shape of the roof can be clearly observed.

6.5 Optimisation of Veto

When the geometry of the veto had been established, more simulations were performed to calculate the levels of gadolinium (Gd) that should be present in

the neutron shielding, the pitch and width of the Gd slots and the effect of gaps within the veto sections.

6.5.1 Gaps Between Barrel Sections

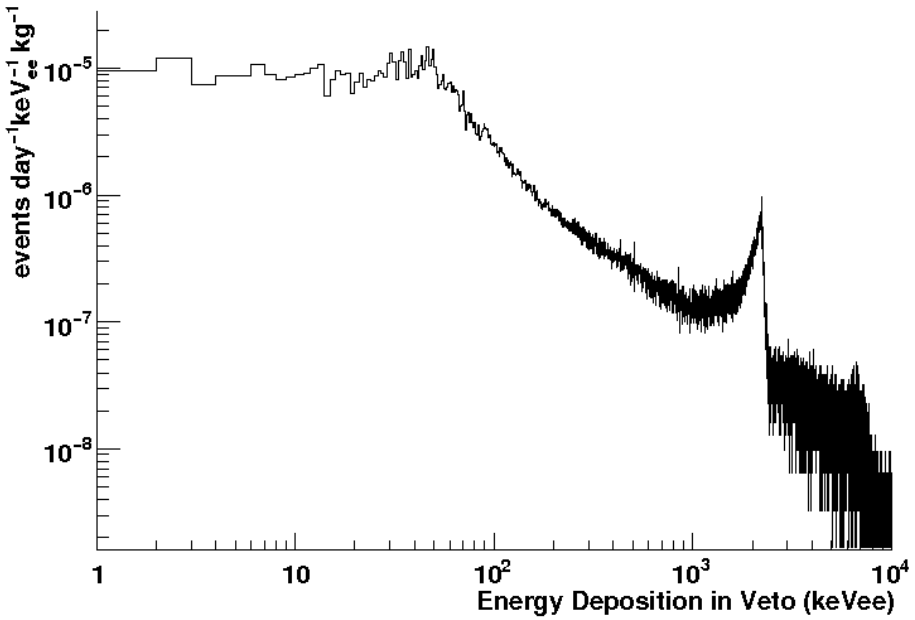

Figure 6.6: *Energy spectrum from the energy depositions due to external neutrons originating from the Boulby laboratory walls. The peak observed at 2.218 MeV is attributed to emitted gamma-rays from neutron capture onto hydrogen.*

There will naturally be inaccuracies in the way the plastic scintillator and neutron shielding has been manufactured, leading to the possibility of air gaps between the segments. Spacing of 2 mm had also been allocated between the scintillator segments to account for the PTFE and light-tight wrapping and manufacturer tolerances. The Monte Carlo simulation was employed to investigate the impact of the gaps that occur in both the active and passive sections.

Two simulations were performed, firstly for gaps within the active section only. A year long exposure of neutrons emitted from the laboratory walls was simulated (see Table 4.2 for rates). Gaps of 2 mm in thickness were present in active shielding only. There were zero events within the ZEPLIN-III active volume for energies of 2 -20 keVee and a 0 photoelectron veto threshold. Only

when the gaps are 20 mm thick 1 event is observed within the ZEPLIN-III active volume.

The same simulation was performed for gaps existing both in the active and passive shielding. The neutron flux was unaffected until the gaps exceed a width of 10 mm, where 3 events are observed. However this simulation is based on the worst case scenario, assuming a direct line of sight to the ZEPLIN-III target volume. In the real detector environment the gaps in the passive shielding will be offset from those in the active shielding to prevent this.

To conclude, the gaps present within the shielding (< 10 mm) will not effect the veto efficiency or increase the level of background depositing energy within the ZEPLIN-III active volume.

6.6 Optimisation of Gadolinium Loading

The veto design relies heavily on the inclusion of gadolinium loading within the polypropylene neutron shielding. The very high neutron capture cross section of ^{157}Gd, combined with the subsequent emission of up to 8 MeV of gamma-rays should improve neutron tagging efficiency. The effect of the gadolinium loading has been fully explored using simulations. Simulations described below detail its impact by significantly increasing the veto efficiency by up to $\sim 30\%$. Further simulations were used to determine how best to implement the loading within the neutron shielding, again to improve the efficiency.

6.6.1 The Gadolinium Mass Fraction

The veto simulation as described in Section 6.2.1, was utilised and adapted for these simulations. There are two important effects attributed to the inclusion of Gd. Firstly, increased amounts of Gd increase the fraction of neutrons captured. Neutrons will also be captured by the hydrogen content of the polypropylene; however the gadolinium should serve to improve the capture rate. The emission of up to four gamma-rays from capture by the ^{157}Gd gives the improvement in tagging efficiencies. Simulations were performed to determine the fraction of gadolinium necessary for optimum performance.

All materials have been simulated to manufacturer specifications (see Section 6.2.1 and [164] for further details). Table 6.2 shows the mass fraction of Gd_2O_3 per strip required to give a particular Gd mass fraction in the shielding.

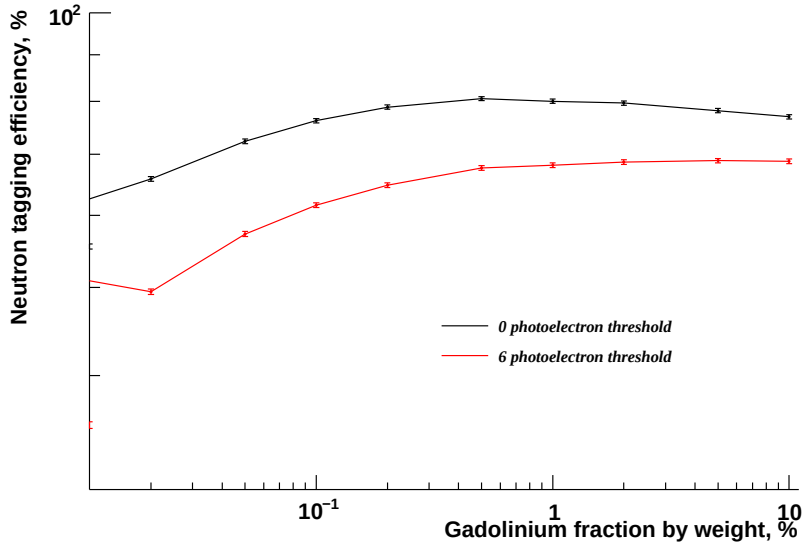

Figure 6.7: *The results of simulations of the veto using increasing mass fractions of Gd. The neutron tagging efficiency is based on coincident events that deposit energy within ZEPLIN-III (following WIMP event criteria) and in the veto.*

Total % of Gd	% Gd required per strip	% Gd_2O_3 required per strip
0.05	0.23	0.26
0.10	0.45	0.52
0.20	0.90	1.04
0.50	2.22	2.56
1.00	4.34	5.00
2.00	8.32	9.59

Table 6.2: *Gadolinium mass as a percentage of the neutron shielding. To obtain the percentage of Gd within the entire neutron shielding (as shown in the first column), the percentage of Gd per strip was calculated. The values for the Gd_2O_3 per strip were input into the simulation.*

Simulations were performed with a range of Gd mass fractions from 0% to 2.00%. For all simulations 10^5 neutrons from the U and Th decay chains, were fired isotropically from the ZEPLIN-III PMTs (equivalent to 848 years of real data) giving excellent statistics. 2 mm gaps were present between the polypropylene and scintillator shielding; only the percentage of the Gd by mass was varied. Only events that deposited energy of 5-50 keVnr (2-20 keVee equivalent) within the active volume (defined as $0 < z <$ 35mm and radius$<$ 156 mm) of ZEPLIN-

III were retained. Thresholds of 0 and 6 photoelectrons were applied to the veto, the results of which are shown in Figure 6.7 (log scales on both x and y axes). A 6 photoelectron (phe) threshold was chosen as it is well above the noise level. The y-axis on Figure 6.7 is defined as tagging efficiency. This is the ability of the veto to 'tag' events that have deposited energy within the ZEPLIN-III active volume within the expected WIMP energy region. A rapid increase in tagging efficiency is observed when the Gd concentration increases from $0-0.5\%$. Above this, little further gain is made. From 1% to 15% it is observed that the tagging efficiency slowly reduces for a 0 phe threshold, a consequence of the reduction in hydrogen concentration impacting the thermalisation process; however for a threshold of 6 phe little improvement is observed.

Based on the results from these simulations, it was decided to use 0.5% Gd by mass in the neutron shielding giving a veto efficiency of $67.6\pm0.6\%$; this quantity of Gd is also optimal from an economic viewpoint. The errors associated here are statistical and only vary slightly due to the high statistics obtained.

6.6.2 Pitch and Width of the Gadolinium Loaded Slots

Simulations have also been performed to investigate the optimal pitch and width of the Gd loaded slots within the neutron shielding. The pitch was limited by mechanical considerations; a decrease in pitch would increase the cost of machining (all passive shield machining was performed at Rutherford Appleton Laboratory).

10^5 neutrons were again fired isotropically from the ZEPLIN-III PMTs. Seven separate simulations were performed where the slot pitch was varied between 1.25 mm to 40 mm, for a total Gd concentration of 0.5%; only events that meet the WIMP search criteria of ZEPLIN-III were retained. Figure 6.8 displays the results. Clearly, as the slot pitch increases the neutron tagging efficiency of the veto drops significantly. This can be attributed to the reduction in the number of the thermalised neutrons being captured onto Gd, i.e, the neutrons sometimes have a trajectory that never happens upon a Gd loaded slot, reducing the total number of captured neutrons.

The effect of slot width has also been investigated; the results of which are shown in Figure 6.9. The slot widths were varied between 0.25 mm to 6.00 mm whilst the slot pitch (10 mm) and total Gd concentration in the neutron shielding

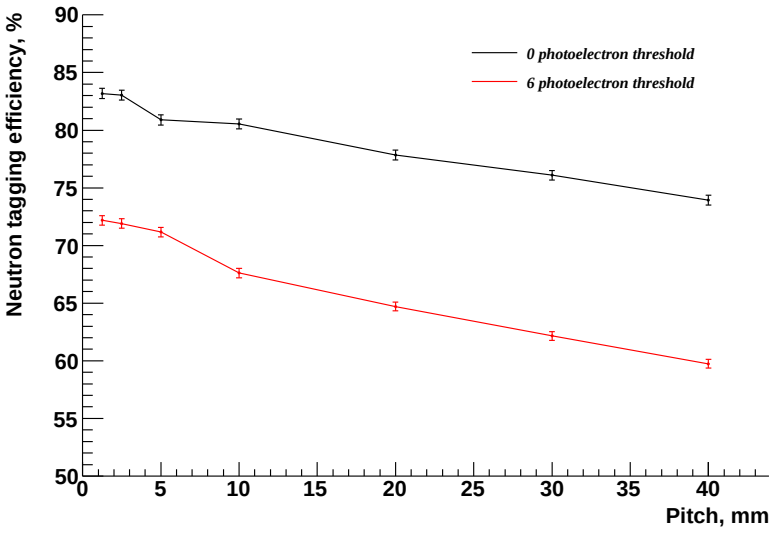

Figure 6.8: *Simulations to optimise the Gd slot pitch. Separate simulations were performed for different sized neutron shielding slot pitches.*

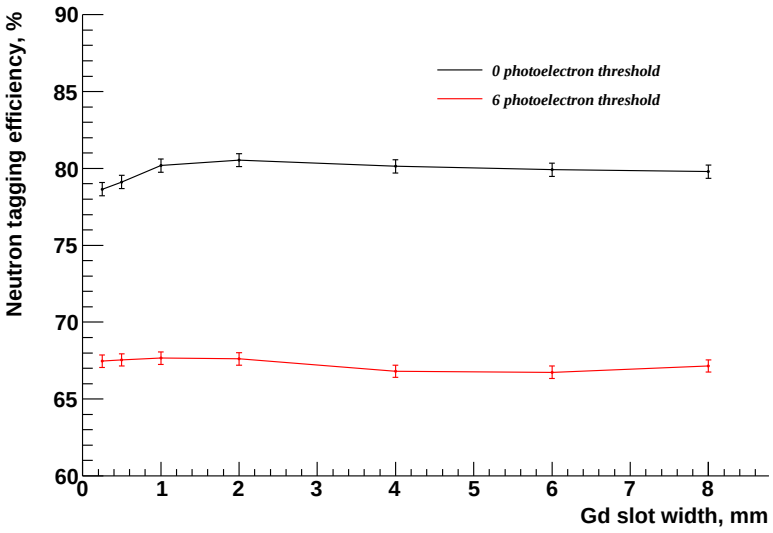

Figure 6.9: *Simulations to optimise the Gd slot width. Separate simulations were performed for different sized neutron shielding slot widths.*

(0.5%) were kept constant. Varying the slot width has a smaller effect on the veto tagging efficiency than the slot pitch.

These simulations displayed the possibilities of having a reasonable width and pitch of the grooves without compromising either the efficiency or the economic viability of the veto. A slot pitch of 10 mm and slot width of 2 mm were chosen for the actual veto construction reflecting these results and mechanical constraints.

6.6.3 Time Between an Event in ZEPLIN-III and the Veto

The time between coincidence events occurring in ZEPLIN-III and the veto was investigated as a function of the Gd loading concentrations. Introducing gadolinium loading into the neutron shielding can reduce the mean time for neutron capture by the passive shielding. This is preferred as shorter capture times enable a larger fraction of coincidence events between ZEPLIN-III and the veto to be 'tagged' within a specified coincidence time window. A shorter coincidence time window can also significantly reduce the data volume.

The majority of the neutrons will be thermalised through inelastic and elastic scattering prior to capture. The capture cross section of Gd (and H) can become very large when reactions are dominated by resonances, off resonance however the cross section decreases with increasing velocity [165]. This means that when the neutron begins to slow after multiple scatters the chances of capture onto Gd and H increases. To confirm that thermalisation is occurring, Figure 6.10 shows the energy distribution of neutrons just prior to capture by Gd and H. The neutrons have an energy distribution close to the Maxwell Boltzmann distribution that would be expected (3/2 kT$\approx$ 0.025 eV).

The time between an energy deposition in ZEPLIN-III and detection by the veto was then calculated. The time in which a particle enters the ZEPLIN-III active volume and deposits energy was recorded (Z_t). The particle could then scatter from the xenon target into the neutron shielding where it was thermalised and captured by Gd; here gamma-rays are released and the time (V_t) is recorded when these gamma-rays enter the scintillator. The mean time (ΔT) difference between the coincident events is calculated, $\Delta T = V_t - Z_t$. Figures 6.11 and 6.12 show ΔT for coincident events that occur for Gd mass loadings of 0% and 15%

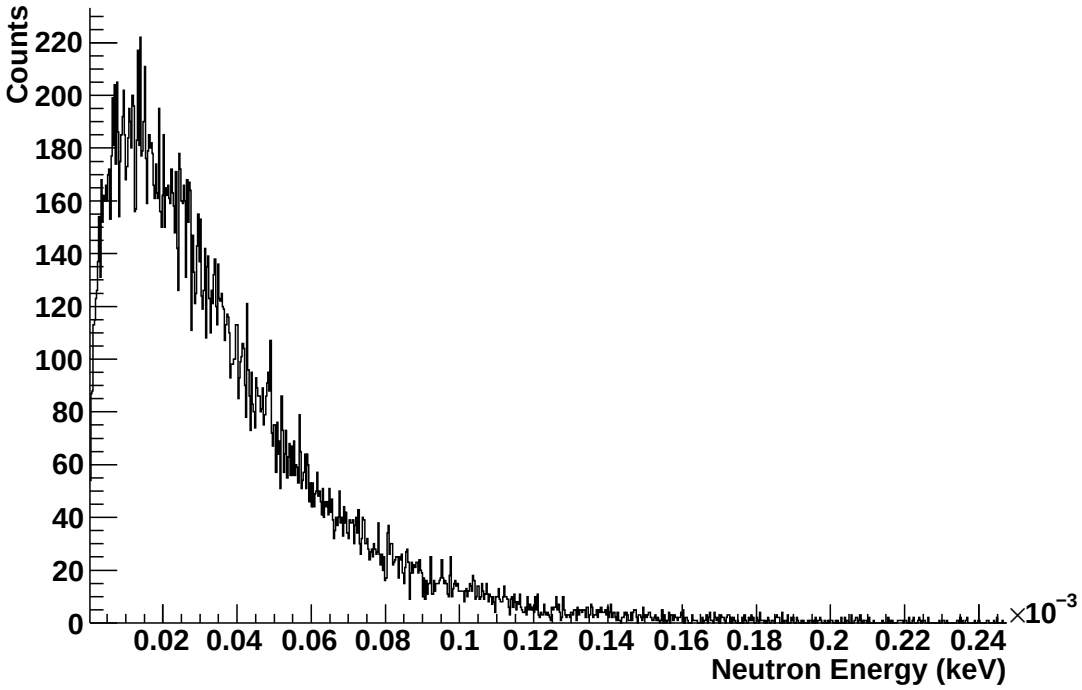

Figure 6.10: *Histogram showing results from a veto simulation of the kinetic energies of neutrons in the neutron shielding prior to capture by Gd or H. These were for external neutrons where the majority are captured on H ($E_{mean} \sim 0.035$ eV). For internal neutrons the majority are captured on Gd ($E_{mean} \sim 0.045$ eV)*

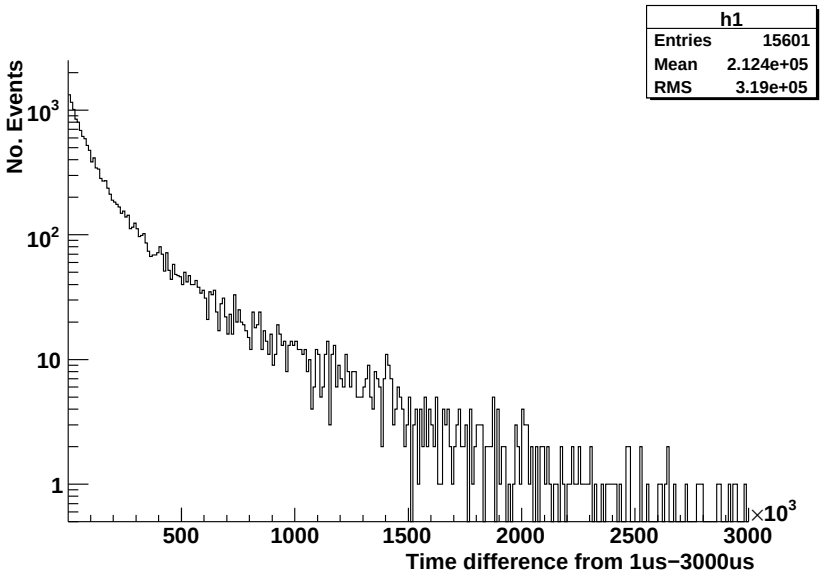

Figure 6.11: *The difference in time between signals in ZEPLIN-III and the veto when no Gd is used to enhance neutron captures. The mean of the distribution is 212.4μs.*

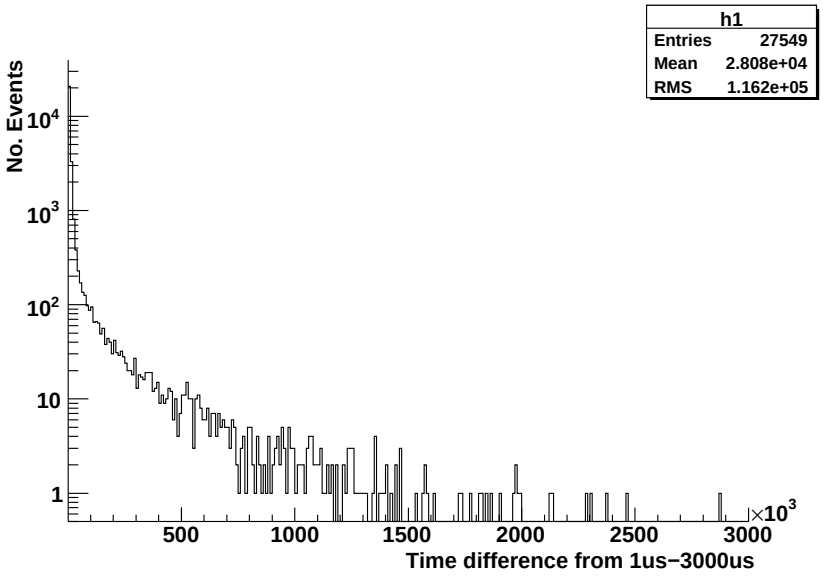

Figure 6.12: *The difference in time between signals in ZEPLIN-III and the veto when 15% Gd (by mass) is used to enhance neutron captures. The mean of the distribution is 28.08μs.*

respectively. To reduce the event rate from spontaneous gamma-ray emission a time window of $1 - 3000\mu$s was selected. These two extremes have been used to display the order of magnitude reduction in the time delay with the inclusion of Gd loading, illustrating the effect of the huge capture cross sections of Gd isotopes.

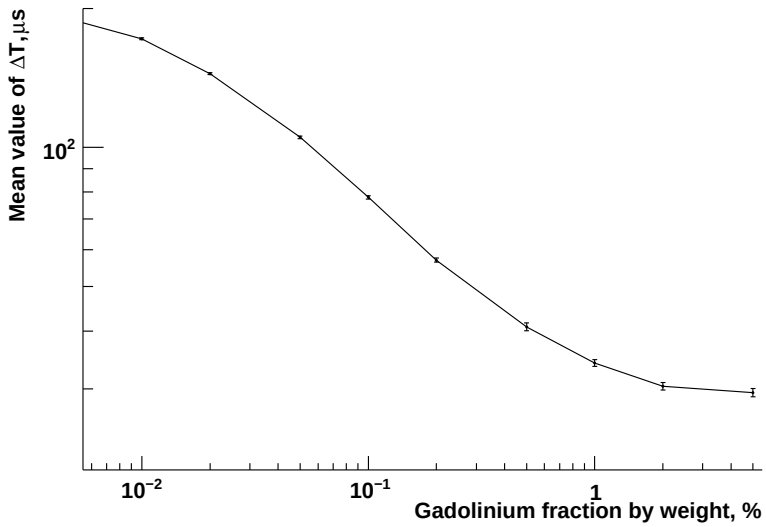

Figure 6.13: *The mean time delay between coincident events between the veto and ZEPLIN-III for various Gd concentrations.*

Figure 6.13 displays the results for ΔT at varying Gd concentrations. A rapid decrease in the mean capture time is observed as the Gd concentration is increased, flattening out at concentrations of $> 1\%$ (w/w).

While Gd allows the mean capture time to be reduced significantly, coincidence events still have large values of ΔT. A real data acquisition will have a limited period over which coincidence events may be searched for. Figure 6.14 shows the fraction of all coincidence events retained for a range of time windows. Two plots are shown. The top plot (black) is the total events retained for a range of time windows for a maximum time window of $1 - 3000$ μs, whilst the lower plot (red) is the total number of events retained for all coincidence events (including spontaneous gamma-rays). 97% of total events will be retained for a time window $1 - 300$ μs, with a 3% reduction in recorded events for a time window of $1 - 3000$ μs. It is also apparent from figures 6.11 and 6.12 that there

are no obvious populations beyond the 300 μs time range. Hence a time window of up 300 μs was chosen to reduce the data volume expected by the veto without removing the ability to observe important populations within a dataset.

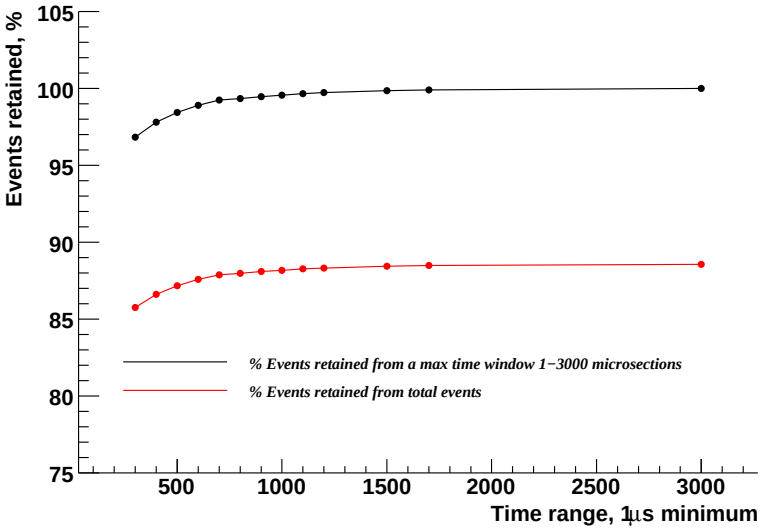

Figure 6.14: *The number of coincident events retained for different time windows. These results were obtained for a gadolinium concentration of 0.5%. The red line shows the percentage of events retained for various time windows from a maximum time window of 1-3000μs. The black line is for all events.*

6.6.4 Summary

Simulations were used to optimise the implementation of Gd loading within the neutron shielding. In summary, 0.5% Gd by mass within the neutron shielding was chosen giving a neutron tagging efficiency of 68% for events that satisfy the WIMP criteria in ZEPLIN-III, and are above the 6 photoelectron veto threshold. This is incorporated in slots of a pitch 10 mm and width 2 mm. A time window of 1-300 μs was shown to be suitable to observe the majority of coincident events. The veto DAQ can be triggered by an event occurring in the ZEPLIN-III target and will have a 20 μs pre-trigger (accounting for S2 signal retrieval) and a 300 μs post-trigger. This shorter window will reduce the data volume expected from the veto. All mechanical and cost considerations have also been accounted for during the design of the Gd loaded neutron shielding.

6.7 Veto Efficiencies

Monte Carlo simulations were also implemented to calculate the veto efficiency. The veto efficiency can be described as the ability to 'tag' background events that have deposited energy within the ZEPLIN-III target, such that they would otherwise satisfy the WIMP search criteria. A series of simulations were performed to assess the veto's tagging efficiency for certain signal sizes, and also to examine performance as a function of the number of segments hit by a single event. The neutron tagging efficiency is based on the number of single scatter events that deposit $2 - 20$ keVee within the ZEPLIN-III xenon active volume that then deposit energy within the veto. Background gamma-rays could also satisfy this criteria and thus could also be vetoed; this too has been explored.

The gamma-ray tagging efficiency was calculated by releasing 10^5 gamma-rays isotropically from the ZEPLIN-III PMTs (resulting from the U, Th and K decay chains). Using customised output, its was possible to determine how many slabs were hit, the total energy deposited in the veto and the equivalent number of photoelectrons generated.

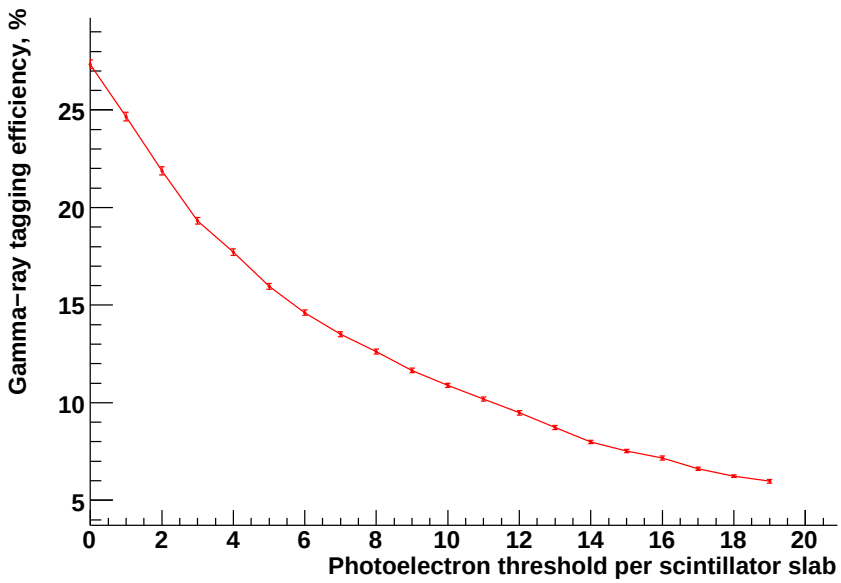

Figure 6.15: *The expected gamma-ray background tagging efficiency as a function of photoelectron threshold. The errors calculated are correlated between each value, hence only statistical errors are plotted.*

Figure 6.15 shows the expected gamma-ray background tagging efficiency. The x-axis displays the photoelectron threshold and the y-axis shows the tagging efficiency based on one veto slab tagging an event that deposited energy within ZEPLIN-III. $27.3 \pm 1.5\%$ (statistical and systematic errors, see Section 6.9 for further details) of gamma-rays would be rejected by the veto for a threshold of 0 phe, in any one slab hit. The actual veto will in fact have a minimum threshold below which events are indistinguishable from the baseline. The marker for this is 6 phe which is the energy equivalent of $\sim$ 132 keV. A 6 phe veto threshold would enable a rejection factor of $14.6 \pm 1.5\%$ (statistical & systematic, see Section 6.9 for further details). Although this rejection factor appears small the primary aim of the veto device is to reject neutron events, but any additional rejection of gamma-rays is obviously welcomed.

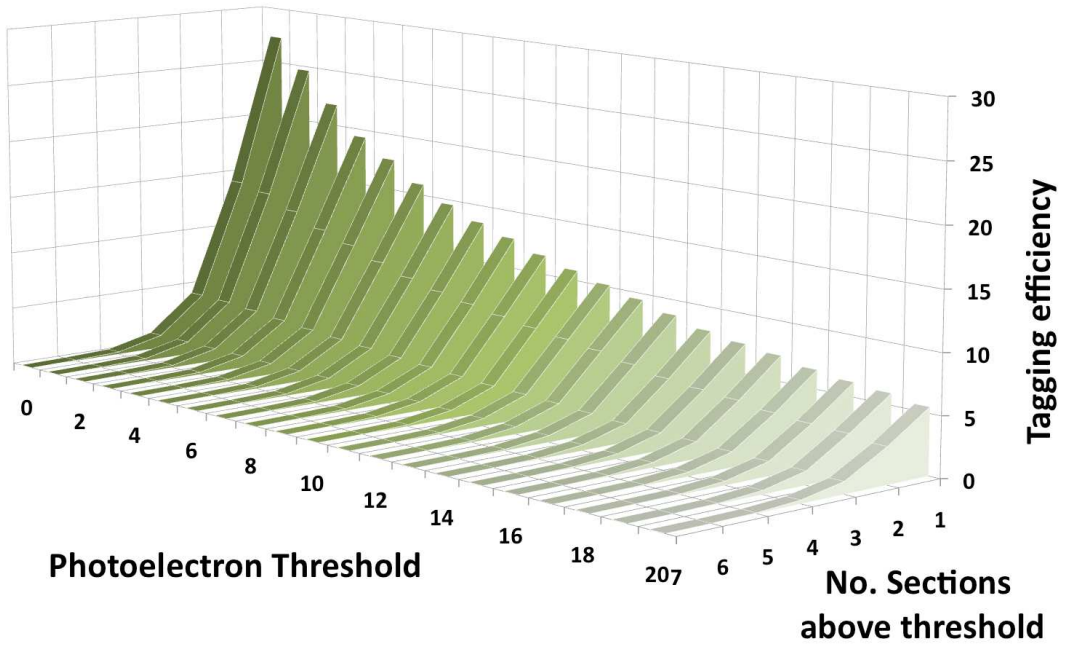

Figure 6.16: *The gamma-ray tagging efficiency for the energy depositions in multiple slabs for certain photoelectron thresholds.*

Figure 6.16 shows the gamma-ray tagging efficiency for the energy depositions in multiple slabs. The three-dimensional figure displays the tagging efficiency of gamma-rays, meeting the criteria previously discussed versus the photoelectron threshold and the number of slabs in which energy was deposited

(z-axis) above a certain threshold. If a coincident event deposited energy within at least two slabs with a 6 phe threshold (in each slab) a corresponding gamma-ray tagging efficiency of $8.6 \pm 1.4\%$ (statistical & systematic) would result. Neutrons will deposit large amounts of energy in multiple slabs however this shows that gamma-rays will not.

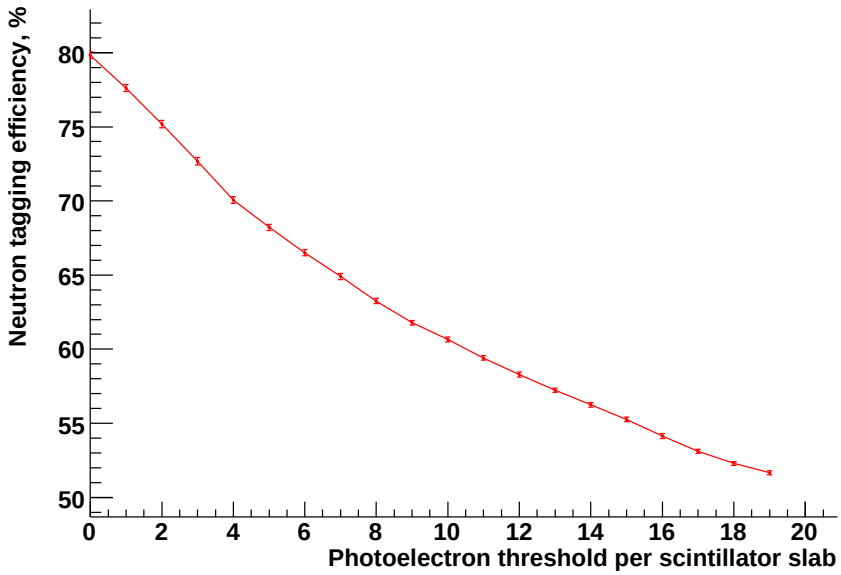

Figure 6.17: *The expected neutron background veto tagging efficiency as a function of photoelectron threshold. The errors calculated are correlated between each value, hence only statistical errors are plotted.*

Next, the neutron tagging efficiency has been estimated. 10^5 neutrons were released from the ZEPLIN-III PMTs. Using SOURCES to generate energy spectra (see Section 6.3) the number of neutrons emitted was calculated for each material, normalised to the mass and measured activities of the components. The primary source of contamination in the ZEPLIN-III PMTs emanates from the silicon glass. U contributes 87 neutrons/year, and Th contributes 31 neutrons/year; these were scaled accordingly to produce a combined 10^5 neutrons from U and Th using the energy spectra expected from such decays.

Figure 6.17 shows the expected neutron background tagging efficiency. The x-axis displays the photoelectron threshold and the y-axis is the tagging efficiency defined as the number of events detected by one veto slab above a photoelectron threshold, which had deposited energy within the ZEPLIN-III active

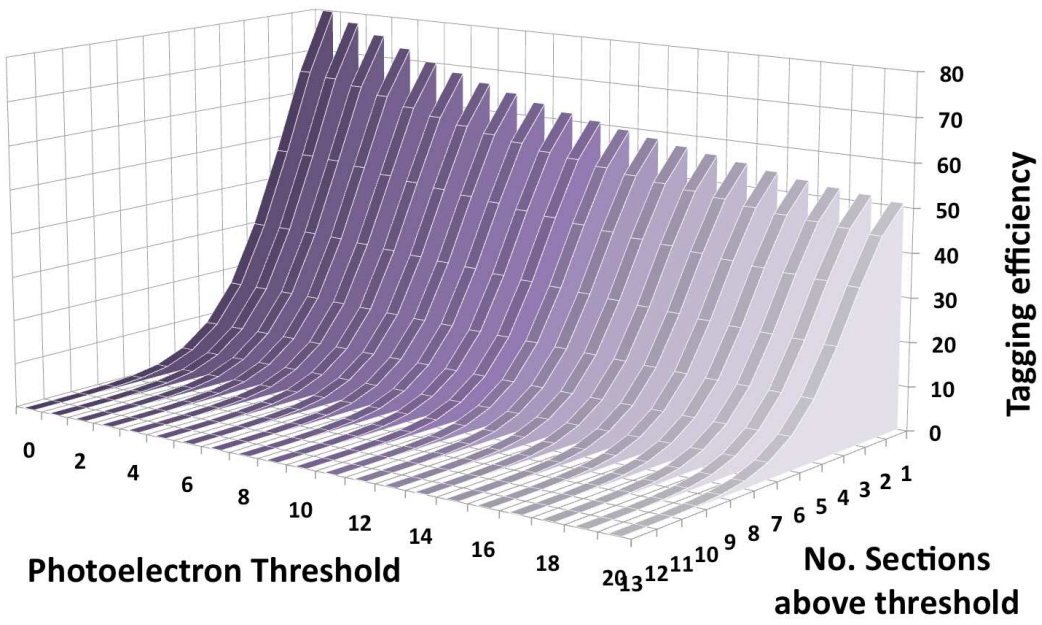

Figure 6.18: *The veto neutron tagging efficiency for energy depositions in multiple slabs as a function of photoelectron threshold.*

volume. From Figure 6.17 it is expected that $79.8 \pm 2.0\%$ (statistical & systematic) of neutrons depositing 2-20 keVee within the ZEPLIN-III active region would be rejected by the veto for a 0 phe threshold. A 6 photoelectron veto threshold would enable rejection of $67.6 \pm 1.9\%$ (statistical and systematic).

Figure 6.17 was also extended to look at multiple veto slab hits from one event. Figure 6.18 shows this, where the y-axis is the neutron tagging efficiency, the x-axis is the photoelectron threshold and the z-axis is the number of veto slabs observing an energy deposition greater than threshold. Figure 6.18 shows that an event trigger that would require two scintillator sections with simultaneous signals of above 6 phe would have a tagging efficiency of $57.4 \pm 1.5\%$ (statistical and systematic).

ZEPLIN-III has already demonstrated excellent discrimination between electron recoils (principally from gamma-rays) and nuclear recoils. However, some of these gamma-rays can leak into the WIMP parameter space. A fraction of these may deposit energy within the veto and can thus be rejected. The rejection of neutron events is also essential for improvements to the background of the detector. Of the total background observed by ZEPLIN-III following the

WIMP search criteria 68% can be rejected. The expected neutron background in the ZEPLIN-III acceptance region background is $\simeq 0.4$ events per year. The veto will reduce this background to less than 0.14 events per year. This is a significant factor in the event of a non-zero observation.

6.8 Background Rate from the Veto Components

6.8.1 Background Rate as Observed by ZEPLIN-III

A possible consequence of the veto system is the addition of unwanted background, such as gamma-rays and neutrons. A detailed discussion on the impact of background in dark matter detectors can be found in Chapter 2.3.1. A thorough approach was employed to control and evaluate the radioactivity content of all items used in the development and building of the veto. The results of these background measurements are summarised in Chapter 4.3. These measurements coupled with Monte Carlo simulations were used to estimate the absolute events rates observed in ZEPLIN-III and also the veto.

A series of simulations was performed to emulate the typical exposure to the ZEPLIN-III detector to events emanating from the veto. Using the results obtained from the HPGe detector measurements (see Table 4.3), exposures of gamma-rays emitted per day, were fired based on the U, Th and K decay chains. The energy depositions in the veto and in ZEPLIN-III that meet the WIMP search criteria were recorded. The daily gamma-ray rate is calculated and fired isotropically from each veto component, the lead shielding and the SSR ZEPLIN-III PMTs. The results are displayed in Figure 6.19, where the scintillator is the largest source of gamma-rays. This is due to the amount of scintillator and neutron shielding used in the veto design and also the fact that this is an overestimate as the activity levels were too low to be measured, and hence only upper-limits could be used.

By summing the individual contributions a total daily gamma-ray rate detected in ZEPLIN-III (obeying the WIMP criteria) due to the veto and including the lead shielding and SSR ZEPLIN-III PMTs is expected to be 0.9 dru. 0.5 dru of this is expected from the veto components.

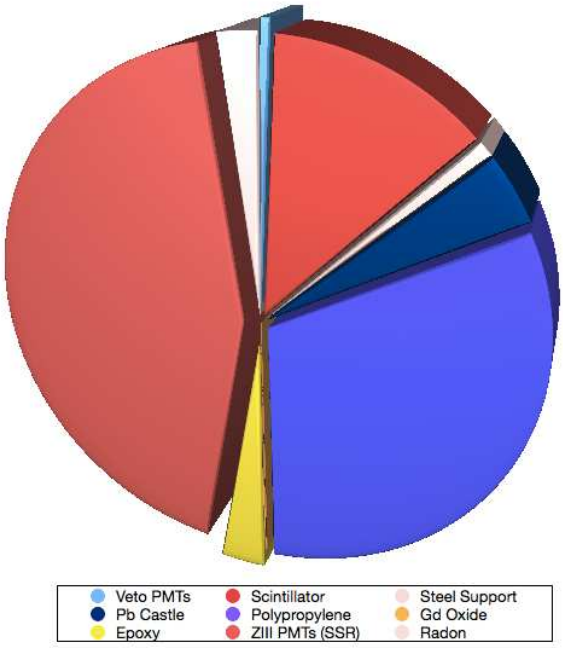

Figure 6.19: *The background contribution to ZEPLIN-III from the veto components. This pie chart gives a breakdown of the main sources of background due to the veto components, the lead castle and the SSR ZEPLIN-III PMTs. The plastic scintillator is the main contributor of gamma-ray events responsible for 7300 gamma-ray events/year for energies of 2-20 keVee within the ZEPLIN-III active volume. However the total contribution from the entire shielding array and the SSR ZEPLIN-III PMTs equates to only 0.9 dru.*

Decay Chain	Quantity	No. gamma-rays/day/kg
U	1ppb	2310
Th	1ppb	958
K	1ppm	278

Table 6.3: *Gamma-rays emitted per day per kg for U, Th and K*

The neutron exposure to ZEPLIN-III from the veto components was also investigated. Using the SOURCES [162] package, the spectra for U and Th decay chains were generated and the number of neutrons emitted per year calculated based on the amount of material and the U and Th content as determined by the HPGe measurements. One year's worth of neutrons were released isotropically from each veto component. An upper limit of 0.19 neutrons/year (single scatter) depositing 5-50 keVnr within the ZEPLIN-III active volume from the veto is expected.

The total gamma-ray rate expected including the ZEPLIN-III detector components and the veto is 1.7 dru (SSR PMTs). This is reduced to 1.4 dru with application of the 15% gamma-ray rejection factor due to the veto. Applying geometrical cuts inclusive of the fiducial mass reduction of the xenon target (as was applied in the FSR analysis) this is reduced to 0.9 dru. The neutron exposures from the veto and ZEPLIN-III materials is $\leq$ 3.9 neutrons/yr. Again applying the FSR geometric mass reduction cuts and the FSR energy box cut (accounting for energies between 2-16 keVee), the neutron rate is reduced to 0.4 neutrons/year. Inclusive of the veto neutron rejection factor of 67% this is reduced further to 0.14 neutrons/year.

The gamma-ray and neutron background from the veto in the ZEPLIN-III second science run is sufficient to retain the low background running of the ZEPLIN-III detector. The veto can also significantly reduce the overall event rate observed by ZEPLIN-III, particularly for neutrons. 0.4 neutrons/year are expected in ZEPLIN-III which are further reduced to 0.14 neutrons/year by the veto. The SSR is expected to run for six months. With these levels of background, ZEPLIN-III could achieve a spin-independent limit of 2.1×10^{-8} pb in the SSR if 6 months of data was obtained (scaled from the FSR result). ZEPLIN-III would surpass the latest CDMS-III result of 3.8×10^{-8} pb [114].

6.8.2 Background Rate as Observed by the Veto

The large volume of plastic scintillator used in the veto, combined with a low threshold, has the potential to create a system that observes a high event rate. The event rate could cause problems in the data acquisition by creating an excessive volume of data. To explore this issue further the method as discussed in Section 6.8.1 was applied to determine the event rate in the veto from gamma-rays.

6.8.2.1 Internal Gamma-rays

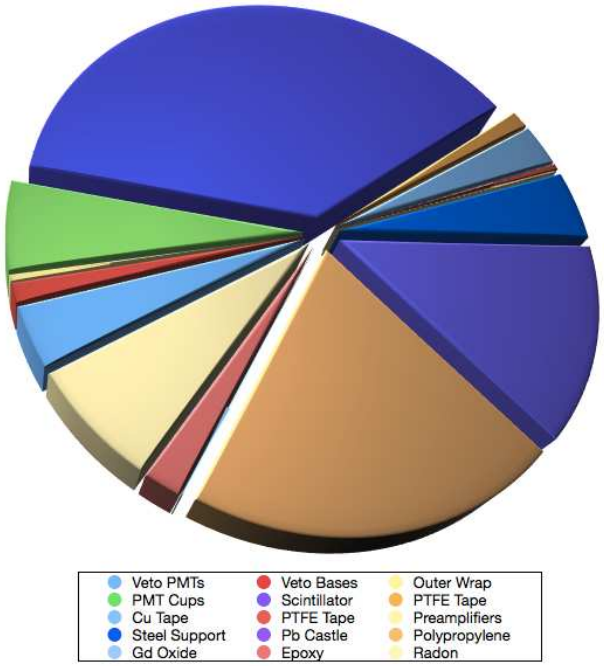

Figure 6.20: *Contribution of total gamma-ray event rate, broken down by component. The plastic scintillator is the biggest contributor of events within the veto due to the amount of material used. A maximum event rate of 23.9 Hz is expected from the plastic scintillator alone. The polypropylene alone will produce a maximum event rate of 12.7 Hz; however this is based on upper limits for the measured contamination levels.*

The total expected event rate in the veto was calculated by summing all the background contributions. By considering the veto as a stand-alone instrument, the raw event rate that is expected in the veto as a function of the number of photoelectrons was estimated. This is for a multiplicity of at least one slab

registering an event. It should be emphasised that for these calculations no coincidence in ZEPLIN-III is required.

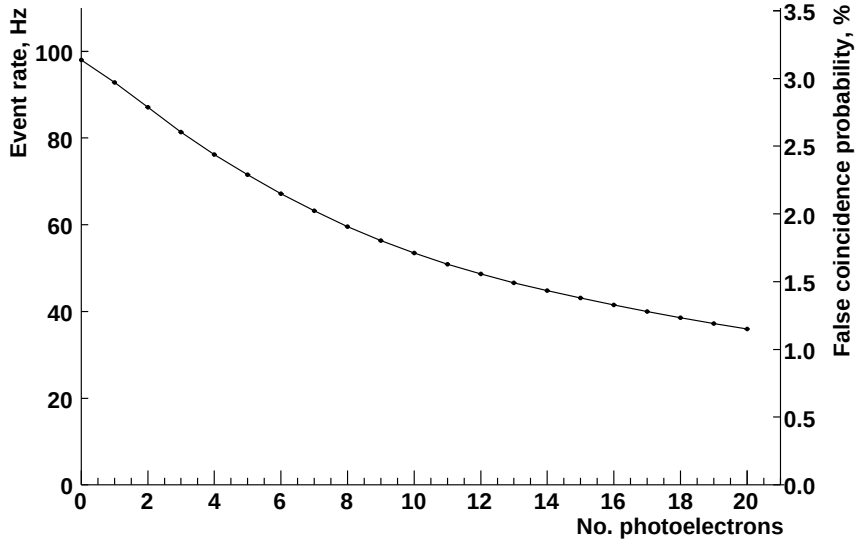

Figure 6.21: *Predicted gamma-ray event rate in the veto, as a function of signal size, based on measured activities of components. Also shown is the probability for events seen in the veto following gamma ray emission from components being misidentified as coincident with ZEPLIN-III events.*

Figure 6.21 shows the simulated event rate observed in the veto with a slab multiplicity of one. Figure 6.21 includes gamma-rays emitted by the lead castle. A rate of $\sim$ 100Hz is expected in the veto from the veto components and lead castle at a 0 photoelectron threshold. If a veto trigger requirement were imposed such that events were recorded if any single scintillator section with an energy deposition of six or more photoelectrons, then a reduced event rate of 64 Hz would be expected.

The right axis from Figure 6.21 shows the false coincidence probability. This describes the probability of mis-identifying events observed in the veto as coincident events with ZEPLIN-III. This is calculated by using the estimated trigger rate from ZEPLIN-III and the time-line of recorded data in the veto. The event rate in ZEPLIN-III will be $\sim$ 1 Hz, and the veto will record data 20 μs prior to, and 300 μs after this. Multiplying the sum of the veto and ZEPLIN-III event rate with the duration of the time-line, the probability of recording a signal due to the background-radioactivity can be determined.

6.9 Uncertainty Estimates

Below is a detailed discussion of the source of errors within the veto simulation.

Generic Tolerances of the Plastic

The manufacturer quoted tolerances in the building of both the active and passive shielding of ±0.1 mm. Previous simulations show no effect to the low background running of ZEPLIN-III and the efficiency of the veto until gaps of $>$ 10 mm were present, well beyond the manufacturers levels. Measurements of the blocks themselves have revealed dimensions broadly consistent with the manufacturer's specifications.

Uncertainties in the Light Collection Equations

It is expected that one of main sources of uncertainty within the Monte Carlo can be attributed to the light curve equations derived from experimental data. The aim was to calculate a corresponding error associated with the neutron and gamma-ray tagging efficiency as they have been derived using the number of photoelectrons output from the Monte Carlo. Five equations were produced in total for the five separate scintillator block geometries. In each equation there are three correlated parameters ($P0$, $P1$ and $P2$) each with an associated error. By perturbing the fit parameters it is possible to examine the robustness of the final solutions. The light curve equations follow the form shown in Equation 6.1,

$$z = (P0 + P1 \times exp(-x/P2)) \,. \tag{6.1}$$

The number of photoelectrons output is heavily dependent on the x value (i.e distance from a PMT see Chapter 5). By perturbing the parameters $P0$, $P1$ and $P2$, for three values of x (positions closest and furthest from the PMT and in the middle of a block) a series of random output values were obtained. The standard deviation and associated error were calculated for each data set for x. This process was then repeated for all five block geometry equations where their parameters differ from one another as determined experimentally. From this an average percentage error for each block geometry has been calculated. To calculate a total error, the separate percentage errors are weighted against each block geometry volume and the number of block types present in the veto (for example, there are 32 barrel sections but only 4 of the smallest roof sections).

This gives a final percentage error of 1.4%. This technique is robust and as expected it is the greatest source of error in the simulation.

Radiological Determination

Simulations to determine the background effects of the veto components on ZEPLIN-III and the veto itself required measurements that were performed using a HPGe detector at the low counting background facility at Boulby mine. All measurements have a corresponding error, and when simulations were performed the expected value including the maximum error value was used. For values < 1 ppb or ppm, a value of 1 ppb was used. This ensured that an upper limit could be set on the background expected from all components within the detector, giving a worst case scenario.

Statistical Error

Statistical errors were calculated assuming a Possonian behaviour, i.e. an error of $\sqrt{N}$ where N is the statistical value being answered.

6.10 Conclusion

The veto for the ZEPLIN-III detector has been simulated using GEANT4 software. The simulation was used extensively throughout the veto design process, to test geometry, and to inform design decisions such as PMT positioning and the distribution and levels of Gd to be used in the polypropylene neutron shielding. The Monte Carlo has provided the means to tune the design to maximise the neutron tagging efficiency (at low cost). The simulation was also used to estimate the timelines required for the veto DAQ and the number of events that would be lost based on the timeline chosen.

The veto Monte Carlo has subsequently been utilised to calculate the overall efficiency of the veto for neutron and gamma-ray rejection. The veto will reject neutrons that otherwise would meet the WIMP search criteria with an efficiency of $80 \pm 2\%$ for a veto threshold of 0 phe. For a threshold of 6 phe a neutron rejection factor of $68 \pm 2\%$ is calculated. For gamma-rays the rejection factor of the veto is lower at $27 \pm 2\%$ (0 phe threshold) and $15 \pm 2\%$ (6 phe threshold).

Another important application of the Monte Carlo is the ability to study the expected background contribution from the veto to ZEPLIN-III. The veto

will contribute 0.19 neutrons/year and 0.5 dru gamma-rays to the ZEPLIN-III detector. This is low enough to allow running of the ZEPLIN-III detector. The total neutron and gamma-ray exposure to ZEPLIN-III from all components (including the veto) is expected to be 3.9 neutrons/year and 1.7 dru, respectively.

These rates will be reduced further, in particular the neutron background rate. By applying the FSR geometric mass reduction cuts and the FSR energy box cut (accounting for energies between 2-16 keVee), the neutron rate is reduced to 0.4 neutrons/year. However, the veto has a neutron rejection factor of 68%, reducing the neutron background further to 0.14 neutrons/year, a significant factor in the event of a non-zero observation. The SSR is expected to run for six months. With these levels of background, ZEPLIN-III could achieve a spin-independent limit of 2.1×10^{-8} pb which would surpass the latest CDMS-II result of 3.8×10^{-8} pb [114].

Chapter 7

Conclusions

There is significant evidence from various independent sources indicating the existence of dark matter. The most favoured explanation is Cold Dark Matter in the form of weakly interacting massive particles (WIMPs) and it is thought that this could account for a large proportion of missing mass within the universe. There are a number of dark matter detectors around the world attempting to prove this assertion by a direct observation of a WIMP interaction. Positive detection would be extremely significant for many cosmological models of the universe and further our understanding as to how the universe developed from its earliest stages through to its eventual fate. In addition, such a discovery would also be significant to particles physics, particularly for physics beyond the standard model.

The ZEPLIN-III detector is a low background, high sensitivity 12 kg, two phase xenon time projection chamber located at Boulby mine in Cleveland and Redcar. It has been developed to observe low energy nuclear elastic recoils resulting from the scattering of WIMPs from xenon nuclei. By using a two phase system, ZEPLIN-III has demonstrated excellent particle discrimination between neutron and electron recoils, with a gamma-ray rejection factor of 5×10^3.

When a particle enters a two phase xenon detector, two signals can be observed. The first is scintillation light (denoted as S1). The second is due to electroluminescence in the gas phase (denoted as S2), which is created by the electrons produced at the interaction site of the original S1 signal and then drifted to the gas phase, where they are accelerated. The S2/S1 ratio, is different for electron recoils and neutron recoils, enabling particle discrimination.

After careful analysis a WIMP region within the data is established, where events that leak into this region effect the overall detector sensitivity.

ZEPLIN-III has completed its first science run (FSR). The FSR data was analysed using strict analysis cuts and corrections. The author's contribution included profiling the historical evolution of the electron lifetime throughout the FSR, and implementing consideration of this to improve the data quality. The electron lifetime can severely impact on the S2 signal as it is reliant on the liberated electrons produced at the interaction site. The electron lifetime can be reduced if the purity of the xenon is insufficient, resulting in the capture of free electrons by electronegative impurities. It was found that the electron lifetime actually improved throughout the FSR. This may be due to the high fields used throughout the FSR removing electronegative particles from the xenon. A historical profile correction was devised to correct the S2 signals from the FSR WIMP data (Figure 3.27 shows the extent of event leakage into the WIMP region without application of the electron lifetime correction). Overall the first phase of the ZEPLIN-III project can be considered a success having excluded a WIMP-nucleon spin-independent cross section above 8.1×10^{-8} pb (90% confidence limit) for a WIMP mass of 60 GeV/c^2 (second best in the world) and also set a 90%-confidence upper limit of a pure WIMP-neutron spin-dependent cross section of 1.9×10^{-2} pb for a 55 GeV/c^2 WIMP mass. The second science run (SSR) is the next stage of the project which will include a number of upgrades to improve the sensitivity of ZEPLIN-III by reducing or identifying any background. The author has been heavily involved in the design, construction, testing and evaluation of a veto to be retrofitted to the ZEPLIN-III detector.

The final veto design includes 1 tonne of 15 cm thick plastic scintillator (UPS-923A) and 15 cm thick gadolinium (Gd) loaded polypropylene neutron shielding. The walls of the veto are comprised of 32 standing parallelepiped segments with the remaining 20 sections forming the roof that extend over the full diameter of the barrel sections, above ZEPLIN-III. 52, PMTs are optically coupled to each scintillator section for readout. The neutron shielding is positioned between the plastic scintillator and ZEPLIN-III where neutrons can be thermalised and then captured to produced gamma-rays that can be eventually detected by the attached PMTs. The veto will detect particles that has previously deposited energy within the ZEPLIN-III target vessel.

The veto design was optimised with the use of Monte Carlo simulations. The author built the simulation of the veto and adapted it based on its findings and changes in the actual veto design. Experimental data based on the performance on the veto PMTs and scintillator sections (light modelling) were used to inform the Monte Carlo. Light curve equations were produced for all scintillator sections, that output the number of photoelectrons as a function of distance from a PMT based on the scintillator block geometry, the quantum efficiency of the PMT and inclusion of light effects.

Using the light curve inputs into the main veto Monte Carlo, simulations were performed to determine the implementation and optimum quantities of Gd loading and to obtain good veto efficiency at low cost to the project. This was found to be 0.5% by mass, loaded in 2 mm width, 10 mm pitch grooves throughout the neutron shielding. The Monte Carlo has also been utilised to predict the veto rejection efficiency for neutrons and gamma-rays. The efficiency of the veto for tagging events that deposit energy within the ZEPLIN-III detector according to WIMP criteria, is expected to be $68 \pm 2\%$ for neutrons and $15 \pm 2\%$ for gamma-rays for a veto threshold of 6 photoelectrons. The simulation was then used to predict the background impact of the veto to ZEPLIN-III. It was found the veto would contribute 0.5 dru gamma-rays and 0.19 neutrons/day. This is deemed sufficiently small to continue the low background running of the ZEPLIN-III detector. The total neutron and gamma-ray exposure to ZEPLIN-III from all components (including the veto) is expected to be 3.9 neutrons/year and 1.7 dru, respectively.

These rates will be significantly reduced further, in particular the neutron background rate. By applying the FSR geometric mass reduction cuts and the FSR energy box cut (accounting for energies between 2-16 keVee), the neutron rate is reduced to 0.4 neutrons/year. However, the veto has a neutron rejection factor of 67%, reducing the neutron background further to 0.14 neutrons/year, a significant factor in the event of a non-zero observation. The SSR is expected to run for six months. With these levels of background, ZEPLIN-III could achieve a spin-independent limit of 2.1×10^{-8} pb which would surpass the latest CDMS-II result of 3.8×10^{-8} pb [114].

Appendix A

Useful Acronyms

Acronyms	Description	Extra Information
dru	events/kg/day/keV	
KeVee	KeV electron equivalent	The keVee energy scale is established as the total number of photoelectrons detected for a single energy point (often 122 keV gamma-rays from ^{57}Co)
KeVnr	KeV nuclear recoil equivalent	Determination of the keVnr energy scale requires calculation of the relative scintillation yield of nuclear recoils. This is discussed in Section 2.2.4.2.
phe	Photoelectrons	
MS/s	Mega samples per second	

Table A.1: *Given above are acronyms and units often used throughout this thesis for quick reference. Some of these are specific to rare particle search experiments.*

Bibliography

[1] G. Hinshaw *et al.* Five-year Wilkinson Microwave Anisotropy Probe observations: Data, processing, sky maps, and basic results. *Astrophysical Journal Supplement Series*, **180**(2):225–245, FEB 2009. (document), 1.1.1.1, 1.3, 1.3, 1.1.3.3, 1.2.3, 1.2.3.1

[2] John A Peacock. *Cosmological Physics*. Cambridge University Press, Cambridge, 2005. 1.1.1.2

[3] J. N. Islam. *Mathematical Cosmology*. Cambridge, 2002. 1.1.1.2

[4] L. Bergström and A. Goobar. *Cosmology and Particle Astrophysics*. Springer, 2004. 1.1.1.2

[5] *WMAP*. http://map.gsfc.nasa.gov/. 1.1, 1.7, 1.3.1.2

[6] R. A. Knop *et al.* New Constraints On Ω_M, Ω_Λ, and w from an Independent Set of 11 High-Redshift Supernovae Observed With the Hubble Space Telescope. *The Astrophysical Journal*, **598**:102–137, 2003. 1.1.1.3, 1.2

[7] A. A. Penzias and R. W. Wilson. A measurement of excess antenna temperature at 4080 mc/s. *The Astrophysical Journal*, **142**:419–421, 1965. 1.1.2.2

[8] J. C. Mather *et al.* A preliminary measurement of the cosmic microwave background spectrum by the Cosmic-Background-Explorer (COBE) satellite. *The Astrophysical Journal*, **354**(2, Part 2):L37–L40, MAY 10 1990. 1.1.2.2

[9] C. L. Bennett *et al.* The Microwave Anisotropy Probe mission. *The Astrophysical Journal*, **583**(1, Part 1):1–23, JAN 20 2003. 1.1.2.2

[10] M. R. Nolta *et al.* Five-Year Wilkinson Microwave Anisotropy Probe Observations: Angular Power Spectra. *The Astrophysical Journal Supplement Series*, **180**:296–305, February 2009. 1.4

[11] A. G. Riess *et al.* Type Ia supernova discoveries at $z > 1$ from the Hubble Space Telescope: Evidence for past deceleration and constraints on dark energy evolution. *The Astrophysical Journal*, **607**(2, Part 1):665–687, JUN 1 2004. 1.5

[12] C. E. Rolfs and W. S. Rodney. *Cauldrons in the Cosmos*. The University of Chicago Press, 1988. 1.1.2.3

[13] R. N. Boyd. *An introduction to nuclear astrophysics*. The University of Chicago Press, 2008. 1.1.2.3

[14] A. G. Riess *et al.* Observational evidence from supernovae for an accelerating universe and a cosmological constant. *Astronomical Journal*, **116**(3):1009–1038, SEP 1998. 1.1.2.3

[15] S. Perlmutter *et al.* Measurements of Omega and Lambda from 42 high-redshift supernovae. *The Astrophysical Journal*, **517**(2, Part 1):565–586, JUN 1 1999. 1.1.2.3

[16] M. Kowalski *et al.* Improved cosmological contraints from new, old, and combined supernova data sets. *The Astrophysical Journal*, **686**(2):749–778, OCT 20 2008. 1.1.2.3, 1.6

[17] Donald Perkins. *Particle Astrophysics*. Oxford University Press, 2003. 1.1.2.3, 1.1.3.1, 1.1.3.4, 1.3.1.2, 1.3.2.1, 1.3.2.2

[18] PJE Peebles and B Ratra. The cosmological constant and dark energy. *Reviews of Modern Physics*, **75**(2):559–606, APR 2003. 1.1.2.3

[19] A. M. Polyakov. Particle Spectrum in Quantum Field-Theory. *JETP LETTERS*, **20**(6):194–195, 1974. 1.1.3.2

[20] KA Milton. Theoretical and experimental status of magnetic monopoles. *Reports on Progress in Physics*, **69**(6):1637–1711, JUN 2006. 1.1.3.2

[21] A.H. Guth. Inflationary universe: A possible solution to the horizon and flatness problems. *Physical Review D*, **23**(2):347–356, 1981. 1.1.3.4

[22] A. B. Linde. A new inflationary universe scenario: A possible solution of the horizon, flatness, homogeneity, isotropy and primordial monopole problems. *Physics Letters B*, **108**(6):389–393, 1982. 1.1.3.4

[23] F. Zwicky. Die Rotverschiebung von extragalaktischen Nebeln. *Helvetica Physica Acta*, **6**:110–127, 1933. 1.2.1.1

[24] AC Fabian and SW Allen. X-rays from clusters of galaxies. In Bandiera, R and Maiolino, R and Mannucci, F, editor, *Texas in Tuscany*, pages 197–208, 2003. 21st Texas Symposium on Relativistic Astrophysics, Florence, ITALY, DEC 09-13, 2002. 1.2.1.1

[25] S. D. M. White *et al.* The Baryon Content of Galaxy Clusters - A Challenge to Cosmological Orthodoxy. *Nature*, **366**(6454):429–433, DEC 2 1993. 1.2.1.1

[26] S. Ettori *et al.* The cluster gas mass fraction as a cosmological probe: a revised study. *Astronomy & Astrophysics*, **501**(1):61–73, jul 2009. 1.2.1.1

[27] S. Ettori, P. Tozzi, and P. Rosati. Constraining the cosmological parameters with the gas mass fraction in local and $z > 0.7$ galaxy clusters. *Astronomy & Astrophysics*, **398**(3):879–890, feb 2003. 1.2.1.1

[28] Marc Kamionkowski. Possible relics from new physics in the early universe: Inflation, the cosmic microwave background, and particle dark matter, 1998. arXiv:astro-ph/9809214v1. 1.8

[29] VC Rubin and WK Ford. Rotation of Andromeda Nebula from a spectroscopic survey of emission regions. *The Astrophysical Journal*, **159**(2):379–&, 1970. 1.2.1.2

[30] A. M Weijmans *et al.* The shape of the dark matter halo in the early-type galaxy NGC 2974. *Monthly Notices of the Royal Astronomical Society*, **383**(4):1343–1358, FEB 1 2008. 1.2.1.3, 1.9

[31] B. H. C. Emonts *et al.* Enormous disc of cool gas surrounding the nearby powerful radio galaxy NGC 612 (PKS 0131-36). *Monthly Notices of the Royal Astronomical Society*, **387**(1):197–208, JUN 11 2008. 1.2.1.3

[32] A. J. Romanowsky *et al.* A dearth of dark matter in ordinary elliptical galaxies. *SCIENCE*, **301**(5640):1696–1698, SEP 19 2003. 1.2.1.3

[33] F. De Lorenzi *et al.* Dearth of dark matter or massive dark halo? Mass-shape-anisotropy degeneracies revealed by NMAGIC dynamical models of the elliptical galaxy NGC 3379. *Monthly Notices of the Royal Astronomical Society*, **395**(1):76–96, MAY 1 2009. 1.2.1.3

[34] *The Hubble Space Telescope webpage.* http://hubblesite.org/gallery/album/entire/pr2008008b/. 1.10

[35] *The Chandra X-Ray Observatory webpage.* http://chandra.harvard.edu/photo/2006/1e0657/. 1.11

[36] Matthias Bartelmann and Peter Schneider. Weak gravitational lensing. *Physics Reports*, **340**(4-5):291 – 472, 2001. 1.2.2

[37] DM Chen. Flux-limited strong gravitational lensing and dark energy. *Astronomy & Astrophysics*, **418**(2):387–392, MAY 2004. 1.2.2

[38] D. Clowe *et al.* A direct empirical proof of the existence of dark matter. *The Astrophysical Journal*, **648**(2, Part 2):L109–L113, SEP 10 2006. 1.2.2

[39] M. Bradac *et al.* Revealing the Properties of Dark Matter in the Merging Cluster MACS J0025.4-1222. *The Astrophysical Journal*, **687**(2):959–967, NOV 10 2008. 1.2.2

[40] D.J. Eisenstein *et al.* Detection of the baryon acoustic peak in the large-scale correlation function of SDSS luminous red galaxies. *The Astrophysical Journal*, **633**(2, Part 1):560–574, NOV 10 2005. 1.2.3

[41] M. Tegmark *et al.* Cosmological constraints from the SDSS luminous red galaxies. *Physical Review D*, **74**(12), DEC 2006. 1.2.3

[42] F. Iocco *et al.* Primordial nucleosynthesis: From precision cosmology to fundamental physics. *Physics Reports*, **472**(1-6):1 – 76, 2009. 1.2.3.1

[43] Gary Steigman. Primordial nucleosynthesis in the precision cosmology era. *Annual Review of Nuclear and Particle Science*, **57**:463–491, 2007. 1.2.3.1

[44] O. Adriani *et al.* An anomalous positron abundance in cosmic rays with energies 1.5-100 GeV. *Nature*, **458**(7238):607–609, APR 2 2009. 1.12, 1.2.4

[45] J. Chang *et al.* An excess of cosmic ray electrons at energies of 300-800 GeV. *Nature*, **456**(7220):362–365, NOV 20 2008. 1.13, 1.2.4

[46] F. Aharonian *et al.* Probing the ATIC peak in the cosmic-ray electron spectrum with HESS. *Astronomy & Astrophysics*, **508**(2):561–564, DEC 2009. 1.2.4, 1.14

[47] A. A. Abdo *et al.* Measurement of the Cosmic Ray e(+)+e(-) Spectrum from 20 GeV to 1 TeV with the Fermi Large Area Telescope. *Physical Review Letters*, **102**(18), MAY 8 2009. 1.2.4

[48] C. Alcock *et al.* The MACHO project: Microlensing results from 5.7 years of Large Magellanic Cloud observations. *The Astrophysical Journal*, **542**(1, Part 1):281–307, OCT 10 2000. 1.3.1.1

[49] C. Afonso *et al.* Limits on Galactic dark matter with 5 years of EROS SMC data. *Astronomy & Astrophysics*, **400**(3):951–956, MAR 2003. 1.3.1.1

[50] P. Tisserand and EROS-2 Collaboration. Limits on the Macho content of the Galactic Halo from the EROS-2 Survey of the Magellanic Clouds. *Astronomy & Astrophysics*, **469**(2):387–U28, JUL 2007. 1.3.1.1

[51] Y. Fukuda *et al.* Evidence for oscillation of atmospheric neutrinos. *Physical Review Letters*, **81**(8):1562–1567, AUG 24 1998. 1.3.1.2

[52] C. Kraus *et al.* Final results from phase II of the Mainz neutrino mass search in tritium beta decay. *European Physical Journal C*, **40**(4):447–468, APR 2005. 1.3.1.2

[53] H. V. Klapdor-Kleingrothaus *et al.* Latest results from the HEIDELBERG-MOSCOW double beta decay experiment. *European Physical Journal A*, **12**(2):147–154, OCT 2001. 1.3.1.2

[54] H. V. Klapdor-Kleingrothaus and I. V. Krivosheina. The evidence for the observation of 0 nu beta beta decay: The identification of 0 nu beta beta events from the full spectra. *Modern Physics Letters A*, **21**(20):1547–1566, JUN 28 2006. 1.3.1.2

[55] S. Abe *et al.* Precision measurement of neutrino oscillation parameters with KamLAND. *Physical Review Letters*, **100**(22):221803, 2008. 1.3.1.2

[56] D. G. Michael *et al.* Observation of muon neutrino disappearance with the minos detectors in the numi neutrino beam. *Physical Review Letters*, **97**(19):191801, 2006. 1.3.1.2

[57] Donald Perkins. *Introduction to High Energy Particle Physics*. Cambridge University Press, 2000. 1.3.2.2, 1.3.2.2

[58] Stephen P. Martin. A supersymmetry primer, 1997. arXiv:hep-ph/9709356v5. 1.3.2.2

[59] H. Murayama. Supersymmetry Phenomenology, 2000. arXiv:hep-ph/0002232v2. 1.15

[60] Nigel Glover. The hunt for the higgs, 2009. Talk given at the University of Edinburgh, http://www.ph.ed.ac.uk/seminars/. 1.16, 1.3.2.2

[61] Gianfranco Bertone, Dan Hooper, and Joseph Silk. Particle dark matter: evidence, candidates and constraints. *Physics Reports*, **405**(5-6):279 – 390, 2005. 1.3.2.2

[62] G. Jungman. Supersymmetric dark matter. *Physics Reports*, **267**:195–373, 1996. 1.3.2.2, 2.2.1, 2.2.1, 2.2.2.1, 2.2.6, 2.2.6

[63] M. Milgrom. A Modification of the Newtonian dynamics as a possible alternative to the hidden mass hypothesis. *The Astrophysical Journal*, **270**(2):365–370, 1983. 1.3.3.1

[64] Garry W. Angus, Huan Yuan Shan, Hong Sheng Zhao, and Benoit Famaey. On the proof of dark matter, the law of gravity, and the mass of neutrinos. *The Astrophysical Journal*, **654**(1, Part 2):L13–L16, JAN 1 2007. 1.3.3.1

[65] Constantinos Skordis. The tensor-vector-scalar theory and its cosmology. *Classical and Quantum Gravity*, **26**(14), JUL 21 2009. 1.3.3.1

[66] C. Ghag. *Simulation, Calibration and Exploitation of the DRIFT-II Directional Dark Matter Detector*. PhD thesis, The University of Edinburgh, 2006. 2.1, 2.2, 6.2, 6.4, 6.2.1.3

[67] Kim Griest. Cross sections, relic abundance, and detection rates for neutralino dark matter. *Phys. Rev. D*, **38**(8):2357–2375, Oct 1988. 2.2.2.1

[68] MA Shifman, AI Vainshtein, and VI Zakharov. Remarks on Higgs-Boson Interactions with nucleons. *Physics Letters B*, **78**(4):443–446, 1978. 2.2.2.1

[69] P.F. Smith J.D. Lewin. Review of mathematics, numerical factors, and corrections for dark matter experiments based on elastic nuclear recoil. *Astroparticle Physics*, **6**:87–112, 1996. 2.2.2.1, 2.2.6

[70] K. A. Olive J. Ellis, A.Ferstl. Exploration of elastic scattering rates for supersymmetric dark matter. *Physical Review D*, **63**, 2001. 2.2.2.2

[71] J. Engel. Nuclear form factors for the scattering of weakly interacting massive particles. *Physics Letters B*, **264**(1,2):114–119, 1991. 2.2.3

[72] V. N. Lebedenko *et al.* Results from the first science run of the ZEPLIN-III dark matter search experiment. *Physical Review D (Particles and Fields)*, **80**(5):052010, 2009. 2.2.4.2, 2.2.4.2, 2.3, 2.3.2.1, 3.1, 3.2, 3.2.1, 3.4, 3.3.2, 3.3.2.2, 3.11, 3.12, 3.5, 3.28, 3.5

[73] P. Sorensen *et al.* The scintillation and ionization yield of liquid xenon for nuclear recoils. *Nuclear Instruments and Methods in Physics Research A*, **601**:339–346, 2009. 2.2.4.2, 2.2.4.2

[74] D. Akimov *et al.* Measurements of scintillation efficiency and pulse shape for low energy recoils in liquid xenon. *Physics Letters B*, **524**(3-4):245 – 251, 2002. 2.2.4.2

[75] E. Aprile *et al.* New measurement of the relative scintillation efficiency of xenon nuclear recoils below 10 keV. *Physical Review C*, **79**(4), APR 2009. 2.2.4.2, 2.2.4.2, 2.3.2.2, 3.2

[76] A Hitachi. Properties of liquid xenon scintillation for dark matter searches. *Astroparticle Physics*, **24**(3):247–256, OCT 2005. 2.2.4.2

[77] A. Manzur *et al.* Scintillation efficiency and ionization yield of liquid xenon for mono-energetic nuclear recoils down to 4 kev, 2009. arXiv:0909.1063. 2.2.4.2, 2.4, 2.2.4.2

[78] E. Aprile, A. E. Bolotnikov, A. I Bolzdynya, and T. Doke. *Noble gas detectors*. Weinheim : Wiley-VCH, 2006. 2.2.4.3, 2.2.4.3, 3.2.1.1, 3.4.1

[79] E. Aprile and T. Doke. Liquid xenon detectors for particle physics and astrophysics. Submitted to Review of Modern Physics, (arXiv:0910.4956v1), 2009. 2.2.4.3, 2.3.2.4, 3.2.1, 3.2.1.1, 3.4

[80] Malcolm Fairbairn and Thomas Schwetz. Spin-independent elastic WIMP scattering and the DAMA annual modulation signal. *JCAP*, **0901**:037, 2009. 2.2.6

[81] Martin C. Smith et al. The RAVE Survey: Constraining the Local Galactic Escape Speed. *Mon. Not. Roy. Astron. Soc.*, **379**:755–772, 2007. 2.2.6

[82] J. Morales *et al.* The canfranc underground laboratory present and future. *Proceedings of the Fifth International Workshop on the Identification of Dark Matter*, **World Scientific**:447–452, 2005. 2.5

[83] D. Yu. Akimov *et al.* The ZEPLIN-III dark matter detector: Instrument design, manufacture and commissioning. *Astroparticle Physics*, **27**(1):46–60, FEB 2007. 2.3.1, 2.3.2.1, 3.2

[84] *Cleveland Potash*. www.clevelandpotash.co.uk. 2.3.2.1

[85] GJ Alner *et al.* Limits on WIMP cross-sections from the NAIAD experiment at the boulby underground laboratory. *Physics Letters B*, **616**(1-2):17–24, JUN 9 2005. 2.3.2.1

[86] NJC. Spooner *et al.* NaI dark matter limits and the NAIAD array - a detector with improved sensitivity to WIMPs using unencapsulated NaI. *Physics Letters B*, **473**(3-4):330–336, FEB 3 2000. 2.3.2.1

[87] B. Ahmed *et al.* The NAIAD experiment for WIMP searches at Boulby mine and recent results. *Astroparticle Physics*, **19**(6):691–702, SEP 2003. 2.3.2.1

[88] http://hepwww.rl.ac.uk/ukdmc/project/ZEPLIN-I/zeplin-i.html. 2.6

[89] G.J. Alner *et al.* First limits on nuclear recoil events from the ZEPLIN I galactic dark matter detector. *Astroparticle Physics*, **23**(5):444–462, JUN 2005. 2.3.2.1, 3.2, 3.2.1.1

[90] G. J. Alner *et al.* The ZEPLIN II dark matter detector: Data acquisition system and data reduction. *Nuclear Instruments & Methods In Physics Research Section A-Accelerators Spectrometers Detectors and Associated Equipment*, **587**(1):101–109, MAR 11 2008. 2.3.2.1

[91] G. J. Alner *et al.* First limits on WIMP nuclear recoil signals in ZEPLIN-II: A two-phase xenon detector for dark matter detection. *Astroparticle Physics*, **28**(3):287–302, NOV 2007. 2.3.2.1, 3.2, 3.4.4

[92] DP Snowden-Ifft, CJ Martoff, and JM Burwell. Low pressure negative ion time projection chamber for dark matter search. *Physical Review D*, **61**(10), MAY 15 2000. 2.3.2.1

[93] G. J. Alner *et al.* The DRIFT-I dark matter detector at Boulby: design, installation and operation. *Nuclear Instruments & Methods In Physics Research Section A-Accelerators Spectrometers Detectors and Associated Equipment*, **535**(3):644–655, DEC 21 2004. 2.3.2.1

[94] G.J. Alner *et al.* The DRIFT-II dark matter detector: Design and commissioning. *Nuclear Instruments & Methods In Physics Research Section A-Accelerators Spectrometers Detectors and Associated Equipment*, **555**(1-2):173–183, DEC 15 2005. 2.3.2.1

[95] S. Burgos *et al.* First measurement of the head-tail directional nuclear recoil signature at energies relevant to WIMP dark matter search. *Astroparticle Physics*, **31**(4):261–266, MAY 2009. 2.3.2.1

[96] S. Burgos *et al.* Measurement of the range component directional signature in a DRIFT-II detector using Cf-252 neutrons. *Nuclear Instruments & Methods In Physics Research Section A-Accelerators Spectrometers Detectors and Associated Equipment*, **600**(2):417–423, MAR 1 2009. 2.3.2.1

[97] *LNGS*. http://www.lngs.infn.it/. 2.3.2.2

[98] L. Baudis. WIMP searches with liquid xenon: The XENON10 experiment. *PoS*, **HEP2005**:006, 2006. 2.8

[99] E. Aprile *et al.* The XENON dark matter search experiment. *New Astronomy Reviews*, **49**(2-6):289–295, MAY 2005. 6th UCLA Symposium on Sources and Detection of Dark Matter and Dark Energy in the Universe, Marina del Rey, CA, FEB 18-20, 2004. 2.3.2.2, 3.4, 3.4.4

[100] J. Angle *et al.* First results from the XENON10 dark matter experiment at the Gran Sasso National Laboratory. *Physical Review Letters*, **100**(2), JAN 18 2008. 2.3.2.2

[101] J. Angle *et al.* Limits on spin-dependent WIMP-nucleon cross sections from the XENON10 experiment. *Physical Review Letters*, **101**(9), AUG 29 2008. 2.3.2.2

[102] R. Bernabei *et al.* Searching for WIMPs by the annual modulation signature. *Physics Letters B*, **424**(1-2):195–201, APR 2 1998. 2.3.2.2

[103] R. Bernabei *et al.* First results from DAMA/LIBRA and the combined results with DAMA/NaI. *European Physical Journal C*, **56**(3):333–355, AUG 2008. 2.9, 2.3.2.2

[104] R. Bernabei et al. Dark matter search. *Riv. Nuovo Cim.*, **26N1**:1–73, 2003. 2.3.2.2

[105] R. Bernabei *et al.* Dark matter particles in the galactic halo: Results and implications from DAMA/NaI. *International Journal of Modern Physics D*, **13**(10):2127–2159, DEC 2004. 2.3.2.2

[106] R. Bernabei *et al.* The dama/libra apparatus. *Nuclear Instruments and Methods in Physics Research Section A: Accelerators, Spectrometers, Detectors and Associated Equipment*, **592**(3):297 – 315, 2008. 2.3.2.2

[107] John March-Russell, Christopher McCabe, and Matthew McCullough. Inelastic dark matter, non-standard halos and the DAMA/LIBRA results. *Journal of High Energy Physics*, **2009**(05):071, 2009. 2.3.2.2

[108] D. B. Cline, W. Ooi, and H. Wang. A constrain on inelastic dark matter signal using ZEPLIN-II results, 2009. arXiv:0906.4119v3. 2.3.2.2

[109] R. Bernabei *et al.* The liquid xenon set-up of the DAMA experiment. *Nuclear Instruments & Methods In Physics Research Section A-Accelerators Spectrometers Detectors and Associated Equipment*, **482**(3):728–743, APR 21 2002. 2.3.2.2

[110] R.J. Gaitskill *et al.* Studies of the dead layer in BLIP dark matter detectors. In Cooper S, editor, *Proceedings of the Seventh International Workshop on Low Temperature Detectors*, pages 221–223, 1997. Seventh International Workshop on Low Temperature Detectors, Munich, 1997. 2.3.2.3

[111] R. Abusaidi *et al.* Exclusion limits on the WIMP-nucleon cross section from the Cryogenic Dark Matter Search. *Physical Review Letters*, **84**(25):5699–5703, JUN 19 2000. 2.3.2.3

[112] D. S. Akerib *et al.* Exclusion limits on the WIMP-nucleon cross section from the first run of the Cryogenic Dark Matter Search in the Soudan Underground Laboratory. *Physical Review D*, **72**(5), SEP 2005. 2.3.2.3

[113] Z. Ahmed *et al.* Search for Weakly Interacting Massive Particles with the First Five-Tower Data from the Cryogenic Dark Matter Search at the Soudan Underground Laboratory. *Physical Review Letters*, **102**(1), JAN 9 2009. 2.3.2.3, 3.2

[114] The CDMS Collaboration and Z. Ahmed. Results from the final exposure of the CDMS II experiment, 2009. arXiv:0912.3592v1. 2.3.2.3, 4.1, 6.1, 6.8.1, 6.10, 7

[115] Ko Abe and XMASS collaboration. The XMASS Experiment - art. no. 042022. In Inoue, K and Suzuki, A and Mitsuri, T, editor, *TAUP2007:*

Tenth International Conference on Topics in Astroparticle and Underground Physics, volume 120 of *Journal of Physics Conference Series*, page 42022, 2008. Sendai, JAPAN, SEP 11-15, 2007. 2.3.2.4

[116] *LUX*. http://lux.brown.edu/index.html. 2.3.2.4

[117] A. Benoit *et al.* First results of the EDELWEISS WIMP search using a 320 g heat-and-ionization ge detector. *Physics Letters B*, **513**(1-2):15 – 22, 2001. 2.3.2.4

[118] V. Sanglard *et al.* Final results of the EDELWEISS-I dark matter search with cryogenic heat-and-ionization Ge detectors. *Physics Review D*, **71**(12), JUN 2005. 2.3.2.4

[119] E. Armengaud *et al.* First results of the EDELWEISS-II WIMP search using Ge cryogenic detectors with interleaved electrodes, 2009. 2.3.2.4

[120] G. Angloher *et al.* Limits on WIMP dark matter using sapphire cryogenic detectors. *Astroparticle Physics*, **18**(1):43–55, AUG 2002. 2.3.2.4

[121] G. Angloher *et al.* Commissioning run of the CRESST-II dark matter search. *Astroparticle Physics*, **31**(4):270 – 276, 2009. 2.3.2.4

[122] M. Bravin *et al.* The CRESST dark matter search. *Astroparticle Physics*, **12**(1-2):107–114, OCT 1999. 2.3.2.4

[123] G. Angloher *et al.* Limits on WIMP dark matter using scintillating CaWO4 cryogenic detectors with active background suppression. *Astroparticle Physics*, **23**(3):325–339, APR 2005. 2.3.2.4

[124] H. Kraus *et al.* EURECA - the European future of dark matter searches with cryogenic detectors. *Nuclear Physics B-Proceedings Supplements*, **173**:168–171, NOV 2007. 7th UCLA Symposium on Sources and Detection of Dark Matter and Dark Energy in the Universe, Marina del Rey, CA, FEB 22-24, 2006. 2.3.2.4

[125] MG Boulay and A Hime. Technique for direct detection of weakly interacting massive particles using scintillation time discrimination in liquid argon. *Astroparticle Physics*, **25**(3):179–182, APR 2006. 2.3.2.4

[126] M. G. Boulay *et.al.* Measurement of the scintillation time spectra and pulse-shape discrimination of low-energy beta and nuclear recoils in liquid argon with DEAP-1, 2009. arXiv:0904.2930v1. 2.3.2.4

[127] K. Borer *et al.* First results with the ORPHEUS dark matter detector. *Astroparticle Physics*, **22**(2):199 – 210, 2004. 2.3.2.4

[128] K. Borer *et al.* Recent results from the ORPHEUS dark matter experiment. *Nuclear Physics B - Proceedings Supplements*, **138**:163 – 165, 2005. Proceedings of the Eighth International Workshop on Topics in Astroparticle and Underground Physics. 2.3.2.4

[129] S. Yoshida *et al.* Search for wimps with the large NaI(Tl) scintillator of ELEGANT V. *Nuclear Physics B - Proceedings Supplements*, **87**(1-3):58 – 60, 2000. Proceedings of the Sixth International Workshop on Topics in Astroparticle and Underground Physics. 2.3.2.4

[130] H. Nishimura *et al.* A Direction-Sensitive Dark Matter Search Experiment (NEWAGE). In *The Physical Society of Japan*, pages 218–220, 2009. Proceedings of the International Workshop in Advances in Cosmic Ray Science. 2.3.2.4

[131] M. Barnab-Heider *et al.* Improved spin-dependent limits from the PICASSO dark matter search experiment. *Physics Letters B*, **624**(3-4):186 – 194, 2005. 2.3.2.4

[132] P. Benetti *et al.* First results from a dark matter search with liquid argon at 87 K in the gran sasso underground laboratory. *Astroparticle Physics*, **28**(6):495 – 507, 2008. 2.3.2.4

[133] H. V. Klapdor-Kleingrothaus, A. Dietz, and I. V. Krivosheina. Search for cold and hot dark matter with the heidelberg-moscow experiment, hdms, genius and genius-tf. *Nuclear Physics B - Proceedings Supplements*, **124**:209 – 213, 2003. Proceedings of the 5th International UCLA Symposium on Sources and Detection of Dark Matter and Dark Energy in the Universe. 2.3.2.4

[134] RJ Gaitskell. Direct detection of dark matter. *Annual Review of Nuclear and Particle Science*, **54**:315–359, 2004. 2.3.2.4

[135] Dmitry Akimov. Detectors for Dark Matter search (review). *Nuclear Instruments & Methods In Physics Research Section A-Accelerators Spectrometers Detectors and Associated Equipment*, **598**(1):275–281, JAN 1 2009. 2.3.2.4, 3.2.1

[136] V. N. Lebedenko *et al.* Limits on the spin-dependent WIMP-nucleon cross sections from the first science run of the ZEPLIN-III experiment. *Physical Review Letters*, **103**(15):151302, 2009. 3.1, 3.5, 3.29

[137] R. Trotta, F. Feroz, M. Hobson, L. Roszkowski, and R.R. de Austri. The impact of priors and observables on parameter inferences in the constrained MSSM. *Journal of High Energy Physics*, (12):024, DEC 2008. 3.2

[138] Enrico Conti's Liquid Xenon Page. www.pd.infn.it/ conti/LXe.html. 3.1

[139] T Doke and K Masuda. Present status of liquid rare gas scintillation detectors and their new application to gamma-ray calorimeters. *Nuclear Instruments & Methods In Physics Research Section A-Accelerators Spectrometers Detectors and Associated Equipment*, **420**(1-2):62–80, JAN 1 1999. 3.2.1.1

[140] S Kubota, M Hishida, and JZ Raun. Evidence for a triplet-state of self-trapped exciton-states in liquid Argon, Krypton and Xenon. *Journal of Physics C-Solid State Physics*, **11**(12):2645–2651, 1978. 3.2.1.1

[141] R. L. Platzman. Total ionization in gases by high-energy particles - an appraisal of our understanding. *International journal of applied radiation and isotopes*, **10**(2-3):116–&, 1961. 3.2.1.1

[142] *SAES getters*. http://www.saesgetters.com/. 3.2.5

[143] S. J. S. Plank. *The DRIFT Dark Matter Project: Directionality, Sensitivity, and Environmental Backgrounds*. PhD thesis, The University of Edinburgh, http://hdl.handle.net/1842/3128, 2008. 3.2.8, 4.2

[144] Laura Baudis. The XENON10 WIMP search experiment at the Gran Sasso Underground Laboratory. *J. Phys. Conf. Ser.*, **65**:012015, 2007. 3.4

[145] G Bakele, U Sowada, and WF Schmidt. Effect of an electric-field on electron-attachment to SF_6, N_2O, and o_2 in liquid argon and xenon. *Journal of physical chemistry*, **80**(23):2556–2559, 1976. 3.25, 3.4.4

[146] *Rutherford Appleton Laboratories Type 71 Mix Epoxy:*. www.rl.ac.uk. 4.2.1

[147] *The Institute of Scintillating Materials, Kharkov, Ukraine.* http://www.isc.kharkov.com/english/. 4.2.2.1, 4.1, 4.2.2.2, 5.3.1, 5.3.2.4, 6.4.1

[148] E. J. Barnes. A high efficiency veto to increase the sensitivity of ZEPLIN-III, a WIMP detector. volume 1166, pages 230–235. AIP, 2009. 4.2.2.2

[149] *Saint Gobain Ceramics & Plastics, Inc.* http://www.detectors.saint-gobain.com/Detector-Assembly-Materials.aspx. 4.2.2.2, 4.2.2.3

[150] *Electron Tubes Ltd.*
9302 B series datasheet: *www.electrontubes.com.* 4.2.4, 5.2.1

[151] *M. I. Cables Ltd.* http://www.micables.ltd.uk/. 4.2.5

[152] *U.S. Geological Survey. http : //gulfsci.usgs.gov/tampabay/data/2_biogeochemical_cycles/radionuclides.html*. 4.13

[153] A. Artikov *et.al.* Properties of the ukraine olystyrene-based plastic scintillator ups 923a. *Nuclear Instruments & and Methods in Physics Research*, **555**:125–131, 2005. 5.3.1

[154] V. Senchyshyn *et al.* Accounting for self-absorption in calculation of light collection in plastic scintillators. *Nuclear Instruments and Methods in Physics Research Section A: Accelerators, Spectrometers, Detectors and Associated Equipment*, **566**(2):286 – 293, 2006. 5.3.1

[155] *Ortec.* http://www.ortec-online.com/. 5.3.1.1

[156] S. Agostinelli *et al.* G4–a simulation toolkit. *Nuclear Instruments and Methods in Physics Research Section A: Accelerators, Spectrometers, Detectors and Associated Equipment*, **506**(3):250 – 303, 2003. 5.3.3.1, 6.2

[157] J. Allison *et al.* Geant4 developments and applications. *Nuclear Science, IEEE Transactions on*, **53**(1):270–278, Feb. 2006. 5.3.3.1, 6.2

[158] *The GEANT 4 webpage*. http://www.geant4.org/geant4/. 5.3.3.1, 5.3.3.2, 6.2

[159] Eugene Hecht. *Optics (4th Edition)*. Addison Wesley, 4 edition, August 2001. 5.3.3.2

[160] A Levin and C Moisan. A more physical approach to model the surface treatment of scintillation counters and its implementation into DETECT. In DelGuerra, A, editor, *1996 IEEE Nuclear Science Symposium - Conference Record, Vols 1-3*, IEEE Nuclear Science Symposium - Conference Record, pages 702–706, 1997. 1996 IEEE Nuclear Science Symposium and Medical Imaging Conference, ANAHEIM, CA, NOV 02-09, 1996. 5.3.3.2

[161] H. M. Araujo *et al.* The ZEPLIN-III dark matter detector: Performance study using an end-to-end simulation tool. *Astroparticle Physics*, **26**(2):140–153, SEP 2006. 6.1, 6.2

[162] W.B. Wilson *et al.* Sources: A code for calculating (α,n), spontaneous fission, and delayed neutron sources and spectra. *Progress in Nuclear Energy*, **51**(4-5):608 – 613, 2009. 6.3, 6.8.1

[163] H. M. Araujo. *private communication*, 2006. 6.4.2

[164] S. Agostinelli *et al.* Geant4 - a simulation toolkit. *Nuclear Instruments and Methods in Physics Research A*, **506**(3):250–303, 2003. 6.6.1

[165] K. S. Krane. *Introductory nuclear physics*. John Wiley and Sons, ltd, 1987. 6.6.3